New Type of sub-THz Oscillator and Amplifier Systems Based on Helical-Type Gyro-TWTs

Zur Erlangung des akademischen Grades eines

DOKTORS DER INGENIEURWISSENSCHAFTEN (Dr.-Ing.)

von der KIT-Fakultät für Elektrotechnik und Informationstechnik des Karlsruher Instituts für Technologie (KIT)

genehmigte

DISSERTATION

von

M.Sc. Alexander Marek
geb. in Heilbronn-Neckargartach

Tag der mündlichen Prüfung: 19.07.2022

Hauptreferent: Prof. Dr.-Ing. John Jelonnek
Korreferent: Prof. a.D. Dr.-Ing. Arne Jacob

Foreword of the Editor

The generation of picosecond pulses at high powers in the sub-THz range is of interest for a wide variety of applications including radar, communications, particle accelerators, and spectroscopy. Many applications require furthermore phase stability and a high coherence of the generated pulses. Among the most exciting applications for pulsed high-power sub-THz sources are novel time-domain pulsed dynamic nuclear polarization (DNP), nuclear magnetic resonance (NMR) spectroscopy methods.

Microwave-driven DNP experiments are enhancing signals in the solid state and solution NMR and imaging by a factor of more than 100. However, to date, only CW sources are available for the generation of the required high-power microwave. The development of pulsed sources with the ability to generate pulse sequences at the relevant frequencies would further improve the resolution and sensitivity. Sources based on gyro-devices are the most promising technology because they offer the possibility of achieving a high power and broad bandwidth even when the frequency of operation moves into the upper sub-THz band.

A technique for generating ultra-short coherent pulses has been recently shown in the Ka-band. By utilizing the effect of passive mode-locking, well known from laser physics, ultra-short coherent high-power microwave pulses can be generated by a source consisting of two electron vacuum tube amplifiers coupled in a feedback loop. Assuming commercially available systems starting from a NMR frequency of 400 MHz, the corresponding microwave sources must operate at 263 GHz and above. Therefore, Dr.-Ing. Alexander Marek has driven the basic idea of mode-locked electron tubes to sub-THz frequencies for the first time.

In order to achieve this aim, a fundamental investigation of the mode-locking method has been carried out. The models developed in laser physics are used, and subsequently adapted and extended to meet the specific requirements.

Furthermore, completely new simulation models and software were developed both for the design of the individual key components and for the complete mode-locked oscillator.

Based on a novel feedback system, Dr.-Ing. Alexander Marek has extended the original concept of a passive mode-locked microwave oscillator to a innovative multi-propose sub-THz source. The multi-propose source allows an operation of two coupled helical gyro-TWTs as a passive mode-locked oscillator, an active mode-locked oscillator, a CW oscillator, and a two-stage amplifier.

The results of this work therefore present a key step towards the first time-domain DNP-NMR spectrometer. Furthermore, Dr.-Ing. Alexander Marek is providing the community of gyrotrons and gyro-devices essential tools for the design and analysis of the beam-wave interaction and future design of quasi-optical components. They will help to analyze and to design advanced high-power sub-THz sources for future novel applications including radar, communications, particle accelerators, and spectroscopy.

Zusammenfassung

Systeme, die in der Lage sind, ultrakurze Hochfrequenz (HF)-Pulse im Sub-THz-Bereich kohärent zu erzeugen und gleichzeitig eine Ausgangsleistung von mehr als einigen Watt zu erreichen, gewinnen in der Forschung zunehmend an Interesse. Diese HF-Systeme könnten die Schlüsselkomponente möglicher zukünftiger THz-Diagnosesysteme werden. Beispiele sind neuartige gepulste Dynamic Nuclear Polarization (DNP)-Nuclear Magnetic Resonance (NMR) Spektroskopiemethoden oder die Diagnostik von dichten Plasmen. In jedem Fall würden neuartige, leistungsstarke HF-Quellen für ultrakurze, kohärente Pulse im Millimeter- und Submillimeter-Frequenzbereich die Wissenschaft in die Lage versetzen, neue Messgeräte mit verbesserter Empfindlichkeit, Auflösung und Datenerfassungsgeschwindigkeit zu entwickeln.

Im Rahmen dieser Arbeit wird die Entwicklung und systematische Untersuchung einer neuartigen Sub-THz-Quelle zur Erzeugung von kohärenten, ultrakurzen Hochleistungspulsen bei 263 GHz vorgestellt. Der Pulserzeugungsmechanismus basiert auf dem Prinzip der passiven Modenkopplung von zwei Gyrotron-Wanderwellenröhren mit helikalem Wechselwirkungsbereich (helical Gyro-TWT). Die betrachtete Frequenz von 263 GHz ist ein etablierter Wert für klassische DNP-NMR-Anwendungen mit kontinuierlicher Mikrowelleneinstrahlung (CW DNP-NMR). Dies soll, basierend auf existierendem Equipment, eine möglichst einfache Entwicklung neuartiger Spektroskopiemethoden wie DNP-NMR im Zeitbereich ermöglichen.

In dieser Arbeit wird zum ersten Mal gezeigt, dass für die Erzeugung von Pulsen mit höchster Kohärenz ein Betrieb der gekoppelten helical Gyro-TWTs mit externer Anregung (hard excitation regime) nötig ist. Weil bisher nur Konzepte für den Betrieb von passiv modengekoppelten helical Gyro-TWTs mit Selbstanregung (soft excitation regime) existieren, wird im Rahmen dieser Arbeit ein neuer, erweiterter, passiver modengekoppelter Oszillator vorgeschlagen, der auch einen Betrieb mit externer Anregung ermöglicht. Darüber hinaus ermöglicht der erweiterte passive modengekoppelte Oszillator die Erzeugung

spezifischer Pulsfolgen, zusätzlich zur Erzeugung von Pulsen mit konstanter Wiederholungsfrequenz. Dies könnte für einige neuartige DNP-NMR-Methoden im Zeitbereich, bei denen wohldefinierte Pulssequenzen erforderlich sind, von besonderem Interesse sein.

Weitere Vorteile für künftige Spektroskopieanwendungen ergeben sich aus einem neuartigen Rückkopplungssystem, welches ebenfalls im Rahmen dieser Arbeit entwickelt wurde. Das entwickelte Rückkopplungssystem ermöglicht alternative Betriebsmodi für zwei gekoppelte helical Gyro-TWTs. Neben dem ursprünglichen Ziel der Pulserzeugung im modengekoppelten Oszillator, erlaubt das entwickelte Rückkopplungssystem die Realisierung eines zweistufigen Verstärkers und die Möglichkeit, die Bauelemente als frequenzabstimmbare, phasengekoppelte Rückwärtswellenoszillatoren (BWO) zu betreiben, um ein CW Signal zu erzeugen.

Mit dem erweiterten, passiven modengekoppelten Oszillator und dem neuartigen Rückkopplungssystem ist ein solches System aus gekoppelten helical Gyro-TWTs eine vielversprechende, neuartige HF Hochleistungsquelle für zukünftige Anwendungen in der Zeitbereichsspektroskopie.

Abstract

Systems which are capable to generate ultra-short radio frequency (RF) pulses coherently, and, at the same time, achieve a reasonable output power of more than a few Watts in the sub-THz frequency range are gaining fundamental interest in the research community. Those RF systems might become the key components of possible future THz diagnostic systems. Examples are novel pulsed Dynamic Nuclear Polarization (DNP)-Nuclear Magnetic Resonance (NMR) spectroscopy methods and diagnostics of dense plasmas. In all cases, novel powerful RF sources of ultra-short coherent pulses in the millimeter and sub-millimeter frequency range would enable the scientific community to develop new devices with performance improvements in the areas of sensitivity, resolution and data acquisition speed.

This work presents the development and systematic investigation of a new sub-THz source for the generation of trains of coherent high-power ultra-short pulses at 263 GHz via passive mode-locking of two coupled helical gyrotron traveling wave tubes (helical gyro-TWT). The investigated frequency of 263 GHz is an established figure for continuous wave (CW) DNP-NMR application and, therefore, the investigated source will allow the development of novel spectroscopy methods such as time-domain DNP-NMR for which powerful sub-THz pulses with highest coherency are required.

For the first time, it is shown that the operation of the passive mode-locked helical gyro-TWTs in the hard excitation regime is of particular importance to reach the optimal coherency of the generated pulses. To enable the operation in the hard excitation regime, a new extended passive mode-locked oscillator is proposed. The extended passive mode-locked oscillator will furthermore enable the generation of specific pulse sequences in addition to the generation of pulses with constant repetition frequency. This could be of particular interest for some time-domain DNP-NMR methods where well-defined pulse sequences are required.

Further benefits for future spectroscopy applications are provided by a novel feedback system. The developed feedback system enables alternative operation regimes for the two coupled helical gyro-TWTs. Besides the original purpose as mode-locked oscillator, the developed feedback system allows the realization of a two-stage amplifier and the possibility of operating the devices as frequency-tunable, phase-locked backward wave oscillators (BWO).

In combination, the extended passive mode-locked oscillator together with the novel feedback system makes such a system of coupled helical gyro-TWTs a very promising new high-power source for future time-domain spectroscopy applications.

Contents

Abbreviations

ACA	Adaptive Cross Approximation
ACA-SVD	Adaptive Cross Approximation with additional Singular Value Decomposition
BBC	Broadband Boundary Condition
BWO	Backward Wave Oscillator
CAP	Complex Absorbing Potential
CPU	Central Processing Unit
CUSP-gun	CUSP-type electron gun
CW	Continuous Wave
ECRH	Electron Cyclotron Resonance Heating
EFIE	Electric Field Integral Equation
FGMRES	Flexible Generalized Minimal Residual Method
FMM	Fast Multipole Method
FT	Fourier Transformation
FWHM	Full Width at Half Maximum
GMRES	Generalized Minimal RESidual method

GPU	Graphic Processing Unit
GSM	Generalized Scattering Matrix
GVD	Group Velocity Dispersion
gyro-TWT	GYROtron Traveling Wave Tube
helical gyro-TWT	GYROtron Traveling Wave Tube with helically corrugated waveguide
HME	Haus Master Equation
HOBF	Higher-Order Basis Functions
LOB	Large Orbit Beam
MFIE	Magnetic Field Integral Equation
MIG	Magnetron Injection Gun
MLFMM	Multilevel Fast Multipole Method
MOM	Method Of Moments
ODE	Ordinary Differential Equation
PEC	Perfect Electric Conductor
PIC	Particle In Cell
PRF	Pulse Repetition Frequency
RF	Radio Frequency
RK	Runge-Kutta method
RMSE	Root-Mean-Square Error

RWG	Rao-Wilton-Glisson basis functions
SACA	Sparsified Adaptive Cross Approximation
SAM	Self Amplitude Modulation
SIMD	Single Instruction-Multiple-Data
SP-ITER Gyrotron	Short Pulse ITER Gyrotron
SSFM	Split-Step Fourier Method
SVD	Singular Value Decomposition
TWT	Traveling Wave Tube
W7-X	Wendelstein 7-X stellarator

List of Symbols

In the following a list of the symbols used in this thesis is given. In this work, the following notation is used:

- scalars are written in *italics* (e.g. x),
- vectors are written in **bold** *italics* (e.g. $\boldsymbol{x}$),
- matrices are written in underlined CAPITAL *italics* (e.g. $\underline{X}$),
- real vector fields in the time-space domain are written in **bold** Fraktur letters (e.g. $\mathfrak{E}$),
- scalar fields and the norm of vector fields in the time-space domain are written in Fraktur letters (e.g. $\mathfrak{E}$),
- complex quantities are indicated by an overline (e.g. $\bar{x}$, $\overline{\boldsymbol{E}}$),
- mathematical functions are written in upright letters (e.g. $\mathrm{sin}()$),
- differential operators are written in calligraphic letters (e.g. $\mathcal{L}$).

Well defined mathematical symbols such as $\mathrm{sin}()$ and $\mathrm{cos}()$ are omitted in the following list.

Mathematical Constants and Operators

j	imaginary unit
δ	Dirac delta function
$\delta_{m,n}$	Kronecker delta function
∇	nabla operator
∇^2, $\nabla_\perp^2$	Laplace operator and transversal Laplace operator
$\mathcal{F}$	Fourier transformation

$O, \mathcal{K}, \mathcal{N}$	generic, generic linear and generic non-linear operator
J_n	n-th Bessel function of the first kind
H	Heaviside step function

Physical Constants

c_0	vacuum speed of light (299792458 m/s)
ϵ_0	vacuum permittivity ($8.8541878128(13) \cdot 10^{-12}\,\mathrm{F{\cdot}m^{-1}}$)
μ_0	vacuum permeability ($1.25663706212(19) \cdot 10^{-6}$ H/m)
Z_0	vacuum impedance ($\pi \cdot 119.9169832\,\Omega$)
e_0	elementary charge ($1.602176634 \cdot 10^{-19}$ C)
m_e	mass of an electron ($9.1093837015(28) \cdot 10^{-31}$ kg)

Coordinates

t	time
x, y, z	Cartesian coordinates
r, ϕ	polar coordinates
$\hat{\boldsymbol{x}}, \hat{\boldsymbol{y}}, \hat{\boldsymbol{z}}$	Cartesian unity vectors
$\hat{\boldsymbol{n}}$	normal unity vector

Fields and Currents

$\mathfrak{E}, \mathfrak{E}_\perp$	electric field and transversal electric field
$\mathfrak{E}^i, \mathfrak{E}^r, \mathfrak{E}^s$	incident, radiated and scattered electric field
$\mathfrak{B}, \mathfrak{B}_\perp$	magnetic flux density and transversal magnetic flux density
$\mathfrak{B}_0$	static magnetic flux density
$\mathfrak{H}, \mathfrak{H}_\perp$	magnetic field strength and transversal magnetic field strength
$\mathfrak{H}_0$	static magnetic field strength
$\mathfrak{A}$	magnetic vector potential
$\mathfrak{V}$	scalar electric potential
Ψ	magnetic flux
$\mathfrak{J}, \mathfrak{J}_\perp$	electric current density and transversal electric current density

$\mathcal{J}_\mathrm{s}$	surface current density

Waveguide Modes

Z, η	impedance and intrinsic impedance
ω, $\Delta\omega$	angular frequency and difference between two angular frequencies
λ	wavelength
v_p, v_g	phase and group velocity of a wave
k, $k_\perp$, $k_\parallel$	wavenumber, perpendicular wavenumber and axial wavenumber
ω_A, ω_B	cut-off frequency of the waveguide eigenmodes A and B
$k_{\perp\mathrm{A}}$, $k_{\perp\mathrm{B}}$	perpendicular wavenumbers of the waveguide eigenmodes A and B
$k_{\parallel\mathrm{A}}$, $k_{\parallel\mathrm{B}}$	axial wavenumbers of the waveguide eigenmodes A and B
$k_{\parallel\mathrm{B}'}$	axial wavenumber of the backward mode B
χ	eigenvalue of a TM mode in a cylindrical waveguide (root of the Bessel function)
χ'	eigenvalue of a TE mode in a cylindrical waveguide (root of the derivative of the Bessel function)
χ'_A, χ'_B	eigenvalues of the TE modes A respectively B
P_RF	transmitted power in a RF wave
$C_\mathrm{A,B}$	coupling coefficient between two eigenmodes A and B of a cylindrical waveguide
C_ellip	coupling coefficient of O and X mode in an elliptical waveguide
$\hat{\boldsymbol{e}}$	orthonormal eigenmode of a waveguide
m_A, m_B	radial index of mode A respectively mode B
ψ	arbitrary phase constant

Slowly Varying Amplitudes

f_0, ω_0	carrier frequency and angular carrier frequency
k_0, $k_{0\parallel}$	free-space and axial wavenumber at the carrier frequency

$k_{0\parallel\mathrm{A}}$, $k_{0\parallel\mathrm{B}}$	axial wavenumbers of the waveguide eigenmodes A and B at the carrier frequency
$\overline{A}$, $\overline{B}$	slowly changing, complex amplitude of mode A respectively mode B
$\tilde{A}$, $\tilde{B}$	FT of the slowly changing, complex amplitude of mode A respectively mode B
a, b	constant amplitude of mode A respectively mode B
Ω	expansion frequency of the wave envelope
ω_m	maximum angular frequency
$\bar{S}$	source term in the Helmholtz equation

Passive Mode-Locked Oscillator

f_r	pulse repetition frequency
W	energy
W_g, W_l	saturation energy of an amplifier respectively an absorber
$P_\mathrm{g,sat}$, $P_\mathrm{l,sat}$	saturation power of an amplifier respectively an absorber
T	long-term time
T_0	initial long-term time
ΔT	long-term time-step
T_r	round-trip time
T_A	relaxation time of an absorber

Parameters for the Haus Master Equation

g_0, g_i, g_s	constant gain, initial gain and saturated gain
l_0, l_i	constant losses and initial losses
l_out, l_slow	linear losses in a feedback system and losses of a slow absorber
I, I_sat	intensity and saturation intensity
s_self	self amplitude modulation coefficient
$\Delta\overline{A}_\mathrm{b}$	change of the amplitude because of bandwidth limitations
ω_b	bandwidth of a bandwidth limited device
$\Delta\overline{A}_\mathrm{disp}$	change of the amplitude because of dispersion effects
d_0	dispersion factor

$\Delta\overline{A}_{\mathrm{g,lin}}$, $\Delta\overline{A}_{\mathrm{g,slow}}$	change of the amplitude because of linear and slow gain
$\Delta\overline{A}_{\mathrm{l,lin}}$, $\Delta\overline{A}_{\mathrm{l,sat}}$, $\Delta\overline{A}_{\mathrm{l,slow}}$	change of the amplitude because of linear, saturated and slow losses
$\Delta\overline{A}_{\mathrm{shift}}$	change of the amplitude because of a time shift
t_{s}	time-shift time

Ultra-Short Pulses

W_{P}	total energy in a pulse
τ_{p}	pulse length
ω_{p}	angular spectral pulse width
c_{p}	minimum possible time-bandwidth product

Parameter of Helical Gyro-TWTs and Gyrotrons

R	radius of a cylindrical waveguide
L	length of a waveguide section
$\tilde{r}$	corrugation amplitude of a helically corrugated waveguide
$\tilde{d}$	corrugation period of a helically corrugated waveguide
$\tilde{k}_{\parallel}$	corrugation wavenumber of a helically corrugated waveguide
$\tilde{m}$	fold number of a helically corrugated waveguide

Electron Beam

γ	Lorentz factor
r_0	initial radius of an electron beam before as magnetic CUSP
r_{L}	Larmor radius or cyclotron radius
r_{g}	guiding center radius
r_{b}	radius of a halo beam
r_{th}	threshold radius if a magnetic CUSP
q	charge of a particle

ρ	charge density
v, $v_\perp$, $v_\parallel$	relativistic velocity and its perpendicular and axial components
p, $p_\perp$, $p_\parallel$	relativistic momentum and its perpendicular and axial components
$\bar{P}_\perp$	slow varying momentum transversal to the z axis
ω_H	cyclotron frequency of gyrating electrons
$\Delta\omega_\mathrm{H}$	cyclotron frequency missmatch
Δ_c	cyclotron resonance detuning
C	coupling coefficient of a gyrating electron beam with a TE mode of a cylindrical waveguide
α	pitch factor of an electron
I	electric current
U_b	beam voltage
E_kin	kinetic energy
m	mass
x_mean, δx	mean and relative spread of a value
$\Delta\Theta$	relative angle between the traversal momentum and the transversal electric field
$I_\perp$	perpendicular adiabatic invariant
L	Lagrangian of a relativistic electron
P	power
s	cyclotron harmonic number

Generalized Scattering Matrix Formalism

$\underline{S}$, $\underline{S_{11}}$, $\underline{S_{12}}$, $\underline{S_{21}}$, $\underline{S_{22}}$	scattering matrices
$\underline{Y}$	admittance matrix
$\underline{K_1}$, $\underline{K_2}$	intermediate matrices for the calculation of scattering matrices
$\underline{C}$	mode coupling matrix
$\boldsymbol{F}$, $\boldsymbol{B}$	vector of modes which travel in positive z direction (forward) respectively in negative z direction (backward)

Dielectric Windows and Lossy Conductors

c	speed of light in a medium
μ	absolute permeability
ϵ	absolute permittivity
$\bar{\epsilon}_{\mathrm{r}}$, $\epsilon_{\mathrm{r}}^{'}$, $\epsilon_{\mathrm{r}}^{''}$	complex relative permittivity and its real respectively imaginary part
$\bar{\gamma}_{\epsilon}$	complex propagation constant in a dielectric material
α_{ϵ}, β_{ϵ}	attenuation and phase constant in a dielectric material
$\tan(\delta)$	a measure of loss-rate of energy of a dissipative system
d_{w}	thickness of a window
f_{trans}	transparent frequency of a single disk window
$\underline{S}_{\mathrm{w}}$	scattering matrix of a dielectric window
$\underline{\bar{\varrho}}$	complex reflection factor
R	ratio of the reflected power to the input power
R_0	ratio of the reflected power to the input power
T_0	ratio of the transmitted power to the input power

Lossy Conductors

σ	conductivity
$\bar{\gamma}$	complex propagation constant
$\bar{\alpha}$	attenuation constant
ϖ	ohmic absorption coefficient
δ_{skin}	skin-depth
R_{surf}	surface resistance
s_{roug}	correction factor for the surface resistance of rough surfaces
R_{q}	root mean squared surface roughness
P_{ohm}	power dissipated in a lossy material

Method of Moments

f	basis functions for the method of moments
$\bar{a}$, $\bar{b}$	weighting factor for basis functions in the method of moments
$\underline{M}$, $\underline{\tilde{M}}$	impedance matrix and approximated impedance matrix
$\underline{U}$, $\underline{V}$	dense, rectangular matrices for the ACA compression

$\underline{Q}$, $\underline{R}$	orthogonal matrix and upper triangular matrix of a QR decomposition
$\underline{\Sigma}$	rectangular diagonal matrix with the singular values of a SVD
R_{res}	residuum
$\boldsymbol{V}$	input vector
$\underline{P}$	preconditioner matrix
$\bar{\boldsymbol{y}}$	vector of unknowns in a preconditioned linear system of equations vector

Polarizer

w_1, w_2	period and width of a rectangular corrugation or grating
h	height of a rectangular corrugation
h_0	optimal grid height of a reflective phase grid for perpendicular incident wave
Φ	grid orientation angle of a reflective phase grid
Θ	incident angle of a wave
d	distance between the wires of a wire-grid
d_{r}	radius of a wire
d_{x}, d_{z}	thickness and depth of conducting plates in a polarizer made of stacked plates
A^{O}, A^{X}	amplitude of an O-mode respectively X-mode
C_{ellip}	coupling coefficient of O and X mode in an elliptical waveguide

Miscellaneous

$\underline{0}$	zero matrix
$\underline{I}$	identity matrix
$\underline{D}$	diagonal matrix
$\underline{T}$	tri-diagonal matrix
$\underline{G}$	Schur complement
$\underline{\underline{\mathrm{G}}}$	Green's function
M	merit function
C^{corr}	correlation of two values

1 Introduction

Systems which are capable to generate ultra-short radio frequency (RF) pulses coherently, and, at the same time, achieve a reasonable RF output power of more than a few Watts in the millimeter and submillimeter (sub-THz) frequency bands are gaining fundamental interest in the research community. Those RF systems might become the key components of possible future THz diagnostic systems. Examples are the diagnostics of dense plasmas, novel pulsed Dynamic Nuclear Polarization (DNP)-Nuclear Magnetic Resonance (NMR) spectroscopy methods, photochemistry and biophysics [1]–[3]. In all cases, novel powerful RF sources of ultra-short coherent pulses in the millimeter and sub-millimeter frequency range would enable the scientific community to develop new devices with performance improvements in the areas of sensitivity, resolution and data acquisition speed.

While coherent pulsed lasers are available since the 1960s, a comparable source of ultra-short coherent pulses at sub-THz frequencies is not available up to now.

1.1 Aims and Objectives

In this work, the development of a novel (in the field of microwave engineering) RF system for the generation of ultra-short, high-power, broadband, coherent pulses is investigated. For that, the mechanism of passive mode-locking in a feedback loop of two broadband gyro-devices, as first proposed in [4], is used. In laser physics, passive mode-locked laser systems are a well-known sources of ultra-short coherent pulses [5], [6]. In the area of microwave engineering this is a new approach for achieving optimal stable pulsed oscillators. The aim of this thesis is to further develop the proposed method of pulse generation towards a realization for sub-THz frequency ranges.

Sources of coherent sub-THz pulses with a reasonable power are of special interest for the development of novel spectroscopy methods such as time domain or pulsed DNP-NMR techniques [7], [8]. DNP methods have been shown to be a very effective technique to enhance the performance of NMR measurements. By coupling the nuclei to the more strongly polarized electrons, the DNP-NMR technique increases the nuclear spin polarization by two to five orders of magnitude and reduces the necessary acquisition time in experiments.

The key for DNP-NMR is the strong irradiation of the NMR sample by high-power microwaves in the sub-THz range. While the state-of-the-art DNP methods are based on continuous wave (CW) microwave sources, time domain or pulsed DNP-NMR techniques offers a significant potential for a more efficient polarization transfer, which can ultimately increase the rate at which the nuclear spins may be polarized, as well as the maximum polarization [9]. The further development of these techniques is part of the current research. However, state-of-the-art DNP experiments are still based on CW methods, simply due to the lack of suitable sources of microwave pulses in the sub-THz frequency range with the required high coherency. Therefore, the proposed microwave source based on mode-locked electron tubes has the potential to become the microwave source of choice for future time domain or pulsed DNP-NMR experiments.

Assuming commercially available systems starting from a NMR frequency of 400 MHz, the corresponding microwave sources must operate in the sub-THz frequency range, at 263 GHz and above. Consequently, in this thesis the development of a high-power microwave source of ultra-short coherent pulses at a center frequency of 263 GHz is investigated. For the first time, the generation of ultra-short coherent high-power pulses based on mode-locked electron tubes is investigated at a frequency of 263 GHz.

For any passive mode-locked oscillator at sub-THz frequency bands and for high power at the same time, three main components are required: a high-power broadband vacuum electronics amplifier, a nonlinear vacuum electronics absorber and a quasi-optical feedback system to couple the active devices. All three key components must have a sufficient bandwidth to allow the generation of the ultra-short pulses. In this thesis, the fundamental designs of all three key components are developed. A detailed analysis of a passive mode-locked oscillator based on the developed components is performed, and, finally, the

original concept is extended and novel operation regimes for the system of coupled electron tubes are demonstrated.

In order to achieve these aims, a fundamental investigation of the mode-locking method is first carried out. Wherever possible, the models developed in laser physics are used, and subsequently adapted and extended to meet the specific requirements. For the design of the individual key components, as well as for the complete mode-locked oscillator, the development of new, optimized simulation tools is required. This includes the development of entirely new software, but also the extension of existing programs.

As a theoretical basis for the newly developed programs, well-known methods which are extended to allow an improved modeling of the problems are used. For the simulation of the electron-wave interaction in electron tubes, a fixed transversal field approach is used. This method is well known in the area of laser physics [10] as well as in microwave engineering. Combined with the approach of slowly varying variables, it has been used successfully for the simulation of electron-wave interactions in gyrotron devices [11]. To enable the simulation of the interaction between ultra-short microwave pulses and an electron beam, the common approaches for the formulation of the source term are extended by a full three-dimensional handling of the electron beam. In addition, this permits the investigation of effects from spreads in electron beams, space charge effects, magnetic field misalignment and current inhomogeneities, which was not possible before in the common formulations. For the simulation of quasi-optical and overmoded waveguide components, the program KarLESSS [12] which was originally developed in a previous work for the simulation of mode converters in high-power gyrotrons, is extended. For the synthesis of broadband waveguide components, horn antennas, and windows, a tool based on the generalized scattering matrix and mode matching method is developed.

The theory and simulation models developed make it possible to design concrete components for a passive mode-locked oscillator at 263 GHz. The main components of the electron vacuum tubes for the amplifier and saturable absorber, namely the interaction spaces, are designed. For the first time, a coupling system based on overmoded waveguides is proposed for the coupling of two electron tubes in a mode-locked oscillator and a complete design of an optimized feedback system is developed. A detailed analysis of the ex-

pected properties and performance for the designed mode-locked oscillator is performed.

Based on the novel feedback system and the experience gained during the development of the 263 GHz passive mode-locked oscillator, the original concept of a passive mode-locked microwave oscillator is extended, which allows new operating regimes. The proposed extension of the developed mode-locked microwave oscillator will allow its operation as a passive mode-locked oscillator, an active mode-locked oscillator, a CW oscillator, and a two-stage amplifier.

1.2 State of the Art

Since the 1960s, the generation of powerful, ultra-short pulses with high repetition rates have been of great interest in laser physics [13]. Such trains of coherent, powerful pulses have important applications in healthcare, fundamental research and industry. For example, they are used in medical imaging, ophthalmology, terahertz spectroscopy and material micromachining [14].

A well known technique for the generation of highest power laser pulses is Q-switching, also known as giant pulse formation [13], [15]. Such a Q-switch was first demonstrated in 1962 by McClung and Hellwarth using an electrically switched Kerr cell shutter in a ruby laser [15]. As indicated by the name, a type of variable attenuator is incorporated into the laser's cavity to control its Q-factor. The laser medium is pumped while the Q-switch is set to a high attenuation, which results in a low Q-factor for the resonator. The pumping produces a high population inversion in the laser medium. At its maximum, the Q-switch is quickly switched so that the resonator's Q-factor increases. Since already a maximum of energy is stored in the laser medium, the stored energy radiates as a so-called giant pulse with highest peak power. While the achievable output power is enormous, this method does not allow the generation of pulses with highest repetition rates [16].

An alternative method for the generation of pulsed lasers is the passive mode-locking of CW lasers [17]. Mode-locked lasers can generate ultra-short pulses (of the order of pico- to femtoseconds) with high repetition rates [16]. In a mode-locked laser, a fixed phase relation between all longitudinal cavity-modes is induced. A train of coherent pulses is generated by the constructive

interference of these modes. Several types of passive mode-locked lasers are available. Using semiconductor technology, mode-locking can be realized in quantum dot lasers and quantum well lasers [5]. They are widely used for the generation of short optical pulses with high repetition rates from a few GHz up to hundreds of GHz [18], [19].

In general, the methods of pulse generation used in optics can be transferred to microwave electronics. A challenge is the availability of the required sources. Although THz lasers exist [20]–[22], until now, none are able to generate short pulses. Reference [23] states "One has to conclude that there is presently no THz laser that directly emits short pulses".

As a solution, near-infrared pulses, generated from a state-of-the-art mode-locked laser, e.g. a titanium-sapphire laser, are converted to THz frequencies. The three main technologies for this are: (a) photoconductive switches, (b) difference frequency mixing and (c) plasma sources.

In photoconductive switches, the laser pulses are used to generate rapidly varying electric currents which radiate electromagnetic waves at the desired THz frequency [24].

Difference frequency mixing is based on nonlinear optics. If a nonlinear medium is irradiated with a high-power laser pulse, higher harmonic frequencies are generated. This technique was first used for the generation of microwave [25] and THz [26] frequencies in 1963 and 1965, respectively.

The generation of THz pulses in plasma also uses nonlinear effects [27]. First, the laser pulse generates a plasma. In the plasma, the simultaneous nonlinear interaction of the fundamental and the second harmonic generates the THz radiation. Since a description of the processes involved is very complex, a complete theory is not available at present [23].

A major problem of the previously described methods is the low conversion efficiency. A more efficient method should therefore not be based on frequency conversion, but should generate the target frequency directly. In [28], a method similar to Q-switching in electron tubes is proposed. A periodic modulation of the feedback factor of an electron backward wave oscillator (BWO), consisting of a slow-wave structure between two reflectors at the ends, could lead to the generation of stable, periodic, short high-power RF pulses. It is shown that Q-switching can increase the averaged electronic efficiency by an order of

magnitude and that the peak power of the generated RF pulses could increase by a factor of $40 - 50$ compared to the CW operation. As a Q-switch, a GaAs semiconductor excited by laser pulses is proposed. The energy in a laser pulse with a wavelength of $700 - 800$ nm for the excitation of the semiconducting reflector is estimated at $0.1 - 10\,\mathrm{nJ/mm^2}$. As mentioned in [4], a drawback of this method is the required exciting laser with a high repetition frequency in the range of hundreds of megahertz. A second drawback of the proposed microwave Q-switch is the requirement of relatively low intensities of the microwave fields inside the cavity since they should not affect the semiconducting reflector.

In this thesis, an alternative idea for the generation of periodic, short microwave pulses in electron tubes is followed, as first proposed in [4]. Instead of the Q-switching approach, the method of mode-locking is transferred from laser physics to microwaves. Similar to the microwave Q-switching approach, the laser device is replaced by an electron tube. Due to the advantageous properties of gyrotron-type tubes for this particular task (see section 2.3), it is focused exclusively on gyro-devices in the following.

An increasing number of leading laboratories is interested in the fundamental research and development of advanced microwave sources (oscillators and amplifiers) based on the induced electron cyclotron radiation [29]. The most powerful microwave source, the gyrotron, is used primarily for heating and current drive of magnetically confined plasmas for nuclear fusion [30]. The Institute of Applied Physics (IAP-RAS, Nizhny Novgorod, Russia), together with the Japan Atomic Energy (Japan) and the Karlsruhe Institute of Technology (KIT, Karlsruhe, Germany), are the major developers of that kind of megawatt-class fusion gyrotrons [31]–[34]. At the same time, a lot of effort has been recently directed towards the development of gyrotrons in the upper sub-THz frequency range for DNP-NMR spectroscopy [35]. The work at Fukui University (Japan), as well as the development of specialized gyrotron systems, combined with spectrometers at Communications & Power Industries (CPI, United States) should be mentioned in this context [36], [37]. In these laboratory setups for spectroscopy, monochromatic radiation is presently used. At the same time, groups, e.g. in Switzerland and the US, are working on the development of frequency-agile gyrotrons for improved spectroscopy setups [38], [39].

The development of amplifying schemes for devices based on electron cyclotron radiation (gyro-devices) is also receiving considerable attention. Theoretical and experimental studies of traditional types of gyro-amplifiers (gyroklystron, gyro-TWT on the basis of regular cylindrical waveguides) are carried out in many laboratories around the world: Communications & Power Industries (CPI, US), Naval Research Laboratory (US), National Tsing Hua University (Taiwan), Beijing Vacuum Electronics Research Institute (China) and University of Electronic Science and Technology of China (China) (to name only a few). An electrodynamic system for a gyrotron traveling wave tube (gyro-TWT) alternative to smooth-walled interaction circuits with high ohmic loss, namely, a waveguide with helical corrugations, was proposed and demonstrated at the IAP by G.G. Denisov, V.L. Bratman and S.V. Samsonov in collaboration with a research team around A.D. Phelps from the University of Strathclyde (Glasgow, UK) [40]. Currently, this group is continuing research of gyro-TWTs and gyro-BWOs based on helically corrugated waveguides. Outstanding results of their work are: the operation of a gyro-BWO that is continuously tunable from 88 to 102.5 GHz, with a maximum peak power of 12 kW and a pulse duration of about 0.4 microseconds [41], and the demonstration of a helical gyro-TWT at 90-100 GHz with a peak output power of 3 kW [42]. Recently, at the IAP a high-gain gyrotron traveling wave tube with helically corrugated waveguide (helical gyro-TWT) in the W-Band was also demonstrated [43]. Both groups verified the suitability of helical gyro-TWTs for the sub-THz frequency range. In addition, the team around A.D. Phelps showed the possibility of machining the required helical structures for frequencies up to 370 GHz [44].

1.3 Method of Mode-Locking in Laser Physics

The emission frequency of a laser is mainly determined by its laser medium and cavity. The laser medium is the source of optical gain within the laser. It is excited by the pump source to produce stimulated emission of photons. The pumping in common lasers is achieved with electrical currents (e.g. semiconductor lasers) or with light, which could even be generated by other lasers [45]. In the simplest case, the cavity can be represented as two flat mirrors surrounded by the laser medium. In the cavity, longitudinal resonator modes exist, which are standing waves created by the superposition of traveling waves

with opposite propagation directions, being reflected back and forth between the mirrors. In the model of a simple plane-mirror cavity, only modes for which the cavity length L is an integer multiple of half the mode wavelength are allowed. Therefore, the frequency separation between any two adjacent longitudinal modes is

$$\Delta\omega = \frac{\pi c}{L} \,, \tag{1.1}$$

where c is the velocity of light in the laser medium.

In Fig. 1.1, the frequency spectrum of the longitudinal modes is shown. The shape of the envelope is given by the frequency-dependent gain over the bandwidth of the laser medium. The electric field at a fixed position in the cavity is given by a superposition of the N dominant longitudinal modes

$$\mathrm{E}(t) = \sum_{n=-N/2}^{N/2} a_n \cos\left[\omega_0 t + (n-1)\Delta\omega t + \phi_n\right] \,, \tag{1.2}$$

where ω_0 is the frequency of the central mode with $n = 0$. The amplitude and phase of a mode n is denoted by a_n and ϕ_n. In general, a_n and ϕ_n are also time-dependent but for simplicity they are assumed as constant in this first simplified consideration.

In a free-running laser, the phases ϕ_n are randomly distributed and each of these modes oscillates independently. In lasers with only a few longitudinal modes, the field E will exhibit a random peak pattern over time and along the cavity due to interference of the modes. Since in practice L is much greater than the wavelength, many thousands of modes exist, so that the interference effects average to a near-constant field distribution over time and space and the laser produces a CW output signal.

In contrast to the previously described free-running laser, in a mode-locked laser, the phases of the longitudinal modes are locked together (therefore, mode-locking is sometimes also referred as phase-locking). Instead of a random or constant distribution, the total field E will have periodic maxima at the points where all modes constructively interfere. Fig. 1.2 shows the formation of a pulse by interference of phase-locked longitudinal modes inside a cavity. Since all modes propagate with the velocity c inside the cavity (as long as dispersion

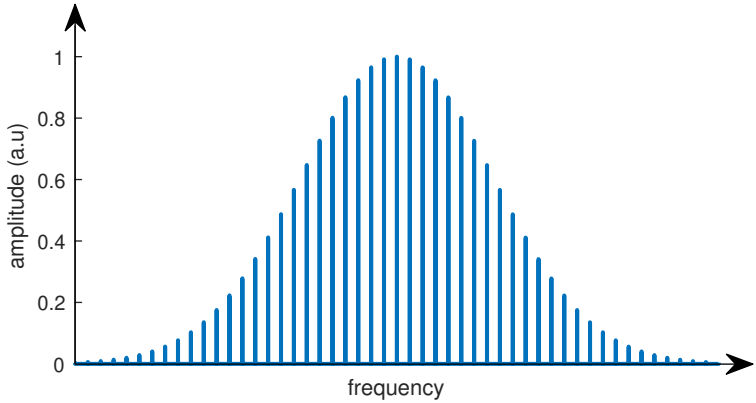

Figure 1.1: The frequency spectrum of longitudinal laser modes.

effects can be neglected), the peaks where all modes add constructively also propagate with c along the resonator.

The consideration of the superposition of different longitudinal modes for the description of a mode-locked laser corresponds to a consideration in the frequency domain. Equivalently, a mode-locked laser can also be examined in the time domain. In the time-domain model, the energy in the cavity is compressed into a short pulse and the shaping mechanism of the traveling pulse in the cavity is modeled and analyzed. The pulse is reflected back and forth between the mirrors of the cavity. At every round-trip, a fraction of the pulse is decoupled from the cavity, for example with with a semi-transparent mirror. Correspondingly, the output signal of a mode-locked laser is a train of short pulses. The time between the pulses in the output signal is determined by the length of the cavity. The repetition frequency f_r of the pulses is the reciprocal of the periodicity of the intracavity pulse's reflection at the output mirror:

$$f_\mathrm{r} = \frac{c}{2L} \,. \tag{1.3}$$

The duration of the mode-locked pulse is mainly determined by the laser's gain bandwidth and the effectiveness of the mode-locking mechanisms. From the frequency-domain model it is clear that the pulses are shorter the more modes

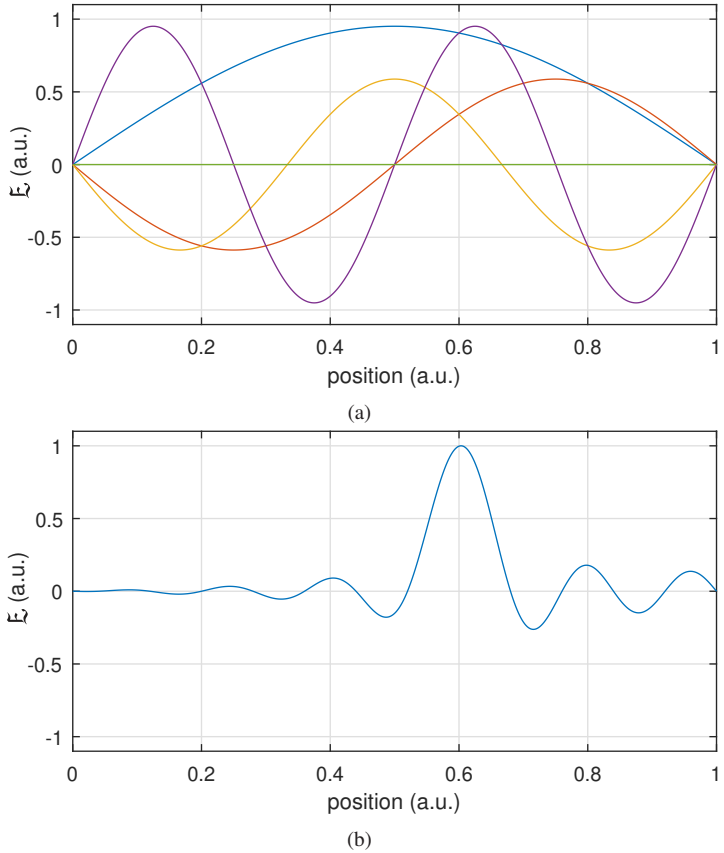

Figure 1.2: Mode-locked longitudinal modes in a fully reflecting cavity. (a) the first 5 longitudinal modes; (b) the total electric field inside the cavity created by the superposition of the longitudinal modes.

are locked and oscillating in phase. The higher the laser's bandwidth (broader peak in Fig. 1.1), the more modes can contribute to the formation of the pulse.

One question that remains open following the previous discussion is how to achieve mode-locking. The typical methods to produce mode-locking can be divided into 'active' and 'passive' methods, where for active methods an

external signal is required to induce the phase-locking while in the passive methods some intensity dependent loss or dispersion mechanism is used and no external signal is required. A combination of both types is also possible as in 'hybrid' and 'doubly mode-locked' lasers, in which both mechanisms are used [46].

For active mode-locking (sometimes also called synchronous mode-locking), the laser medium is excited at a repetition rate synchronized with the spacing $\Delta\omega$ of the longitudinal cavity modes, which results in a modulation of the laser medium's gain. Since the spacing of the longitudinal modes corresponds to the repetition frequency of the pulses (compare (1.1) and (1.3)), in the time-domain model the excitation can be seen as a small modulation of the gain synchronized with the pulse circulating in the cavity. In the frequency domain this can be seen as follows: the modulation of the gain results in a modulation of the field's amplitude with the frequency $\Delta\omega$ along the cavity. The amplitude modulation with $\Delta\omega$ of the electric field with a carrier frequency of ω_0 results in sidebands that correspond to the two longitudinal modes adjacent to the central mode and therefore the modes are phase-locked together.

An advantage of active mode-locking is that a broader range of laser media can be used than in the case of passive mode-locking, e.g. semiconductor lasers and laser dyes [46]. It should be also mentioned that active mode-locking can also be used only as a starting mechanism for a passive mode-locked device (called hard excitation).

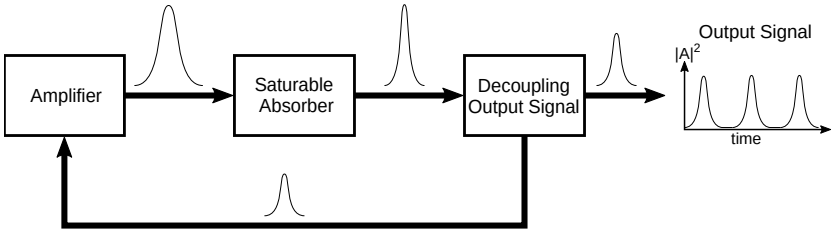

Figure 1.3: Schematic representation of a basic model for a pulse circulating in a passive mode-locked laser.

In a typical passive mode-locked laser, pulses are favored over CW signals by reducing the cavity losses for high intensities. Therefore, in contrast to active

mode-locking, the gain of the laser medium is not modulated by an external excitation but rather by the pulse oscillating in the cavity itself.

A schematic representation of a passive mode-locked laser is shown in Fig. 1.3. The amplifier part in Fig. 1.3 represents the usual laser medium which amplifies the pulse. The saturable absorber is an element with a transmission depending on the field intensity. It causes the intensity-dependent modulation of losses in the laser and hence leads to mode-locking. The nonlinear absorption narrows the pulses and broadens the frequency spectrum. At every round trip, a fraction of the pulse oscillating in the laser is decoupled from the feedback loop. In this way, a train of high-power, ultra-short pulses is generated. In simulations of mode-locked lasers, the decoupling of the output signal is often described by a linear loss.

The narrowing of a pulse in the saturable absorber is best illustrated in the time domain. For a pulse propagating through the saturable absorber, portions with low intensity are strongly attenuated and portions with a high intensity only experience a weak attenuation. Therefore, the leading and trailing edges of a pulse experience a stronger attenuation than the peak of the pulse which narrows the pulses (see Fig. 1.4 for an illustration). The narrowing is limited by the gain bandwidth of the laser medium. Additional limitations of the minimum pulse width arise from dispersion and nonlinear effects [46].

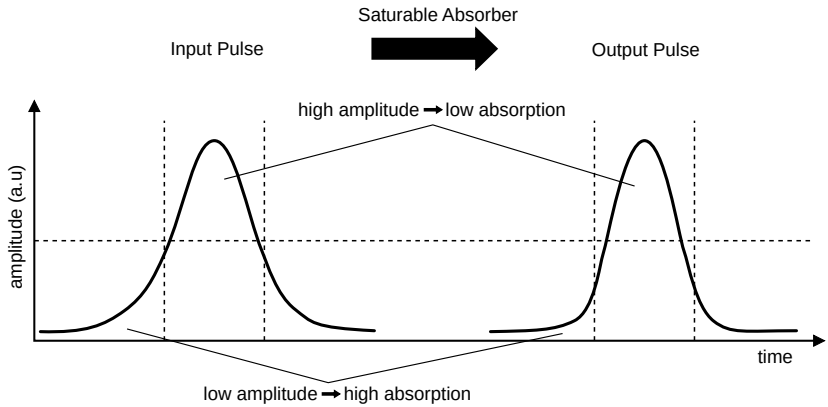

Figure 1.4: Illustration of the pulse narrowing in a nonlinear, saturable absorber.

The technique of passive mode-locking was successfully realized in a variety of laser types such as Ruby lasers [17], dye lasers [47] and semiconductor lasers [18]. The passive mode-locking allows the realization of lasers producing trains of ultra-short pulses with pulse widths in the range of a few hundreds of femtoseconds in semiconductor lasers down to sub 5 fs pulses obtained from titanium-sapphire lasers [48].

1.4 From Optics to Microwaves

While mode-locking is a well-researched topic in laser physics, this approach has not yet been applied to frequencies in the microwave range. In 2015, Ginzburg et al. [4] proposed to transfer the idea of passive mode-locking to microwave wavelengths. The basic approach is quite simple: for the realization of a mode-locked microwave source, all components of a passive mode-locked laser (see Fig. 1.3) must be replaced by corresponding devices operating at microwave frequencies. In this frequency range, vacuum electron tubes are the technology that provides the highest power [49] and therefore, they are the appropriate devices for a realization of the active components, namely amplifier and saturable absorber.

In the original proposal [4], a simplified, general model of electron tubes with prevailing inertial particle grouping (e.g. Cherenkov traveling wave tubes, gyro-TWTs, free-electron lasers) is investigated. Based on these preliminary investigations, it is proven that a passive mode-locked oscillator for microwave frequencies based on electron tubes is possible. Due to a lack of well-known devices available for the realization of a microwave saturable absorber, an ideal saturable absorber is assumed in this first preliminary investigation.

In [50], the first idea of a realistic saturable microwave absorber, suitable for high power, is proposed. It is based on the cyclotron resonance absorption by a rectilinear electron beam, guided by a static magnetic field, in a cylindrical waveguide. The absorption saturation is caused by the relativistic dependence of the gyro-frequency of the electrons on their kinetic energy. At the same time, a helical gyro-TWT is identified as a suitable high power, broadband amplifier for a passive mode-locked oscillator operating in the Ka-band.

A further investigation of helical gyro-TWTs has shown an alternative possibility for the realization of a saturable absorber: a helical gyro-TWT that is operated in the Kompfner dip regime [51]. The possibility to operate a helical gyro-TWT in the Kompfner dip regime has been shown first by Ginzburg et al. in [52].

Since the helical gyro-TWT is identified as promising technology for the high-power amplifier as well as the saturable absorber, detailed analysis of the properties of a passive mode-locked oscillator based on two helical gyro-TWTs operating in the Ka-band are performed in the following [53]–[55]. While a passive mode-locked oscillator based on two helical gyro-TWTs promises advantages particularly for frequencies in the sub-THz region, the first realization of a passive mode-locked oscillator, which is under preparation at the IAP [56], operating in the Ka-band, will use the originally proposed cyclotron absorber [56]–[59].

Besides an amplifier and a saturable absorber, a mechanism to couple both devices in a feedback-loop (mode-locked oscillator) and to decouple the output signal from it, is required (see Fig. 1.3). Well known techniques for the transmission of broadband, high power microwave radiation involve transmission lines based on quasi-optics or overmoded waveguides. Both techniques have been used successfully for plasma heating in nuclear fusion research [60] and radar technologies [61]. Furthermore, both techniques are also suitable for the development of a mode-locked microwave oscillator and for the first proof-of-concept experiments at the IAP, a feedback system based on a quasi-optical transmission will be used [56].

1.5 Outline

This work is organized as follows. The theoretical fundamentals of mode-locking at microwave frequencies are discussed in chapter 2. The major components of the vacuum electron tubes used for the realization of the amplifier and saturable absorber and the different technologies for an implementation of the feedback system are introduced in chapter 3. For the simulation of the electron tubes a new theoretical approach is derived and implemented in chapter 4. Based on the developed simulation tool, the amplifier and saturable absorber for a passive mode-locked 263 GHz oscillator are designed in chapter 5. A

detailed study of the mode-locked oscillator assembled from the designed amplifier and saturable absorber is performed in chapter 6. The numerical framework for the simulation of the passive components of the feedback system is constructed in chapter 7. In chapter 8, the numerical tools are used to develop a novel feedback system for a mode-locked oscillator at 263 GHz. In addition to the passive mode-locking regime, this novel feedback system will enable new operation regimes of the coupled electron tubes. Finally, the work carried out is summarized in chapter 9 and suggestions are made for future developments.

2 Fundamental Theory of Passive Mode-Locked Oscillators

In this chapter a fundamental theoretical model for the description of passive mode-locking is given. For this propose, the so called Haus Master Equation (HME) as introduced by Hermann A. Haus [62], [63] is used. The HME is a common model in laser physics for the description of the pulse evolution in a passive mode-locked oscillator. Using the HME, the significant physical properties of a passive mode-locked oscillator can be clarified and important conclusions for a realization at microwave frequencies are drawn at the end of the chapter.

2.1 Characteristics of Ultra-Short Pulses

For the description of time-dependent processes involving electromagnetic waves with a narrow center frequency, the standard theoretical method in laser physics, as well as in the theory of electron tubes, is the slowly varying amplitude approximation [10] (sometimes also called slowly varying envelope approximation).

2.1.1 Slowly Varying Amplitudes

In the slowly varying amplitude approximation, it is assumed that the field envelope function $\overline{A}(t,z)$ is slowly changing compared to the carrier frequency ω_0. It changes slowly over the time and space, i.e. the spectrum of $\overline{A}(t,z)$ has the maximal frequency ω_m with $\omega_\mathrm{m} \ll \omega_0$:

$$\left|\frac{\partial \overline{A}}{\partial t}\right| \ll \omega_0 \left|\overline{A}\right| \tag{2.1}$$

and

$$\left|\frac{\partial^2 \overline{A}}{\partial t^2}\right| \ll \omega_0 \left|\frac{\partial \overline{A}}{\partial t}\right| . \tag{2.2}$$

Therefore, the rapidly varying part (carrier) of the electric field in the time-space domain $\mathfrak{E}(t, r, \phi, z)$ can be separated from the slowly varying envelope $\overline{A}(t, z)$. Under this assumption, the behavior of the field is fully described by its complex envelope $\overline{A}$. Assuming that the transverse profile of the electric field is constant over time and is given by $\hat{\boldsymbol{e}}(r, \phi)$, the electric field in the time-space domain can be expressed as

$$\mathfrak{E}(t, r, \phi, z) = \mathrm{Re}\left\{\overline{A}(t, z)\, \mathrm{e}^{\,j\omega_0 t}\, \hat{\boldsymbol{e}}(r, \phi)\right\} . \tag{2.3}$$

In the following, the slow-time-scale assumption is used to derive equations for the behavior of $\overline{A}(t, z)$ in various types of amplifiers, absorbers and mode-locked oscillators.

2.1.2 Ultra-Short Pulses

As the generation of ultra-short pulses is discussed, an exact definition of the duration of a pulse and of the term 'ultra-short' is necessary, respectively. In the following, the length of a pulse τ_p is defined as the full width at half maximum (FWHM) of the pulse's intensity profile, which is given by the absolute square of the slowly varying amplitude $|\overline{A}(t)|^2$. The corresponding spectral width (bandwidth) ω_p is consequently defined as the FWHM of the spectral intensity $|\tilde{A}(\omega)|^2$, where $\tilde{A}(\omega)$ is the Fourier transformation (FT) of $\overline{A}(t)$. The bandwidth and the pulse length are related to each other through the FT and therefore, for a given bandwidth, there is a lower limit for the pulse length. A pulse that reaches this limit is called bandwidth-limited pulse. For pulses without chirp and analytical pulse shapes a minimum duration-bandwidth product c_p for bandwidth-limited pulses can be defined by

$$c_\mathrm{p} = \frac{\tau_\mathrm{p}\omega_\mathrm{p}}{2\pi} . \tag{2.4}$$

For a Gaussian pulse c_p is 0.441 and for a Sech pulse 0.315. The minimum duration-bandwidth product is useful to calculate the minimum pulse length for a given bandwidth and pulse shape. Assume a passive mode-locked oscillator

based on an amplifier and a saturable absorber with bandwidths of 10 GHz each. If this oscillator generates pulses with a Gaussian shape, the lower limit for the pulse length is 44 ps. It should be mentioned that for chirped pulses, the definition of the minimum duration-bandwidth product is more complicated (see chapter 1.1.4 in [46]).

So far, the definition of 'ultra-short' remains open. But even in laser physics there seems to be no clear definition of ultra-short pulses. Typically, optical pulses with a length of a few picoseconds down to femtoseconds are called 'ultra-short' [46]. A possible definition for sub-THz frequencies could be a scaling of the pulse duration with the ratio of optical to sub-THz frequencies. A typical mode-locked Ti:sapphire laser generates pulses with a length of the order of 100 fs at a wavelength of about 1000 nm (300 THz) [46]. For a pulse with a center frequency of 263 GHz this corresponds to a pulse length of 0.1 ns and a bandwidth of 4 GHz (assuming a Gaussian pulse shape).

In this context, another interesting property is the minimum possible pulse length. To find this value, the argumentation given in [23] is used: Since for any pulse propagating in free space the integral of the electric field over the time must vanish, $\int \mathfrak{E}(t)\,\mathrm{d}t = 0$, the shortest possible pulse is a half-cycle pulse. For such a short pulse the previous definition of the pulse length as the FWHM gets problematic. Therefore, in [23] an alternative definition is given, which can be used for extremely short pulses and still leads to the same pulse length (same FWHM) for longer pulses:

$$\tau_\mathrm{p} = \sqrt{\frac{8\log 2}{I}\int_{-\infty}^{\infty} \mathfrak{E}(t)^2 (t-t_0)^2\,\mathrm{d}t}\,, \tag{2.5}$$

with the intensity $I = \int_{-\infty}^{\infty} \mathfrak{E}(t)^2\,\mathrm{d}t$ and $t_0 = \frac{1}{I}\int_{-\infty}^{\infty} \mathfrak{E}(t)^2 t\,\mathrm{d}t$. Consequently, the duration of a half-cycle pulse is $\tau_\mathrm{p} = 0.5 {f_0}^{-1}$.

It can be concluded that at a frequency of 263 GHz every pulse with a length in the range 0.002 - 0.1 ns can be called ultra-short.

2.2 Haus Master Equation of Passive Mode-Locked Oscillators

In laser physics, the HME introduced by Hermann A. Haus [62], [63] describes the fundamental mechanisms behind the pulse evolution in a passive mode-locked laser. It is a partial differential equation (a special form of the complex cubic Ginzburg-Landau equation) and describes the slowly varying envelope $\overline{A}(t)$ of a pulse circulating within the laser medium. For convenience, in the following the amplitudes $\overline{A}(t)$ are normalized so that $|\overline{A}(t)|^2$ is the power.

The HME describes the evolution of a single pulse at a fixed position in the laser rather than a train of pulses. For convenience, a position just before the output coupler is chosen in the following. The overall time delay corresponding to the round-trip time T_r of a pulse in the oscillator is not considered in the HME and the pulse remains centered near $t = 0$. At every round trip n of the pulse in the laser, the amplitude $\overline{A}_n$ changes:

$$\overline{A}_{n+1} = \overline{A}_n + \Delta\overline{A}_n \ . \tag{2.6}$$

If $\Delta\overline{A}$ vanishes, a steady-state is reached and the pulse is a solution of the mode-locked oscillator.

For the transient buildup or decay of a pulse and an analysis of the stability a differential equation for the amplitude $\overline{A}$ can be found [64]. To derive a continuous equation, the individual physical effects of the various laser components are averaged in space over the full length of the laser and in time over one round trip. Therefore, the index n is replaced with a second, long-term time variable $T = n\,T_\mathrm{r}$ and the amplitude becomes a function of both, the short and long-term time variables $\overline{A} = \overline{A}(T, t)$ which results in the differential equation

$$\frac{\partial}{\partial T}\overline{A}(T,t) = \frac{\Delta\overline{A}(T,t)}{T_\mathrm{r}} \ . \tag{2.7}$$

An important assumption in (2.7) is that the difference $\Delta\overline{A}_n$ is only a slight modification of the original pulse. This assumption is necessary to allow the averaging of all effects over the complete laser medium. Haus gives a value of up to $20\,\%$ for this modification [62].

To obtain the HME for a specific oscillator, the change of the amplitude $\Delta\overline{A}$ during a round trip in the oscillator must be found. For this, it is assumed that a passive mode-locked oscillator can be separated into a series of separate components, each with a specific effect on the pulse. Then $\Delta\overline{A}$ is a sum of the changes caused by the N individual components

$$\Delta\overline{A} = \sum_{i}^{N} \Delta\overline{A}_i \tag{2.8}$$

and the HME for a specific passive mode-locked laser can be assembled. This is illustrated in Fig. 2.1, where a passive mode-locked oscillator as a series of individual components is shown.

In the following, the differences in the amplitude caused by amplification, saturable attenuation, group velocity dispersion, time shifts and bandwidth limitations are derived. These allow a solution for the pulse envelope and the calculation of the pulse length, chirp, and spectral bandwidth as functions of the oscillator parameters. Because a derivation in the frequency domain is beneficial for some of the values, the frequency domain values are marked by a tilde for a better distinction between time and frequency domain.

2.2.1 Amplification

The simplest possible amplification function is a linear gain. The change of the amplitude $\Delta\overline{A}_{\mathrm{g,lin}}$ caused by a linear gain is described by

$$\Delta\overline{A}_{\mathrm{g,lin}}(T,t) = g_0\overline{A}(T,t) \tag{2.9}$$

with the small-signal gain g_0. The Δ indicates that the given value describes the gain rather than the total amplitude after the amplification. The total amplitude after the amplification is consequently

$$\overline{A}(T+T_{\mathrm{r}},t) = \Delta\overline{A}_{\mathrm{g,lin}}(T,t) + \overline{A}(T,t)\ . \tag{2.10}$$

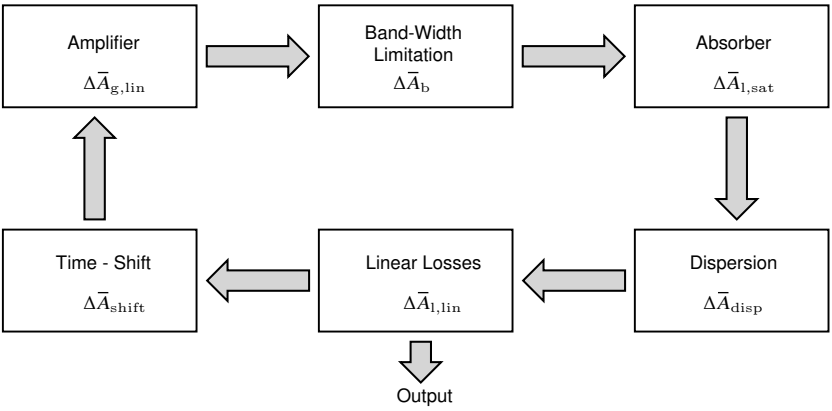

Figure 2.1: Schematic of the HME. The operator that describes the dynamics of a pulse during a single round trip in the oscillator is a sum of the operators for the individual components of the passive mode-locked oscillator.

Real devices usually have a bandwidth limitation. If a Lorentzian line shape of the amplifier's gain with a FWHM of ω_{g} is assumed, a bandwidth limited gain in the frequency domain is given by [65]:

$$\Delta\tilde{A}_{\mathrm{g,band}}(\omega) = \frac{g_0}{1+\left(\frac{\omega-\omega_0}{\omega_{\mathrm{g}}}\right)^2}\tilde{A}(\omega) \tag{2.11}$$

$$\approx g_0\left(1-\frac{(\omega-\omega_0)^2}{{\omega_{\mathrm{g}}}^2}\right)\tilde{A}(\omega)\ . \tag{2.12}$$

The expansion (2.12) is sufficient if it is assumed that the deviation from the central gain frequency ω_0 is small compared to the bandwidth ω_{g}. The gain in the time domain can be determined via an inverse Fourier transformation of (2.12):

$$\Delta\overline{A}_{\mathrm{g,band}}(T,t) \approx g_0\left(1+\frac{1}{{\omega_{\mathrm{g}}}^2}\frac{\mathrm{d}^2}{\mathrm{d}t^2}\right)\overline{A}(T,t)\ . \tag{2.13}$$

Depending on the investigated mode-locked oscillator, a separation of the bandwidth limitation from the gain can be advantageous. In this case, the

difference in the amplitude caused by the filtering action of a limited bandwidth (of Lorentzian line shape) can be expressed by [65]

$$\Delta\bar{A}_{\mathrm{b}}(T_{\mathrm{r}},t) = \frac{1}{{\omega_{\mathrm{g}}}^2}\frac{\mathrm{d}^2}{\mathrm{d}t^2}\bar{A}(T_{\mathrm{r}},t)\ . \tag{2.14}$$

In the context of the previous considerations about the gain operator it must be mentioned that in general the HME is not stable for an unrestricted gain without saturation [64]. However, a stable solution can be achieved if a cumulative saturation of the gain is introduced. For this, the constant small signal gain g_0 can be replaced by a slowly saturating gain that depends on the long term time T [64]

$$g_{\mathrm{s}}(T) = \frac{g_0}{1+\frac{W_{\mathrm{P}}(T)}{W_{\mathrm{g}}}}\ , \tag{2.15}$$

with the saturation energy of the gain medium W_{g} and the energy W_{P} of the pulse

$$W_{\mathrm{P}}(T) = \int_{-\infty}^{\infty}|\bar{A}(T,t)|^2\,\mathrm{d}t\ . \tag{2.16}$$

With g_{s}, the gain is kept constant during the passage of a single pulse, but saturates cumulatively for a high total pulse energy. For a laser, this assumption is valid if the relaxation time of the laser medium is much longer than the round-trip time of a pulse in the laser.

2.2.2 Saturable Loss and Self Amplitude Modulation

The saturable loss and the associated self amplitude modulation (SAM) in the saturable absorber are the dominant effect of pulse formation in a passive mode-locked oscillator. In the saturable absorber, the losses must be high for low intensity signals while pulses of high intensity should experience only low

losses. The saturable losses depend on the intensity $I(t)$ of a pulse and can be described by the equation [62]:

$$\Delta\overline{A}_{\mathrm{l,sat}}(T,t) = \frac{l_0}{1 + I(t)/I_{\mathrm{sat}}}\overline{A}(T,t) \tag{2.17}$$

$$= \frac{l_0}{1 + \left|\overline{A}(T,t)\right|^2/P_{\mathrm{l,sat}}}\overline{A}(T,t)\ , \tag{2.18}$$

with the unsaturated loss l_0 and the absorber saturation intensity I_{sat}. In (2.18) the chosen normalization is used. Therefore, the square of the amplitude divided by the effective area of the mode gives the intensity and the saturable losses can be expressed in terms of the amplitude and the saturation power $P_{\mathrm{l,sat}}$ of the absorber.

2.2.3 Dispersion

The group velocity dispersion (GVD) is the result of a dependence of the group velocity on the frequency in the propagation medium (dispersive medium). The effect of a dispersive element on a pulse can be easily specified in the frequency domain. For simplicity, a quadratic dependence of the phase velocity on the frequency is assumed in the following. This is a common approximation for the dispersion in waveguides that follows from the slowly varying amplitude approximation (see chapter 4.1.2 for details). If a quadratic dependence of the phase velocity on the frequency is assumed, the change in the amplitude is given as

$$\Delta\tilde{A}_{\mathrm{disp}}(\omega) = -j d_0\,(\omega - \omega_0)^2\,\tilde{A}(\omega) \tag{2.19}$$

for the dispersion [65]. In the time domain, the dispersion can be expressed as:

$$\Delta\overline{A}_{\mathrm{disp}}(T,t) = j d_0 \frac{\mathrm{d}^2}{\mathrm{d}t^2}\overline{A}(T,t)\ . \tag{2.20}$$

The GVD term smoothens the envelope of the pulse and is therefore a counterpart to the pulse forming process. In addition, the pulse experiences a chirp due to the different propagation velocities for components with different frequencies. In laser physics, the terms ‘positive’ and ‘negative’ GVD are used.

If a pulse experiences positive GVD, the high-frequency components travel slower than the low frequency components and the pulse becomes positively chirped. For a negative GVD, the high frequency components travel faster than lower frequencies and the pulse becomes negatively chirped.

2.2.4 Slow Components

Regarding the active components in a passive mode-locked oscillator, i.e. amplifier and saturable absorber, it has to be distinguished between 'fast' and 'slow' components. A fast component recovers almost immediately, compared with the pulse length, its initial properties and therefore its gain/absoption behavior does not depend on the pulse length. In contrast, a slow component cannot recover its initial properties on the timescale of an ultra-short pulse and, therefore, the gain/absoption behavior changes during the pulse.

The dynamics of fast and slow components are illustrated in Fig. 2.2. In the bottom the pulsed intensity profile is given. Above, the time dependent behavior of the gain in the amplifier and the losses in the saturable absorber are illustrated. In the first row, the gain and losses for an ideal amplifier and an ideal saturable absorber are shown. The areas of attenuation are highlighted with a gray shading and the areas of amplification are shaded with gray lines. For the ideal devices, a symmetric pulse undergoes a symmetric amplification/absorption because of the fast recovery of the gain/loss. This can be seen by the symmetrical form of the amplification and absorption areas. In the second row, the ideal saturable absorber is replaced with a slow saturable absorber. The slow saturable absorber cannot recover its initial properties on the timescale of the pulse which results in unsymmetrical losses. This can be clearly seen by the unsymmetrical amplification and absorption areas. In the third column, a slow amplifier is shown. The slow amplifier can only amplify the pulse's leading edge with full capacity. The gain decreases during the pulse and requires a specific time before it fully recovers. Again, an unsymmetrical amplification and absorption of the pulse is the consequence. In the following, descriptions of the loss and gain of slow devices are derived.

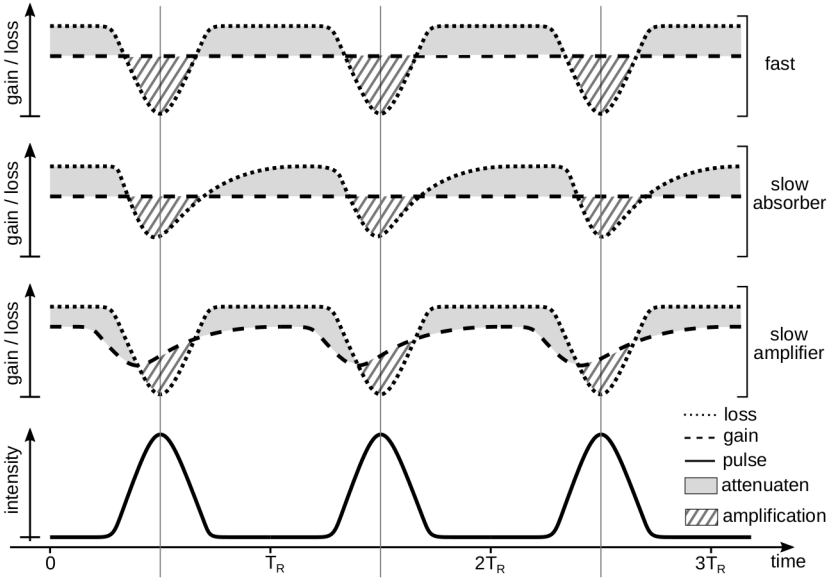

Figure 2.2: Dynamics and pulse-shaping mechanism for passive mode-locked oscillators with fast and slow devices (based on [64]). First row: ideal amplifier and ideal saturable absorber; Second row: ideal amplifier and slow saturable absorber; Third row: slow amplifier and ideal saturable absorber; Forth row: signal intensity.

In [63], a derivation of the losses of a slow saturable absorber based on a rate equation analysis is given. It is shown that a typical slow absorber for passive mode-locked lasers saturates according to

$$\frac{\mathrm{d}l_{\mathrm{slow}}(t)}{\mathrm{d}t} = \frac{l_0 - l_{\mathrm{slow}}}{T_{\mathrm{A}}} - l_{\mathrm{slow}} \frac{|\bar{A}(T,t)|^2}{W_{\mathrm{l}}} \,, \tag{2.21}$$

where T_{A} is the relaxation time of the absorber and W_{l} is the saturation energy of the absorber. Assuming T_{A} is long compared to the pulse length, the first term of (2.21) can be neglected. Under this assumption (2.21) is solved by the ansatz [63]

$$l_0(T,t) = l_{\mathrm{i}} \exp\left[-\frac{W_{\mathrm{P}}(T,t)}{W_{\mathrm{l}}}\right] \bar{A}(T,t) \,, \tag{2.22}$$

where l_i is the initial value of the loss and $W_\mathrm{P}(t)$ is the cumulative energy in the pulse, given by

$$W_\mathrm{P}(T,t) = \int_{-\infty}^{t} |\overline{A}(T,t)|^2 \,\mathrm{d}t \ . \tag{2.23}$$

Using the relation

$$\frac{\mathrm{d}}{\mathrm{d}t}\left(\int_{-\infty}^{t} \frac{|\overline{A}(T,t)|^2}{W_\mathrm{l}} \,\mathrm{d}t\right) = -\frac{|\overline{A}(T,t)|^2}{W_\mathrm{l}} \tag{2.24}$$

it can be shown by a simple substitution of (2.22) into (2.21) that the ansatz solves the differential equation.

With (2.22), the losses in a slow saturable absorber can be defined

$$\Delta\overline{A}_\mathrm{l,slow}(T,t) = l_\mathrm{i} \exp\left[-\frac{W_\mathrm{P}(T,t)}{W_\mathrm{l}}\right] \overline{A}(T,t) \ . \tag{2.25}$$

Analogous to the slow saturable absorption, the gain of a slow amplifier can be derived:

$$\Delta\overline{A}_\mathrm{g,slow}(T,t) = g_\mathrm{i} \exp\left[-\frac{W_\mathrm{P}(T,t)}{W_\mathrm{g}}\right] \overline{A}(T,t) \ , \tag{2.26}$$

where g_i is the initial value of the gain. It should be noted that the initial loss and gain do not necessarily equal the unsaturated loss l_0 and gain g_0, if the relaxation time T_A is longer than the round trip time T_r. In this case, the initial loss/gain will depend on the long-term time variable ($g_\mathrm{i} \equiv g_\mathrm{i}(T)$; $l_\mathrm{i} \equiv l_\mathrm{i}(T)$).

2.2.5 Time-Shift

Due to asymmetrical modulations of the pulse envelope, the pulse center can be shifted slightly at every round trip. However, for an effective solution of the

HME the pulse must be centered at a fixed time $t_0 = 0$. The additional delays or advances can be compensated by introducing a shift

$$\Delta\overline{A}_{\mathrm{shift}}(T,t) = t_{\mathrm{s}}\frac{\mathrm{d}}{\mathrm{d}t}\overline{A}(T,t)\ , \tag{2.27}$$

to the HME, where t_{s} is the time delay by which a pulse is shifted from the center t_0 during a single round trip in the oscillator.

2.2.6 Typical Values

For an identification of the critical parameters of a passive mode-locked oscillator at sub-THz frequencies, first typical ranges and values for all parameters must be estimated.

If the propagation velocity of the microwaves is assumed to be approximately the speed of light in vacuum, and the dimension of the complete oscillator is assumed to be in the order of meters, the round trip time T_{r} is of the order of nanoseconds. The time variable T describes the long-scale behavior of the laser pulse and is therefore of the same order as T_{r}.

The counterpart to T is the so-called 'local-time' t, which describes the behavior of the pulse during a single round trip in the oscillator. It is convenient to switch to a reference frame for the local time so that the peak of the pulse is always centered at $t = 0$. Therefore, t is approximately equal to the pulse length. For a microwave passive mode-locked oscillator with a center frequency of 263 GHz, the expected pulse length is approximately 0.1 ns (see section 2.1).

The small signal gain g_0 is a dimensionless quantity of a few percent. In a passive mode-locked laser, a fast amplifier's gain saturates with the average power. Thus, the gain is assumed to be constant during a single pulse but saturates according to (2.15) over a series of pulses. In a slow amplifier, the gain saturates during a single pulse and is described by (2.26).

Similar to the gain, the loss l_0 is a positive, dimensionless number in a similar range. The total loss that a pulse experiences is the sum of the linear loss l_{out} from the decoupling of the output signal and the nonlinear loss from the saturable absorber (see (2.18) and (2.25)).

The bandwidth limitation, whether from the amplifier or other components, is implemented as a dispersive term in the HME. Since in the derivation of the bandwidth limitation a Lorentzian line shape is assumed, the bandwidth parameter ω_g corresponds to the FWHM of a Lorentzian peak. For sub-THz components, the bandwidth parameter ω_g is typically around $10\,\%$ of the center frequency.

The intracavity dispersion per round trip is described by the parameter d_0. It can be obtained from the dispersion relation $\omega(k)$ and is defined as

$$\mathrm{GVD}(\omega_0) = \left[\frac{\partial}{\partial\omega}\frac{1}{v_\mathrm{g}}\right]_{\omega=\omega_0} . \tag{2.28}$$

As mentioned previously, both a positive and a negative GVD are possible. For passive mode-locked microwave oscillators, only the latter one is important and is investigated exclusively in this work. The GVD has the dimension $\frac{\mathrm{time}^2}{\mathrm{length}}$. Since in the HME all effects experienced by a pulse are averaged over the complete oscillator, the dispersion parameter d_0 is given by the integral of the GVD over the length of the oscillator. Consequently, the dispersion parameter d_0 is a negative number and has units of time^2. Typical values of d_0 for a fundamental mode circular waveguide around a center frequency of $263\,\mathrm{GHz}$ are in the range of $-0.01\,\mathrm{ns}^2$ to $-10\,\mathrm{ns}^2$.

For a HME with a fast amplifier/absorber and without dispersion effects, Haus obtained a sech-pulse

$$\overline{A}(T,t) = \overline{A}_0\,\mathrm{sech}\left(\frac{t}{\tau_\mathrm{p}}\right) \tag{2.29}$$

as solution analytically [62], [63]. Although a number of more complex solutions, including for example dispersion effects, are available [66], the complex cubic Ginzburg-Landau equation does not possess analytical solutions in general and a numerical solution is necessary.

2.3 Passive Mode-Locked Oscillators for MW Frequencies

The basic approach to transfer the idea of passive mode-locking to microwave systems is straight forward: for the realization of a mode-locked microwave source, all components of a passive mode-locked laser are replaced by corresponding devices operating at microwave frequencies [4]. As shown by the preliminary investigations about mode-locking at microwave frequencies by Ginzburg et al. , electron tubes are the appropriate devices for a realization of the active components, namely amplifier and saturable absorber [50], [52].

Besides amplifier and saturable absorber, a mechanism to couple both devices in a feedback loop (mode-locked oscillator) and to decouple the output signal from it, is required. Well-known techniques for the transmission of broadband, high power microwave radiation are transmission lines based on quasi-optics or overmoded waveguides [60], [61].

For the following investigations, the HME is solved numerically with the common approach of the split-step Fourier method (SSFM) (see appendix A.1). The steady-state solution is found by simulating the HME until a steady state is reached. If no steady state could be reached, the simulation is stopped after 1000 simulated round trips. As an initial seed, a long, low power sech pulse according to (2.29) is used. Details of the numerical methods are given in the appendix A.1.

2.3.1 Fast and Slow Components

As mentioned previously, for mode-locked lasers the active components, i.e. amplifier and saturable absorber, can be divided into ‘fast’ and ‘slow’ components. A slow component cannot recover its initial properties on the timescale of an ultra-short pulse, so that the gain/absoption behavior changes during the pulse, while a fast component recover almost immediately and the gain/absoption behavior does not depend on the pulse length.

Following the approach given in chapter 1.4, the laser medium and the saturable absorber must be replaced by two electron tubes in order to transfer the principle of passive mode-locked lasers to sub-THz frequencies. This raises the question

whether the terms ‘fast’ and ‘slow’ are also applicable to electron tubes. Based on the previous work from Ginzburg et al. [67], this can be answered clearly with ‘yes’. For the classification, the decisive factor is the relationship between the wave’s group velocity and the translation velocity of the electron beam (for details about electron tubes, see the following chapter). If the group velocity of the wave is equal to the translation velocity of the electron beam (below referred to as the ‘synchronized operation regime’ following the terminology introduced in [67]), the tube has the properties of a fast component. If the wave propagates faster than the electron beam (with a group velocity greater than the electron’s translation velocity, below referred to as the ‘slippage operation regime’ [67]), the tube has the properties of a slow component.

As will be shown in chapter 5, an electron tube operated as saturable absorber must be operated in the synchronized regime. For the amplifier, which is realized as helical gyro-TWT, an operation in both regimes, synchronized and slippage, is generally possible. However, the slippage regime is preferable to achieve the maximum output power [67], [68].

In the following, the HME is used to investigate the behavior of both cases. First, the HME for a passive mode-locked oscillator with a fast amplifier and a fast, saturable absorber is investigated. Next, the HME for an oscillator with a fast absorber but a slow amplifier is given. While the first case is common in laser physics, the combination of a slow amplifier with a fast absorber cannot be found in the standard literature.

2.3.2 Fast Amplifier and Fast Absorber

Starting from (2.7), the HME for a specific passive mode-locked oscillator can be assembled. For this, the change of the amplitude $\Delta\overline{A}$ during a single round trip of the pulse in the oscillator is assembled by the previously derived expressions.

The HME for a passive mode-locked oscillator consisting of a feedback-loop from a fast amplifier and a fast saturable absorber is given by:

$$\begin{aligned} T_\mathrm{r}\frac{\partial}{\partial T}\overline{A}(T,t) &= \Delta\overline{A}(T,t) \\ &= \Delta\overline{A}_{\mathrm{g,lin}}(T,t) + \Delta\overline{A}_\mathrm{b}(T,t) + \Delta\overline{A}_\mathrm{disp}(T,t) \\ &\quad - \Delta\overline{A}_{\mathrm{l,lin}}(T,t) - \Delta\overline{A}_{\mathrm{l,sat}}(T,t) \\ &= \left[g_\mathrm{s}(T) - l_\mathrm{out} + \left(\frac{1}{{\omega_\mathrm{g}}^2} + j d_0\right)\frac{\partial^2}{\partial t^2} + \frac{l_0}{1+\frac{|\overline{A}(T,t)|^2}{P_{\mathrm{l,sat}}}} \right] \overline{A}(T,t)\ . \end{aligned} \tag{2.30}$$

The losses are separated into linear losses l_out, corresponding to the decoupling of a fraction of the oscillating pulse at every round trip, and the nonlinear losses from the absorber. While in (2.30) the bandwidth limitation could be also included into the gain (see (2.13)) this is not possible in an easy way for the HME with a slow amplifier (see following section). Therefore, a separate bandwidth limiting term is introduced for a better comparability of both HMEs.

Of special interest for the design of a passive mode-locked oscillator are the influences of the following four parameters:

- small-signal gain g_0,
- unsaturated loss l_0,
- bandwidth ω_g and
- dispersion d_0.

The effect of these parameters on the stability and the generated output signal of a passive mode-locked oscillator can be evaluated by solving the corresponding HME (2.30) for reasonable values. Fig. 2.3 shows selected results of various simulations for different combinations of the four critical parameters. In all simulations, the saturation power of the absorber is $P_{\mathrm{l,sat}} = 0.25\,\mathrm{kW}$ and the saturation power of the amplifier is $P_{\mathrm{g,sat}} = 1.0\,\mathrm{kW}$.

In Fig. 2.3a, the steady-state solutions of (2.30) for different small-signal gains are shown. In the first slice ($g_0 = 0$), the initial pulse used for the startup of the oscillator is shown. As expected, no pulse can be formed as long as the net gain

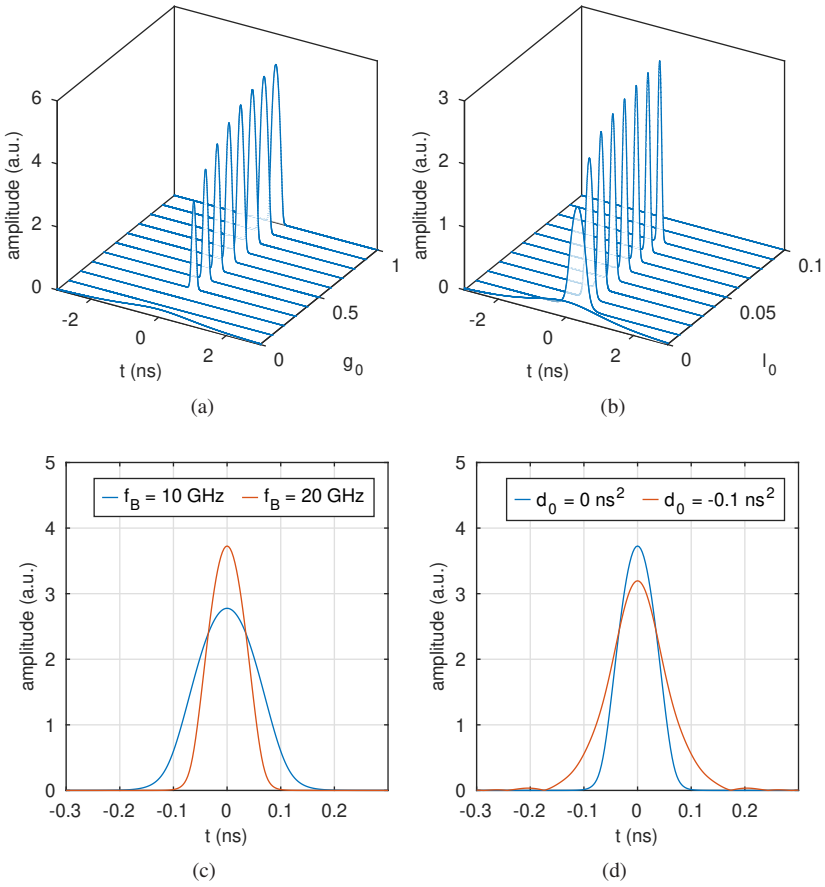

Figure 2.3: Solutions of (2.30) for different g_0 (a), l_0 (b), ω_b (c) and d_0 (d). The decoupling losses are set to $l_\mathrm{out} = 15\,\%$, the saturation power of the absorber is $P_\mathrm{l,sat} = 0.25\,\mathrm{kW}$ and the saturation power of the amplifier $P_\mathrm{g,sat} = 1.0\,\mathrm{kW}$.

that the initial pulse experiences is lower than the losses. Since the linear loss is set to $l_\mathrm{out} = 0.15$ and the unsaturated loss is $l_0 = 0.06$, the small signal gain must exceed 0.21 to allow a startup of the oscillator with a low-power pulse. With increasing gain, the peak power of the pulse increases. The steady-state

peak power is reached when the losses and gains experienced by a pulse are in balance.

For a high gain, the nonlinear effect a pulse experiences decreases since the saturable absorber is operated far beyond the saturation power. This results in an increased pulse length. In contrast, an increase of the unsaturated loss l_0 for a fixed g_0 results in a shortening of the pulses. This can be seen in Fig. 2.3b. Here, the generated pulses for a fixed g_0 of 0.3 and different values for the unsaturated loss l_0 are shown. It becomes clear that the saturable absorber is crucial for the formation of the pulses. With increasing l_0, the pulses are shortened, while the peak power increases. A limit is reached when the total losses in the absorber dominate the gain and the pulses experience a net loss.

In Fig. 2.3b, this is the case for $l_0 > 0.08$. At first it may seem surprising that the peak power increases despite higher losses. This is caused by the saturation behavior of the amplifier. As mentioned before, a similar saturation behavior as for a laser is assumed for the fast amplifier. Since this saturation depends only on the average power, the peak power increases for a shortening of the pulse. However, it is questionable whether this saturation behavior is also valid for an amplifier realized as electron tube. As discussed in the previous section, an electron tube amplifier operated in the synchronized regime, i.e. the wave group velocity is synchronized with the electron translation velocity, acts as a fast amplifier. Consequently, as soon as a pulse has left the tube, all electrons that were participating in the interaction also leave the tube. Therefore, no saturation effect based on an accumulation over many round-trips could occur in such an electron tube. Nevertheless, this model can be still useful for some general conclusions.

In Fig. 2.3c and Fig. 2.3d, the effects of bandwith limitation and dispersion are evaluated by a direct comparison of solutions for different ω_b and d_0, respectively. As expected, bandwidth and dispersion limit the minimal length of the pulses. The pulses shown in Fig. 2.3c are calculated without dispersion ($d_0 = 0\,\mathrm{ns}^2$) and the pulses shown in Fig. 2.3d are calculated for a bandwidth of $\omega_\mathrm{b} = 2\pi \cdot 20\,\mathrm{GHz}$. By a comparison of Fig. 2.3c and Fig. 2.3d it can be see that a low dispersion is crucial for the generation of ultra-short pulses. Even if a high bandwidth for all components could be realized, a high dispersion would inhibit the formation of ultra-short pulses. It should be noted that the variation in the peak power of the pulses is again caused by the saturation behavior of the amplifier.

2.3.3 Slow Amplifier and Fast Absorber

While slow saturable absorbers are an important and well studied topic in laser physics (see [69] for an overview), a passive mode-locked oscillator consisting of a slow amplifier with a fast absorber is not common in laser physics but of particular interest for a passive mode-locked oscillator at microwave frequencies. The HME for a passive mode-locked oscillator with a slow amplifier and a fast saturable absorber reads as:

$$\begin{aligned} T_\mathrm{r}\frac{\partial}{\partial T}\overline{A}(T,t) &= \Delta\overline{A}_{\mathrm{g,slow}}(T,t) + \Delta\overline{A}_\mathrm{b}(T,t) + \Delta\overline{A}_\mathrm{disp}(T,t) \\ &\quad - \Delta\overline{A}_\mathrm{l,lin}(T,t) - \Delta\overline{A}_\mathrm{l,sat}(T,t) + \Delta\overline{A}_\mathrm{shift}(T,t) \qquad (2.31) \\ &= \left[g_0 \mathrm{e}^{-\frac{W(t)}{W_\mathrm{g}}} - l_\mathrm{out} + t_\mathrm{s}\frac{\partial}{\partial t} + \left(\frac{1}{{\omega_\mathrm{b}}^2} + jd_0\right)\frac{\partial^2}{\partial t^2} \right. \\ &\quad \left. + \frac{l_0}{1+\frac{|\overline{A}(T,t)|^2}{P_\mathrm{l,sat}}} \right] \overline{A}(T,t)\ . \end{aligned}$$

As described in section 2.2.5, the pulse center is shifted slightly at every round trip due to asymmetrical modulations of the pulse envelope caused by the slow gain. Consequently, the time-shift t_s must be introduced to allow a steady-state solution.

It should be noted that in (2.31), it is assumed that the gain is completely restored between two round-trips and therefore g_i is replaced with g_0.

In Fig. 2.4, selected solutions of (2.31), solved for a long, low power initial sech-pulse, are shown. In Fig. 2.4a, the steady-state solutions of (2.31) for different small-signal gains are shown. In the first slice ($g_0 = 0$), the initial pulse used for the start-up of the oscillator is shown. It can be seen that for a slow amplifier, only a very narrow window ($g_0 \in [0.1, 0.11]$) of stable operation exists. In contrast to a passive mode-locked oscillator with fast devices, here a stable operation is only possible if the net gain experienced by the initial pulse is very low. For an increasing gain, the initial pulse splits up and a multi-pulse

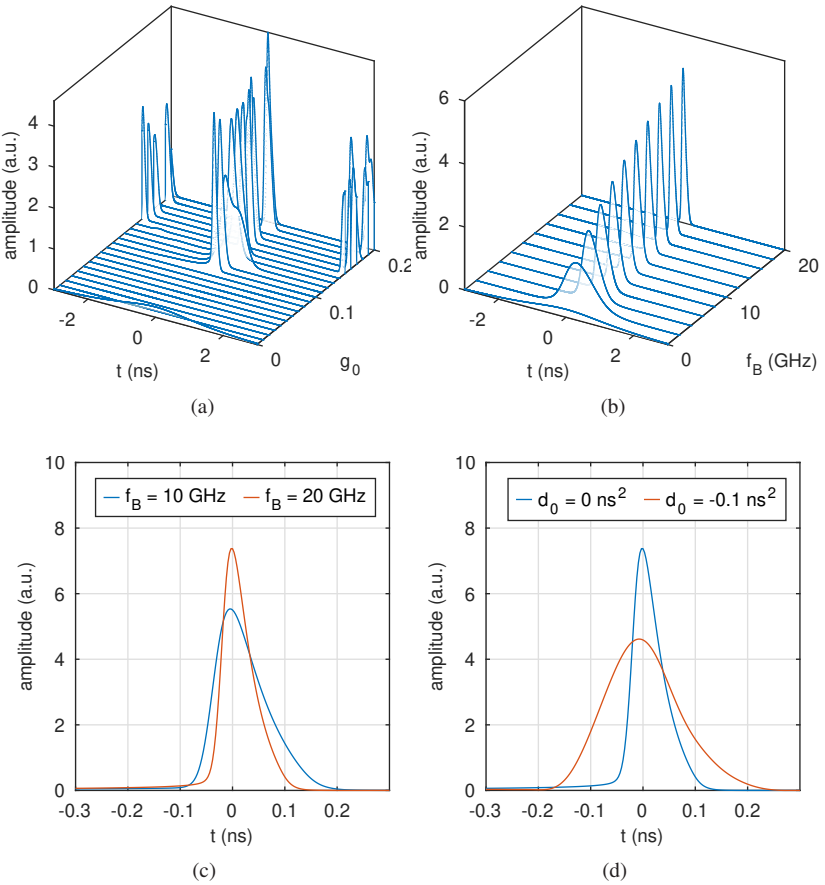

Figure 2.4: Solutions of (2.31) for different g_0 (a), ω_b (b+c) and d_0 (d). The decoupling losses are set to $l_\mathrm{out} = 10\,\%$, the saturation power of the absorber is $P_\mathrm{l,sat} = 0.25\,\mathrm{kW}$ and the saturation power of the amplifier $W_\mathrm{g} = 10^{-6}\,\mathrm{J}$.

regime occurs. The multiple pulses are in constant motion with respect to each other and the resulting pulse train is not any longer stationary.

Similar instabilities are well known from laser physics in passive mode-locked lasers with a slow absorber (see [69]). The reason for a higher stability against

a multiple-pulse breakup in mode-locked oscillators with fast devices than in oscillators with slow devices is that fast devices saturate with the peak power while slow devices saturate with the pulse energy. If a pulse breaks up into two pulses, each with half the energy, the peak power of the pulses is reduced by a factor of four. Consequently, such a break is suppressed more strongly in fast devices than in slow devices. In conclusion, an operation of the saturable absorber in the oversaturation regime is not possible for a passive mode-locked oscillator with slow devices while an oscillator with exclusively fast devices could be still operated in such a regime.

In Fig. 2.4b and Fig. 2.4c, the effects of a limited bandwidth are shown. As expected, the pulse length is limited by the bandwidth and an increasing bandwidth results in shorter pulses (Fig. 2.4b). An obvious difference with respect to the results of fast components is the asymmetric pulse shape (Fig. 2.4c). It is caused by the asymmetrical modulations of the pulse envelope in the slow amplifier. While the leading edge experiences the full gain, the trailing edge is amplified with a reduced gain. For the same reason, the pulse center is shifted slightly at every round trip and the effective round trip time is slightly changed.

To evaluate the effect of dispersion, the pulses of an oscillator with $g_0 = 0.15$, $l_0 = 0.1$ and a bandwidth of $\omega_\mathrm{b} = 2\pi \cdot 20\,\mathrm{GHz}$, are shown in Fig. 2.4d, once with and once without dispersion. Similar to the previous results for fast devices, a low dispersion is crucial for the generation of ultra-short pulses.

2.4 Conclusion

Based on the discussion in the previous sections, a conclusion can be drawn about the important aspects and properties of a passive mode-locked oscillator.

The steady-state operation of a passive mode-locked oscillator is reached when the net gain and net loss experienced by a pulse are in equilibrium. A stable equilibrium of gain and loss occurs when the amplifier and absorber are operated in saturation. In saturation, the losses are dominated by the linear losses which correspond to the decoupling of a fraction of the oscillating pulse from the oscillator. The decoupling factor is usually in the range of a few $10\,\%$ and consequently the saturated gain of the amplifier is of a similar order. This operation regime is unusual for electron tube amplifiers for common

applications, where high gains are required. However, an optimal amplifier for a passive mode-locked oscillator must provide a high saturation power and a low gain. As shown by Ginzburg et al. [68], helical gyro-TWTs offer a special operation regime with highest saturation power and a moderate gain. For this, the helical gyro-TWT is operated in the slippage regime, when the electromagnetic wave propagates faster than the electron beam (group velocity greater than the translation velocity of the electrons). As a result, the saturated output power is significantly increased while the gain is reduced. Therefore, a helical gyro-TWTs operated in the slippage regime is an excellent candidate for a passive mode-locked oscillator at microwave frequencies. It must be noted that an electron tube operated in the slippage regime behaves as a slow device (see section 2.3.1). Consequently, the region of stable operation is limited.

A clear result from the analysis of the HME is the importance of the bandwidth. In the HME, the bandwidth limitation is implemented as a dispersive term and equally distributed over the complete oscillator. In a real oscillator, the bandwidth limitation is mainly caused by the amplifier and absorber devices. For the generation of ultra-short pulses with a center frequency of $263\,\mathrm{GHz}$, a required bandwidth in the order of 10 to $20\,\mathrm{GHz}$ is expected.

Besides the bandwidth, a low dispersion is crucial for the generation of ultra-short pulses. As with all other effects, in the HME, the dispersion is equally distributed over the complete oscillator. In a real device, the dispersion will vary for the different components. To reduce the negative effects of dispersion, the $\mathrm{GVD}(\omega_0)$ of all components should be as low as possible, and the transmission length through components with higher $\mathrm{GVD}(\omega_0)$ should be as short as possible. As for a passive mode-locked oscillator at sub-THz frequencies, the length of the feedback system coupling both electron tubes (amplifier and saturable absorber) is much longer than the electron tubes, the dispersion of the feedback-system is of special interest. For the same reason, the oscillator is very sensitive to ohmic losses in the feedback system. Since ohmic losses belong to the category of linear losses, all ohmic losses directly reduce the output power of a passive mode-locked oscillator. For this reason, a technology with lowest possible dispersion and ohmic losses should be chosen for the feedback system as e.g. transmission lines based on quasi-optics or overmoded waveguides.

3 MW Components for Passive Mode-Locked Oscillators

A passive mode-locked oscillator can be divided into three major parts: the amplifier, the saturable absorber and the feedback system. For a realization at microwave frequencies, all three parts must be realized by components operating at microwave frequencies.

In this chapter, an overview of the different technologies and functional principles is given. First, technologies for the realization of the amplifier and absorber, namely helical gyro-TWTs and cyclotron absorbers are introduced. In the second part of the chapter, the available technologies for the realization of a quasi-optical feedback system are discussed.

3.1 Helical Gyro-TWTs

The historical development of electron tubes can be roughly divided into three phases: (1) grid-controlled electron tubes were devised; (2) electron tubes for the generation of microwave radiation with slow-wave structures or cavities were developed; and (3) high-power millimeter-wave, submillimeter-wave, and terahertz devices with novel fast-wave interaction mechanisms were developed [70]. The helical gyro-TWT belongs to the last group.

In general, gyro-devices use the electron cyclotron maser principle where the electron beam transfers a part of its azimuthal kinetic energy to a transversal electromagnetic wave. In a gyro-amplifier, coherent electromagnetic radiation is amplified by a stimulated emission of bremsstrahlung from the gyrating electrons in the beam. In so-called classical gyro-TWTs, a simple, cylindrical waveguide is used as a region for the electron-wave interaction. The optimal operation regime of classical gyro-TWTs is at frequencies near the waveguide cutoff frequency when the axial velocity of the electrons is close to the group

velocity of the wave. Correspondingly, the frequency band is limited and their stability against parasitic gyrotron oscillations is low. If classical gyro-TWTs are operated in an alternative operation regime, with highly relativistic electron velocities, the bandwidth can be increased, however, they are very sensitive to velocity spreads in the electron beam because of the high Doppler up-shift.

Since the realization of an amplifier based on the electron cyclotron maser principle with a classical interaction region (in the form of a cylindrical waveguide) poses several problems, Denisov et al. proposed a new type of gyrotron amplifier, the helical gyro-TWT [40]. The helical gyro-TWT avoids the previously mentioned problems by using a waveguide with helical corrugations (see Fig. 3.2) as an interaction region instead of a cylindrical one. In the helically corrugated waveguide, the dispersion is radically changed for longitudinal wavenumbers close to zero. This allows a resonant electron-wave interaction over a significantly increased bandwidth. At the same time, the sensitivity to velocity spreads in the electron beam is reduced.

A schematic drawing of a helical gyro-TWT is shown in Fig. 3.1. The axis encircling electron beam is generated in a CUSP-type electron gun (see section 3.1.4) consisting of the gun-coil (a), the anode (b) and the cathode with the electron emitter (c). The low power microwave input signal (d) is coupled into the vacuum tube through a broadband microwave window (e). For the coupling into the electron-wave interaction region, typically a sidewall coupler with a T-junction structure and a reflector, which prevents the propagation of the wave towards the electron gun, is used (f). The electron beam (j) is guided through the interaction region (i), a helically corrugated waveguide, by a strong, axial magnetic field generated by a superconducting magnet (g). In the interaction region, the electrons transfer a fraction of their kinetic energy to the electromagnetic wave and thereby amplify the signal (see section 3.1.2). A polarizer (h) after the interaction region is used to convert the circularly polarized $\mathrm{TE}_{1,1}$ wave into a linearly polarized one. Subsequently, the generated high power radiation is converted into a $\mathrm{HE}_{1,1}$ mode by a horn antenna with a smooth profile (k). At the same time, the horn takes over the task of the collector, which recovers the electron beam (see section 3.1.6). Finally, the high power microwave radiation is coupled out through a broadband mircowave window (l). Typically, such windows are realized as multiple-layer windows (see section 3.1.6).

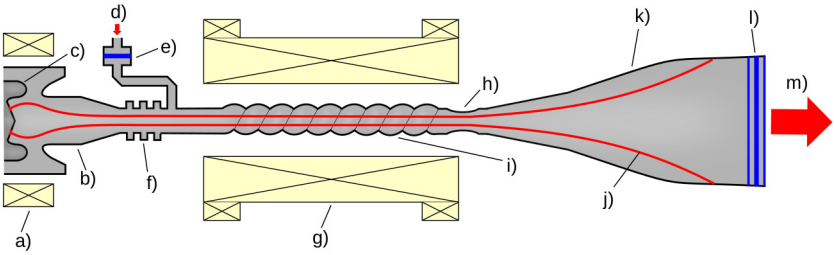

Figure 3.1: Diagram of a helical gyro-TWT with a) gun-coil, b) anode, c) cathode with the emitter, d) low power input signal, e) vacuum window at the input, f) reflector, g) main-coil, i) helically corrugated interaction region, h) polarizer, k) horn antenna and collector, j) electron beam, l) broadband vacuum window, m) high power output signal.

3.1.1 Helically Corrugated Waveguides

The inner surface of a helically corrugated waveguide takes the form of

$$r(\phi, z) = R + \tilde{r}\cos(\tilde{m}\phi - \frac{2\pi}{\tilde{d}}z) \ , \tag{3.1}$$

with the mean radius R of the uncorrugated circular waveguide, the amplitude $\tilde{r}$ of the corrugation and the axial period $\tilde{d}$. The so called fold number $\tilde{m}$ determines which modes of a regular, cylindrical waveguide, are coupled by the corrugation. Two modes $\mathrm{TE}_{m_\mathrm{A},1}$ and $\mathrm{TE}_{m_\mathrm{B},1}$ are coupled with each other, if they fulfill the condition [71]

$$\tilde{m} = m_\mathrm{A} - m_\mathrm{B} \tag{3.2}$$

together with the Bragg resonance condition

$$\frac{2\pi}{\tilde{d}} \approx k_{\parallel\mathrm{A}} - k_{\parallel\mathrm{B}} \ , \tag{3.3}$$

where $k_{\parallel\mathrm{A}}$ and $k_{\parallel\mathrm{B}}$ are the axial wavenumbers of the two coupled modes A and B. In the following, three-fold helically corrugated waveguides ($\tilde{m} = 3$) are investigated exclusively. An example of such a three-fold helically corrugated waveguide is shown in Fig. 3.2.

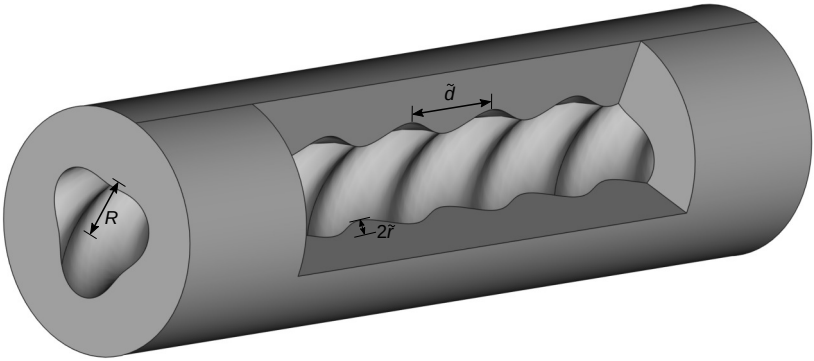

Figure 3.2: Waveguide with a threefold helically corrugated surface.

For an optimal stability and broadband behavior of the helical gyro-TWT, the parameters of the three-fold helical corrugation are chosen such that the two partial waves of lowest order, namely the $\mathrm{TE}_{2,1}$ and $\mathrm{TE}_{1,1}$ modes, of a regular waveguide are coupled. From the coupling condition (3.2) with $\tilde{m} = 3$ it follows that this coupling is only possible if mode B is a counter-rotating $\mathrm{TE}_{-1,1}$ mode.

For a suppression of higher-order parasitic modes, the radius R is set such that the $\mathrm{TE}_{2,1}$ mode is near to cut-off at the operation frequency band and the cut-off frequency of the $\mathrm{TE}_{1,1}$ mode is far below the operating frequency. Consequently, the Bragg resonance condition (3.3) simplifies to:

$$\begin{aligned} k_{\parallel \mathrm{A}} &\approx 0 \,, \\ k_{\parallel \mathrm{B}} &\approx k \,, \\ \Rightarrow \frac{2\pi}{\tilde{d}} = \tilde{k}_{\parallel} &\approx k_{\parallel \mathrm{B}} \,. \end{aligned} \tag{3.4}$$

As a consequence of the Bragg resonance condition (3.4), the coupling occurs between the first spatial harmonic of mode B (axial wavenumber shifted by $\tilde{k}_{\parallel}$) and the fundamental mode A.

The wave equations for the coupled modes in a helically corrugated waveguide can be derived from the inhomogeneous Helmholtz equation

$$\bar{\boldsymbol{S}} = \nabla^2 \boldsymbol{\mathcal{E}} - \frac{1}{c^2}\frac{\partial^2}{\partial t^2}\boldsymbol{\mathcal{E}} \,, \tag{3.5}$$

where $\bar{\boldsymbol{S}}$ is a source term and the electric field $\boldsymbol{\mathcal{E}}$ should be an eigenmode $\hat{\boldsymbol{e}}$ of the waveguide with a harmonic time dependence:

$$\boldsymbol{\mathcal{E}} = \mathrm{Re}\left\{\bar{A}(z)\mathrm{e}^{\,j\omega t}\hat{\boldsymbol{e}}(r,\phi)\right\} \,. \tag{3.6}$$

It should be noted that here the wave envelope $\bar{A}(z)$ does not depend on the time.

In the helically corrugated waveguide, two modes A and B (here $\mathrm{TE}_{2,1}$ and $\mathrm{TE}_{-1,1}$) are coupled with each other. For a description of this coupling, two source terms $\bar{\boldsymbol{S}}_{\mathrm{A,B}}$ and $\bar{\boldsymbol{S}}_{\mathrm{B,A}}$ are required that couple the mode B into the mode A and the mode A into the mode B, respectively:

$$\bar{\boldsymbol{S}}_{\mathrm{A,B}} = \mathrm{Re}\left\{C_{\mathrm{A,B}}\bar{B}(z)\mathrm{e}^{\,j\omega t}\hat{\boldsymbol{e}}_{\mathrm{A}}(r,\phi)\right\} \,, \tag{3.7}$$

$$\bar{\boldsymbol{S}}_{\mathrm{B,A}} = \mathrm{Re}\left\{C_{\mathrm{B,A}}\bar{A}(z)\mathrm{e}^{\,j\omega t}\hat{\boldsymbol{e}}_{\mathrm{B}}(r,\phi)\right\} \,. \tag{3.8}$$

where $C_{\mathrm{A,B}}$ and $C_{\mathrm{B,A}}$ are coupling coefficients that determine the strength of the coupling. If it is further assumed that the envelope changes only slowly with z and therefore has a narrow bandwidth, it is valid to solve (3.5) only for one side band. Under these assumptions, the Helmholtz equations for both modes A and B calculates as:

$$\begin{aligned} C_{\mathrm{A,B}}\bar{B}(z)\mathrm{e}^{\,j\omega t}\hat{\boldsymbol{e}}_{\mathrm{A}}(r,\phi) = {} & \left(\frac{\partial^2}{\partial z^2} + \nabla_\perp^2\right)\left[\bar{A}(z)\mathrm{e}^{\,j\omega t}\hat{\boldsymbol{e}}_{\mathrm{A}}(r,\phi)\right] \\ & + k^2\bar{A}(z)\mathrm{e}^{\,j\omega t}\hat{\boldsymbol{e}}_{\mathrm{A}}(r,\phi) \,, \end{aligned} \tag{3.9}$$

$$\begin{aligned} C_{\mathrm{B,A}}\bar{A}(z)\mathrm{e}^{\,j\omega t}\hat{\boldsymbol{e}}_{\mathrm{B}}(r,\phi) = {} & \left(\frac{\partial^2}{\partial z^2} + \nabla_\perp^2\right)\left[\bar{B}(z)\mathrm{e}^{\,j\omega t}\hat{\boldsymbol{e}}_{\mathrm{B}}(r,\phi)\right] \\ & + k^2\bar{B}(z)\mathrm{e}^{\,j\omega t}\hat{\boldsymbol{e}}_{\mathrm{B}}(r,\phi) \,, \end{aligned} \tag{3.10}$$

where k is the free-space wavenumber. Using the orthonormality of the eigenmodes $\hat{\boldsymbol{e}}_{\mathrm{A}}$ and $\hat{\boldsymbol{e}}_{\mathrm{B}}$ together with the relations $\nabla_{\perp}^2\hat{\boldsymbol{e}} + k_{\perp}^2\hat{\boldsymbol{e}} = 0$ and $k_{\parallel}^2 = k^2 - k_{\perp}^2$, the equations (3.9) and (3.10) can be expressed as:

$$C_{\mathrm{A,B}}\overline{B}(z) = \frac{\partial^2}{\partial z^2}\overline{A}(z) + k_{\parallel}^2\overline{A}(z)\ , \tag{3.11}$$

$$C_{\mathrm{B,A}}\overline{A}(z) = \frac{\partial^2}{\partial z^2}\overline{B}(z) + \left(k_{\parallel} - \tilde{k}_{\parallel}\right)^2\overline{B}(z)\ . \tag{3.12}$$

In the second equation (3.12), the Bragg resonance condition (3.3) is already taken into account (coupling with the first spatial harmonic of mode B).

To calculate the dispersion of the resulting eigenwave in the helically corrugated waveguide, constant amplitudes with a harmonic z dependence and waves that propagate in positive z-direction are assumed for both modes A and B:

$$\overline{A}(z) = a\,\mathrm{e}^{\,-jk_{\parallel\mathrm{A}}z}\ , \tag{3.13}$$

$$\overline{B}(z) = b\,\mathrm{e}^{\,-jk_{\parallel\mathrm{B}}z}\ . \tag{3.14}$$

After applying the approach to the coupled mode equations (3.11) and (3.12), the resulting equations can be multiplied to derive an eigen-equation for the dispersion of the eigenmodes in a helically corrugated waveguide:

$$C_{\mathrm{A,B}}C_{\mathrm{B,A}} = \left(k_{\parallel}^2 + k_{\perp\mathrm{A}}^2 - k^2\right)\left(\left(k_{\parallel} - \tilde{k}_{\parallel}\right)^2 + k_{\perp\mathrm{B}}^2 - k^2\right)\ . \tag{3.15}$$

For a given wavenumber $k_{\parallel}$, four roots of (3.15) can be found. Two of them have a practical physical meaning and correspond to two eigenmodes of the helically corrugated waveguide. It is common to name them as the upper and lower eigenmodes. For a three-fold helically corrugated waveguide, the cutoff-frequency of the upper mode is higher than the cut-off frequency of the $\mathrm{TE}_{2,1}$ mode. Since a helical gyro-TWT is usually operated at frequencies below the $\mathrm{TE}_{2,1}$ cut-off frequency, only the lower eigenmode participates in the electron-wave interaction. It should be mentioned that for vanishing coupling coefficients $C_{\mathrm{A,B}}$ and $C_{\mathrm{B,A}}$, the dispersion equation (3.15) degenerates again into two separate dispersion curve functions of the uncoupled eigenmodes.

The coupling coefficient $C_{\mathrm{A,B}}$ for two TE modes can be calculated based on equation (2.98a) in [72] (see also [73]). For the two TE modes A and B with

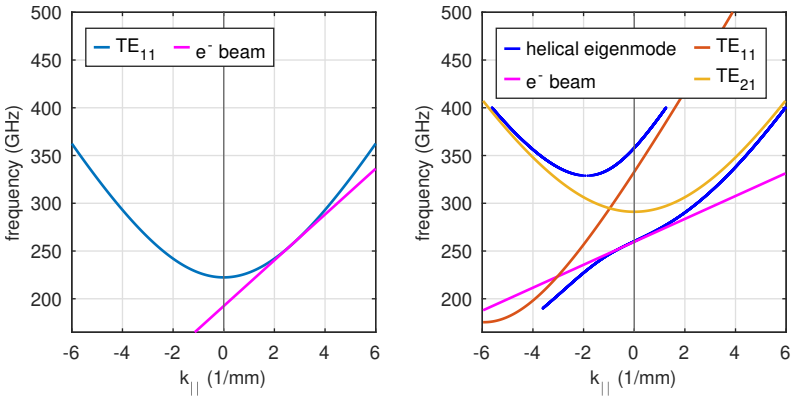

(a) (b)

Figure 3.3: Dispersion diagrams of the eigenmodes and the cyclotron resonance condition (pink line) for a smooth waveguide (a) and a helically corrugated waveguide (b).

the radial indices m_{A}, m_{B}, and the cut-off wavenumber $k_{\perp\mathrm{A}} = \frac{\chi'}{R}$, the coupling coefficient calculates as [74]

$$C_{\mathrm{A,B}} = \frac{\tilde{r}}{2R^3} \frac{\chi'^{\,2}_{\mathrm{A}} \chi'^{\,2}_{\mathrm{B}} - R^2 m_{\mathrm{A}} m_{\mathrm{B}} \left(k^2_{\perp\mathrm{A}} + \tilde{k}_{\parallel} k_{\parallel\mathrm{A}} \right)}{\sqrt{\chi'^{\,2}_{\mathrm{A}} - m^2_{\mathrm{B}}} \sqrt{\chi'^{\,2}_{\mathrm{B}} - m^2_{\mathrm{B}}}} \,. \tag{3.16}$$

Near the resonant coupling ($k_{\parallel\mathrm{B}} \approx k$), the coupling from mode A to mode B and the reverse coupling from mode B to mode A are similar and only weakly frequency dependent [74]. Therefore, a single coupling coefficient $C_{\mathrm{A,B}}$ is sufficient.

In Fig. 3.3, the dispersion curves for a cylindrical waveguide and a helically corrugated waveguide, used as interaction regions for a cyclotron absorber respectively a helical gyro-TWT at 263 GHz, are plotted. It can be seen that the eigenwave of the helically corrugated waveguide has a wide linear region around $k_{\parallel} = 0$. If the interaction between the electron beam and the eigenmode takes place in this region, this ensures a lower sensitivity to velocity spreads of the electron beam and allows an interaction over a broad frequency band.

For an illustration of the region of electron-wave interaction, the cyclotron resonance condition (see section 3.1.2 for details) is plotted as pink line in Fig. 3.3. The interaction between the electron beam and the eigenmode happens at synchronized phase velocities of the mode and the gyrating electron beam (intersection of the dispersion curves and the cyclotron resonance condition). In contrast to the helical waveguide, a broadband electron-wave interaction in the cylindrical waveguide is only possible at high axial wavenumbers which increases the sensitivity to spreads in the electron beam. Furthermore, the dispersion in the helical waveguide can be efficiently controlled by the parameters of the corrugation. As it will be shown in the following, this flexibility allows additional specialized operation regimes for helical gyro-TWTs which are of particular interest for a passive mode-locked oscillator.

3.1.2 Electron Cyclotron Maser Interaction

The electron-wave interaction in gyro-devices is based on the electron cyclotron maser principle where electrons move along helical trajectories guided by a homogeneous magnetostatic field $\mathfrak{B}_0 = \mathfrak{B}_0\hat{z}$. A resonant interaction between the electron beam and the electromagnetic wave occurs if the cyclotron resonance condition

$$\omega - k_{\parallel} v_{\parallel} \approx s\omega_{\mathrm{H}} \tag{3.17}$$

is fulfilled. Here, ω and $k_{\parallel}$ are the frequency and axial wavenumber of the wave. The axial velocity of the electrons and the cyclotron frequency are given by $v_{\parallel}$ and ω_{H}, respectively. The cyclotron frequency calculates as

$$\omega_{\mathrm{H}} = \frac{e_0 \mathfrak{B}_0}{m_{\mathrm{e}} \gamma} \,, \tag{3.18}$$

where $\mathfrak{B}_0$ is the magnetic field that guides the electron beam, e_0 is the elementary charge and m_{e} the rest mass of an electron. The Lorentz factor γ is defined by

$$\gamma = \frac{1}{\sqrt{1 - \left(\frac{v}{c_0}\right)^2}} \tag{3.19}$$

and describes the relativistic effects for high energy electrons with a velocity v relative to the laboratory frame. The cyclotron harmonic number s in (3.17) is

a positive integer that defines at which harmonic of the cyclotron frequency the interaction takes place. For three-fold helically corrugated waveguides, as used in the helical gyro-TWTs investigated in this work, the resonant interaction between the electron beam and the electromagnetic wave takes place at the second cyclotron harmonic ($s = 2$).

A key element of the cyclotron electron-wave interaction is the so-called phase bunching process, which is illustrated in Fig. 3.4. For an explanation of the phase bunching process, the cross-section of a single beamlet of gyrating electrons can be considered. The electrons gyrate with a given cyclotron frequency ω_{H} while the electromagnetic field oscillates with frequency ω. It is clear that an electron is accelerated or decelerated from the electric field, depending on its movement direction relative to the orientation of the electric field. As a result, it gains energy from the electric field or transfers energy to the field, respectively.

The relative orientation between the movement direction of the electrons and the direction of the electric field is essential for the interaction. A simple expression for this relative orientation can be found if phasors for the transversal momentum of the electrons and the transversal electric field are introduced:

$$\bar{p}_\perp = p_x + j p_y = |\bar{p}_\perp| \mathrm{e}^{\,j\omega_{\mathrm{H}} t + \phi_0} \,, \tag{3.20}$$

$$\overline{E}_\perp = \xi_x + j \xi_y = |\overline{E}_\perp| \mathrm{e}^{\,j\omega t} \,. \tag{3.21}$$

Now, the movement direction of the electrons relative to the orientation of the electric field can be described by an angle

$$\Delta\Theta = \arg(\overline{E}_\perp) - \arg(\bar{p}_\perp) \,. \tag{3.22}$$

In Fig. 3.4, the bunching process is illustrated in momentum space. Initially, the electrons in the beamlet are uniformly distributed (=uniform distribution of ϕ_0) which is shown on left hand side of Fig. 3.4. The blue arrows represent the orientation of the RF electric field. The single diagrams in Fig. 3.4 are snapshots taken at the time-steps $t_n = n\frac{2\pi}{\omega}$. Therefore, the direction of the electric field does not change from snapshot to snapshot while the phase of the electrons changes if their cyclotron frequency is different from the RF frequency. For $0 < \Delta\Theta < \pi$, electrons are accelerated and energy is transferred from the electric field to the electrons. Electrons with $\pi < \Delta\Theta < 2\pi$ are

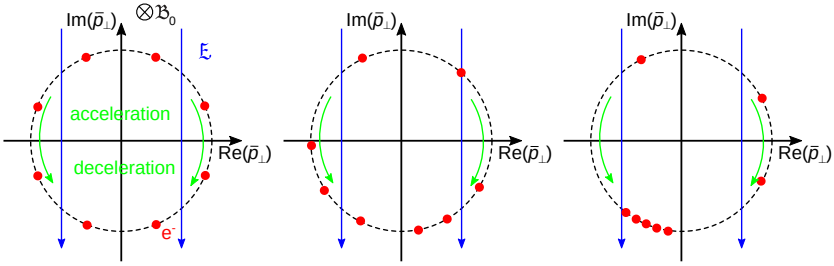

Figure 3.4: Schematic of the electron bunching mechanism during the cyclotron electron-wave interaction in the phase space. The single diagrams are snapshots taken at the time-steps $t_n = n\frac{2\pi}{\omega}$.

decelerated and energy is transferred from the electrons to the electric field. Correspondingly, for an uniformly distributed beam, half of the electrons gain energy while the other half loses an equivalent amount of energy and the overall energy of the electromagnetic field is preserved.

Next, it is important to note that the cyclotron frequency depends on the kinetic energy of an electron (because of the Lorentz factor in (3.18)). The relativistic mass $m = m_e\gamma$ of electrons which are decelerated, decreases and as a result their cyclotron frequency increases. At the same time, the cyclotron frequency decreases for electrons which are accelerated, because of their increasing relativistic mass. As a consequence of the changing cyclotron frequencies, the relative phase angle $\Delta\Theta$ between the electric field and the electrons' momentum changes after every period $T = \frac{2\pi}{\omega}$ and a bunching of the electrons occurs (see Fig. 3.4 center and right).

If the initial cyclotron frequency is slightly lower than the frequency of the electromagnetic wave, the electrons are bunched in the deceleration phase and energy is transferred from the electron beam to the electromagnetic wave. An amplifier must be operated in this regime. On the other hand, for the realization of an absorber, energy should be transferred from the electromagnetic wave to the electron beam and thus the electrons must be bunched in the acceleration phase. A bunching in the acceleration phase occurs for an initial cyclotron frequency slightly below the frequency of the electromagnetic wave.

For a better illustration, a realistic bunching process in a helical gyro-TWT is shown in Fig. 3.5. With the simulation model described in chapter 4, the

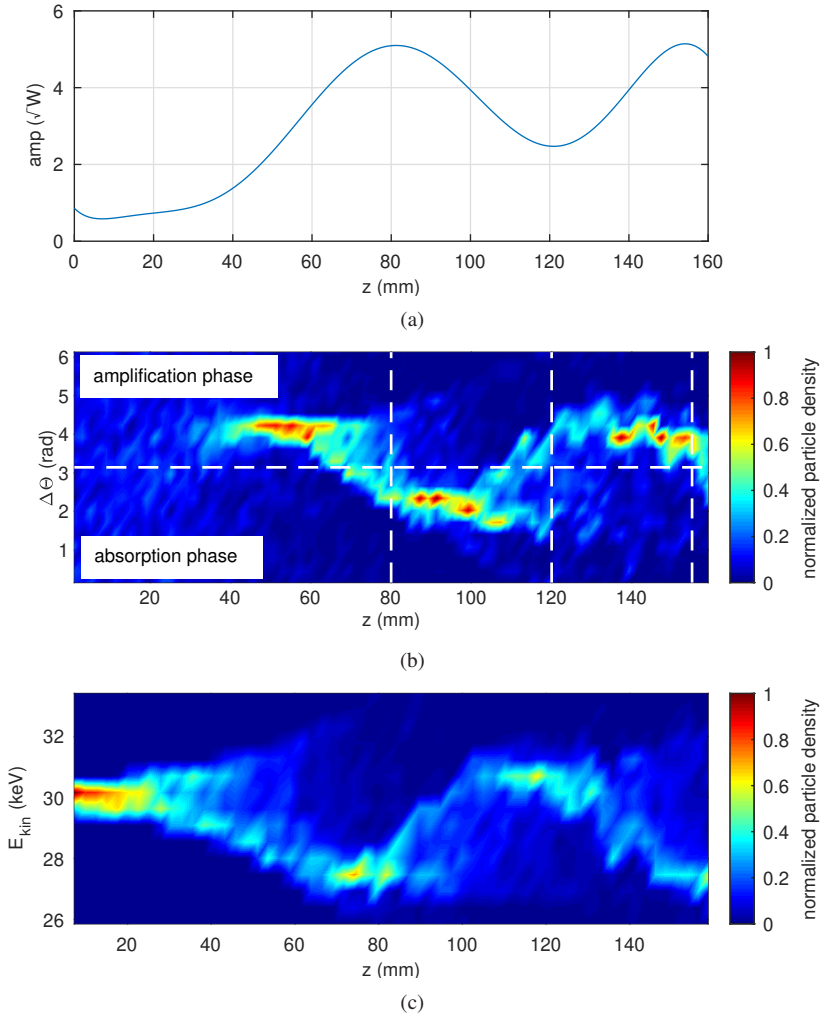

Figure 3.5: Electron bunching in a helical gyro-TWT. (a) Amplitude along the interaction space; (b) Relative phase shift between the cyclotron phase and the electromagnetic wave; (c) Kinetic energy distribution of the electrons.

amplification of an 1 W CW input signal at 263 GHz in a helical gyro-TWT is simulated. The helical gyro-TWT has a helical interaction region with $R = 0.534\,\text{mm}$, $\tilde{r} = 0.085\,\text{mm}$ and $\tilde{d} = 1.06\,\text{mm}$. It is driven by an electron beam with $I = 0.1\,\text{A}$ and $\alpha = 1.1$ at $\mathfrak{B}_0 = 4.8\,\text{T}$.

In Fig. 3.5a, the distribution of the amplitude along the interaction space is shown. It can be seen that the input signal is not immediately amplified. The reason for this behavior can be found in Fig. 3.5b. Here, the phase difference $\Delta\Theta$ between the electrons and the electromagnetic wave is shown. Initially, the phase of the electrons is uniformly distributed and, as a consequence, no effective energy transfer between the electromagnetic wave and the electron beam is possible ($z < 30\,\text{mm}$). This corresponds to the left side of Fig. 3.4. Subsequently, the dependence of the cyclotron frequency on the relativistic electron mass causes a bunching of the electrons. In Fig. 3.5b, this bunching can be seen for $z > 30\,\text{mm}$. The electrons are bunched in the amplification phase ($\pi < \Delta\Theta < 2\pi$) and consequently, the electromagnetic wave is amplified (see $z > 30\,\text{mm}$ in Fig. 3.5a). As the electromagnetic field increases, the energy in the electron beam decreases. This is shown in Fig. 3.5c, where the kinetic energy distribution of the electron beam is plotted.

It can be seen that the maximal RF power is reached for $z = 80\,\text{mm}$. From this point on, the electromagnetic wave is attenuated. From Fig. 3.5b and Fig. 3.5c it is clear why this happens: the electrons transfer energy to the electromagnetic wave and as a consequence, the electron bunch slowly shifts from the amplification phase to the absorption phase ($0 < \Delta\Theta < \pi$) and the electric field is attenuated. The shift of the bunched electrons between the amplification and absorption phase continues in the following ($z > 80\,\text{mm}$).

An important outcome of this discussion is that the length of an amplifier is a critical parameter that must be carefully chosen to achieve the maximum gain.

3.1.3 Large Orbit Electron Beams

In helical gyro-TWTs, a so called large orbit beam (LOB) is used to improve the robustness of the tube against the excitation of unwanted, parasitic electron-wave interactions. A LOB is an axis-encircling electron beam where the electrons gyrate with the cyclotron frequency around the center axis of the interaction region. When the electron trajectories are projected onto the cross-

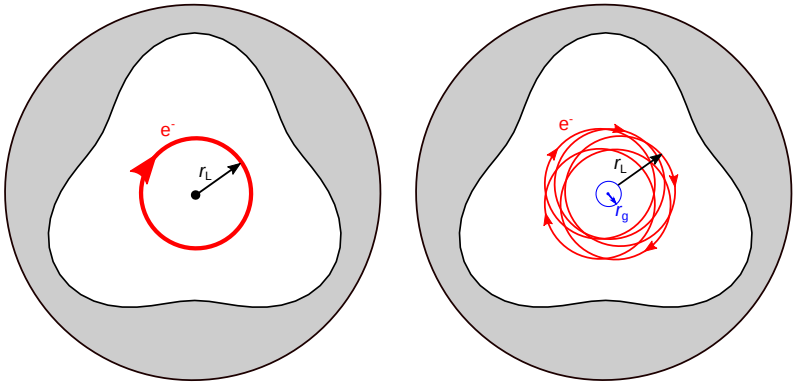

(a) (b)

Figure 3.6: Projection of the electron trajectories onto the cross-section of a helical waveguide for a perfect large orbit beam (a) and a non-perfect large orbit beam (b).

section of the waveguide, they form a circle with a radius equal to the Larmor radius r_{L}. This is shown for an ideal LOB in Fig. 3.6a. In a more realistic case, the center of the cyclotron gyration is not exactly in the center of the waveguide but is distributed on a circle with radius r_{g} around it, the so-called guiding center radius. This is illustrated in Fig. 3.6b.

For a LOB, the best selectivity of the electron-wave interaction is ensured. Only modes which are co-rotating with the gyrating electrons and with an azimuthal index that coincides with the cyclotron harmonic number can interact with the electrons.

This can be illustrated most simply by considering the coupling coefficient $C_{m,n}$ of a gyrating electron with a $\mathrm{TE}_{m,n}$ eigenmode of a cylindrical waveguide [75]:

$$C_{m,n}^2 = \frac{s^2}{2^s s!} \frac{\mathrm{J}_{m\pm s}^2(k_{\perp m,n} r_{\mathrm{g}})}{(\chi_{m,n}'^2 - m^2)\mathrm{J}_m^2(\chi'_{m,n})} \,. \tag{3.23}$$

Here, $\chi'_{m,n}$ is the n-th root of the derivative of the Bessel function of the first kind J_m and $k_{\perp m,n}$ is the transverse wavenumber of the waveguide mode. The sign $\pm$ refers to the counter- and co-rotating modes $\mathrm{TE}_{\pm m,n}$ where the rotation is given with respect to the electron gyration. A derivation of the coupling

coefficient can be found in [75] and is not repeated here, since in chapter 4 a more general coupling coefficient is derived.

Nevertheless, the selectivity of a LOB can be illustrated by (3.23). Considering that only the Bessel function of zero order J_0 is non-zero at 0, (3.23) immediately shows that for $r_\mathrm{g} = 0$ the coupling coefficient is different from zero only for modes $\mathrm{TE}_{s,n}$. Since the square of the mode's eigenvalue $\chi'_{m,n}$ occurs in the denominator of the coupling coefficient, the interaction with modes of radial index $n = 1$ is favored for a LOB, while modes with higher-order radial index are quadratically suppressed.

Utilizing this strong selectivity of LOBs for helical gyro-TWTs with a three-fold helically corrugated waveguide, the properties of the electron beam are chosen such that the electrons only interact with the near cut-off part of the eigenwave ($\mathrm{TE}_{2,1}$) at the second cyclotron harmonic. This ensures a high stability against the excitation of parasitic modes. Furthermore, this has the advantage of a reduced magnetic field (see (3.18)) compared to a usual tube operated at the fundamental cyclotron harmonic. This becomes important especially for tubes operating at sub-THz frequencies since the required field strengths for tubes operated at the fundamental cyclotron harmonic can easily exceed 10 T.

3.1.4 CUSP-Type Electron Guns

From the previous section it becomes clear that the LOB is a key feature of a stable helical gyro-TWT. The motion of electrons in the electron tubes under investigation is a superposition of a uniform drift along a static magnetic field and a uniform gyration on a circle of radius r_L with frequency ω_H. The radius is the Larmor radius, the center of the Larmor orbit is the guiding center r_g and ω_H is the cyclotron frequency. For an ideal LOB, the guiding center radius r_g is zero. Nevertheless, in a realistic case r_g never vanishes, e.g. because of the finite width of the electron emitter ring. In [76], a guiding center radius of $r_\mathrm{g} \leq 0.2\lambda$ is given as an admissible value to retain the favorable properties of a LOB. This limit is adopted in the following.

For a given magnetic field, a LOB is defined by the electrons' kinetic energy E_{kin} and the pitch factor

$$\alpha = \frac{v_\perp}{v_\parallel} \tag{3.24}$$

which is the ratio of the velocity $v_\perp$ transverse to the central axis and the velocity $v_\parallel$ parallel to it. A high quality electron beam is characterized by small spreads of its parameters E_{kin} and α. In this work, the spread δx of a value x is given as a relative value which is defined as the standard deviation of the corresponding distribution divided by the mean value of the distribution:

$$\delta x = \frac{1}{x_{\mathrm{mean}}} \sqrt{\frac{1}{N} \sum_{i=1}^{N} (x_i - x_{\mathrm{mean}})^2} \,. \tag{3.25}$$

Often, a Gaussian distribution of the values is assumed.

While the first LOBs were created by electron guns with an asymmetric magnetic field (for example the first helical gyro-TWT had an electron gun with kicker magnet [40]), the current state-of-the-art are so-called CUSP-type electron guns (CUSP-guns). A schematic illustration of a CUSP-gun and the associated magnetic field is shown in Fig. 3.7. The electrons are emitted from an annular electron emitter at the cathode and are accelerated by an applied acceleration voltage towards the anode. They are guided by a static magnetic field. A non-adiabatic transition of the magnetic field from negative to positive values (the so-called cusp) allows a conversion of the electrons' axial velocity into a transverse velocity component. By this mechanism, the originally rectilinear electron beam emitted from the cathode is transformed to a LOB. The cusp is followed by a weakly inhomogeneous field, which causes an adiabatic compression. During the adiabatic compression, a further part of the electrons' axial velocity is converted into a transverse velocity component and, consequently, the pitch factor increases.

Adiabatic compression is based on the conservation of the perpendicular adiabatic invariant (see chapter 1.6 in [77])

$$I_\perp = \frac{p_\perp^2}{\mathfrak{B}} = \mathrm{const} \,. \tag{3.26}$$

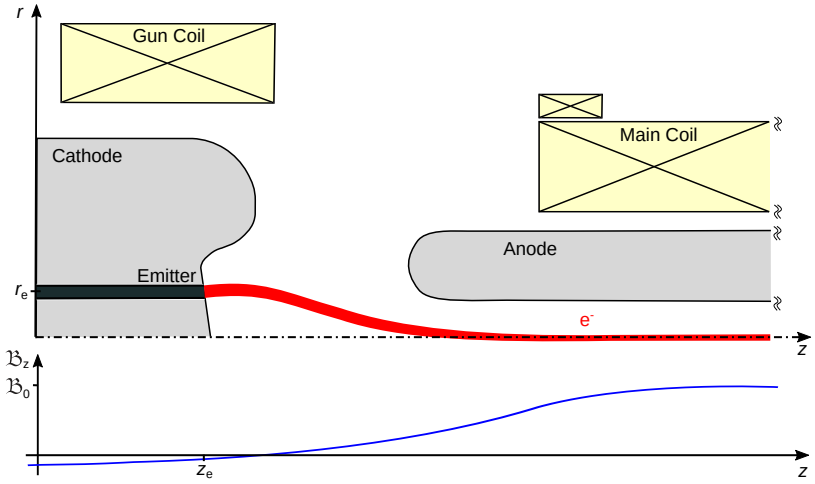

Figure 3.7: Schemata of a CUSP-gun. Top: Geometry of the gun. Bottom: $\mathfrak{B}_z$ component of the magnetic field.

The magnetic flux Ψ depends on the perpendicular adiabatic invariant and has the meaning of a magnetic flux through the Larmor circle:

$$\Psi = \pi r_{\mathrm{L}}^2 \mathfrak{B} = \frac{\pi}{e_0^2} I_\perp \ . \tag{3.27}$$

As a consequence of the conservation of energy and magnetic flux, the axial momentum of a gyrating electron is converted to a transverse momentum component in a convergent magnetic field.

For an idealized cusp, in the form of a step-function (see Fig. 3.8), analytical expressions for the relativistic electron trajectories can be found. The magnetic field and vector potential for a step-like cusp are

$$\begin{aligned} \mathfrak{B}_z &= \mathfrak{B}_0 \left(1 - 2\mathrm{H}(z)\right) \ , \\ \mathfrak{A}_\phi &= \frac{r\mathfrak{B}_0}{2} \left(1 - 2\mathrm{H}(z)\right) \ , \end{aligned} \tag{3.28}$$

with the Heaviside step function $\mathrm{H}(z)$. Although such an idealized cusp seems to be an unrealistic simplification, it allows the derivation of the basic behavior

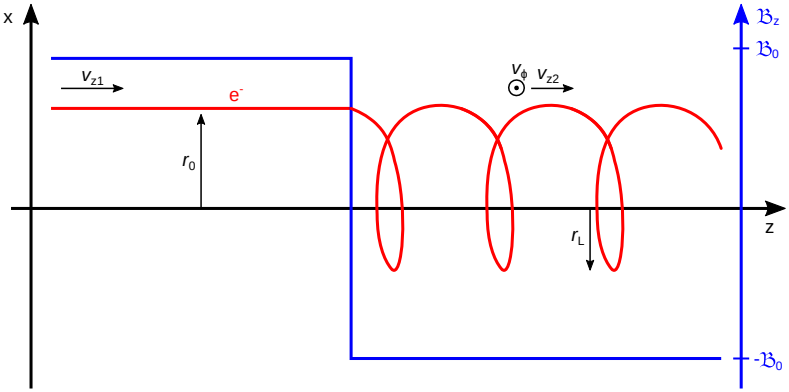

Figure 3.8: Ideal magnetic field step (cusp) with an electron trajectory (based on [78]).

of electron trajectories in CUSP-guns. In a realistic CUSP-gun the objective of design is to realize a cusp that approaches an ideal cusp, meaning that the transition from negative to positive magnetic field should happen as abruptly as possible.

For a derivation of the electron trajectories, the Lagrangian formalism is used. Starting from the Euler-Lagrange equation:

$$\frac{\mathrm{d}}{\mathrm{d}t}\frac{\partial L}{\partial \dot{\boldsymbol{r}}} = \frac{\partial L}{\partial \boldsymbol{r}} \,, \tag{3.29}$$

the Lagrangian L of an electron in an electromagnetic field is given as [77]

$$L = \frac{-m_\mathrm{e} c_0^2}{\gamma} - e_0 \dot{\boldsymbol{r}} \cdot \mathfrak{A} + e_0 \mathfrak{V} \,, \tag{3.30}$$

where γ is the Lorentz factor and the dot-notation symbolizes a partial time derivative ($\partial/\partial t$). The magnetic vector potential and the scalar electric poten-

tial are $\mathfrak{A}$ and $\mathfrak{V}$, respectively. In cylindrical coordinates, the Lagrangian takes the form:

$$L = -m_e {c_0}^2 \sqrt{1 - \frac{1}{c_0^2}\left(\dot{r}^2 + r^2\dot{\phi} + \dot{z}^2\right)} - e_0\left(\dot{r}\mathfrak{A}_r + r\dot{\phi}\mathfrak{A}_\phi + \dot{z}\mathfrak{A}_z\right) + e_0\mathfrak{V} \,. \tag{3.31}$$

Since the magnetostatic fields are produced from radially symmetric coils, only the $\mathfrak{A}_\phi$ component of the vector potential is non-zero and the Lagrangian simplifies to [79]:

$$L = -m_e c_0^2 \sqrt{1 - \frac{1}{{c_0}^2}\left(\dot{r}^2 + r^2\dot{\phi}^2 + \dot{z}^2\right)} - e_0 r\dot{\phi}\mathfrak{A}_\phi + e_0\mathfrak{V} \,. \tag{3.32}$$

From the Euler-Lagrange equation and the Lagrangian the equations for the radial, angular and axial coordinates can be found:

$$\frac{\mathrm{d}}{\mathrm{d}t}\left(m_e\gamma\dot{r}\right) = m_e\gamma r\dot{\phi}^2 - e_0\dot{\phi}\mathfrak{A}_\phi \,, \tag{3.33}$$

$$\frac{\mathrm{d}}{\mathrm{d}t}\left(m_e\gamma r^2\dot{\phi}\right) = 0 \,, \tag{3.34}$$

$$\frac{\mathrm{d}}{\mathrm{d}t}\left(m_e\gamma\dot{z}\right) = -e_0 r\dot{\phi}\frac{\partial\mathfrak{A}_\phi}{\partial z} \,. \tag{3.35}$$

The Lagrangian is independent of the ϕ coordinate and, therefore, the angular momentum p_ϕ is conserved (this can be seen from (3.34)). The generalized angular momentum calculates as:

$$p_\phi = \frac{\partial L}{\partial\dot{\phi}} = m_e\gamma r^2\dot{\phi} - e_0 r\mathfrak{A}_\phi = \mathrm{const} \,. \tag{3.36}$$

For an electron with an initial radius of r_0, a given magnetic field strength $\mathfrak{B}_0$ and in the absence of an electric field with a ϕ-component ($\Rightarrow \dot{\phi} = 0$), the angular momentum evaluates for $t = 0$ as

$$p_\phi|_{t=0} = -\frac{e_0 r_0^2\mathfrak{B}_0}{2} \,. \tag{3.37}$$

If a constant γ is assumed (no acceleration of the electron in the cusp region), the Euler-Lagrange equation (3.35) for the z-coordinate can be decoupled from the azimuthal motion. Therefore, (3.28), (3.36) and (3.37) are used to find an expression for $r^2\dot{\phi}$ which is applied to (3.35):

$$r^2\dot{\phi} = \frac{\omega_\mathrm{H}}{2}\Big(r^2\big(1-2\mathrm{H}(z)\big)-r_0^2\Big) \tag{3.38}$$

$$\Rightarrow \ddot{z} = \frac{\omega_\mathrm{H}^2}{2}\Big(r^2\big(1-2\mathrm{H}(z)\big)-r_0^2\Big)\delta(z) \tag{3.39}$$

where the definition (3.18) of the cyclotron frequency is used. The Dirac delta function $\delta(z)$ arises from the derivation of the Heaviside step function.

The axial position z and velocity v_z in (3.39) can be separated by the relation

$$\frac{\mathrm{d}}{\mathrm{d}t} = v_z\frac{\mathrm{d}}{\mathrm{d}z} \tag{3.40}$$

which allows a simple integration of (3.39). For an electron with the initial axial velocity $v_{z,1}$ before the cusp, the axial velocity $v_{z,2}$ after the cusp calculates as

$$v_{z,2}^2 = v_{z,1}^2 - r_0^2\omega_\mathrm{H}^2\,. \tag{3.41}$$

This leads to two important observations: (1) the transfer from axial to transversal velocity ($v_\perp = v_{z,2}-v_{z,1}$) depends on the radius of the electron beam before the cusp; (2) a threshold velocity $r_0\omega_\mathrm{H}$ exists below which the electron is reflected at the cusp. Since the threshold velocity depends on the initial radial position of the electron, it is also possible to define an equivalent threshold radius:

$$r_\mathrm{th} = \frac{v_{z,1}}{\omega_\mathrm{H}}\,. \tag{3.42}$$

During the design of a CUSP-gun, the two relations above are the main limiting factors for the geometry of the ring-shaped emitter. The finite thickness of the annular emitter causes a spread in the radius of the emitted beam, which is the dominant source of spreads in the pitch factor in the LOB. The threshold radius is a strongly limiting factor for the maximum radius of the emitter.

As for the z-coordinate, the Euler-Lagrange equation for the r-coordinate can be decoupled from the azimuthal motion by applying (3.38):

$$\ddot{r} = -r\frac{\omega_{\mathrm{H}}^2}{4}\left(1 - \frac{r_0^4}{r^4}\right) . \tag{3.43}$$

Since an analytical solution of this nonlinear differential equation is challenging, in [79] a comparison of (3.43) with the well-known equation of circular motion in space with a constant angular frequency is presented. If a gyration with the angular frequency ω_{H} and Larmor radius r_{L} around a center at r_{g} is assumed, the equation of motion is given by:

$$\ddot{r} = -r\frac{\omega_{\mathrm{H}}^2}{4}\left(1 - \frac{\left(r_{\mathrm{g}}^2 - r_{\mathrm{L}}^2\right)^2}{r^4}\right) . \tag{3.44}$$

A comparison of (3.43) and (3.44) leads to two equations that describe the relation between the guiding center radius and the Larmor radius:

$$r_{\mathrm{g}}^2 - r_{\mathrm{L}}^2 = r_0^2 \quad \text{for} \quad r_{\mathrm{g}} > r_{\mathrm{L}} , \tag{3.45}$$

$$r_{\mathrm{L}}^2 - r_{\mathrm{g}}^2 = r_0^2 \quad \text{for} \quad r_{\mathrm{g}} < r_{\mathrm{L}} . \tag{3.46}$$

In a CUSP-gun, the electrons are emitted as a hollow, rectilinear beam from an annular emitter. Therefore, $r_{\mathrm{L}} \ll r_0$ holds before the CUSP and (3.45) is valid. After the cusp, the electrons encircle the axis of symmetry and (3.46) holds. If only a magnetic field but no potential is present, the total electron velocity is a constant of the motion and (3.41) can be applied to derive expressions for the Larmor radius and the guiding center radius after the cusp:

$$v = v_{z,1}^2 + r_{\mathrm{L}1}^2\omega_{\mathrm{H}}^2 = v_{z,2}^2 + r_{\mathrm{L}}^2{\omega_{\mathrm{H}}}^2 , \tag{3.47}$$

$$r_{\mathrm{L}}^2 = r_0^2 + r_{\mathrm{L}1}^2 , \tag{3.48}$$

$$r_{\mathrm{g}}^2 = r_{\mathrm{L}}^2 - {r_0}^2 = r_{\mathrm{L}1}^2 . \tag{3.49}$$

From these relations, two important rules can be extracted: First, the Larmor radius of the electrons after the transit through the cusp and, therefore, the transfer of axial velocity to transversal velocity, is controlled by the radius of the electron beam before the cusp. Second, if the electron beam is not

perfectly rectilinear before the cusp, the guiding center radius of the created LOB is non-zero.

It is also possible to derive equations for the electron trajectories in more realistic, non-ideal cusps in an analytical manner, at least if some restrictions on the initial vales and approximations are introduced. Details can be found in [79] and [80]. For the investigation of arbitrary cusp configurations, numerical methods can be used to calculate the electron trajectories. This approach is applied in [78]. In [78], a systematic analysis of the influences from realistic cusp configurations and influences from the gun geometry is performed. Based on these investigations and on the analytical calculations, the following design criteria for a CUSP-gun are found:

1. The cusp height $\Delta\mathfrak{B}$ has to be small for feasible values of r_{th} to avoid reflected electrons.
2. It is essential to operate far from threshold radius r_{th} if the CUSP-gun should support a wide range of possible pitch factors α.
3. The threshold radius r_{th} and therefore the cusp height $\Delta\mathfrak{B}$ limit the maximum radius of the annular electron emitter.
4. Since the transfer from axial to transversal velocity depends on the radius of the initial electron beam, a spread in the radial position leads to a spread in the pitch factor after the cusp. Therefore, the thickness of the annular electron emitter should be as thin as possible in order to minimize the thickness of the generated electron beam.
5. To minimize the guiding center radius r_{g}, the cusp should be located as close as possible to the electron emitter to ensure a minimum transversal velocity component of the electron beam before the cusp.
6. A symmetric cusp is necessary to minimize the guiding center radius r_{g} and to generate a high quality LOB.

For the simulation of CUSP-guns, so-called electrostatic tracking-solvers are well suited. As part of this work, the two in-house implementations of this method, Ariadne [81] and Esray [82] were evaluated and have shown to produce feasible results for CUSP-guns.

3.1.5 Waveguide Polarizers

At the end of the helical interaction region, the amplitude of the corrugation is slowly reduced to convert the helically corrugated waveguide into a cylindrical one. In this transition section, the eigenwave of the helical waveguide is converted into a $\mathrm{TE}_{1,1}$ mode of a circular waveguide. During the mode conversion, the wave is also decoupled from the electron beam since no interaction of the LOB with the $\mathrm{TE}_{1,1}$ mode is possible (see (3.23)). Thus, the output of the interaction region is a circular $\mathrm{TE}_{1,1}$ mode. For the feedback system that couples the amplifier and absorber devices in a passive mode locked oscillator, a linear polarized signal is beneficial (see section 3.4). Therefore, a polarizer is usually placed directly after the interaction region to convert the circularly polarized $\mathrm{TE}_{1,1}$ to a linearly polarized one.

The circular polarization can be considered as a superposition of two linearly polarized waves orthogonal to one another, with equal magnitudes but a phase difference of any odd integer multiple of $\pi/2$. A short, elliptical waveguide section with smooth transitions to the circular waveguide at both ends is sufficient to serve as a polarizer [83]. Such polarizers are well known and can reach a low cross-polarization [84]. An elliptical waveguide section acts as a polarizer, since a wave with an $\mathfrak{E}_r$ component along the major axis (the longest diameter of an ellipse) and a wave with an $\mathfrak{E}_r$ component along the minor axis (the shortest diameter of an ellipse) will have different phase velocities in these regions [85].

The surface of an elliptical waveguide is defined by

$$r(z,\phi) = R + \tilde{r}(z)\sin(2\phi)\ , \tag{3.50}$$

where $\tilde{r}(z)$ is the difference between the semi-minor axis (half of the minor axis) and the waveguide radius R along the waveguide. To calculate the polarization effect of an elliptical polarizer, the wave is decomposed into so-called X and O-modes, which are linearly polarized modes with $\mathfrak{E}_r$ components rotated by $45°$ with respect to the major and minor axis of the ellipse (see Fig. 3.9). The 'O-mode' stands for 'ordinary mode' and describes in this context a mode with a dispersion of the cylindrical input waveguide. The 'X-mode' is an 'extraordinary mode' with a dispersion changed because of the elliptical waveguide cross-section.

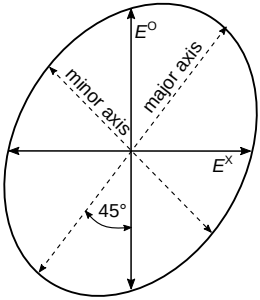

Figure 3.9: Cross-section of an elliptical waveguide (based on [84]).

If an input O-mode wave is assumed, a part of the wave is coupled to the X-mode by a passage through the polarizer. A coupling coefficient C_{ellip} for the X and O-mode can be derived [86]:

$$C_{\mathrm{ellip}} = \frac{1}{2R^2} \frac{\chi'^2}{\sqrt{(kR)^2 - \chi'^2}} \frac{\chi'^2 + 1}{\chi'^2 - 1} \,. \tag{3.51}$$

Here χ' is the eigenvalue of the mode (1.8412 for a $\mathrm{TE}_{1,1}$) and k is the free-space wavenumber. Now the amplitudes A^{O} and A^{X} at every position z along the elliptical polarizer can be calculated:

$$\begin{pmatrix} A^{\mathrm{O}}(z) \\ A^{\mathrm{X}}(z) \end{pmatrix} = \begin{pmatrix} \cos(\psi) & j\sin(\psi) \\ j\sin(\psi) & \cos(\psi) \end{pmatrix} \begin{pmatrix} A^{\mathrm{O}}(0) \\ A^{\mathrm{X}}(0) \end{pmatrix} \,. \tag{3.52}$$

Here, ψ is a phase constant defined by integration along the elliptical waveguide of length L:

$$\psi = 2C_{\mathrm{ellip}} \int_0^L \tilde{r}(z)\,\mathrm{d}z \,. \tag{3.53}$$

A circularly polarized wave can be expressed by a superposition of an O and X-mode with the amplitudes $A^{\mathrm{O}}(0) = j/\sqrt{2}$ and $A^{\mathrm{X}}(0) = 1/\sqrt{2}$. Because a linearly polarized mode corresponds to $A^{\mathrm{O}}(0) = 0$ and $A^{\mathrm{X}}(0) = 1$, the relation

$$|\psi| = \frac{\pi}{4} \tag{3.54}$$

must apply for a polarizer which converts between a circular and a linear polarization.

With the previous equations, the geometry for an elliptical polarizer can be found. In [83], Denisov et al. have pointed out that the maximum average radius R is limited since it should be slightly smaller than the critical radius for the $\mathrm{TM}_{1,1}$ mode to avoid mode conversion into this mode or the excitation of this mode by the electron beam. The limitation in the radius also limits the bandwidth of the polarizer. The reason for this is the kR dependence of the coupling coefficient of O- and X-modes (see (3.51)). For large R, a small change of the wavenumber k only has a small impact on the coupling coefficient. But for decreasing R, the impact of small changes of the wavenumber k increases. Denisov et al. give a maximal bandwidth for an elliptical polarizer in the Ka-band of about $\approx 7\,\%$ [83].

A possible alternative to an elliptical waveguide polarizer is presented in [87]. Instead of an elliptical waveguide, a rectangular waveguide with sinusoidal corrugations is used. They showed a significantly improved bandwidth in the order of $20\,\%$. Nevertheless, while elliptical polarizers are already successfully used in high power helical gyro-TWTs (e.g. in a Ka-band amplifier [88]), no examples are known where the rectangular polarizer is used in an experimental application.

3.1.6 Horn Antenna and Collector

A beam with a high coupling to a fundamental Gaussian mode is usually preferred as an output of the helical gyro-TWT by typical applications. This is also the case for the devices in a passive mode-locked microwave oscillator (see section 3.4). Therefore, the polarizer is followed by a mode converter, converting the $\mathrm{TE}_{1,1}$ mode to a balanced $\mathrm{HE}_{1,1}$ mode.

Usually, the mode converter is part of an integrated output system. It consists of a horn antenna to transform the $\mathrm{TE}_{1,1}$ mode to a $\mathrm{HE}_{1,1}$ mode, a collector which separates the RF and the electron beam, an optional energy recovery system to increase the overall system efficiency by recovering a part of the kinetic energy of the spent electron beam, and a broadband microwave window to decouple the microwave from the vacuum tube.

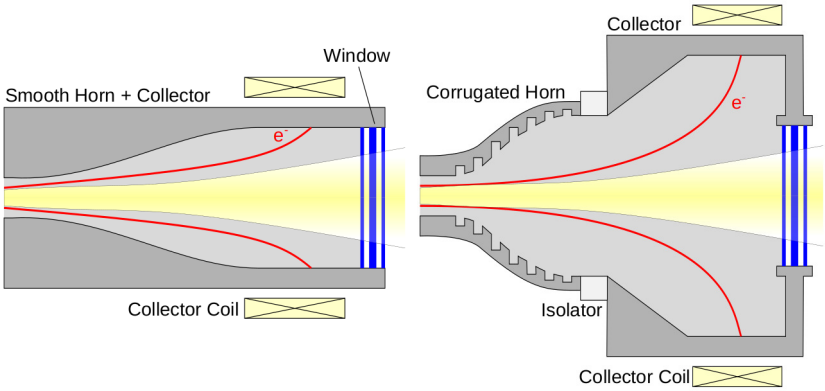

Figure 3.10: Schemata of two integrated output systems for a helical gyro-TWT. (a) A smooth horn with an integrated collector and a multi-layer output window. (b) Corrugated horn with a depressed collector and a multi-layer output window (based on [90]).

Each component of the output system must minimize back-reflections through the entire operating frequency band. Especially for the sub-THz range this is important because manufacturing tolerances become hard to achieve, which could increase the back-reflections of the final component. Unwanted reflections in an amplifier or a passive mode-locked oscillator could cause parasitic oscillations.

While in classical high-power microwave tubes such as gyrotrons quasi-optical systems based on optimized Vlasov launchers [89] are used to transform the cavity mode to a Gaussian like beam and to separate the electron beam from the RF, this type of mode-converter is insufficient for broadband signals. Therefore, in broadband gyro-TWTs, horn antennas are typically used to transform the $\mathrm{TE}_{1,1}$ mode to a $\mathrm{HE}_{1,1}$ mode. The $\mathrm{HE}_{1,1}$ mode is closely coupled to the fundamental free space Gaussian mode ($\mathrm{TEM}_{0,0}$) and can therefore be effectively radiated to free-space or fed into an oversized corrugated waveguide.

In Fig. 3.10, two possible configurations of integrated output systems are shown. In Fig. 3.10a, a combined horn antenna/collector is shown. A long smooth horn antenna [91] is used to convert the $\mathrm{TE}_{1,1}$ mode to a $\mathrm{HE}_{1,1}$ mode. At the same time, the horn antenna is used as collector to recover the electron

beam. An electromagnetic coil surrounding the horn directs the electron beam to the collector. A similar output system was used in the first W-Band helical gyro-TWT [42], [91].

An alternative to the smooth horn antenna is a corrugated one [90]. Because of the fine corrugations, the horn has to be separated from the collector section. Otherwise, the incident electron beam could damage the corrugations. An advantage of the separation of mode converter and collector is the possibility of pairing it with a depressed collector to recover a part of the spent electron beam's kinetic energy and to increase the overall system efficiency. Such a system is shown in Fig. 3.10b. The corrugated horn converts the amplified microwave signal in the $\mathrm{TE}_{1,1}$ mode to the fundamental $\mathrm{HE}_{1,1}$ mode. The Gaussian-like beam then propagates across an isolation gap and passes through the depressed collector. The electron beam is decelerated by an applied depression voltage between the horn and the collector.

Aside from the energy recovery, a main advantage of this system is the lower thermal wall loading. This is achieved by the recovery of kinetic energy of the electron beam before it hits the collector wall. Moreover, a larger radius of the collector is possible in this configuration, which increases the surface of the collector and therefore further decreases the thermal wall load.

3.1.7 Broadband Windows

Finally, the microwave beam passes through the output vacuum window. The primary function of the window is to maintain the vacuum inside the electron tube. At the same time, the window must be highly transparent with minimum absorption and reflection over the complete frequency band of operation.

The window disk has a higher electric permittivity than the vacuum inside the tube and the air outside the tube. This results in two permittivity discontinuities at the front and rear sides of the window. For an incident electromagnetic wave, traveling through the window, a fraction is reflected at these discontinuities. To reduce the total reflections at the window, the thickness of the window disk can be chosen as an integer multiple of half of the wavelength. In this case the reflections at both discontinuities interfere destructively and the window becomes almost completely transparent.

The frequency of highest transparency f_{trans} for a window of thickness d_{w} calculates as

$$f_{\mathrm{trans}} = \frac{c_0}{2\sqrt{\epsilon_{\mathrm{r}}^{'}} d_{\mathrm{w}}} \,, \tag{3.55}$$

where $\epsilon_{\mathrm{r}}^{'}$ is the real part of the window's complex relative permittivity $\bar{\epsilon}_{\mathrm{r}} = \epsilon_{\mathrm{r}}^{'} - j\epsilon_{\mathrm{r}}^{''}$ and $\tan(\delta) = \epsilon_{\mathrm{r}}^{''}/\epsilon_{\mathrm{r}}^{'}$ [92].

The scattering matrix of a window with a single dielectric disc is given by [93]:

$$S_{\mathrm{w}} = \frac{1}{1 - \bar{\varrho}^2 \mathrm{e}^{-2\bar{\gamma}_\epsilon d_{\mathrm{w}}}} \begin{pmatrix} \bar{\varrho} - \left(1 - \mathrm{e}^{-2\bar{\gamma}_\epsilon d_{\mathrm{w}}}\right) & \left(1 - \bar{\varrho}^2\right) \mathrm{e}^{-\bar{\gamma}_\epsilon d_{\mathrm{w}}} \\ \left(1 - \bar{\varrho}^2\right) \mathrm{e}^{-\bar{\gamma}_\epsilon d_{\mathrm{w}}} & \bar{\varrho} - \left(1 - \mathrm{e}^{-2\bar{\gamma}_\epsilon d_{\mathrm{w}}}\right) \end{pmatrix} . \tag{3.56}$$

Here, $\bar{\gamma}_\epsilon$ is the complex propagation constant in a dielectric material and $\bar{\varrho}$ is the complex reflection factor. For a TEM mode, it calculates as

$$\bar{\varrho} = \frac{1 - \sqrt{\bar{\epsilon}_{\mathrm{r}}}}{1 + \sqrt{\bar{\epsilon}_{\mathrm{r}}}} \,. \tag{3.57}$$

The reflectivity (the ratio of the reflected power to the input power), the transmissivity, and the absorptivity can be calculated from (3.56). In the following, only the explicit expression for the reflectivity is given:

$$R = \frac{R_0 \left(1 - 2T_0 \cos\left(2\beta_\epsilon d_{\mathrm{w}}\right) T_0^2\right)}{1 - 2R_0 T_0 \cos\left(2\beta_\epsilon d_{\mathrm{w}} - 2\arg(\bar{\varrho})\right) + R_0^2 T_0^2} \,. \tag{3.58}$$

Here, $R_0 = |\bar{\varrho}|^2$ is the absolute square of the complex reflection factor. $T_0 = \mathrm{e}^{-2\alpha_\epsilon d_{\mathrm{w}}}$ is defined by the attenuation constant α_ϵ and phase constant β_ϵ of an electromagnetic wave in a lossy dielectric material:

$$\alpha_\epsilon = \frac{1}{2} k_0 \sqrt{\epsilon_{\mathrm{r}}^{'}} \tan(\delta) \,, \tag{3.59}$$

$$\beta_\epsilon = k_0 \sqrt{\epsilon_{\mathrm{r}}^{'}} \sqrt{\frac{1}{2} + \frac{1}{2}\sqrt{\tan(\delta)^2 + 1}} \,. \tag{3.60}$$

A derivation of the given equations can be found in [93].

In Fig. 3.11a, the schematic reflectivity R for a single-disc window is given. As can be seen from (3.58), a window consisting of a single disc is transparent

only in a very narrow frequency band. For the application in a helical gyro-TWT with a large bandwidth this is an issue. Fortunately, several strategies for widening the transmission bandwidth are known. The most common techniques are [94]

- Brewster widows (e.g. [95] for a W-band Brewster window),
- windows with a dielectric coating,
- multi-layer windows (e.g. [96] for a W-band multi-disc window),
- meta-surface windows (e.g. [97] Q-band meta-surface window).

Brewster windows retain their good transmission properties only for waves with a linear polarization fixed to the window plane [93]. Since for the application in a passive mode-locked oscillator a broadband transmission independent of the wave's polarization is required (see section 3.1.8), this technology is out of the question for electron tubes operated with a single vacuum window for the input and output.

Windows with dielectric coating and multi-disc windows are both based on the same principle. In a multi-disc window, additional matching discs are added at each side of the central, separated by a vacuum or air gap. This results in additional resonant passbands around the transmission frequency of the central disc. In a window with a dielectric coating, additional layers of dielectric material are directly coated onto the main disc. No air gaps separate the different dielectric layers. The challenge of coated windows is the following requirement on the permittivities $\epsilon_{\mathrm{r}1}^{'}$ and $\epsilon_{\mathrm{r}2}^{'}$ at the interface of two layers [94]:

$$\epsilon_{\mathrm{r}1}^{'} = \sqrt{\epsilon_{\mathrm{r}2}^{'}} \,. \tag{3.61}$$

This significantly limits the choice of possible window materials.

An alternative could be meta-surface windows. For this type of window, the surface of the window is provided with a periodic set of corrugations (the so-called meta-surface). In the simplest case, the meta-surface consist of periodic lattices [97]. The structured surface of the window changes the effective permittivity of the material and, therefore, a meta-surface window is equivalent to a windows with a dielectric coating. The advantage of meta-surface windows is that the permittivity of the 'coating' does not depend on

the material but on the structure of the surface. However, the dimensions of the meta-surface structure must be far below $\lambda/4$ which could be problematic for sub-THz frequencies. To the author's knowledge, there are no meta-surface windows for frequencies in the sub-THz range to date.

In contrast, multi-disc windows have shown already a good performance at low sub-THz frequencies (W-band) [96] and, therefore, multi-disc windows are the most promising candidates for a realization of the broadband microwave windows required for the electron tubes of a passive mode-locked microwave oscillator. A schematic of a three-disc window and the corresponding reflectivity is shown in Fig. 3.11b. It can be seen that the transmission band is significantly broadened by the additional resonant passbands around the transmission frequency of the central disc. As for a single-disc window, the reflectivity, the transmissivity and the absorptivity for a multi-disc window can be calculated from the scattering matrix.

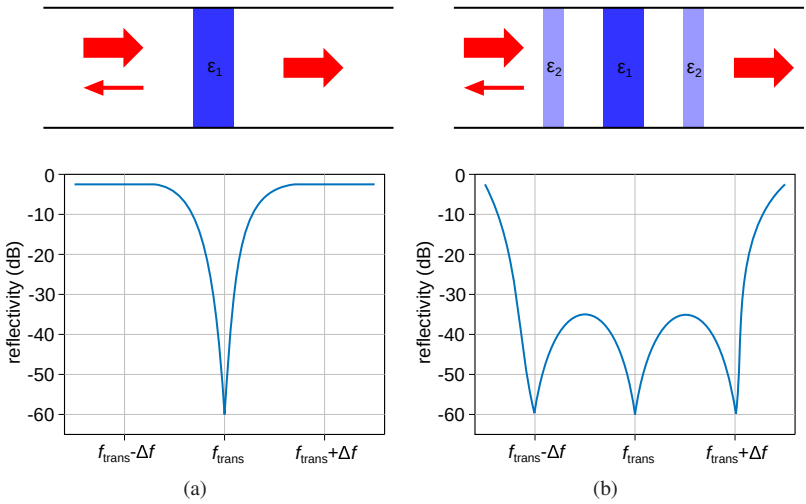

Figure 3.11: Schemata (top) and reflectivities (bottom) of a single-disc window (a) and a multi-disc window (b).

The given equations are only valid for discs with a diameter equal to the waveguide diameter. In a real window, the disc diameter always exceeds the diameter of the waveguide (see e.g. [96] for the geometry of a real three-disc

window). The change in the waveguide diameter causes a coupling to other waveguide modes which can change the transmission properties of a window significantly. Therefore, the given equations can only be a starting point for the design of a microwave window. During this thesis, a generalized scattering-matrix code was developed which is sufficient for the simulation and synthesis of realistic broadband multi-layer windows.

3.1.8 In- and Out-coupling of High-Power Signals

A major challenge in the development of amplifier and absorber devices for a passive mode-locked oscillator is the effective injection of high-power signals into the devices. State-of-the-art helical gyro-TWTs as shown in Fig. 3.1 can only handle low power input signals (several Watts). Based on an innovative idea developed by Denisov et al. [83], this challenge can be solved: helical gyro-TWTs offer the possibility of being operated with a single window that is used for the input as well as the output signal.

The diagrams of a helical gyro-TWT modified for single-window operation is showed in Fig. 3.12. Compared to Fig. 3.1, it can be seen that only a single modification is necessary: the removal of the low-power input coupler. Through the high-power broadband window (d), the input signal (e) is injected as a linearly polarized Gaussian beam or a linearly polarized $\mathrm{HE}_{1,1}$ mode into the tube.

Assume the input signal is polarized in the $\hat{\boldsymbol{y}}$ direction in the following. The wave propagates in the direction opposite to the electron beam along the tube towards the electron gun. In the horn antenna, the input mode is converted to a linearly polarized $\mathrm{TE}^{y}_{1,1}$ mode. A polarizer (c) follows the horn antenna and converts the linearly polarized $\mathrm{TE}^{y}_{1,1}$ into a circularly polarized $\mathrm{TE}_{1,1}$ mode.

The lefthanded $\mathrm{TE}_{1,1}$ mode does not fulfill the coupling condition (3.2) and is therefore not coupled with a $\mathrm{TE}_{2,1}$ mode in the helically corrugated interaction region (b). Correspondingly, no interaction of the electromagnetic wave with the electron beam occurs.

At the reflector (a) following the interaction region, the $\mathrm{TE}_{1,1}$ mode is reflected. After the reflection, the mode changes its propagation direction, while retaining

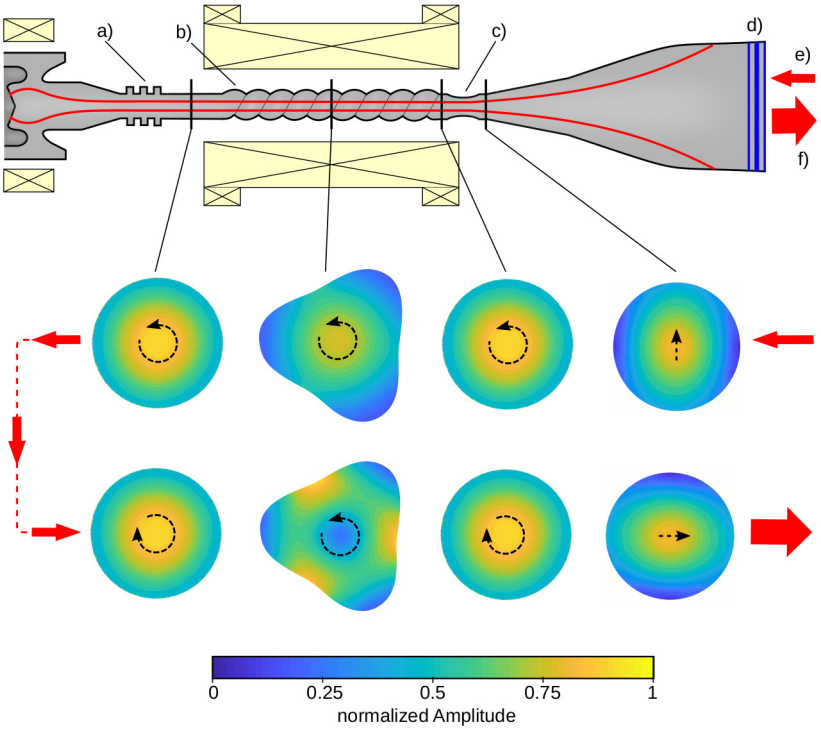

Figure 3.12: Diagram of a single-window helical gyro-TWT with a) reflector, b) helically corrugated interaction region, c) polarizer, d) input signal, e) high power output signal. On the bottom the amplitude patterns of the electric field at different positions in the tube is shown. The black arrows indicate the polarization.

the direction of its azimuthal rotation. The left-hand polarized $\mathrm{TE}_{1,1}$ mode becomes a right-hand polarized $\mathrm{TE}_{-1,1}$ one.

The reflected wave propagates in the same direction as the electron beam towards the output of the tube. Because of the change of polarization, the $\mathrm{TE}_{-1,1}$ fulfills the coupling condition (3.2) of the helically corrugated interaction region and an interaction with the electron beam is possible. This results in convective amplification of the mode as it propagates through the interaction region.

After the interaction region, the circularly polarized mode passes through the polarizer and is converted to a $\mathrm{TE}^{x}_{1,1}$ mode, linearly polarized in the $\hat{\boldsymbol{x}}$ direction. The horn antenna converts the $\mathrm{TE}^{x}_{1,1}$ mode to a linearly polarized Gaussian beam, which leaves the tube through the same window.

It is important to note that the output signal polarization is orthogonal to the input signal polarization. This allows a separation of input and output signal by a polarization splitter (see section 3.4.2), which is a key point for the feedback system developed in chapter 8.

A major advantage of a single-window helical gyro-TWT is the possibility of using a high-power signal as an input. This is a key feature for a passive mode-locked oscillator where high power pulses are circulating in a feedback loop of an amplifier and an absorber. Without this feature, a realization of a passive mode-locked microwave oscillator would be impossible. In this context, it should also be noted that the idea of a single-window helical gyro-TWT was not introduced until one year after the publication of the fundamental idea of a passive mode-locked microwave oscillator by Ginzburg et al. (2015).

3.2 Cyclotron Absorber

Due to a lack of available well-known devices for the realization of a microwave saturable absorber, Ginzburg et al. [4] assumed an ideal saturable absorber in the first preliminary investigations of a passive mode-locked microwave oscillator. In [50], the first ideas for the realization of a realistic saturable microwave absorber, suitable for high power, are proposed. It is based on the cyclotron resonance absorption of an electromagnetic wave in a cylindrical waveguide by an initially rectilinear electron beam which is guided by a static magnetic field.

A schematic of a cyclotron absorber is shown in Fig. 3.13. It can be seen that the general construction is similar to a helical gyro-TWT in a single-window configuration. The main difference is that the helical interaction area is replaced by a cylindrical one.

The cyclotron absorber is operated with an initially rectilinear, halo electron beam. If an electromagnetic wave which fulfills the cyclotron resonance condition is fed into the interaction region (3.17), the electrons are accelerated, gain

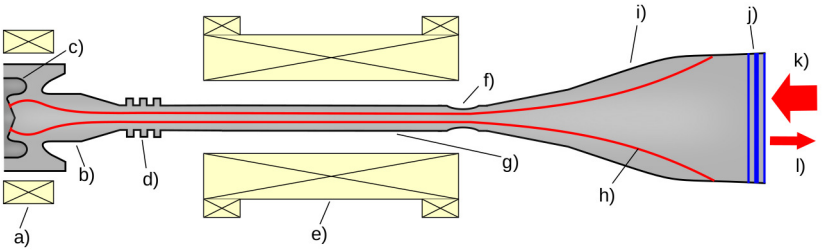

Figure 3.13: A single-window cyclotron absorber with a) gun-coil, b) anode, c) cathode with the emitter, d) reflector, e) main-coil, f) polarizer, g) circular interaction region, h) electron beam, i) horn antenna and collector, j) broadband vacuum window, k) high power output signal, i) input signal.

a tangential velocity component $v_\perp$, and start to gyrate in the static magnetic field $\mathfrak{H}_0 = \mathfrak{H}_0\hat{z}$. Consequently, the kinetic energy of the electrons increases and the energy in the electromagnetic wave is absorbed by the electron beam.

This is represented in Fig. 3.14. The initially rectilinear, halo electron beam with radius r_b (Fig. 3.14a) absorbs the energy of the electromagnetic wave and the electrons start to gyrate with the Larmor radius r_L. The centers of the gyration are located on the circle of the initial beam (see Fig. 3.14a). Therefore, the generated electron beam after the absorption process is not a large orbit electron beam as in a helical gyro-TWT but rather a classical gyrating, halo electron beam as used for example in high-power gyrotrons.

The saturation of the absorption is caused by two effects: (1) the relativistic dependence of the gyro-frequency on the kinetic energy of the electrons (see (3.18)); (2) the effect of phase bunching.

From the first effect, the maximum energy that an electron beam can absorb from an electromagnetic wave can be calculated. With increasing kinetic energy, the Lorentz factor γ increases and the cyclotron frequency ω_H decreases. Therefore, after the electrons have absorbed a certain amount of energy, the cyclotron resonance condition is not fulfilled anymore and a further interaction between the electromagnetic field and the electron beam is prevented.

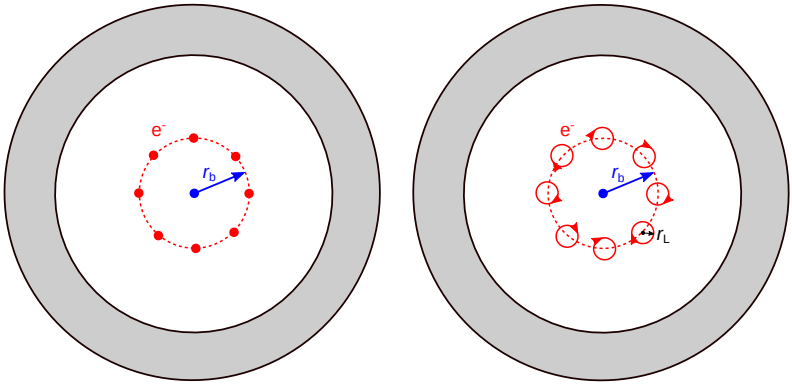

(a) (b)

Figure 3.14: Projection of the electron trajectories in a cyclotron absorber onto the cross-section of the interaction region. For the initially rectilinear electron motion before (a) and gyrating electron motion after (b) the absorption of energy from the electromagnetic wave.

Assuming that the electron-wave interaction is only possible in a certain range $\Delta\omega_\mathrm{H}$ around the cyclotron frequency and neglecting higher harmonics, the following relation holds for the maximal energy that can be absorbed:

$$\omega - k_\parallel v_\parallel = \omega_\mathrm{H} - \Delta\omega_\mathrm{H} = \frac{e_0 \mathfrak{H}_0}{m_\mathrm{e}\,(\gamma + \Delta\gamma)} \,. \tag{3.62}$$

With (3.62), the increase in the Lorentz factor caused by the absorbed energy, calculates as

$$\Delta\gamma = \frac{e_0 \mathfrak{H}_0}{m_\mathrm{e}\,(\omega_\mathrm{H} - \Delta\omega_\mathrm{H})} - \gamma \,. \tag{3.63}$$

Therefore, the energy that a single electron can absorb from the electromagnetic wave is given as:

$$\Delta W = \Delta\gamma m_\mathrm{e} c_0^2 \,. \tag{3.64}$$

Consequently, an electron beam with a current I can absorb a maximal power of

$$\Delta P = \frac{\Delta W}{e_0} I \,. \tag{3.65}$$

It can be seen that ΔP is defined by the beam current I and the upper limit of the cyclotron frequency mismatch $\Delta\omega_{\mathrm{H}}$.

While the existence of an upper limit for the absorbed energy indicates that a cyclotron absorber acts as a saturable absorber, its real behavior is more complicated because of the phase bunching effect (see section 3.1.2 for a description of phase bunching). To understand this effect, the phase bunching in a single beamlet is discussed in the following. A beamlet is a bunch of electrons gyrating with a Larmor radius r_{L} around a guiding center which is located on the halo electron beam of radius r_{b} (see Fig. 3.14).

The parameters of the cyclotron absorber are chosen such that the electrons bunch and cluster in an acceleration phase ($\omega > \omega_{\mathrm{H}}$) and the electron beam extracts energy from the RF field (as an absorber is expected to do). After the initial bunching, the electrons synchronously gain energy. As a result, the cyclotron frequency of the bunch decreases and the bunch moves towards the deceleration phase. In the deceleration phase, the electrons in the bunch emit energy to the RF field and the absorber starts amplifying the RF signal instead of absorbing it. Since the electrons begin losing energy now, their cyclotron frequency increases again and the bunch slowly moves back into the acceleration phase.

This is illustrated in Fig. 3.15. Shown are the amplitude distributions along a cyclotron absorber (with $R = 0.36\,\mathrm{mm}$, $E_{\mathrm{kin}} = 35\,\mathrm{keV}$ and $I = 0.03\,\mathrm{A}$) for CW input signals of different powers at 263 GHz. The amplitude distributions are simulated with the model developed in chapter 4. In Fig. 3.15, both previously described effects can be seen: the limitation of the maximal power that can be absorbed by the electron beam because of the relativistic dependence of the gyro-frequency on the kinetic energy, and the change from the absorption to the amplification regime because of the phase bunching. A similar behavior was observed previously for a helical gyro-TWT (see Fig. 3.5). After absorbing a certain amount of energy, an absorber switches from an absorption to an amplification regime. Fortunately, this is an advantage for the realization of a nonlinear saturable absorber.

An important observation is that the period for the change from absorption to the amplification regime decreases as the power of the input signal increases. This behavior can be used to improve the saturation effect of the absorber. If the length of the absorber is chosen such that low-power signals are optimally

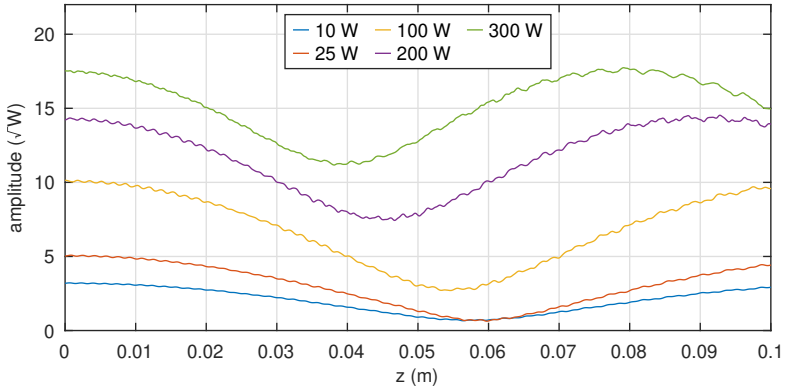

Figure 3.15: Simulated amplitude distribution along a cyclotron absorber ($R = 0.36\,\mathrm{mm}$, $E_{\mathrm{kin}} = 35\,\mathrm{keV}$ and $I = 0.03\,\mathrm{A}$) for CW input signals of different powers at 263 GHz.

absorbed ($z = 0.06\,\mathrm{m}$ in Fig. 3.15), for higher-power signals the absorber will already be in the amplification regime when the signal leaves the absorber. Therefore, the total absorption for high-power signals can be below the absorption limit caused by the relativistic dependence of the gyro-frequency on the kinetic energy of the electrons.

As for the phase bunching in a helical gyro-TWT, simulations are performed for a better illustration of the effect. For the case of an ideal, initially rectilinear electron beam, the phase difference $\Delta\Theta$ between the electrons in a single beamlet and the electromagnetic wave is shown in Fig. 3.16a. For the initially rectilinear beam, the electrons do not gyrate at $z = 0\,\mathrm{mm}$. Once the electrons interact with the electromagnetic field, they start to gyrate (the resonance condition (3.17) must be fulfilled). Since the gyration of the electrons is caused by the interaction with the electromagnetic wave, all electrons start the gyration synchronously in the absorption phase. As in the previous discussions, the dependence of the cyclotron frequency on the kinetic energy of the electrons causes a slow transition from the absorption phase to the amplification phase.

In Fig. 3.16b, the average Larmor radius of the gyrating electrons is plotted. Initially, the Larmor radius is zero since the electrons do not gyrate. As long as the electrons are in the absorption phase the Larmor radius increases. Once the amplification phase is reached ($z = 40\,\mathrm{mm}$) the Larmor radius decreases

because the electrons amplify the electromagnetic wave and are losing energy. At $z = 80\,\mathrm{mm}$, the electrons have transferred all previously gained energy back to electromagnetic wave and stop gyrating. Therefore, in the special case of an initially ideal rectilinear electron beam, the initial conditions can be recovered and the process of absorption/amplification restarts. In Fig. 3.16a, this can be seen by a phase jump at $z = 80\,\mathrm{mm}$.

Instead of an ideal rectilinear electron beam, a slightly gyrating beam is more realistic. For such a beam with $\alpha_{\mathrm{init}} = 0.05$ the evolution of the phase shift between the electrons and the electromagnetic field is shown in Fig. 3.16c. The main difference compared to the ideal rectilinear beam is that an initial phase bunching process occurs ($z < 10\,\mathrm{mm}$). As a consequence, the initial conditions cannot be completely recovered at the end of the first absorption-amplification period. This causes that the energy absorbed from the electron beam cannot be completely returned to the electromagnetic wave. Fortunately, this is irrelevant for the realization of a real cyclotron absorber, since in every case the absorber is too short to reach the point of complete energy recovery, even for very powerful input signals.

The previous discussion was limited to the transversal velocity component of the electrons. However, if the saturable absorber should be used for ultra-short pulses as is the case in a passive mode-locked oscillator, the axial velocity of the electrons is of particular interest. It is important to note that the axial velocity of the electrons must be aligned to the group velocity of the wave (previously referred to as the synchronized operation regime). Only in this case, the phase bunching process can be utilized to improve the saturation effect. If the velocities are not matched, the pulse would slip over the electron beam. As a result, ‘fresh’ electrons with a uniform phase distribution would constantly contribute to the electron-wave interaction. Then, the transition from the absorption to the amplification regime is never reached and high-power RF signals cannot recover energy from the electron beam.

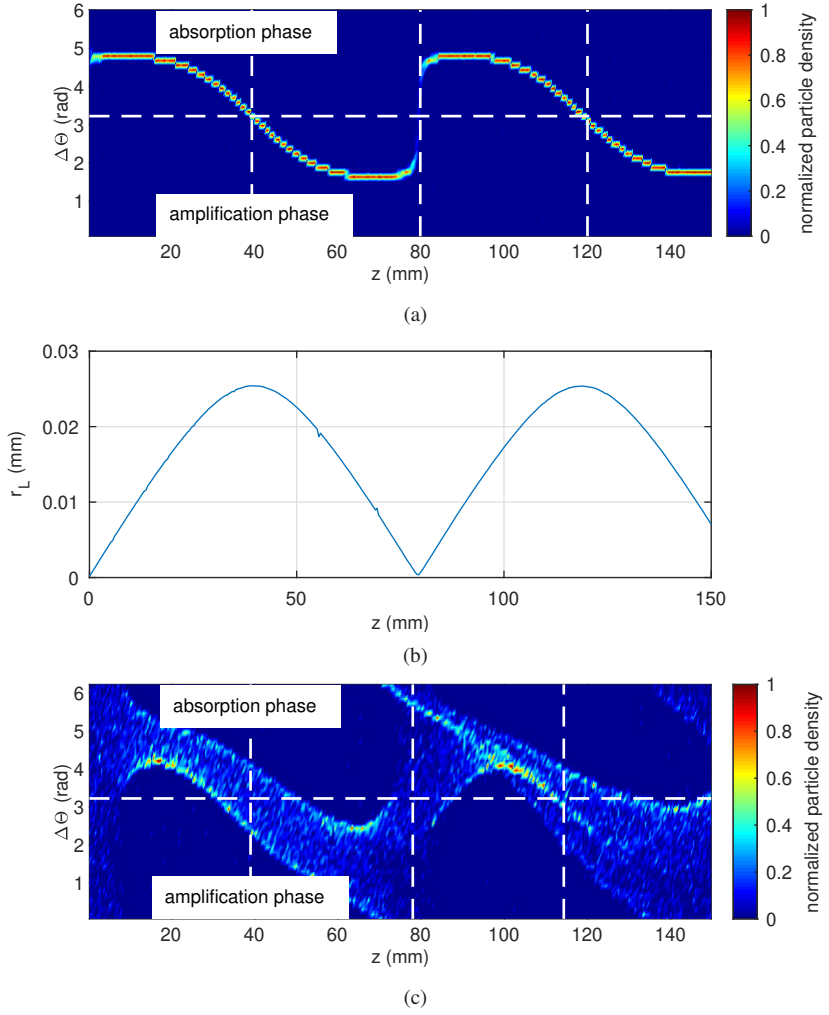

Figure 3.16: Relative phase-shift between the cyclotron phase and the electromagnetic wave for an ideal rectilinear beam (a) and a realistic beam (c). In (b), the Larmor radius is shown for the ideal case.

3.3 Helical Gyro-TWTs as Saturable Absorbers

One year after the idea of a passive mode-locked microwave oscillator, the open question of a suitable high-power broadband amplifier was investigated by Ginzburg et al.. In the following investigation, an alternative operation regime of helical gyro-TWTs was observed: a helical gyro-TWT operated in the Kompfner dip regime [51] acts as a saturable absorber [52].

The so-called Kompfner dip regime was originally studied for Cherenkov TWTs driven by straight electron beams by Kompfner [51]. For a rectilinear electron beam with a particular velocity below the characteristic phase velocity in the slow wave circuit of a traveling wave tube (TWT), an input signal is completely absorbed by the electron beam [98]. A characteristic dip observed in the amplification curve is therefore commonly referred to as the Kompfner dip.

While originally studied in classical TWTs, the Kompfner dip regime is also observed in gyro-devices [99], [100]. It must be noted that in gyro-devices, the Kompfner dip is caused by a completely different mechanism than in classical TWTs. In a TWT with a rectilinear electron beam, the Kompfner dip occurs when the slow electromagnetic wave of the circuit is coupled to a fast space charge wave of the electron beam, which results in an attenuation of the RF signal [101]. In contrast, the absorption of an electromagnetic wave in gyro-devices is based on the mechanisms described in the previous section about cyclotron absorbers. When talking about the Kompfner dip regime in the following, no reference is made to the underlying interaction process, but rather to the fact that an electromagnetic wave in this regime is absorbed by the electron beam.

The absorption of a RF signal in a helical gyro-TWT is based on the same mechanism as in a cyclotron absorber. However, in contrast to a cyclotron absorber, the electron-wave interaction happens at the second cyclotron harmonic, as is the case for the amplification regime of helical gyro-TWTs. A second difference with respect to a cyclotron absorber is the initial electron beam. While a cyclotron absorber operates with an initially rectilinear hollow electron beam, the helical gyro-TWT absorber operates as usual with a gyrating, large orbit electron beam. The reason is simple: as shown in section 3.1.2, the second harmonic interaction with a $\mathrm{TE}_{2,1}$ mode is only possible for gy-

rating electrons with a vanishing guiding center radius. However, as shown in Fig. 3.14, a rectilinear electron beam would lead to a gyrating beam with a large guiding center radius. Consequently, the coupling coefficients of the $\mathrm{TE}_{2,1}$ mode would be very low for a rectilinear electron beam.

3.4 Passive Components

As the amplifier and saturable absorber will be realized in two separate gyro-devices, a feedback system is required to couple both of them in a feedback loop. The feedback system has also to handle the decoupling of the output signal from the feedback loop. During the thesis, two different concepts for feedback systems are developed (see chapter 8). Both concepts are based on passive microwave components for a quasi-optical transmission of the microwave signals (which in the following includes the transmission in highly overmoded waveguides). In this section, a brief overview of the individual components required to implement a quasi-optical feedback system are given.

3.4.1 Jones Calculus

In the proposed feedback systems, power is transmitted via a Gaussian beam ($\mathrm{TEM}_{0,0}$) over the free-space or through the balanced $\mathrm{HE}_{1,1}$ mode in overmoded, corrugated, cylindrical waveguides. In both cases, the polarization characteristics of the $\mathrm{TEM}_{0,0}$ / $\mathrm{HE}_{1,1}$ modes are used for the separation of signal paths.

For quasi-optical Gaussian beams, as well as for the balanced $\mathrm{HE}_{1,1}$ mode in oversized waveguides with a waveguide diameter of $D \geq 12\,\lambda$ (where λ is the free-space wavelength), a plane wave approximation can be used [102]. Therefore, the polarization of $\mathrm{TEM}_{0,0}$ and $\mathrm{HE}_{1,1}$ modes can be described by Jones vectors [103], which is a well-known formalism used in laser physics for the description of polarized laser beams. Again, a formalism from laser physics is used for the description of a microwave system which highlights the close connection of microwave engineering and laser physics.

Assuming a plane wave traveling in the positive z direction

$$\begin{pmatrix} \underline{E}_{\mathrm{x}}(t,z) \\ \underline{E}_{\mathrm{y}}(t,z) \\ 0 \end{pmatrix} = \mathrm{Re}\left\{ \begin{pmatrix} \underline{E}_{0,\mathrm{x}} \mathrm{e}^{\,j\phi_{\mathrm{x}}} \\ \underline{E}_{0,\mathrm{y}} \mathrm{e}^{\,j\phi_{\mathrm{y}}} \\ 0 \end{pmatrix} \mathrm{e}^{\,j(\omega t - k_{\parallel} z)} \right\} , \tag{3.66}$$

then the complex vector

$$\begin{pmatrix} \underline{E}_{0,\mathrm{x}} \mathrm{e}^{\,j\phi_{\mathrm{x}}} \\ \underline{E}_{0,\mathrm{y}} \mathrm{e}^{\,j\phi_{\mathrm{y}}} \end{pmatrix} \tag{3.67}$$

is called Jones vector. It represents the amplitude and phase of the electric field in the x and y directions. A mode which is linearly polarized in the x or y direction, is represented by the Jones vectors

$$\bar{\boldsymbol{e}}_{\mathrm{x}} = \begin{pmatrix} 1 \\ 0 \end{pmatrix} , \tag{3.68}$$

$$\bar{\boldsymbol{e}}_{\mathrm{y}} = \begin{pmatrix} 0 \\ 1 \end{pmatrix} , \tag{3.69}$$

and the Jones vectors for left- and right-handed circularly polarized modes are given by

$$\bar{\boldsymbol{e}}_{\mathrm{r}} = \frac{1}{\sqrt{2}} \begin{pmatrix} 1 \\ +j \end{pmatrix} , \tag{3.70}$$

$$\bar{\boldsymbol{e}}_{\mathrm{l}} = \frac{1}{\sqrt{2}} \begin{pmatrix} 1 \\ -j \end{pmatrix} . \tag{3.71}$$

Here, j refers to the imaginary unit. If a corresponding Jones matrix for all individual components in the feedback system could be found, the complete feedback system can be described in a simple way by a product of Jones matrices.

The main components of the proposed feedback system are polarization splitters and tunable polarizers. The matrices for the transmission and reflection

paths of the polarization splitting components (e.g. graded mirrors or polarizing wire grids) are given by:

$$\underline{S_{\mathrm{T}}} = \begin{pmatrix} 1 & 0 \\ 0 & 0 \end{pmatrix}, \tag{3.72}$$

$$\underline{S_{\mathrm{R}}} = \begin{pmatrix} 0 & 0 \\ 0 & 1 \end{pmatrix}. \tag{3.73}$$

The polarization splitters are chosen such that an incident wave linearly polarized in the x direction is transmitted and an incident wave linearly polarized in the y direction is reflected.

Tunable polarizers are realized, for example, as rotatable reflective phase grids (see following sections). They can be represented by a Jones matrix that delays a component of the $\underline{E}$-field by a phase. For simplicity, it is assumed that for an angle $\Theta = 0°$ the polarizer delays the x component of the $\underline{E}$-field by $\pi/2$:

$$\underline{P_{\mathrm{x}}} = \begin{pmatrix} e^{-j\frac{\pi}{2}} & 0 \\ 0 & 1 \end{pmatrix}. \tag{3.74}$$

For an arbitrary rotation angle Θ of the reflective phase grid, the Jones matrix for a polarizer is then given by the matrix product

$$\underline{P_{\Theta}} = \underline{R_{\Theta}}\ \underline{P_{\mathrm{x}}}\ \underline{R_{\Theta}^{T}} \tag{3.75}$$

with the rotation matrix

$$\underline{R_{\Theta}} = \begin{pmatrix} \cos\Theta & -\sin\Theta \\ \sin\Theta & \cos\Theta \end{pmatrix}. \tag{3.76}$$

For a discussion of the feedback system, the effects of the active devices, namely the amplifier and the absorber, on the power of the signals is neglected. Only their effect on the polarization is important and is modeled using Jones matrices. The tubes are designed such that the input and output signals are

cross-polarized to each other, and therefore the Jones matrix for the tubes is given by:

$$\underline{D} = \begin{pmatrix} 0 & 1 \\ 1 & 0 \end{pmatrix}. \tag{3.77}$$

Although, strictly speaking, the Jones calculus is only valid for monochromatic waves, it allows the behavior of the feedback system to be described in a simple way. An advantage of the description via the Jones calculus is that it allows an easy inclusion of the feedback system into interaction simulations based on the approach presented in chapter 4. In addition, if the given matrices of ideal components are replaced with matrices for non-ideal components, the effects of these components on the performance of the feedback system can be evaluated.

3.4.2 Polarization Splitter

For the separation of two linearly cross-polarized Gaussian beams or $\mathrm{HE}_{1,1}$ modes, several approaches are possible (a good overview can be found in [104]). In the following, two of them are discussed in detail: sinusoidal corrugated mirrors and wire-grid splitters. Representations of both are shown in Fig. 3.17.

A wire-grid polarization splitter consists of an array of thin parallel conductive wires. The wire-grid reflects incoming radiation if the electric field is polarized parallel to the wires, and transmits the radiation if the electric field is polarized orthogonal to the wires. In this way, the wire-grid separates two linearly cross-polarized waves and can be used as a polarizing element.

These polarization splitters are widely used in optics (e.g. [105]). For optical frequencies, typical diameters of a single wire are in the range of $5\,\mu\mathrm{m}$ - $50\,\mu\mathrm{m}$. For mechanical stability reasons, the wire-grid is usually embedded in transparent dielectric materials. For microwave frequencies, the wires can have a thickness of a few tenths of a millimeter, which allows a free-standing wire-grid polarization splitter. While the performance of a wire-grid polarization splitter increases with a decreasing wire diameter (see chapter 8.2), the minimum diameter is limited by the ohmic losses and the resulting thermal loads.

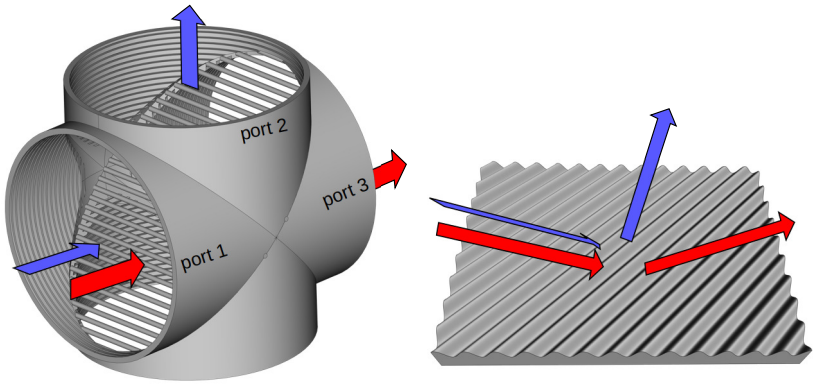

(a) (b)

Figure 3.17: Representations of a wire-grid polarization splitter (a) and a sinusoidal graded mirror polarization splitter (b). Blue and red arrows symbolize horizontally (blue) and vertically (red), linearly polarized waves.

The wire-grid polarization splitter shown in Fig. 3.17a is realized as an all-metal waveguide component. It can be seen as a $90°$ intersection of two identical, corrugated, circular waveguides for the transmission of an $\mathrm{HE}_{1,1}$ mode. The wire-grid is arranged at a $45°$ angle relative to the propagation direction of the incident wave at port 1. If an incident wave is assumed as a superposition of a vertically and a horizontally polarized $\mathrm{HE}_{1,1}$ mode, the two polarizations are separated by the wire-grid. An $\mathrm{HE}_{1,1}$ mode with the electric field polarized parallel to the wires is reflected at the wire-grid towards port 2, while an $\mathrm{HE}_{1,1}$ mode with the electric field polarized orthogonal to the wire-grid is transmitted to port 3. In chapter 8.2, a wire-grid polarization splitter is used for a feedback system realized as a waveguide transmission line.

An alternative method for the separation of two orthomode wavebeams is the use of mirrors with periodic gratings [106], [107]. A common type of grating is a sinusoidal one

$$s(x) = \tilde{r} \sin\left(\frac{2\pi}{\tilde{d}} x\right) , \tag{3.78}$$

where $\tilde{r}$ is the amplitude and $\tilde{d}$ is the period of the grating. At sub-THz frequencies, both are of the order of millimeters. In Fig. 3.17b, a mirror with a

sinusoidal grating is shown. In laser optics, such sinusoidal gratings are often referred to as holographic gratings [108].

The grating reflects incident waves with TM and TE polarizations at different angles. This is symbolized in Fig. 3.17b. For a TM-polarized wave, the grating acts in a similar way to a plane mirror: the wave is reflected with the angle of incidence (also called specular reflection). A TE-polarized wave is diffracted under the angle corresponding to the first diffraction maximum.

Such a polarization splitter is suitable for quasi-optical feedback systems based on mirrors, where a Gaussian beam propagates in free space. In such a system, the diffraction broadening of the Gaussian beam can be compensated by additional focusing mirrors [104].

Ohmic losses, mode conversion, spurious radiation and the frequency dependence of the diffraction angle are the most critical factors of a real polarization splitter. While ohmic losses mainly limit the structure dimensions, mode conversion and spurious radiation can be reduced by a properly chosen mirror geometry. However, the frequency dependence of the diffraction angle limits the broadband behavior of the polarization splitters. As part of this work, a feedback system based on quasi-optical mirrors and two mirrors with sinusoidal gratings used as polarization splitters was designed. It has shown that the frequency dependency of the diffraction angle limits the bandwidth of the feedback system to $\approx 10\,\mathrm{GHz}$. Therefore, this approach was abandoned in favor of a feedback system based on overmoded waveguides which provides a higher bandwidth ($\approx 20\,\mathrm{GHz}$) and further advantages (see chapter 8).

For a design of the shown quasi-optical components, suitable simulation methods, that include all relevant effects, are necessary. For example the classical approach of calculating reflections on sinusoidal gratings with coupled plane waves (see [109], [110]) is not sufficient for taking into account mode conversion or ohmic losses. To include all relevant effects, all polarization splitters in this work are simulated exclusively using full-wave simulations based on the electric field integral equation (EFIE) as described in chapter 7.

3.4.3 Polarizers

In fusion technology, mirrors with a rectilinear phase grid (see Fig. 3.18) are commonly used as polarizers. An incident wave is reflected, and a change of the polarization can be achieved. The basic principle is simple: while field components with an electric field component perpendicular to the grating are reflected at its top surface, those with an electric field component parallel to the grating penetrate into the grating and are reflected at its bottom surface [111]. This results in a difference in the propagation time and thus a phase shift between the field components parallel and perpendicular to the grating arises. As can be seen from the Jones vectors (3.70) and (3.71), for a circularly polarized wave, a phase shift of $90°$ between the two orthogonal linearly polarized components is necessary. For an incident wave perpendicular to the polarizer ($\Theta = 0°$), the phase shift can be achieved by a grid height of $h_0 = \lambda/8$ and an orientation of $\Phi = 45°$ relative to the plane of the linearly polarized input wave. For waves incident at an angle Θ, the height of the grid must be adjusted according to [112]:

$$h = \frac{h_0}{\cos\left(\Theta\right)} \,. \tag{3.79}$$

Here, h_0 is the optimal grid height of a reflective phase grid for perpendicular incident waves. In the developed feedback systems, such a polarizing grid is used as mirror in a $90°$ miter bend (in the following also called a polarizing miter bend). In such a polarizing miter bend, the angle of incident is $\Theta = 45°$.

The periodicity of the structure is of special importance for the performance of the polarizer. If the periodicity exceeds a critical size, the phase grating acts as a diffraction grating. The incident wave is then reflected not only into the desired main maxima but also into undesired secondary maxima. To avoid this, the period w_1 must fulfill [102]:

$$w_1 < \frac{\lambda}{1 + \sin\left(\Theta\right)\cos\left(\Phi\right)} \,. \tag{3.80}$$

If production tolerances, diffraction effects, and ohmic losses are neglected, the performance of a polarizing grid could reach $100\,\%$ for a single frequency. However, the performance decreases for a broadband signal. Therefore, in

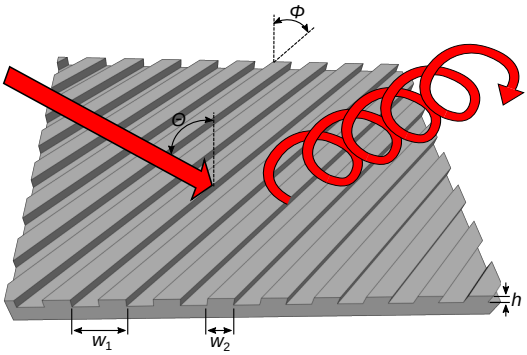

Figure 3.18: Structure of a polarizing phase grid. An incident linearly polarized wave with a polarization plane at an angle of 45° relative to the grid orientation is transformed into a circularly polarized wave.

[113], [114] a method to synthesize the geometry of a polarizing grating with an optimized broadband performance is developed. The method is based on a plane wave approximation which is valid for quasi-optical transmissions via Gaussian beams in free space and $\mathrm{HE}_{1,1}$ modes in highly oversized waveguides. As a consequence, the polarizing grid can be modeled as a unit cell with periodic Floquet boundaries [115]. This reduces the required simulation time and makes it possible to perform parameter studies.

In the parameter studies, the geometric parameters are varied over a wide range. For every parameter combination, several simulations at discrete frequency points distributed equally over the desired frequency band are performed and a merit function $\mathrm{M}(h, w_1, w_2)$ is evaluated. The merit function is chosen as

$$\mathrm{M}(h, w_1, w_2) = \frac{1}{N} \sum_{i}^{N} \left| \left(\frac{\partial \phi}{\partial \omega} \right)_{\omega=\omega_i} \right| , \tag{3.81}$$

where $\frac{\partial \phi}{\partial \omega}$ is the rate of change of the phase between the two cross-polarized components of the wave with the frequency. For a polarizer with an ideal broadband performance, the rate of change would vanish and the metric function would evaluate to zero. To optimize the structure of the grating, a classical minimization algorithm can be used.

The synthesis of an optimized, broadband polarizer with the described method can be done with the commercial simulation program CST Microwave Studio [116], or with the full-wave simulation program presented in chapter 7. For the final check of the performance, the simulation of ohmic losses and investigations of possible mode conversions are performed exclusively with the self-developed full-wave simulation software presented in chapter 7.

4 Simulation Model for Gyro-Devices

In this chapter, a novel approach for the simulation of the electron-wave interaction in helically corrugated and circular interaction regions is developed. In the following, the theory, the numerical solution methods, and their implementations are shown.

The existing approaches for the simulation of the non-linear beam-wave interaction in gyrotron devices can be categorized into two groups: The first group consists of particle in cell (PIC)-codes which usually include a three dimensional (3D) description of the particle motion and a full-wave simulation of the RF-field. The commercial software packages CST Microwave Studio [116] and MAGIC [117] belong to this group as well as the open-source tool PICLas [118]. These programs are designed for universal application and are suitable for the simulation of almost all types of vacuum tubes. The disadvantage is the required high computing effort and the high amount of memory.

The programs in the second group use simplified physical models. Several models and programs for the transient simulation of gyro-devices were developed and published during the last five decades [11], [119]–[122] (This list does not pretend to be exhaustive). Most of them are based on the slowly varying amplitude approximation for the electromagnetic field simulation. They differ mainly in their handling of the electron beam, the modeling of the electron-wave interaction and the applied numerical methods.

The approach for the simulation of the electron-wave interaction in gyrotron resonators presented in [120] must be particularly emphasized. It is the only approach that is based on an expansion of the electric and magnetic fields in the gyrotron resonator into a complete set of eigenfunctions for the equivalent closed resonator. In addition, the approach includes the mode conversion due to radial variations of the cavity. While this approach has many advantages for the simulation of gyrotron resonators, it becomes insufficient for long traveling wave structures with low quality factors of the investigated interaction region.

In [68], a transient model for the simulation of passive mode-locked microwave oscillators with a source term based on a differential equation for the transverse electron momentum is presented. This model is successfully used for the simulation of helical gyro-TWTs as well as for cylindrical cyclotron absorbers with a rectilinear electron beam [50], [52], [67]. Besides the fact that no implementation of the model is available, it has a number of conceptual disadvantages. The modeling of spreads in the electron beam are challenging and more complex effects as a misaligned magnetic field or space-charge effects are not possible within the model.

In the following, an alternative model is developed. In contrast to the state-of-the-art gyrotron simulation programs it does not use the slowly varying amplitudes approximation. Another distinctive feature is the 3D PIC handling of the electron beam and a source term derived for an arbitrary electron beam without restriction of the generality.

The proposed model provides a number of advantages:

1. simulation of the electron-wave interaction over a broad bandwidth;
2. support of arbitrary electron beams (for example with velocity spreads, energy spreads, offsets of the guiding center from the symmetry axis of the device, etc.);
3. inclusion of additional physical effects such as influences of space-charge fields;
4. simulation of the electron-wave interaction at arbitrary harmonics of the cyclotron frequency.

Compared to full-wave PIC simulations the developed model retains a significant gain of simulation speed and it still allows a detailed investigation and separation of the involved physical effects.

The basics of the underlying theoretical model are presented in the following and details about the numerical solution and the implementation of the derived equations are given (section 4.1 - 4.3). The developed model and implementation are verified by a comparison with experiments (see appendix A.2). At the end of the chapter, a detailed comparison of the new simulation model with the existing approach for the simulation of helical gyro-TWTs [68] is performed.

4.1 Field Equations

Similar to chapter 3.1.1 (derivation of the dispersion relation of a helically corrugated waveguide), the inhomogeneous Helmholtz equation

$$\frac{1}{c_0^2}\frac{\partial^2 \mathfrak{E}}{\partial t^2} - \nabla^2 \mathfrak{E} = \mu_0 \frac{\partial \mathfrak{J}}{\partial t} \tag{4.1}$$

is the starting point for the derivation of simplified interaction equations. Here, c_0 is the speed of light, μ_0 is the vacuum permeability, the electric field is given by $\mathfrak{E}$ and $\mathfrak{J}$ is the current density.

Without loss of generality, the real Helmholtz equation can be extended into a complex form by replacing the real quantities $\mathfrak{E}$ and $\mathfrak{J}$ by the complex quantities $\overline{\boldsymbol{E}}$ and $\overline{\boldsymbol{J}}$. Then the physical solutions $\mathfrak{E}$ and $\mathfrak{J}$ are given by the real parts of the quantities $\overline{\boldsymbol{E}}$ and $\overline{\boldsymbol{J}}$:

$$\mathfrak{E} = \mathrm{Re}\left\{ \overline{\boldsymbol{E}} \right\} \tag{4.2}$$

$$\mathfrak{J} = \mathrm{Re}\left\{ \overline{\boldsymbol{J}} \right\} \tag{4.3}$$

for every solution $\overline{\boldsymbol{E}}$ and $\overline{\boldsymbol{J}}$ that fulfill the complex Helmholtz equation

$$\frac{1}{c_0^2}\frac{\partial^2 \overline{\boldsymbol{E}}}{\partial t^2} - \nabla^2 \overline{\boldsymbol{E}} = \mu_0 \frac{\partial \overline{\boldsymbol{J}}}{\partial t} \ . \tag{4.4}$$

In cylindrical and helically corrugated interaction regions it is sufficient to expand the electric field into a sum of transverse eigenmodes $\hat{\boldsymbol{e}}_i$. In addition, it is advantageous for the subsequent numerical solution to extract the expected operating frequency of the device under investigation:

$$\overline{\boldsymbol{E}}(t, r, \phi, z) = \sum_i \overline{A}_i(t, z)\, \mathrm{e}^{\,j\omega_0 t}\, \hat{\boldsymbol{e}}_i(r, \phi) \ . \tag{4.5}$$

Here, $\overline{A}_i$ is the complex envelope of the eigenmodes $\hat{\boldsymbol{e}}_i$ and ω_0 is the carrier frequency which is usually chosen close to the expected operating frequency of the device. To increase clarity, the time and space dependencies are assumed to be implicit in the following.

For the simulation of the gyrotron interaction in a circular waveguide, the eigenmodes $\hat{\boldsymbol{e}}_i$ are the corresponding TE modes of the waveguide. In the following, only a single mode $\hat{\boldsymbol{e}}_\mathrm{A}$ is considered for simplicity. Applying (4.5) to (4.4) and expanding the derivatives gives:

$$\begin{aligned}
-\mu_0 \frac{\partial}{\partial t}\bar{\boldsymbol{J}} = &\left(\frac{\partial^2}{\partial z^2} + \nabla_\perp^2\right)\left[\bar{A}\mathrm{e}^{\,j\omega_0 t}\hat{\boldsymbol{e}}_\mathrm{A}\right] \\
&- \frac{1}{c_0^2}\frac{\partial^2}{\partial t^2}\left[\bar{A}\mathrm{e}^{\,j\omega_0 t}\hat{\boldsymbol{e}}_\mathrm{A}\right] \\
=&\frac{\partial^2 \bar{A}}{\partial z^2}\mathrm{e}^{\,j\omega_0 t}\hat{\boldsymbol{e}}_\mathrm{A} + \bar{A}\mathrm{e}^{\,j\omega_0 t}\nabla_\perp^2\hat{\boldsymbol{e}}_\mathrm{A} \\
&- \frac{1}{c_0^2}\left[\frac{\partial}{\partial t}\left(\frac{\partial \bar{A}}{\partial t}\mathrm{e}^{\,j\omega_0 t} + j\omega_0\bar{A}\mathrm{e}^{\,j\omega_0 t}\right)\right]\hat{\boldsymbol{e}}_\mathrm{A}\,.
\end{aligned} \tag{4.6}$$

In the state-of-the-art simulation models for gyrotron devices, the slowly changing amplitude assumption

$$\left|\frac{\partial^2 \bar{A}}{\partial t^2}\right| \ll \left|\omega_0^2 \bar{A}\right| \tag{4.7}$$

is used to simplify (4.6). This is equivalent to the assumption that the change of the complex wave envelope $\bar{A}(t,z)$ of the eigenmode $\hat{\boldsymbol{e}}_\mathrm{A}$ is slow compared to the phase term $\mathrm{e}^{\,j\omega_0 t}$. Consequently, the big brace in the last term of (4.6) can be approximated as

$$\begin{aligned}
\frac{\partial}{\partial t}\left(\frac{\partial \bar{A}}{\partial t}\mathrm{e}^{\,j\omega_0 t} + j\omega_0\bar{A}\mathrm{e}^{\,j\omega_0 t}\right) &= \left(\frac{\partial^2 \bar{A}}{\partial t^2} + j\omega_0\frac{\partial \bar{A}}{\partial t} + j\omega_0\frac{\partial \bar{A}}{\partial t} - \omega_0^2\bar{A}\right)\mathrm{e}^{\,j\omega_0 t} \\
&\approx \left(2j\omega_0\frac{\partial \bar{A}}{\partial t} - \omega_0^2\bar{A}\right)\mathrm{e}^{\,j\omega_0 t}\,.
\end{aligned} \tag{4.8}$$

For the investigation of narrow banded operation regimes, this approximation is accurate. However, for the investigation of broadband operation regimes the neglection of terms proportional to the second order time derivative leads to significant deviations of the wave dispersion. This is proven in section 4.1.2. Therefore, the slowly changing amplitude approximation (4.8) is not used for the developed electron-wave interaction model.

However, the relations

$$\nabla_\perp^2 \hat{\boldsymbol{e}} + k_\perp^2 \hat{\boldsymbol{e}} = 0 \tag{4.9}$$

and

$$k_\parallel^2 = k_0^2 - k_\perp^2 \tag{4.10}$$

can be used to further simplify (4.6), if a circular waveguide with only slowly varying radius is assumed. The resulting equation can be reduced to a scalar equation for the amplitude $\bar{A}$ by using the orthogonality of the eigenmodes $\hat{\boldsymbol{e}}_i$. For this, the equation is multiplied from the right with $\hat{\boldsymbol{e}}_\mathrm{A}^*$ and integrated over the cross-section $S_\perp$ of the waveguide:

$$\frac{\partial^2 \bar{A}}{\partial z^2} + k_{0\parallel}^2 \bar{A} - j\frac{2k_0^2}{\omega_0}\frac{\partial \bar{A}}{\partial t} - \frac{k_0^2}{\omega_0^2}\frac{\partial^2 \bar{A}}{\partial t^2} = \underbrace{-\mu_0 \, \mathrm{e}^{\,-j\omega_0 t} \iint\limits_{S_\perp} \frac{\partial \bar{\boldsymbol{J}}}{\partial t} \cdot \hat{\boldsymbol{e}}_\mathrm{A}^* \, \mathrm{d}S_\perp}_{=\bar{S}_\mathrm{A}} \, . \tag{4.11}$$

The term $\bar{S}_\mathrm{A}$ is called source term and describes an excitation of the field by an external source. This source can be an electron beam or another eigenmode B that is coupled with mode A such as in a helically corrugated waveguide. A derivation of a source term for an arbitrary 3D particle beam is shown in section 4.2.1.

Since the slowly changing amplitude approximation (4.7) is not used for the derivation of (4.11), the equation is a 'fixed transversal field' approximation rather than a classical slowly changing amplitude approximation.

4.1.1 Helically Corrugated Waveguide

While (4.11) is suitable for the simulation of gyro-devices with a cylindrical interaction region, e.g. a cyclotron absorber or a gyrotron, it cannot be directly applied for the simulation of helical gyro-TWTs. In a helical gyro-TWT, the electron-wave interaction takes place in a helically corrugated waveguide (see chapter 3.1.1) with an inner surface

$$r(\phi, z) = R + \tilde{r}\cos(\tilde{m}\phi - 2\pi z/\tilde{d}) \, , \tag{4.12}$$

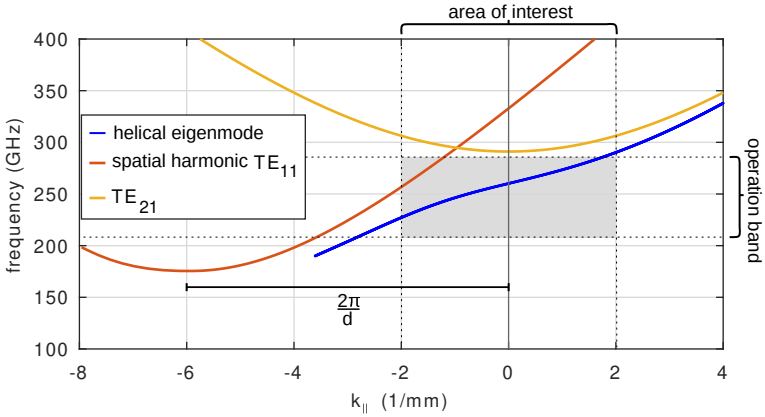

Figure 4.1: Dispersion diagram of the $\mathrm{TE}_{1,1}$ mode's first spatial harmonic in the helically corrugated waveguide, the $\mathrm{TE}_{2,1}$ mode and the eigenmode resulting from a coupling of the counter-rotating $\mathrm{TE}_{-1,1}$ and co-rotating $\mathrm{TE}_{2,1}$ modes.

where R is the waveguide mean radius; $\tilde{r}$, $\tilde{m}$ and $\tilde{k}_{\parallel} = 2\pi/\tilde{d}$ are the amplitude, azimuthal and axial number of the corrugation.

For small corrugation amplitudes, the electric field inside the helically corrugated waveguide can be described by two coupled $\mathrm{TE}_{\mathrm{m,n}}$ modes A and B of a circular waveguide which fulfill the conditions (3.2) and (3.3). Consequently, a pair of coupled equations is required to describe the electron-wave interaction.

For a stable operation of a helical gyro-TWT, typically the center frequency at the operation point is chosen slightly below the cut-off frequency of mode A ($k_{\parallel \mathrm{A}} \rightarrow 0$). Therefore, to fulfill the Bragg condition (3.3), a coupling of mode A can only take place with a spatial harmonic of mode B. This is illustrated in Fig. 4.1. The operation band is located below the cut-off frequency of mode A ($\mathrm{TE}_{2,1}$) and the corresponding wavenumbers of the eigenmode in the helically corrugated waveguide (blue line in Fig. 4.1) are located around $k_{\parallel} = 0\,\mathrm{mm}^{-1}$.

To derive a wave equation for the amplitude $\overline{B}(t,z)$ of the spatial harmonic mode B, the expansion (4.5) is extended with an additional phase term $\mathrm{e}^{-j\tilde{k}_{\parallel} z}$:

$$\overline{\boldsymbol{E}}(t,r,\phi,z) = \overline{B}(t,z)\,\mathrm{e}^{\,j\left(\omega_0 t - \tilde{k}_{\parallel} z\right)}\,\hat{\boldsymbol{e}}_{\mathrm{B}}(r,\phi)\,. \tag{4.13}$$

Applying this expansion to the Helmholtz equation (4.4) yields the following wave equation:

$$\begin{aligned}-\mu_0 \frac{\partial}{\partial t}\bar{\boldsymbol{J}} &= \left(\frac{\partial^2}{\partial z^2} + \nabla_\perp^2\right)\left[\bar{B}\mathrm{e}^{\,j\omega_0 t}\hat{\boldsymbol{e}}_\mathrm{B}\right] - \frac{1}{c_0^2}\frac{\partial^2}{\partial t^2}\left[\bar{B}\mathrm{e}^{\,j\omega_0 t}\hat{\boldsymbol{e}}_\mathrm{B}\right] \\ &= \frac{\partial \bar{B}}{\partial z}\left(\frac{\partial \bar{B}}{\partial z}\mathrm{e}^{\,j\omega_0 t} - j\tilde{k}_\parallel \bar{B}\mathrm{e}^{\,j\omega_0 t}\right)\hat{\boldsymbol{e}}_\mathrm{B} + \bar{B}\mathrm{e}^{\,j\omega_0 t}\nabla_\perp^2\hat{\boldsymbol{e}}_\mathrm{B} \\ &\quad - \frac{1}{c_0^2}\left[\frac{\partial}{\partial t}\left(\frac{\partial \bar{B}}{\partial t}\mathrm{e}^{\,j\omega_0 t} + j\omega_0 \bar{B}\mathrm{e}^{\,j\omega_0 t}\right)\right]\hat{\boldsymbol{e}}_\mathrm{B}\,.\end{aligned} \tag{4.14}$$

Since mode B is a traveling mode, operated far away from cut-off, the group velocity of the mode is almost constant for the operation frequency band. This can be clearly seen in Fig. 4.1. While the phase velocity of the $\mathrm{TE}_{2,1}$ mode has a parabolic shape, the phase velocity of the spatial harmonic $\mathrm{TE}_{1,1}$ mode is almost linear in the area of interest. Therefore, (4.11) can be simplified by neglecting dispersion effects. This is equivalent to the assumption that the amplitude $\bar{B}(t,z)$ is slow in space and the second spatial derivative becomes small in the area of interest:

$$\left|\frac{\partial^2 \bar{B}}{\partial z^2}\right| \ll k_0 \left|\frac{\partial \bar{B}}{\partial z}\right|\,. \tag{4.15}$$

Using (4.15), the spatial derivatives can be simplified:

$$\begin{aligned}&\frac{\partial \bar{B}}{\partial z}\left(\frac{\partial \bar{B}}{\partial z}\mathrm{e}^{\,j(\omega_0 t - \tilde{k}_\parallel z)} - j\tilde{k}_\parallel \bar{B}\mathrm{e}^{\,j(\omega_0 t - \tilde{k}_\parallel z)}\right) \\ &\quad = \left(\frac{\partial^2 \bar{B}}{\partial z^2} - j\tilde{k}_\parallel \frac{\partial \bar{B}}{\partial z} - j\tilde{k}_\parallel \frac{\partial \bar{B}}{\partial z} - \tilde{k}_\parallel^2 \bar{B}\right)\mathrm{e}^{\,j(\omega_0 t - \tilde{k}_\parallel z)} \\ &\quad \approx \left(-2j\tilde{k}_\parallel \frac{\partial \bar{B}}{\partial z} - \tilde{k}_\parallel^2 \bar{B}\right)\mathrm{e}^{\,j(\omega_0 t - \tilde{k}_\parallel z)}\,.\end{aligned} \tag{4.16}$$

Applying this approximation together with (4.9) and (4.10) to the Helmholtz equation (4.14) for mode B, it reduces to

$$\tilde{k}_{\parallel}\frac{\partial \overline{B}}{\partial z}+\frac{k_0}{c_0}\frac{\partial \overline{B}}{\partial t}-\frac{j}{2}\left(k_{0\parallel}^2-\tilde{k}_{\parallel}^2\right)\overline{B}-\frac{jk_0^2}{2\omega_0^2}\frac{\partial^2 \overline{B}}{\partial t^2} = \underbrace{\frac{j}{2}\left(-\mu_0\right)\mathrm{e}^{-j\left(\omega_0 t-\tilde{k}_{\parallel}z\right)}\iint\limits_{S_{\perp}}\frac{\partial \overline{\boldsymbol{J}}}{\partial t}\cdot\hat{\boldsymbol{e}}_{\mathrm{B}}^{*}\,\mathrm{d}S_{\perp}}_{=\overline{S}_{\mathrm{B}}}\,. \tag{4.17}$$

Finally, a set of two coupled equations describing the eigenwave in a helically corrugated waveguide can be assembled:

$$\frac{\partial^2 \overline{A}}{\partial z^2}-i2\frac{k_0}{c_0}\frac{\partial \overline{A}}{\partial t}+k_{0\parallel\mathrm{A}}^2\overline{A}-\frac{k_0^2}{\omega_0^2}\frac{\partial^2 \overline{A}}{\partial t^2}=\overline{S}_{\mathrm{A}}+C_{\mathrm{B,A}}\overline{B}\,, \tag{4.18}$$

$$\tilde{k}_{\parallel}\frac{\partial \overline{B}}{\partial z}+\frac{k_0}{c_0}\frac{\partial \overline{B}}{\partial t}-\frac{j}{2}\left(k_{0\parallel\mathrm{B}}^2-\tilde{k}_{\parallel}^2\right)\overline{B}-\frac{jk_0^2}{2\omega_0^2}\frac{\partial^2 \overline{B}}{\partial t^2}=\frac{j}{2}C_{\mathrm{A,B}}\overline{A}\,. \tag{4.19}$$

Here, $C_{\mathrm{A,B}}$ and $C_{\mathrm{B,A}}$ are the coupling factors for the coupling of mode A to mode B and vice versa (see (3.16)). For a helically corrugated waveguide, $C_{\mathrm{A,B}}=C_{\mathrm{B,A}}$ can be assumed.

In (4.19) it is already taken into account that in a helical gyro-TWT typically a large orbit electron beam is used to enhance the mode selection and to prevent the excitation of parasitic modes. Such an electron beam can excite only resonant modes with the azimuthal indices equal to the electron cyclotron harmonic number s (see chapter 3.1.2). If for an imperfect electron beam a parasitic excitation of mode B at a lower cyclotron harmonic should be taken into account, the source term $\overline{S}_{\mathrm{B}}$ must be added to the right hand side of (4.19).

4.1.2 Range of Validity

The approach of slowly varying amplitudes (see (4.7)) is often used for simulation of gyro devices. However, it is only valid for narrow signal bandwidths around the carrier frequency. This is not a limitation in the simulation of

the narrow-banded electron-wave interaction in gyrotrons, but for the simulation of the electron-wave interaction in a broadband amplifier this could become problematic. Therefore, the simulation model developed as part of this work ((4.11), (4.18) and (4.19)) does not use the slowly varying amplitudes approximation. To determine the importance of this for the simulation of broadband electron-wave interactions, the dispersion relations of the slowly varying amplitudes approximation and the equations (4.11), (4.18) and (4.19) are compared with the exact dispersion relations below.

Circular Waveguide

The dispersion of (4.11) for an eigenmode in a circular waveguide can be derived if a harmonic wave is assumed for the envelope of the wave:

$$\overline{A} \propto \mathrm{e}^{\,j(\Omega t - k_{\parallel} z)} \; . \tag{4.20}$$

Applying (4.20) to (4.11), gives the dispersion equation:

$$k_{\parallel}{}^2 - k_{0\parallel\mathrm{A}}^2 - \frac{2k_0}{c_0}\Omega - \frac{1}{c_0^2}\Omega^2 = 0 \; . \tag{4.21}$$

In a similar manner, the dispersion equation for the slowly varying amplitudes approximation can be derived:

$$k_{\parallel}{}^2 - k_{0\parallel\mathrm{A}}^2 - \frac{2k_0}{c_0}\Omega = 0 \; . \tag{4.22}$$

The dispersion curves $\Omega(k_{\parallel})$ can be found by solving (4.21) respectively (4.22) for fixed values of Ω. Since the time dependence of the electric field in (4.11) is expressed relative to a harmonic carrier signal with frequency ω_0, the physical frequency ω and the expansion frequency Ω are correlated over

$$\Omega = \omega - \omega_0 \; . \tag{4.23}$$

The exact dispersion of an eigenmode in a circular waveguide can be found by solving the Helmholtz equation and is given by

$$k_{\parallel}^2 + k_{\perp}^2 - \frac{1}{c_0^2}\omega^2 = 0 \tag{4.24}$$

$$\Leftrightarrow\ k_{\parallel}^2 - k_{0\parallel\mathrm{A}}^2 - \frac{2k_0}{c_0}\Omega - \frac{1}{c_0^2}\Omega^2 = 0\,. \tag{4.25}$$

A comparison of (4.25) with the slowly varying amplitude approximation (4.22) shows that (4.22) is equivalent to a first-order approximation of the dispersion around ω_0. In contrast, a comparison of (4.25) and (4.21) shows that both equations are equal. This is not surprising, since (4.11) is still the exact Helmholtz equation for the axial field distribution $\bar{A}(t,z)$ of an eigenmode in a circular waveguide.

For the slowly varying amplitude approximation, the phase and group velocities are exact at the carrier frequency ω_0. Therefore, the approximation is optimally suited for the simulation of a narrow-banded electron-wave interaction at the carrier frequency. This can be seen in Fig. 4.2a. The dispersion curves of a circular waveguide and the slowly varying amplitude approximation are plotted for the cylindrical interaction region of a 263 GHz cyclotron absorber ($R = 0.36\,\mathrm{mm}$). For frequencies different from ω_0, the deviations in the phase velocity are increasing. However, in a broad bandwidth around the carrier frequency ($\pm 10\,\mathrm{GHz}$), the relative errors in the phase and the group velocities remain small. For the group velocity, the deviations are higher than for the phase velocity ($\pm 5\,\%$ for $\pm 10\,\mathrm{GHz}$ around the carrier frequency). This can slightly influence the broadband behavior of the simulated electron-wave interaction. To evaluate the expected influences of the deviations in the dispersion onto the electron-wave interaction, the deviations can be compared with the influences of a non-perfect electron beam. If it is assumed that in a real experiment the pitch factor of the electron beam has uncertainties of about $\pm 5\,\%$ [42], the deviations caused by the approximation of the wave equation are within the range of the experimentally expected uncertainties.

It can be concluded that the slowly varying amplitude approximation for a circular waveguide is suitable for an electron-wave interaction simulation over a relative bandwidth of up to $10\,\%$ around the carrier frequency. Therefore,

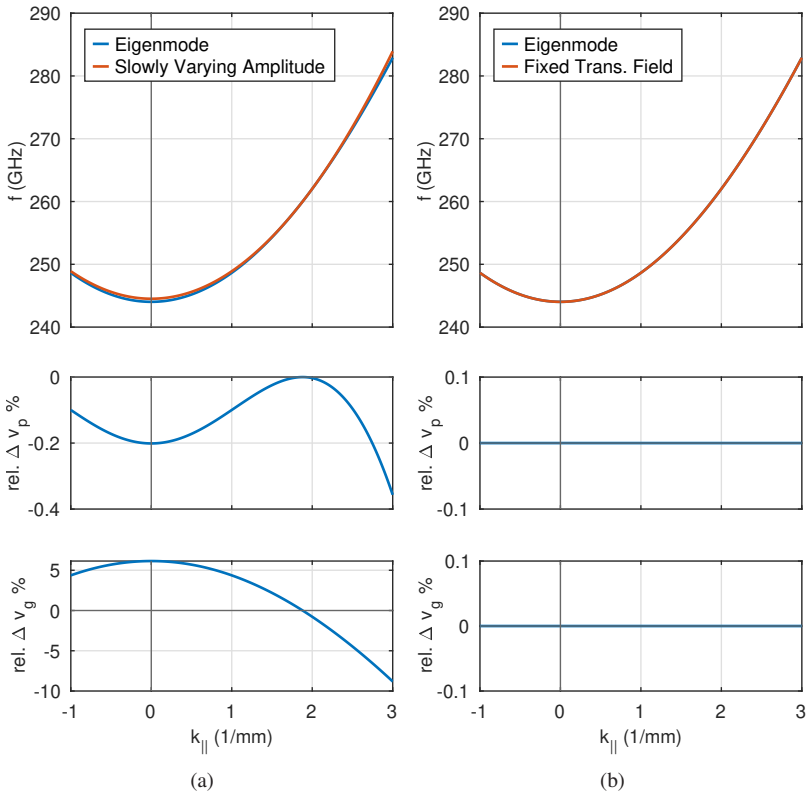

Figure 4.2: Dispersion of a cylindrical interaction space for a 263 GHz cyclotron absorber with radius $R = 0.36\,\mathrm{mm}$. Comparison of the original dispersion relations, the slowly varying amplitude approximation, and the fixed transversal field approximation (4.11). The carrier frequency is $f_0 = 260\,\mathrm{GHz}$.

the slowly varying amplitude approximation would be still suitable for the simulation of a cyclotron absorber.

However, if an excitation of a mode simultaneously at several harmonics of the cyclotron frequency should be investigated, the slowly varying amplitude approximation is not suitable anymore. This should be considered in particular for the simulation of the electron wave interaction in overmoded waveguides such as in high power gyrotrons.

Helically Corrugated Waveguide

For a helically corrugated waveguide (see (4.18) and (4.19)), the dispersion relation is given by a multiplication of the dispersion relations of the two coupled circular waveguide eigenmodes A and B:

$$k_{\parallel}^2 - k_{0\parallel\mathrm{A}}^2 - \frac{2k_0}{c_0}\Omega - \frac{1}{c_0^2}\Omega^2 = 2C_{\mathrm{B,A}} \,, \tag{4.26}$$

$$k_{\parallel} - \frac{\tilde{k}_{\parallel}k_0}{c_0}\Omega - \frac{1}{2\tilde{k}_{\parallel}}\left(k_{0\parallel\mathrm{B}}^2 - \tilde{k}_{\parallel}^2\right) - \frac{1}{2\tilde{k}_{\parallel}c_0^2}\Omega^2 = -\frac{1}{\tilde{k}_{\parallel}}C_{\mathrm{A,B}} \,, \tag{4.27}$$

$$\Rightarrow k_{\parallel}^3 + Nk_{\parallel}^2 + Mk_{\parallel} + MN + \frac{2}{\tilde{k}_{\parallel}}C_{\mathrm{B,A}}C_{\mathrm{A,B}} = 0 \tag{4.28}$$

with $M = -\left(k_{\parallel\mathrm{A}}^2 + 2\frac{k_0}{c_0}\Omega + \frac{1}{c_0^2}\Omega^2\right)$ and $N = \frac{-1}{2\tilde{k}_{\parallel}}\left(k_{0\parallel\mathrm{B}}^2 - \tilde{k}_{\parallel}^2 + 2\frac{k_0}{c_0}\Omega + \frac{1}{c_0^2}\Omega^2\right)$. The dispersion equation (4.28) is a third-order equation. For a given propagation constant $k_{\parallel}$, the equation has three eigenvalues. However, only two of them have a practical physical meaning, describing an upper and a lower eigenmode of the helically corrugated waveguide. For an operation of the helical gyro-TWT in the designed frequency band only the lower eigenmode can propagate and therefore only it will be considered in the following. It should be noted that if there is no coupling between the two modes A and B ($C_{\mathrm{B,A}} = C_{\mathrm{A,B}} = 0$) the eigenfunction degenerates into the two separate dispersion curves of the original modes A and B.

In Fig. 4.3a and Fig. 4.3b, the resulting dispersion curves for the fixed transversal field approach ((4.18) and (4.19)) and the slowly varying amplitude approximation (additional neglection of terms $\propto \frac{\partial^2}{\partial t^2}$ in (4.18) and (4.19)) is shown. It can be seen, that the additional approximations made in the slowly varying amplitude approximation introduce an increased error in the dispersion. Therefore, terms $\propto \frac{\partial^2}{\partial t^2}$ are not neglected in the developed model which is a difference to the state-of-the-art transient models for helical gyro-TWTs [68].

In contrast to the equations for the circular waveguide, for the helically corrugated waveguide the deviations between approximation and original equation do not vanish at the carrier frequency for neither of the approaches. However, this is not problematic since the carrier frequency typically is set to the cut-off

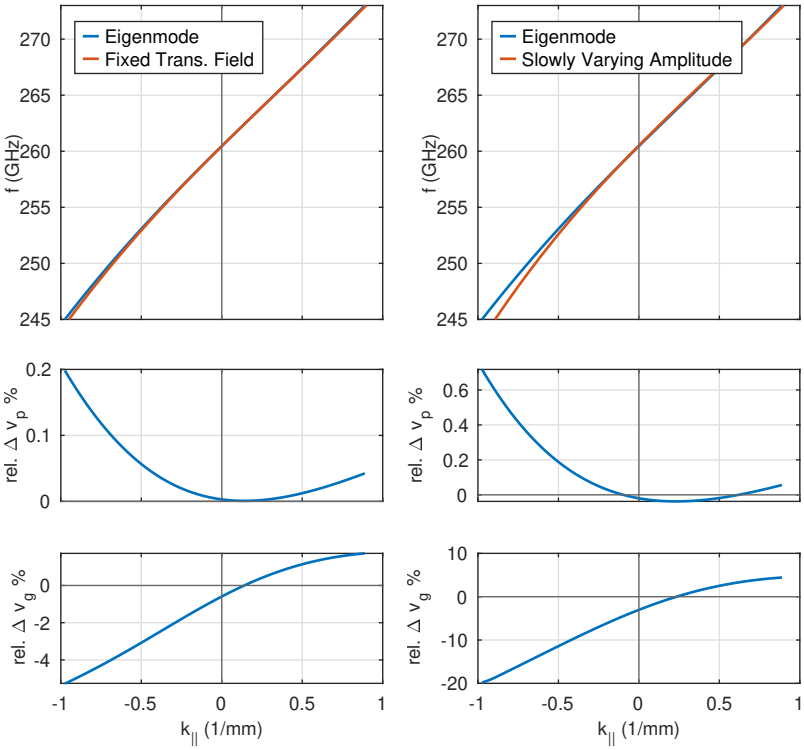

Figure 4.3: Dispersion of a threefold helically corrugated waveguide for a 263 GHz gyro-TWT with $R = 0.528\,\mathrm{mm}$, $\tilde{r} = 0.08\,\mathrm{mm}$ and $\tilde{d} = 1.11\,\mathrm{mm}$. Comparison of the original dispersion relations, the fixed transversal field approximation (4.11), and the slowly varying amplitude approximation. The carrier frequency is $f_0 = 273\,\mathrm{GHz}$.

frequency ω_A of mode A, while the device should be always operated below this frequency, around $k_\parallel = 0\ \mathrm{mm}^{-1}$.

It can be clearly seen that the deviations in the phase as well as in the group velocity are significantly higher in the slowly varying amplitude approximation. For the developed model, the deviations are within a marginal level of $\pm 0.2\,\%$ for the phase velocity and $\pm 5\,\%$ for the group velocity for $\pm 15\,\mathrm{GHz}$.

To evaluate the expected influences of the observed deviations, a similar argumentation as for a cylindrical interaction space can be used. In a CUSP-gun for sub-THz devices, the spread in the pitch factor is usually in the order of $\pm 5\,\%$ [42] and the resulting influences on the electron-wave interaction therefore exceed the influences introduced by the model. In addition, the manufacturing of a helically corrugated waveguide for sub-THz frequencies is challenging and the unavoidable deviations in the geometry cause deviations of the phase velocity of up to $1\,\%$ [44]. Therefore, the uncertainties introduced by the developed fixed transversal field approach are far below the uncertainties expected in an experiment.

It should be mentioned that in contrast to the previous discussion of circular waveguides, for the helically corrugated waveguide the models are compared with a dispersion derived from the perturbation theory (see chapter 3.1.1) which is not equivalent to the real, exact dispersion of a helically corrugated waveguide. Depending on the parameter of the waveguide, this dispersion can differ significantly from the real dispersion. If this is the case, a possible solution is the calculation of the exact dispersion with a full-wave simulation (see chapter 7.5) and an adaption of the parameters R and $\tilde{r}$ in the perturbation model until the perturbation model matches the full-wave simulation result. Since the perturbation model is derived only in first order accuracy (in terms of $\tilde{r}$), occurring correction terms for the modes' eigenvalues (which are of second order [123]) are neglected. Therefore, an adaption of R and $\tilde{r}$ is a legitimate approach and corresponds to a correction of the eigenvalues.

4.1.3 Multi-Mode Simulations

The previously presented equations are derived for a single eigenmode A of a circular waveguide and for a single eigenmode W of a helically corrugated waveguide (where W is described as a coupling of two circular waveguide modes A and B). Assuming the radius of the waveguide varies only slowly and smoothly, the coupling between different eigenmodes by the geometry can be neglected. Then the eigenmodes of the interaction region are only weakly coupled via the electron beam. As a result, a multi-mode simulation can be reduced to N independent simulations of N modes with amplitudes $\overline{A}_n$ and a shared electron beam. For the solution of the equations of motion (see the

following section), the electromagnetic field resulting from the superposition of all modes has to be used.

Especially for the simulation of gyrotrons with their oversized cavities, multi-mode simulations are important for a precise simulation of startup scenarios and mode competition [124], [125]. However, in the cylindrical interaction region of a cyclotron absorber only the fundamental $\mathrm{TE}_{1,1}$ mode is above cut-off at the desired operation frequency. Therefore, parasitic modes can be neglected.

For helical gyro-TWTs and in general for all forward wave amplifiers, a critical issue in the development is the self-excitation of parasitic backward waves [126]. Therefore, it is of particular interest to include the backward wave W^- corresponding to the forward traveling, main operation mode W, in the simulation of helical gyro-TWTs. Similar to the forward propagating mode W, the backward eigenmode W^- can be described by two coupled modes A and B′ of a circular waveguide. The modes have to fulfill the Bragg resonance condition for a backward wave:

$$\frac{2\pi}{\tilde{d}} = \tilde{k}_{\parallel} \approx k_{\parallel \mathrm{A}} + k_{\parallel \mathrm{B}'} \ . \tag{4.29}$$

Since (4.29) differs from the Bragg resonance condition for forward waves (3.3) only by the sign of $k_{\parallel \mathrm{B}'}$, equation (4.19) with the substitution $\tilde{k}_{\parallel} \rightarrow -\tilde{k}_{\parallel}$ can be used for the description of a backward wave in a helically corrugated waveguide.

4.2 Equations of Motion

The relativistic motion of charged particles in an electromagnetic field is described by the Lorentz equation

$$\frac{\mathrm{d}\boldsymbol{p}}{\mathrm{d}t} = q\,(\mathfrak{E} + \boldsymbol{v} \times \mathfrak{B}) \ , \tag{4.30}$$

where $\boldsymbol{p}$, $\boldsymbol{v}$ and q are the relativistic momentum, the velocity and the charge of a particle. $\mathfrak{E}$ and $\mathfrak{B}$ are the electric and magnetic fields.

In classical, trajectory based, models for the simulation of stationary operation of gyrotrons (e.g. SELF [119], TWANG [122], EURIDICE [121] ...), the time derivative in (4.30) is replaced with $v_{\parallel}\frac{\mathrm{d}\boldsymbol{p}}{\mathrm{d}z}$ and thus, the entire electron motion can be solved in the spatial domain. This approach is valid as long as the variation of the field profile is slow compared to the transition time of the electron through the interaction region. For the simulation of ultra-short pulses in amplifier and absorber tubes with long interaction regions this approach is inappropriate. This limitation can be overcome by solving (4.30) in the time domain. In classical time domain codes used for gyro-devices (e.g. [127], [121]) a 1D PIC approach is used for the description of the electron beam. The coupling between the electron beam and the waveguide eigenmode is described by coupling coefficients for gyrating electrons derived from the Graf's addition theorem [11], [128] at a given cyclotron harmonic.

While in the classical simulation codes for gyro-devices (mainly gyrotrons), the interaction region is limited to circular waveguides, in [68], a time domain self-consistent theory for helical gyro-TWTs is developed. The equations of motion are simplified to non-isochronous oscillator equations for the transverse momentum of the electrons. The electron-wave coupling is again described by coupling coefficients for a gyrating electron with a circular waveguide eigenmode derived from the Graf's addition theorem (see section 4.4 for a detailed comparison of the model developed in the frame of this work with the model in [68]).

In contrast to the existing approaches, in the frame of this work an alternative approach for the solution of the motion equations is being pursued: the equations of motion (4.30) are solved in full 3D, for arbitrary electric and magnetic fields. In addition, the source term calculation differs from classical approaches: the source term is directly calculated from an arbitrary electron beam, without the requirement of any approximations or assumptions, e.g. a gyrating electron beam. This has the advantages that electron beams with arbitrary offsets of the waveguides symmetry axis can be simulated and even oblique electron beams caused for example by a misaligned electron gun or misaligned magnetic field are supported. Furthermore, additional effects depending on additional fields, such as space charge fields, can be taken into account. Also interactions at higher cyclotron harmonics are natively supported.

4.2.1 Source Term

While it is common to simplify the source term $\bar{S}$ in (4.11) by the Graf's addition theorem to a simple coupling coefficient (see (3.23)), here, the source term is directly evaluated for an arbitrarily moving electron and an arbitrary eigenmode $\hat{\boldsymbol{e}}$. In the following, a brief overview of the derivation of this 'full' source term is given.

In (4.11), the source term is defined as the time derivative of a current density $\mathbb{J}$, integrated over the cross section of the waveguide:

$$\bar{S} = \mu_0 \iint_{S_\perp} \frac{\partial \mathbb{J}}{\partial t} \cdot \hat{\boldsymbol{e}}^* \, \mathrm{e}^{\,-j\omega_0 t} \, \mathrm{d}S_\perp \, . \tag{4.31}$$

For point particles (as electrons), the electric current density can be expressed as

$$\mathbb{J} = \sum_i q_i \delta(\boldsymbol{r} - \boldsymbol{r}_i) \boldsymbol{v}_i \, , \tag{4.32}$$

where $\delta(\boldsymbol{r} - \boldsymbol{r}_i)$ is the 3D delta distribution which writes in cylindrical coordinates as

$$\delta(\boldsymbol{r} - \boldsymbol{r}_i) = \delta(z - z_i)\delta(r - r_i)\delta(\phi - \phi_i)\frac{1}{r_i} \, . \tag{4.33}$$

After applying the definition of the delta distribution to (4.31) and multiple applications of the chain rule, the source term $\bar{S}_i$ of a single particle i can be expressed as:

$$\begin{aligned}\bar{S}_i = \mu_0 q_i \, \mathrm{e}^{\,-j\omega_0 t} \iint\limits_{S_\perp} \Big[\hat{\boldsymbol{e}}^* \cdot \Big(& -\delta'(z-z_i)\delta(r-r_i)\delta(\phi-\phi_i)\frac{\dot{z}_i}{r_i}v_i \\ & -\delta(z-z_i)\delta'(r-r_i)\delta(\phi-\phi_i)\frac{\dot{r}_i}{r_i}v_i \\ & -\delta(z-z_i)\delta(r-r_i)\delta'(\phi-\phi_i)\frac{\dot{\phi}_i}{r_i}v_i \\ & -\delta(z-z_i)\delta(r-r_i)\delta(\phi-\phi_i)\frac{\dot{r}_i}{r_i^2}v_i \\ & +\delta(z-z_i)\delta(r-r_i)\delta(\phi-\phi_i)\frac{1}{r_i}\dot{v}_i\Big)\Big] \,\mathrm{d}S_\perp \,. \end{aligned} \tag{4.34}$$

Here, the dot on values represents the time derivative $\frac{\partial}{\partial t}$. In a final step, the integral over the cross-section $S_\perp$ of the waveguide can be evaluated. For this, the definition of the derivative of the delta function

$$\langle \delta'(x-b), f \rangle = -f'(b) \tag{4.35}$$

is used to obtain the source term $\bar{S}_i$ of a single particle:

$$\begin{aligned}\bar{S}_i = \mu_0 q_i \mathrm{e}^{\,-j\omega_0 t} \Big[& -\delta'(z-z_i)\dot{z}_i \boldsymbol{v}_i \cdot \hat{\boldsymbol{e}}^*(r_i,\phi_i) \\ & +\delta(z-z_i)\dot{\boldsymbol{v}}_i \cdot \hat{\boldsymbol{e}}^*(r_i,\phi_i) \\ & +\delta(z-z_i)\dot{r}_i \boldsymbol{v}_i \cdot \left.\frac{\partial \hat{\boldsymbol{e}}^*(r,\phi_i)}{\partial r}\right|_{r=r_i} \\ & +\delta(z-z_i)\dot{\phi}_i \boldsymbol{v}_i \cdot \left.\frac{\partial \hat{\boldsymbol{e}}^*(r_i,\phi)}{\partial \phi}\right|_{\phi=\phi_i} \Big] \,. \end{aligned} \tag{4.36}$$

It is worth emphasizing that no assumptions about the electron beam, the waveguide, the eigenmode or the cyclotron-harmonic of the interaction are made in this derivation of the source term. Therefore, (4.36) can be applied for arbitrary electric fields and waveguides which allows an easy extension of

the developed program for future applications. In addition, this source term is valid for interactions at all cyclotron harmonics.

Probably, the most important advantage of the derived source term is the support of an arbitrary eigenmode $\hat{\boldsymbol{e}}$. The developed simulation tool directly implements (4.36) and no analytical form of $\hat{\boldsymbol{e}}$ is necessary. Rather, it is possible to use the solution of a numerical eigenmode solver and thus to support arbitrary waveguide structures. Nevertheless, the present work is limited to eigenmodes of circular waveguides.

4.2.2 Space Charge

In contrast to classical TWTs, space-charge effects (sometimes also referred as RF-space charge) are of minor importance for gyro-devices and in many interaction simulations of gyro-devices, space-charge effects are neglected [129].

However, for helical gyro-TWTs with very long interaction regions and high currents, space-charge effects could probably decrease the quality of the electron beam and influence the electron-wave interaction. An adventage of the chosen PIC approach is the possibility to include these effects which could become important for future highest-gain helical gyro-TWTs with very long interaction regions.

In a beam of gyrating electrons, space-charge effects are caused by a non-uniform distribution of the electrons in the electron beam. Two kinds of non-uniform distributions can occur in a gyrating electron beam: (1) a non-uniform distribution of the electrons in azimuthal direction caused by the azimuthal bunching of electrons in their gyro-orbits (see chapter 3.1.2); (2) a non-uniform distribution of the electrons in axial direction caused by the relativistic increase/decrease of the electron mass. However, it must be noted that these space-charge effects are orders of magnitudes lower than in classical TWTs.

For the simulation of space-charge effects in the electron beam, a three-dimensional Poisson solver as presented in [130], is used. The solver is based on an eigenmode expansion in the transverse direction and a finite difference method in the axial direction. The expansion into the eigenmodes

of the waveguids has the advantage that effects of the conducting waveguide walls are automatically taken into account. The downside is that for a complex charge distribution in a highly oversized waveguide an impracticable number of modes must be taken into account. However, since the investigated large orbit electron beams are highly symmetric and the interaction regions are almost fundamental mode waveguides, a moderate number of modes is sufficient and the method is well suited for helical gyro-TWTs and cyclotron absorbers. For the sake of completeness, a short summary of the method described in [130] is given.

The electrostatic potential $\mathfrak{V}$ from the space charge field created by a charge density ρ is described by the Poisson equation, which can be written for circular coordinates in the following form:

$$\frac{\partial^2 \mathfrak{V}}{\partial r^2} + \frac{1}{r}\frac{\partial \mathfrak{V}}{\partial r} + \frac{1}{r^2}\frac{\partial^2 \mathfrak{V}}{\partial \phi^2} + \frac{\partial^2 \mathfrak{V}}{\partial z^2} = -\frac{\rho}{\epsilon_0} \,. \tag{4.37}$$

For a circular waveguide, the Bessel functions $\mathrm{J}_m(x)$ are the corresponding eigenfunctions and therefore the appropriate choice for an expansion of the scalar potential $\mathfrak{V}$ and the charge density ρ in the radial direction:

$$\mathfrak{V}(r,\phi,z) = \sum_{m=-N_m/2}^{N_m/2-1} \sum_{n=1}^{N_n} \mathfrak{V}^{mn}(z)\mathrm{J}_m(\chi_{mn} r)\mathrm{e}^{\,-jm\phi} \,, \tag{4.38}$$

$$\rho(r,\phi,z) = \sum_{m=-N_m/2}^{N_m/2-1} \sum_{n=1}^{N_n} \rho^{mn}(z)\mathrm{J}_m(\chi_{mn} r)\mathrm{e}^{\,-jm\phi} \,. \tag{4.39}$$

Inserting the expansions into the Poisson equation (4.37), multiplying with $r\mathrm{e}^{\,jm\phi}\mathrm{J}_m(\chi_{mn} r)$ and evaluating the integrals over the cross-section of the waveguide, gives an equation for the z-dependence of the electrostatic potential:

$$\frac{\partial^2 \mathfrak{V}^{mn}}{\partial z^2} - \chi_{mn}^2 \mathfrak{V}^{mn} = -\frac{\rho^{mn}}{\epsilon_0} \,. \tag{4.40}$$

Here, ρ^{mn} are the expansion coefficients of the charge density which are given by:

$$\rho^{mn}(z) = \frac{1}{\pi R^2 \mathrm{J}_m'^2(\chi_{mn} R)} \iint\limits_{S_\perp} \rho \, \mathrm{e}^{\,-jm\phi} \mathrm{J}_m(\chi_{mn} r) \, \mathrm{d}S_\perp \, . \tag{4.41}$$

They can be easily evaluated for a sum of point particles. With (4.41), the differential equation (4.40) for the z-dependence of the electrostatic potential can be solved using a central finite difference scheme (see [130] for details).

4.3 Numerical Solution

In the following, the numerical methods used for a solution of the equations (4.11), (4.18), (4.19) and (4.30) are presented. For the numerical integration of the equations, the time domain as well as the spatial domain of interest are discretized into N_t time steps of length Δt and N_z space steps of length Δz. In Fig. 4.4, a runtime diagram of the numerical solution process is given. For the calculation of a new time step $t + \Delta t$, first the field equations (4.11), (4.18) and (4.19) are solved by an implicit method (see section 4.3.1). With the known amplitude distribution of the waveguide modes along the interaction region, the source terms $\bar{S}_i$ for all particles in the interaction region can be calculated. The source term calculation is followed by the calculation of additional effects as space-charge fields. Finally, the equations of motion are solved for all particles. In the following sections, the single steps of the algorithm are described in more detail.

It should be noted that there is always a time shift of Δt between the particles and the amplitudes for the presented algorithm. Since the 3D particle pushing requires a small time step ($\approx \frac{2\pi}{100\omega_\mathrm{H}}$) it was observed that the influences of this time shift are negligible.

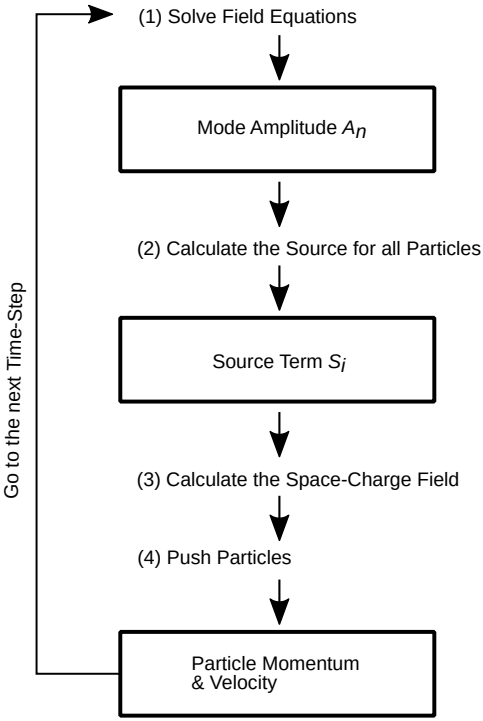

Figure 4.4: Runtime diagram for the numerical algorithm to integrating the interaction model.

4.3.1 Field Equations

As shown in the flow chart Fig. 4.4, in a first step, the differential field equations are solved. For the numerical solution, the implicit finite difference Crank-Nicolson scheme [131] is used which is of second-order, both in time and space.

In the Crank-Nicolson scheme, the explicit first order forward finite difference for time step t and the implicit first order backward finite difference for time step $t + \Delta t$ are combined for a discretization of the time derivatives. For the

spatial derivatives a central difference scheme of second order is used. This gives the following discretization which can be applied to the field equations:

$$\overline{A} = \frac{1}{2}\left(\overline{A}_z^{t+1} + \overline{A}_z^{t}\right) \tag{4.42}$$

$$\frac{\partial \overline{A}}{\partial t} = \frac{\overline{A}_z^{t+1} - \overline{A}_z^{t}}{\Delta t} \tag{4.43}$$

$$\frac{\partial^2 \overline{A}}{\partial t^2} = \frac{\frac{5}{4}\overline{A}_z^{t+1} - 2\overline{A}_z^{t} + \frac{3}{4}\overline{A}_z^{t-1}}{\Delta t^2} \tag{4.44}$$

$$\frac{\partial \overline{A}}{\partial z} = \frac{1}{2}\left(\frac{\overline{A}_{z+1}^{t+1} - \overline{A}_{z-1}^{t+1}}{2\Delta z} + \frac{\overline{A}_{z+1}^{t} - \overline{A}_{z-1}^{t}}{2\Delta z}\right) \tag{4.45}$$

$$\frac{\partial^2 \overline{A}}{\partial z^2} = \frac{1}{2}\left(\frac{\overline{A}_{z+1}^{t+1} - 2\overline{A}_{z}^{t+1} + \overline{A}_{z-1}^{t+1}}{\Delta z^2} + \frac{\overline{A}_{z+1}^{t} - 2\overline{A}_{z}^{t} + \overline{A}_{z-1}^{t}}{\Delta z^2}\right) \tag{4.46}$$

The expression for the second derivative of the time at $t + \frac{\Delta t}{2}$ is derived by averaging the second order central finite difference at t and the first order backward finite difference at $t + \Delta t$. This is a slight modification of the original Crank-Nicolson scheme where a first order forward finite difference is used at t. It has been shown that the method used here is slightly more stable.

After applying the discretization (4.42)-(4.46) to (4.11), the unknown amplitude values $\overline{A}^{t+1}$ can be separated to form a system of n linear equations, where n is the number of grid points used for the discretization of the z-coordinate. The resulting system of linear equations is of the form

$$\underline{T_{\mathrm{A}}}\,\overline{\boldsymbol{A}} = \boldsymbol{V}_{\mathrm{A}} \ , \tag{4.47}$$

where $\underline{T_{\mathrm{A}}}$ is a tridiagonal matrix, $\overline{\boldsymbol{A}}$ is a vector with the n unknown amplitude values at time step $t + \Delta t$ for every space point, and $\boldsymbol{V}_{\mathrm{A}}$ is a vector calculated from the known amplitude values from the previous time step t.

The system of equations (4.47) has to be solved at every time step. With the Thomas algorithm this can be efficiently done in $O(n)$ floating point operations. A slightly slower, but, because of an included pivoting method, numerically more stable alternative is the usage of the LAPACK method `zgttrs` [132].

4.3.2 Coupled Equations of Helical Waveguides

For a solution of the coupled equations (4.18) and (4.19) of a helically corrugated waveguide also the Crank-Nicolson scheme is used. After a discretization of both wave equations following the Crank-Nicolson scheme ((4.42)-(4.46)), a coupled system of linear equations

$$\underline{D_{\mathrm{B}}}\overline{\boldsymbol{B}} + \underline{T_{\mathrm{A}}}\overline{\boldsymbol{A}} = \boldsymbol{V}_{\mathrm{A}} \tag{4.48}$$

$$\underline{T_{\mathrm{B}}}\overline{\boldsymbol{B}} + \underline{D_{\mathrm{A}}}\overline{\boldsymbol{A}} = \boldsymbol{V}_{\mathrm{B}} \tag{4.49}$$

is derived, where $\underline{D_{\mathrm{A,B}}}$ represent diagonal matrices and $\underline{T_{\mathrm{A,B}}}$ represent tri-diagonal matrices. The coupled equations can be rewritten as a single system of linear equations:

$$\begin{pmatrix} \underline{D_{\mathrm{B}}} & \underline{T_{\mathrm{A}}} \\ \underline{T_{\mathrm{B}}} & \underline{D_{\mathrm{A}}} \end{pmatrix} \begin{pmatrix} \overline{\boldsymbol{B}} \\ \overline{\boldsymbol{A}} \end{pmatrix} = \begin{pmatrix} \boldsymbol{V}_{\mathrm{A}} \\ \boldsymbol{V}_{\mathrm{B}} \end{pmatrix} . \tag{4.50}$$

This system of linear equations can be efficiently solved by the 'Schur-Complements' method:

$$\underline{G} = \underline{D_{\mathrm{A}}} - \underline{T_{\mathrm{B}}}\underline{D_{\mathrm{B}}^{-1}}\underline{T_{\mathrm{A}}} \tag{4.51}$$

$$\Rightarrow \underline{G}\overline{\boldsymbol{A}} = \boldsymbol{V}_{\mathrm{B}} - \underline{T_{\mathrm{B}}}\underline{D_{\mathrm{B}}^{-1}}\boldsymbol{V}_{\mathrm{A}} \tag{4.52}$$

$$\Rightarrow \overline{\boldsymbol{B}} = \underline{D_{\mathrm{B}}^{-1}}\boldsymbol{V}_{\mathrm{A}} - \underline{D_{\mathrm{B}}^{-1}}\underline{T_{\mathrm{A}}}\overline{\boldsymbol{A}} . \tag{4.53}$$

With this method the original problem of a $(2n) \times (2n)$ system of equation can be reduced to a $(n) \times (n)$ system of equations (4.52) and a simple back-substitution (4.53). In the given case this is possible because the inverse $\underline{D_{\mathrm{B}}^{-1}}$ for a diagonal matrix can be easily found.

The so-called Schur complement $\underline{G}$ is a penta-diagonal matrix. For a solution of the resulting system of linear equations, optimized algorithms are available, e.g. the `zgbtrs` function in the LAPACK [132]. It can solve the penta-diagonal system of linear equations within $O(n)$ floating point operations.

It should be mentioned that the described method is only valid, as long as all of the diagonal elements of $\underline{D_{\mathrm{B}}}$ are non-zero. In the given problem that corresponds to a non-zero coupling coefficient $C_{\mathrm{A,B}}$ in the equations (4.18)

and (4.19). This is fulfilled for all helically corrugated waveguides. Also, this method will become numerical unstable for very small or very large elements in $\underline{D}_{\mathrm{B}}$ (bad conditioned matrix). But for typical coupling coefficients in helical gyro-TWTs and for floating point types in double precision, it was observed that the method remains numerically stable.

4.3.3 Source Term and Equations of Motion

In the second step of the algorithm, the contributions of all particles to the source term are calculated with equation (4.36) (see section 4.2.1). For the numerical evaluation of (4.36), the remaining $\delta(z)$ and its derivatives $\delta'(z)$ must be approximated. Because the amplitude is solved on an equidistant grid with step-width Δz, it can be assumed that $\delta(z)$ can be approximated by a one-variable function $\Phi(x)$ that scales with the mesh-width in the following manner:

$$\delta(z) \rightarrow \frac{1}{\Delta z}\Phi(\frac{z}{\Delta z}) = \frac{1}{\Delta z}\Phi(\hat{z}) \quad \text{with} \quad \hat{z} \equiv \frac{z}{\Delta z}\,, \tag{4.54}$$

$$\delta'(z) \rightarrow \frac{1}{\Delta z^2}\Phi'(\hat{z})\,. \tag{4.55}$$

For the function $\Phi(\hat{z})$, the cosine-approximation is used (a detailed derivation can be found in [133]). It allows a fast numerical evaluation and has a continuous derivative:

$$\Phi(\hat{z}) = \begin{cases} \frac{1}{4}\left(1+\cos\frac{\pi\hat{z}}{2}\right), & |\hat{z}| \le 2 \\ 0, & \text{otherwise} \end{cases} \tag{4.56}$$

$$\Phi'(\hat{z}) = \begin{cases} \frac{-1}{8}\sin\frac{\pi\hat{z}}{2}, & |\hat{z}| \le 2 \\ 0, & \text{otherwise}\,. \end{cases} \tag{4.57}$$

In the third step of the algorithm, additional fields as the space-charge field are calculated. The space-charge fields are calculated by the method described in section 4.2.2. Since a sufficient number of waveguide eigenmodes must be considered, the calculation of the space-charge field can require a significant part of the total computing time. The high calculation costs can be slightly relaxed if the space-charge field is not updated at every time step.

After the electromagnetic fields are known (solution of the field equations from the first step and the optional space-charge fields), in the last step, the particle positions and velocities are updated. This is done by a solution of the Lorentz equation (4.30). For the integration of (4.30), various particle integrators (particle pushers) have already been developed, for example for applications in plasma physics or astrophysics [134]. Most of these algorithms are suitable for the given propose. So far the developed tool was successfully tested with an explicit fourth-order Runge-Kutta method [135], the well known Boris algorithm [136] and a synchronized version of the Boris algorithm [137]. Since the particle pushing requires a significant amount of the total computation time, the faster Boris algorithms should be preferred to the RK4 method.

4.3.4 Implementation and GPU Acceleration

The numerical methods given in the previous sections are implemented in an object-oriented framework with the programming language C++ [138]. Via an interface to the scripting language Lua [139], the simulations can be controlled, complex simulation setups can be easily created and advanced post-processing is available.

The developed implementation is validated by a comparison with experimental data (see appendix A.2). For a validation of the electron-wave interaction in a cylindrical interaction region the simulation model is compared with measurements of the short pulse ITER gyrotron (SP-ITER Gyrotron) [140]. The SP-ITER Gyrotron is developed, produced and tested at the IHM and therefore sufficient setup data and experimental results are available.

Since no helical gyro-TWT was available for experiments during this thesis, for a verification of the electron wave interaction in a helically corrugated waveguide, comparisons with published experimental results are performed. For the comparison, the first sub-THz helical gyro-TWT (W band) developed from He et al. at the University of Strathclyde (Glasgow, UK) [42] is used.

Parallelization

To take advantage of the full computing capabilities of modern computers, the developed algorithms must be parallelized wherever possible. Therefore, the developed implementation utilizes parallelization on multi-core central processing units (CPUs) as well as on the graphic processing unit (GPU).

In the algorithm shown in Fig. 4.4, the particle pushing, the source term calculation and the space charge calculation are well suited for a parallel calculation. Since the typical number of particles in a simulation is of the order of 10^6, all calculations related with particles are calculated on the GPU which is optimally suited for massive parallel calculations. In contrast, the number of waveguide modes in a typical simulation is low (in the order of 100) and a parallel solution of the related linear equation systems does usually scale not optimally with the parallelization. Therefore, all steps related with the amplitude calculation are exclusively evaluated on the CPU.

The major challenge for such a hybrid CPU/GPU implementation is a careful management of the simulation data to ensure data consistency between the main memory (RAM) and the GPU memory (VRAM). Since copying data between RAM and VRAM is additionally slow, the communication between CPU and GPU should be minimized.

In Fig. 4.5, a diagram of the parallel execution and the data transfer for the simulation of a single time step on the CPU/GPU is shown. In the first step of the simulation, the amplitude distributions for the N simulated modes along the interaction region is calculated on the CPU. If the number of simulated modes is greater than or equal to the number of available threads on the CPU ($N \geqslant M$), a parallelization of this calculation step is trivial. Since it is assumed that no coupling between individual eigenmodes of the interaction region occurs, the equations for every eigenmode can be solved in parallel by the available threads of the CPU. But if the number of modes is less than the available threads ($N < M$), an utilization of the full computing power is challenging. For those cases, a parallel solver based on the method described in [141] is implemented. Even the speed-up of the parallel solver does not linearly increase with the number of threads, it can reduce the required calculation time for the solution of typical systems of linear equations by a factor of two when four threads are used.

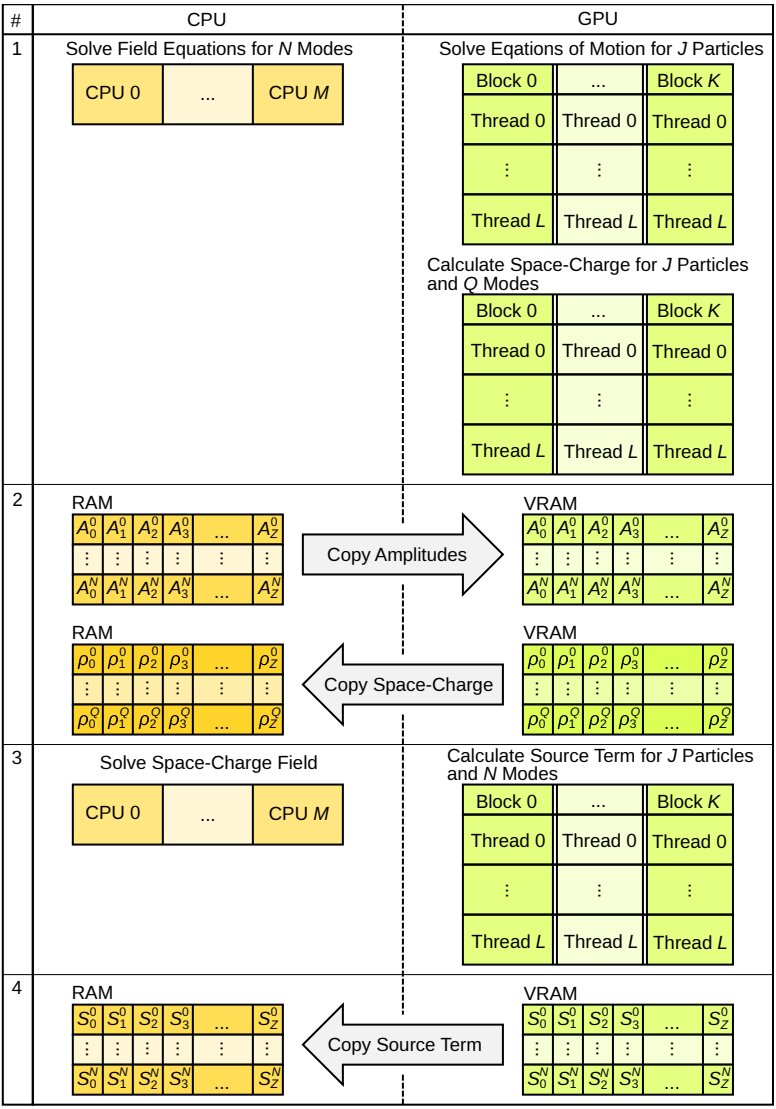

Figure 4.5: Parallel execution and data transfer for the simulation of a single time step on the CPU and GPU.

In parallel to the calculation of the amplitudes on the CPU, the equations of motion are solved for the particles on the GPU. Since direct interactions between individual particles are neglected in the model (the particles can only interact with each other by the external space charge field), the equations of motion can be solved independently and in parallel for all J particles. As shown in Fig. 4.5, the single threads on GPUs are grouped into blocks for a better process and data mapping. The GPU consists of several streaming multiprocessors (SM) that are able to execute multiple blocks in parallel. As soon as one of the blocks on a SM has completed execution, it takes up the serially next block. For a parallel calculation, the list of particles is split-up into $\frac{J}{K \cdot L}$ sub-lists (where L is the number of threads in a block and K the number of blocks) that are executed each from a single thread. The optimal number for L and K as well as the number of calculations actually executed in parallel depends on the architecture of the used GPU.

Once the equations of motion are solved, the coefficients ρ (see (4.41)) for the space charge field are calculated. Again this calculation is independent for every particle and can be efficiently performed in parallel on the GPU.

In the second step of the algorithm, the CPU and the GPU must be synchronized to copy the new amplitude distributions to the GPU and to copy the space charge coefficients from the GPU to the CPU. It must be mentioned that it would be also possible to shift the synchronization of the amplitude values to a later step in the calculation, e.g. after step 3. However, a simultaneous copy of data from CPU to GPU and vice versa is usually faster than a serial copy of the data and, therefore, the shown data copy pattern leads to a slight speed-up.

In step three, the space charge field is calculated from the coefficients ρ. This step involves the solution of Q systems of linear equations, where Q is the number of modes used for the expansion of the space charge field. The Q systems of linear equations are calculated in parallel on the CPU similar to the amplitude calculation in the first calculation step. At the same time, the source terms for every particle and all waveguide modes are calculated on the GPU.

In the final step of the algorithm, CPU and GPU are synchronized again to copy the source terms from the GPU to the CPU memory, before the calculation of the next time step can be started.

4.4 Comparison with Existing Approaches

The developed time-domain model for the simulation of the electron-wave interaction in helically corrugated waveguides is not the first one of its kind. In 2015, Ginzburg et al. presented a time-domain interaction model for helical gyro-TWTs [68]. Nevertheless, there are important differences between the two models which are discussed below.

While in [68] the slowly varying amplitude approximation is utilized for a description of the electric field, this approximation is not applied in the developed interaction code. Although this leads to a slightly improved approximation of the dispersion relation of helically corrugated waveguides in the developed model, it does not lead to significant differences for helical gyro-TWTs as shown in section 4.1.2. The main difference between the models is the different derivation of the high-frequency electric current density $\mathcal{J}$ on the right hand side of (4.18).

In this work, the electron beam is modeled as a beam of macro particles and the equations of motion are solved by a 3D particle pusher. From the particles, the electric current density $\mathcal{J}$ is derived in a PIC like manner as shown in section 4.2.1.

In [68], the electric current density $\mathcal{J}$ is derived from a differential equation for the transverse momentum of the electrons. Two assumptions are made: (1) a subrelativistic transverse electron velocity (relativistic effects are ignored); (2) the variation of the transversal momentum $\bar{p}_\perp$ (see definition in chapter 3.1.2, equation (3.20)) is slow compared to the carrier frequency. Therefore, a slow transversal momentum $\overline{P}_\perp$, similar to the slow amplitudes $\overline{A}$ and $\overline{B}$, can be introduced:

$$\bar{p}_\perp = \overline{P}_\perp \mathrm{e}^{\,j\omega_\mathrm{A} t} \,. \tag{4.58}$$

This allows the derivation of a non-isochronous oscillator equation for the slow transversal momentum $\overline{P}_\perp$ from the equation of motion [68]:

$$\begin{aligned} \frac{2v_{\parallel,0}}{c_0 k_{\perp\mathrm{A}}} \frac{\partial \overline{P}_\perp}{\partial z} + \frac{2}{\omega_\mathrm{A}} \frac{\partial \overline{P}_\perp}{\partial t} + j\overline{P}_\perp \Delta_\mathrm{c} - j \frac{v_{\parallel,0}^2}{2c_0^2} \overline{P}_\perp \left(1 - \frac{|\,\overline{P}_\perp\,|^2}{|\,\overline{P}_{\perp,0}\,|^2}\right) \\ = j \left(\frac{e_0}{m_\mathrm{e} c_0^2}\right)^2 \frac{\overline{A}\overline{P}_\perp^*}{\gamma_0 k_{\perp\mathrm{A}}} \,. \end{aligned} \tag{4.59}$$

Here, the cyclotron resonance detuning

$$\Delta_c = \frac{\omega_A - s\omega_{H,0}}{\omega_A} \tag{4.60}$$

is introduced.

For the description of a large orbit electron beam, (4.59) must be solved for several initial values of $\bar{P}_{\perp,0}$, distributed over the cyclotron rotation phase

$$\bar{P}_{\perp,0} = \mid \bar{p}_{\perp,0} \mid \mathrm{e}^{\,j\Theta_0} \quad \text{with} \quad \Theta_0 \in [0, 2\pi) \; . \tag{4.61}$$

Typically, a number of 16-64 initial phases is required for a sufficient description of an ideal large orbit electron beam[1]. From the slow transversal momentum, the electric current density $\underline{J}$ is calculated by a coupling factor similar to the coupling factor given in (3.23).

Consequently, the simulation of the electron-wave interaction of a perfect large orbit electron beam in a helically corrugated waveguide requires the solution of 32+2 coupled differential equations (32 equations for the transversal momentum and 2 equations for the amplitudes of the coupled modes). If it is assumed that (4.59) is solved on a 1D grid (with an explicit or implicit solver) and if a similar spatial resolution as for the grid used for the solution of the amplitudes is assumed, the number of grid points in a simulation of a typical helical gyro-TWT is in the order of 10 000. Thus, the number of grid points in the model [68] is in a similar order as the required number of macro particles in the developed model with 3D particle beam. Therefore, even without knowing the numerical solution procedure used by Ginzburg et al., for a solution of the equations, it seems reasonable that the required computational effort is comparable in both models.

Besides the comparable computational complexity of both models, the description of the particle beam by a 3D PIC method has a number of advantages compared to the model based on a slow transversal momentum. First of all, relativistic effects are included in the 3D PIC model while they are neglected in the slow momentum method. Such an effect is for example the change of the parallel velocity component $v_{\parallel}$ because of the relativistic mass change.

[1] This number is based on a personal discussion with Prof. Ginzburg

Also the handling of spreads of the kinetic energy, the pitch factor and the guiding center radius, are more natural in the 3D PIC approach. The generation of the corresponding initial particle distributions is simple and the results of common gun simulation tools (e.g. ESRAY, Ariadne, CST) can be directly used. In the slow momentum method, besides an adjustment of the initial beam parameters also the calculation of separate coupling coefficients for every initial beam parameter is necessary which increases the complexity of the implementation. In addition, the number of equations required for a sufficient sampling of the spread distributions would also significantly increase.

A further advantage of the presented 3D PIC model is that it allows the investigation of additional beam parameters which is not possible with the slow momentum method. For instance, the influences of an off-axis beam guiding center, a non-symmetric guiding magnetic field and space-charge effects can be studied.

Last but not least, the solution of the equation of motion for a 3D beam can be easily implemented in a parallel algorithm (important for a GPU acceleration of the program) while this is difficult for (4.59).

In conclusion, the developed simulation model based on a fixed transversal field approach combined with a 3D particle beam provides a more accurate description of the involved physics than the model presented in [68]. Further, it supports the investigation of additional effects as space-charge, a non-symmetric guiding magnetic field and misaligned electron beams.

5 Design of Amplifier and Absorber

In this chapter the developed active components of the passive mode-locked oscillator, namely the amplifier and the saturable absorber, are presented. Both devices will be realized as electron tubes. A helical gyro-TWT was previously identified as optimal candidate for the amplifier (see chapter 3.1). For the saturable absorber, two concepts are suitable: a helical gyro-TWT operated in the Kompfner dip regime and a cyclotron absorber (see chapter 3.2 and chapter 3.3).

Since the development of complete physical designs for the electron tubes would be beyond the scope of this thesis, the investigation is limited to that part which mostly differs from state-of-the-art gyro-TWTs: the beam-wave interaction. Based on the simulation tool presented in the previous chapter, optimized interaction regions are designed and suitable operation points are identified. The required production tolerances for a realization of these interaction regions are discussed at the end of this chapter.

Because the magnetic system is strongly correlated with the beam-wave interaction, a realistic magnetic field profile is used for all simulations in this chapter. The designed magnetic system and its magnetic field profile is shown in Fig. 5.1. The magnetic system consists of a gun coil, the main coil and two auxiliary coils. By tuning the gun coil current, the magnetic system allows the creation of a rectilinear electron beam and a large orbit electron beam in a CUSP-gun as well. The auxiliary coils enable an almost constant magnetic field over the complete interaction region.

In the following, an ideal electron beam without velocity spreads is assumed. A discussion on the influence of a more realistic non-ideal beam is given in the frame of the system design in chapter 6.

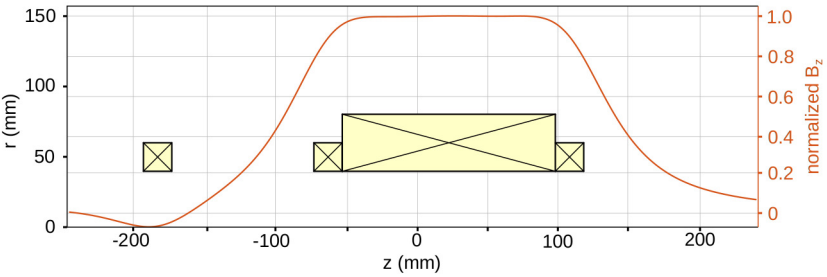

Figure 5.1: Magnetic system for a realistic design of the amplifier and absorber devices.

5.1 Amplifier

A helical gyro-TWT is the chosen amplifier for the sub-THz passive mode-locked oscillator. It has a sufficient bandwidth, is suitable to handle high-power input signals and has a low dispersion. Helical gyro-TWTs can be operated in two alternative operation regimes: the 'synchronized operation regime' and the 'slippage operation regime'. In the synchronized operation regime, the group velocity of the wave is equal to the translation velocity of the electron beam while in the slippage operation regime the wave propagates faster than the electron beam.

In chapter 2.3.1, it was shown that the different operation regimes correspond to slow and fast components in a passive mode-locked laser and that a passive mode-locked oscillator for sub-THz frequencies can be realized with both of them. Because it is not possible to determine a priori which operation regime is more suitable for a passive mode-locked oscillator at 263 GHz, helical gyro-TWTs for both operation regimes are developed.

While in the literature helical gyro-TWTs in the synchronized and slippage regime are realized by different helical interaction regions [68], this approach is unfavorable, at least for a first prototype passive mode-locked oscillator. For first experiments and a comparison with theoretical predictions, it would be a great adventure if the helical gyro-TWT can be operated in both, the synchronized and the slippage regime. This can be realized, if the operation regime is determined by the electron beam rather than the geometry of the

interaction region. Since a CUSP-gun allows an adjustment of the beam parameters over a wide range, this is a promising approach which is used in the following.

5.1.1 Helical Interaction Region

To allow a resonant interaction of the gyrating electrons and the wave, the cyclotron resonance condition (3.17) must be fulfilled. In a dispersion diagram this corresponds to sections where the wave's dispersion curve and the beam line intersect. Therefore, a dispersion diagram is an efficient tool for the design of a helically corrugated interaction space.

In a first step of the synthesis procedure, the mean waveguide radius R is chosen. For reasons of manufacturability and breakdown resistance, R should be as large as possible. However, to prevent a parasitic excitation of the upper eigenmode, the operation frequency band must be below its cutoff frequency which defines an upper limit for R. Since the helical gyro-TWT should provide a bandwidth of at least $\pm 10\,\mathrm{GHz}$ around the center frequency of $263\,\mathrm{GHz}$, the mean waveguide radius is set to $R = 0.528\,\mathrm{mm}$ which gives an upper limit for the operation frequency of $276\,\mathrm{GHz}$.

The values of the corrugation amplitude $\tilde{r}$ and period $\tilde{d}$ are obtained by a fit of the waveguide dispersion to the beam line. Care should be taken to keep the corrugation amplitude $\tilde{r}$ small. This has two reasons: (1) the perturbation theory approach would become invalid for a corrugation amplitude exceeding $\lambda/10$; (2) a large $\tilde{r}$ increases the diffraction from the main operating eigenmode to a parasitic backward wave.

The beam parameters for an operation in the synchronized operation regime are estimated with $\alpha = 0.8$ and $E_{\mathrm{kin}} = 40\,\mathrm{keV}$. These beam parameters are in the range of beams that can be created by a typical CUSP-gun. By a fit to the beam parameters, the parameters for the helically corrugated interaction region are determined as $R = 0.528\,\mathrm{mm}$, $\tilde{r} = 0.08\,\mathrm{mm}$ and $\tilde{d} = 1.11\,\mathrm{mm}$.

In a final step of the synthesis process, beam parameters for an operation of the helical gyro-TWT in the slippage regime are searched. Realistic beam parameters are found to be $\alpha = 1.3$ and $E_{\mathrm{kin}} = 30\,\mathrm{keV}$.

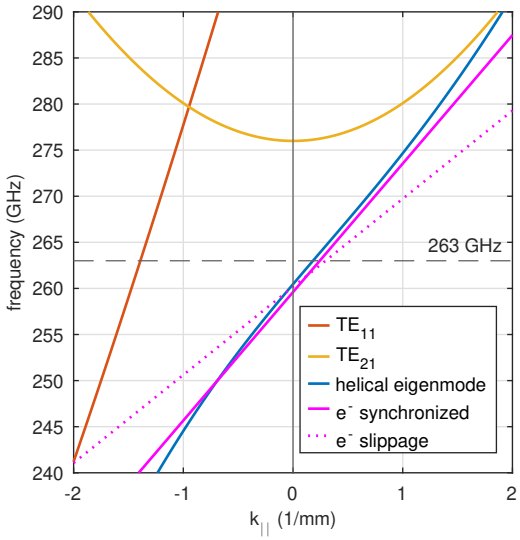

Figure 5.2: The dispersion curve of a helical gyro-TWT with $R = 0.528\,\mathrm{mm}$, $\tilde{r} = 0.08\,\mathrm{mm}$ and $\tilde{d} = 1.11\,\mathrm{mm}$. The beam lines for an operation in the synchronized (solid purple) and the slippage regime (doted purple) are shown.

In Fig. 5.2, the dispersion curves of the designed helically corrugated waveguide and the corresponding $\mathrm{TE}_{1,1}$ and $\mathrm{TE}_{2,1}$ modes of the unperturbed waveguide are shown together with the beam lines for an operation in the synchronized and the slippage regime.

5.1.2 Power Capability

In the passive mode-locked oscillator a high-power pulse oscillates. The power level of this oscillating pulse is important for the design of the amplifier and absorber devices. In the previous investigations performed by Ginzburg et al. [52], [55], [57], [59], [142], passive mode-locked oscillators are only investigated at lower frequencies up to the Ka-band. At these frequencies, the power of the oscillating pulse is mainly limited by the saturation power of the amplifier. In the synchronized operation regime the saturation of the output

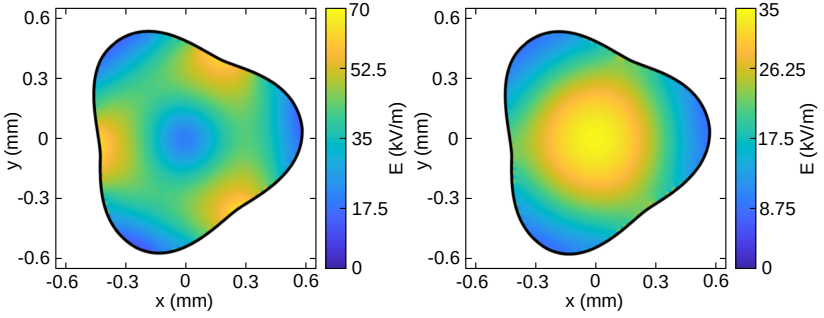

Figure 5.3: Transverse electric field in the helically corrugated interaction region for an input signal of 1 W. (a) eigenmode ($\mathrm{TE}_{1,1}$ + $\mathrm{TE}_{-2,1}$); (b) $\mathrm{TE}_{-1,1}$ mode .

power is associated with the trapping of electrons by the electromagnetic wave [68] which usually occurs at powers above 100 kW. In the slippage operation regime, the saturation power even exceeds this level significantly [68] and is limited by the quality of the electron beam (amplification of noise in the electron beam). However, for sub-THz helical gyro-TWTs, the maximum output power is limited by the ohmic loading of the interaction region.

Since the dimensions of the helically corrugated interaction region are in the order of the wavelength, the ohmic loading at sub-THz frequencies is significantly increased compared to Ka-band devices which results in a strong heating of that region. Especially for the eigenmode interacting with the electron beam, the ohmic loading in helically corrugated interaction regions is high because of the specific field distribution of the eigenmode. In Fig. 5.3a, the electric field for a 1 W signal at 263 GHz is shown for the designed helically corrugated waveguide. The highest values of the electric field appear at the waveguide wall which results in a high ohmic loading.

In [143], alternative cooling concepts are investigated by thermomechanical simulations and it is shown that an angular gap cooling is most suitable for sub-THz helical gyro-TWTs. It is shown that such a cooling is capable to keep a helical gyro-TWT with an average CW ohmic loading of 150 W/cm^2 below 100 °C.

The ohmic loading in the interaction region can be calculated with the developed tool KarLESSS (see chapter 7). For the calculation of the ohmic loading it is important to take into account the input signal. Therefore, a superposition of the input signal and the output signal (Fig. 5.3a and Fig. 5.3b) must be used for the calculation of the ohmic loading. For the designed helically corrugated interaction region (made of copper), the average ohmic loading for a 1 W input and an output signal of similar power is calculated as $0.5\,\mathrm{W/cm^2}$.

Since the passive mode-locked oscillator is a pulsed source, the equivalent CW average ohmic loading V_{ohm} can be calculated from the power P, the pulse length τ_{p} and the pulse repetition frequency f_{r}:

$$V_{\mathrm{ohm}} = V_{\mathrm{ohm,1W,CW}} \frac{P}{1\,\mathrm{W}} \tau_{\mathrm{p}} f_{\mathrm{r}} \,. \tag{5.1}$$

For the final passive mode-locked oscillator the pulse length should be in the order of 0.1 ns and the pulse repetition frequency will be several hundred MHz. Based on this, a peak power of 5 kW and a pulse repetition frequency of 600 MHz can be specified as an upper limit for the following design process of the amplifier and the absorber devices.

A second open question, also correlated with the maximal output power of the helical gyro-TWT, is the maximal possible current of the electron beam. To estimate a realistic beam current, existing helical gyro-TWTs can be used as a reference.

The maximum current of an electron emitter is limited by the allowed current surface density, and therefore, depends on the surface of the emitter. The quality of the electron beam in turn depends on the geometry of the electron emitter ring (see chapter 3.1.4). A thinner width and a smaller radius of the emitter ring are increasing the beam quality. A ring width of 0.5 mm as used in actual W-band CUSP-guns [144] is practically the minimum and should not be further reduced. However, the emitter radius can be scaled to estimate an upper limit for the current. This results in a linear dependency of the maximal beam current from the operation frequency. By a scaling from the W-band helical gyro-TWT [42], which is operated with a 1.5 A beam, an upper limit for the beam current of 0.5 A can be be estimated for a 263 GHz helical gyro-TWT. To allow an adjustment of the beam current for a fine tuning of the final

passive mode-locked oscillator, the default working point of all devices that are investigated in the following, is set in the range of $0.2\,\mathrm{A}$ to $0.4\,\mathrm{A}$.

5.1.3 Synchronized Operation Regime

In the synchronized operation regime, the group velocity of the electromagnetic wave is matched to the axial propagation velocity of the electrons. This allows a beam-wave interaction over a broad bandwidth. For the designed helically corrugated waveguide, the synchronized operation regime is fulfilled for an electron beam with $\alpha = 0.8$ and $E_{\mathrm{kin}} = 40\,\mathrm{keV}$. While the parameters of the corrugated waveguide and the beam are already fixed, the optimal length L of the interaction region and the magnetic field strength $\mathfrak{B}_0$ are still unknown. In the following, the latter one is investigated.

A possible method to find the optimum magnetic field strength $\mathfrak{B}_0$ is to perform interaction simulation with different $\mathfrak{B}_0$ values. For these simulations, the length of the interaction region is set to $L = 20\tilde{d}$ and the beam current is set to $I = 0.2\,\mathrm{A}$. To investigate the frequency dependence of the beam-wave interaction for a given $\mathfrak{B}_0$, the interaction simulations are performed with input signals at different frequencies.

In Fig. 5.4, the results of the performed parameter sweeps are shown. It can be seen that a magnetic field strength of $\mathfrak{B}_0 = 5\,\mathrm{T}$ leads to the highest amplifications. As expected, the synchronized operation regime enables the beam-wave interaction over a broad bandwidth and a $3\,\mathrm{dB}$ bandwidth of almost $20\,\mathrm{GHz}$ around a center frequency of $263\,\mathrm{GHz}$ can be reached.

The shown results give the impression that even for frequencies significantly above $273\,\mathrm{GHz}$ an efficient amplification would be possible. However, this is not the case because parasitic modes could be excited at higher frequencies (>$276\,\mathrm{GHz}$). To simplify the simulation, these parasitic excitations are neglected and, consequently, all investigation in the following must be limited to frequencies below $276\,\mathrm{GHz}$.

It is important to note that for magnetic field strengths above $5.025\,\mathrm{T}$ an absorption regime is reached where the electron beam absorbs energy from the electromagnetic wave. This indicates that the designed corrugated waveguide

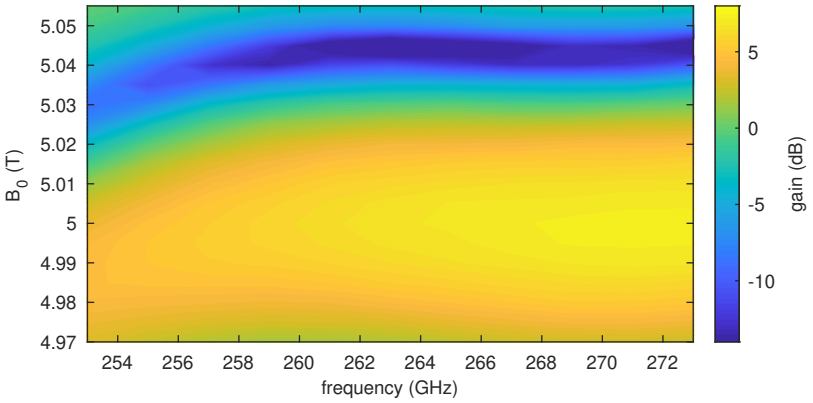

Figure 5.4: Output power of the helical gyro-TWT operated in the synchronized regime with different magnetic field strengths and for different frequencies of the input signal. A 5 W CW signal is used as input.

in combination with an electron beam in the synchronized regime can also be operated as a helical gyro-TWT absorber (see section 5.2.1).

5.1.4 Slippage Operation Regime

In the slippage operation regime, the electromagnetic wave propagates faster than the electron beam and can therefore slip along the beam and interact with, and gain energy from, more electrons than in the synchronized operation regime. As it can be seen in the dispersion diagram Fig. 5.2, the slippage regime can be realized for the designed corrugated waveguide with an electron beam of $\alpha = 1.3$ and $E_{\mathrm{kin}} = 30\,\mathrm{keV}$.

The optimum magnetic field strength $\mathfrak{B}_0$ and the frequency dependence of the electron-wave interaction for an operation in the slippage regime is determined in a similar manner as for the synchronized operation regime. Simulations are performed for different $\mathfrak{B}_0$ values and frequencies of the input signal. The length of the interaction region is kept constant at $30\tilde{d}$ and the beam current is set to $I = 0.2\,\mathrm{A}$.

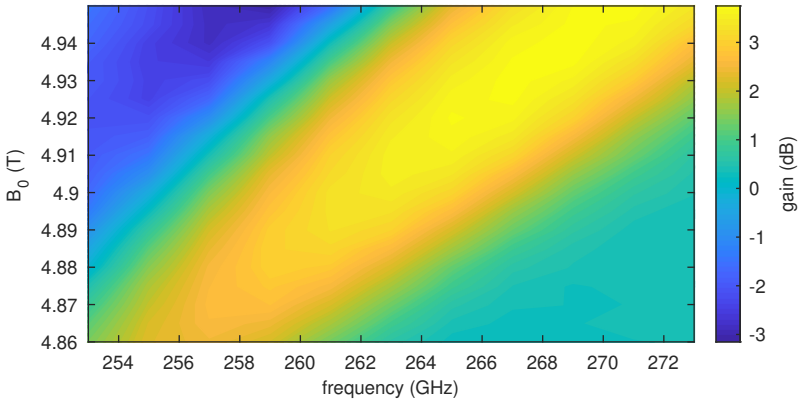

Figure 5.5: Output power of the helical gyro-TWT operated in the slippage regime with different magnetic field strengths and for different frequencies of the input signal. A 5 W CW signal is used as input.

In Fig. 5.5, the results of the performed parameter sweeps are shown. As expected from the dispersion diagram, the 3 dB bandwidth of the beam-wave interaction is significantly decreased compared to the synchronized operation regime (10 GHz compared to 20 GHz). The optimum magnetic field strength for signals with a frequency of 263 GHz is $\mathfrak{B}_0 = 4.91$ T.

It must be noted that the absolute values of the power gain cannot be directly compared with the synchronized operation since the power of the electrons contained in the transversal movement differs for both operation regimes. In addition, interaction regions with different lengths are used for the simulations.

5.1.5 Length of the Interaction Region

Helical gyro-TWTs are typically used for applications where a high small-signal gain is required, e.g. high-power radar systems. However, in chapter 2 it was shown that high small-signal gains are obstructive for passive mode-locked oscillators. On the other hand, it was shown that the saturated power a signal gains during a single round trip (saturated power gain) in the oscillator determines the maximal output power of the passive mode-locked oscillator

and should be therefore sufficiently high. Furthermore, the gain should be independent from the power of the input signal. For a simultaneous realization of a low small-signal gain, a low dependence of the gain on the signal power and a high saturation power gain, the length of the interaction region must be carefully chosen.

In Fig. 5.6, the dependence of the gain on the length of the tube is illustrated. The gain of two alternative tubes with different length of the interaction region is shown for the synchronized and the slippage operation regime, respectively. For a better comparability, the synchronized operation regime is simulated with an electron beam of $I = 0.25\,\mathrm{A}$ while for the slippage regime an electron beam with $I = 0.2\,\mathrm{A}$ is used. Therefore, the power contained in the transverse momentum of the electron beam

$$P_{\mathrm{beam},\perp} = U_\mathrm{b}\, I \frac{v^2}{v_\parallel^2 + v_\perp^2} = \frac{U_\mathrm{b}\, I}{1 + \frac{1}{\alpha^2}}\,, \tag{5.2}$$

is approximately equal for both operation regimes ($P_{\mathrm{beam},\perp} \approx 3.8\,\mathrm{kW}$).

It can be seen that the variation of the gain with the power of the input signal is significantly stronger for the long interaction region than for the short interaction region. For the slippage operation regime, a shorter interaction region does balance the power dependency but also reduces the overall gain of the helical gyro-TWT. In the synchronized regime, the gain for lower powers strongly reduces. However, for a high input power, the gain can even exceed the gain of the helical gyro-TWT with long interaction region. The reason is that an over-bunching occurs for high power. The electron beam reabsorbs energy from the wave (see chapter 3.1.2).

For a future prototype of a passive mode-locked oscillator it would be advantageous, if the helical gyro-TWT could be operated in the slippage operation regime as well as in the synchronized operation regime. Therefore, both operation regimes were realized by different electron beams rather than different helically corrugated waveguides. Continuing this approach, the same length of the interaction region must be chosen for both operation regimes as well.

Based on a detailed analysis, an interaction region with a length of $L = 24\tilde{d}$ is used in the following for the helical gyro-TWT. It must be mentioned that this is an atypically short interaction region for helical gyro-TWTs. In typical

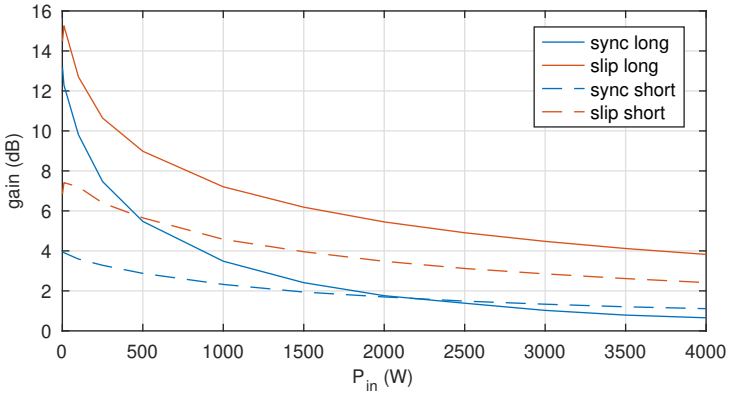

Figure 5.6: Power dependence of the gain for a pulse of length $\tau_\mathrm{p} = 0.1$ ns for helical gyro-TWTs of different length (long = $40\tilde{d}$, short = $24\tilde{d}$), operated in the synchronized and the slippage operation regime, respectively.

application for electron tubes, such as radar applications, usually a high small-signal gain is favored and, thus, long interaction regions are required.

5.1.6 Amplification of Ultra-Short Pulses

Besides the low small-signal gain, a further difference to classical applications of helical gyro-TWTs are the significantly shorter pulses. In a passive mode-locked oscillator ultra-short, pulses with sub-nanosecond pulse lengths must be amplified. To analyze the performance of the designed tube and the behavior of the ultra-short pulses in the helical gyro-TWT, simulation results for the helical gyro-TWT in both operation regimes and with input pulses of various pulse length and power are discussed in the following.

Gain and Maximal Power

In Fig. 5.7 and Fig. 5.8, the output power and gain for pulses of different length τ_p and different input power P_in are shown for the helical gyro-TWT in the synchronized and slippage operation regime, respectively. In the synchronized op-

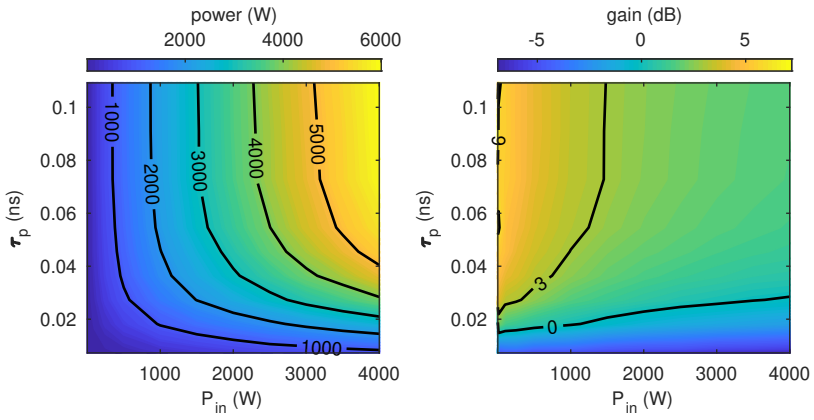

(a) (b)

Figure 5.7: Output power and gain for pulses of different length τ_p and different input powers. The center frequency of the pulses is 263 GHz. The helical gyro-TWT is operated in the synchronized regime.

eration regime, an electron beam with $I = 0.4$ A, $E_\mathrm{kin} = 40$ keV and $\alpha = 0.8$ is used. For an operation in the slippage regime, an electron beam with $I = 0.2$ A, $E_\mathrm{kin} = 30$ keV and $\alpha = 1.3$ is used. The higher current for the synchronized operation regime is chosen to compensate the overall lower gain compared to the slippage regime (see Fig. 5.6). As a consequence, the transversal beam power in the synchronized operation regime is significantly higher ($P_\mathrm{beam,\perp} \approx 6250$ W) than in the slippage operation regime ($P_\mathrm{beam,\perp} \approx 3800$ W).

As shown in Fig. 5.7, the small-signal gain is up to 10 dB for the synchronized operation regime. However, for input pulses of higher power, the gain decreases. The minimal pulse length that can be amplified in the amplifier is given by the 0 dB line in Fig. 5.7b. The limit for the pulse length is 0.02 ns for low power signals and linearly increases with the pulse power up to 0.03 ns. Above this limit, the absolute power a pulse gains increases with the input power. Considering the previously derived power limit of 5000 W (5000 W line in Fig. 5.7a), the maximal power that a pulse can gain is 1900 W for an input power of 3100 W and a pulse length of > 0.07 ns. As a consequence, the theoretical maximal power that can be extracted from a passive mode-locked oscillator with this amplifier is 1900 W. For the highest efficiency, the pulses

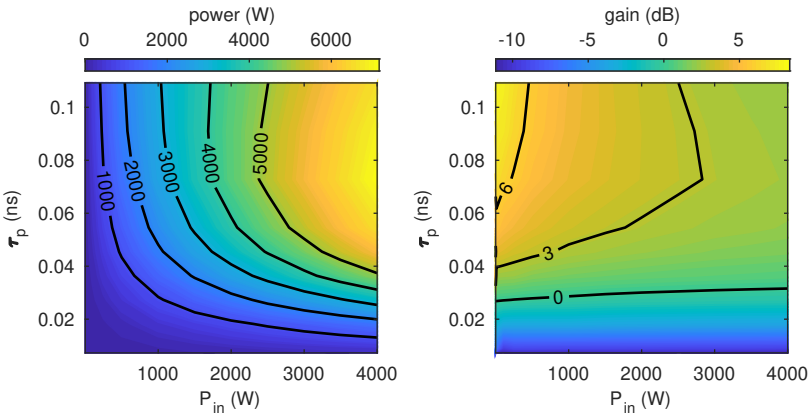

(a) (b)

Figure 5.8: Output power and gain for pulses of different length τ_p and different input powers. The center frequency of the pulses is 263 GHz. The helical gyro-TWT is operated in the slippage regime.

in the passive mode-locked oscillator should not be shorter than 0.07 ns. It should be noted that the 1900 W are significantly below the transversal beam power of 6250 W.

In Fig. 5.8, the output power and gain of the helical gyro-TWT operated in the slippage regime is shown. Even the beam power is significantly below the synchronized operation point, the obtainable output power and gain in the slippage regime are higher. The limit for the minimal pulse length is in a similar range as for the synchronized regime, around 0.03 ns. Pulses with a power of 2400 W and a length of 0.075 ns gain a maximal power of 2600 W. In order to remain under the power limit of 5000 W, no pulses with a peak power of more than 2400 W should be fed into the amplifier. For a passive mode-locked oscillator using this helical gyro-TWT in the slippage regime, output pulses with a length of 0.075 ns are expected. The theoretical maximal power that can be extracted from such an oscillator is 2600 W.

Pulse Shape and Spectrum

In addition to the gain, the evolution of the pulse shapes in the amplifier is of particular importance for the performance of the passive mode-locked oscillator. For an investigation of this, the pulse shapes and corresponding spectra before and after the amplification are shown in Fig. 5.9 and Fig. 5.10. As input, a pulse with a $\sin^2$ shape is used. The evolution of a longer and a shorter 1000 W pulse are evaluated (0.1 ns and 0.05 ns) for an operation in the synchronzed and slippage regime, respectively.

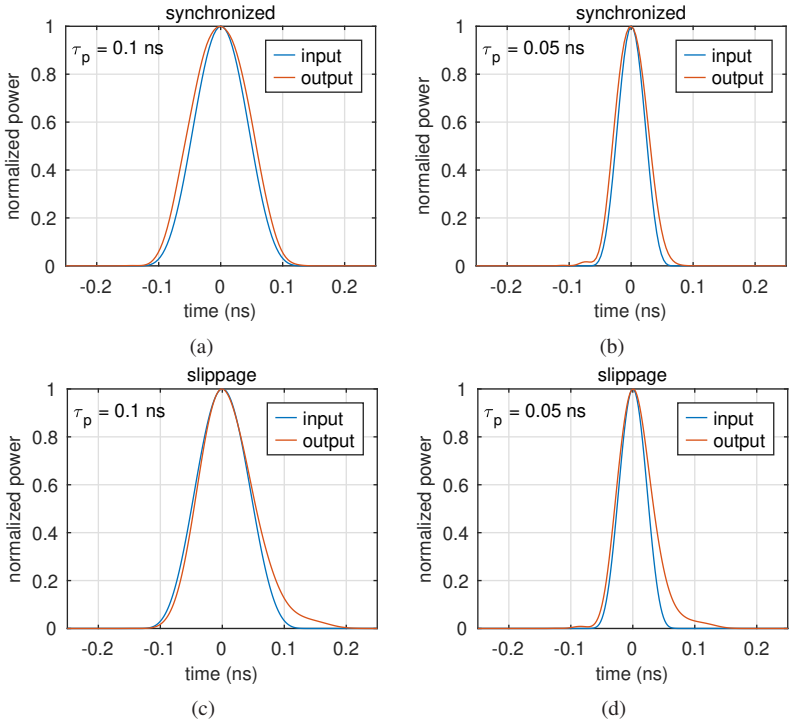

Figure 5.9: The shapes of pulses before and after the amplification in the synchronized helical gyro-TWT (a+b) and the slippage helical gyro-TWT (c+d) for different pulse lengths (τ_p = 0.1 ns and τ_p = 0.05 ns).

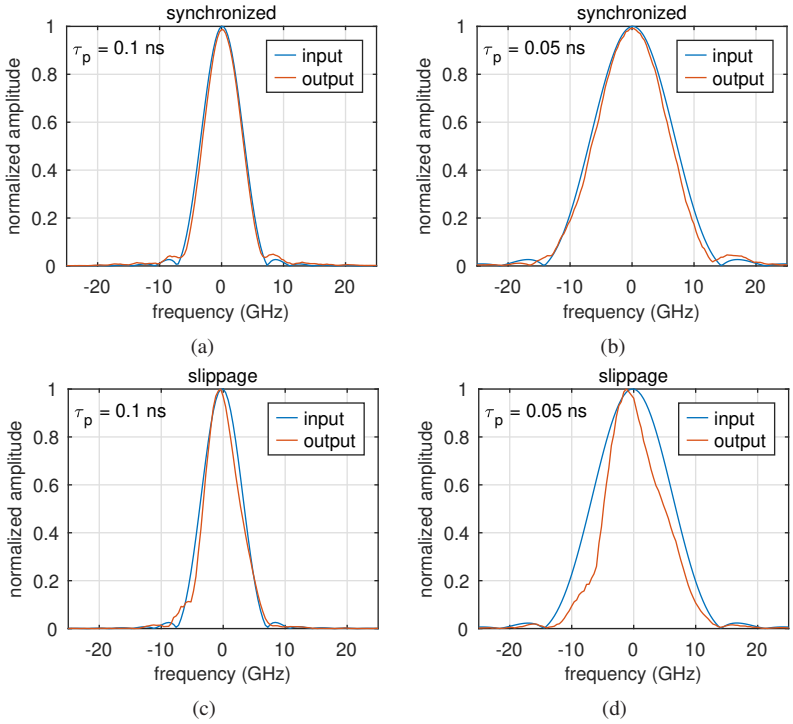

Figure 5.10: The spectra of pulses before and after the amplification in the synchronized helical gyro-TWT (a+b) and the slippage helical gyro-TWT (c+d) for different pulse lengths ($\tau_p = 0.1$ ns and $\tau_p = 0.05$ ns).

In Fig. 5.9a and Fig. 5.9b, it can be seen that an amplification in the synchronized operation regime clearly leads to a broadening of the pulses. For both pulse lengths, the broadening is $\approx 18\,\%$. Also in the spectra this broadening can be observed by a slightly decreased bandwidth (Fig. 5.10a and Fig. 5.10b). For the 0.1 ns pulse, the pulse shape remains unchanged which can be seen in the time domain as well as the frequency domain. The spectra with the side lobes are typical for the $\sin^2$ pulse shape which is used as input signal. For the 0.05 ns pulse, a slight change of the pulse shape at the leading edge is observed. In the spectra, this change results in a suppression of the side lobe at lower frequencies.

The helical gyro-TWT operated in the slippage regime has a different behavior. The shape of the amplified pulses is slightly unsymmetrical. The leading edge becomes steeper and the pulses have a low power tail. Both effects are in a good agreement with [68], where the slippage operation regime was proposed for the amplification of ultra-short pulses for the first time. For the 0.1 ns pulse, the pulse length is almost unchanged. However, the 0.05 ns pulse is broaden by roughly the same amount as in the synchronized operation regime ($\approx 18\,\%$).

A reason for the broadening of the 0.05 ns pulse can be found by a comparison of the corresponding spectra with the bandwidth of the amplifier in the slippage regime (see Fig. 5.5). It is found that the spectrum of the 0.05 ns pulse exceeds the bandwidth of the amplifier while the spectrum of the 0.1 ns pulse is completely covered by the bandwidth. As a result, not all frequency components of the shorter pulse are involved in the beam-wave interaction which leads to the deformed spectra and a broadening of the pulse.

5.2 Saturable Absorber

Two concepts of a saturable absorber at sub-THz frequencies are identified previously: a helical gyro-TWT operated in the Kompfner dip regime and a cyclotron absorber (see chapter 3.2 and chapter 3.3).

Both concepts have individual advantages and disadvantages. A helical gyro-TWT absorber operates at the second cyclotron harmonic which reduces the required magnetic field strength for 263 GHz from 10 T to 5 T. On the other hand, in [59] it was mentioned that a helical gyro-TWT absorber could lead to an undesirable amplification of some frequency components for ultra-short pulses with broad spectra. This could eventually lead to a parasitic self-excitation of the oscillator. A cyclotron absorber is more stable against the excitation of parasitic self-excitations. However, the high magnetic field strengths and the increased dispersion compared to a helical gyro-TWT are disadvantageous.

Because neither of the two technologies can be favored a priori, in the following basic designs for both absorber types are discussed.

5.2.1 Helical Gyro-TWT Absorber

In the previous section it was found that the designed helical gyro-TWT operated in the synchronized regime can also be used as an absorber if the magnetic field strength is carefully chosen. From Fig. 5.4, it can be seen that for a magnetic field strength of $\mathfrak{B}_0 = 5.045\,\mathrm{T}$ and an electron beam with $E_{\mathrm{kin}} = 40\,\mathrm{keV}$ and $\alpha = 0.8$, input signals are absorbed over a broad frequency band of 16 GHz.

As shown in chapter 3.2, the length of the interaction region is particularly important for a proper saturation effect. To find the optimal length of the interaction region, the transmission coefficient for different interaction region lengths L and input signal powers P_{in} are simulated and plotted in Fig. 5.11. For the simulations, a CW input signal at 263 GHz is used. It is found that a good absorption of low-power signals and a good saturation of the absorption for high power-signals can be achieved at a length of $L = 30\,\mathrm{mm} \approx 27\tilde{d}$.

For the shown simulations, an electron beam with a current of $I = 0.2\,\mathrm{A}$ is used. It is important to note that the optimum length L of the absorber depends on the beam current and decreases for an increasing current.

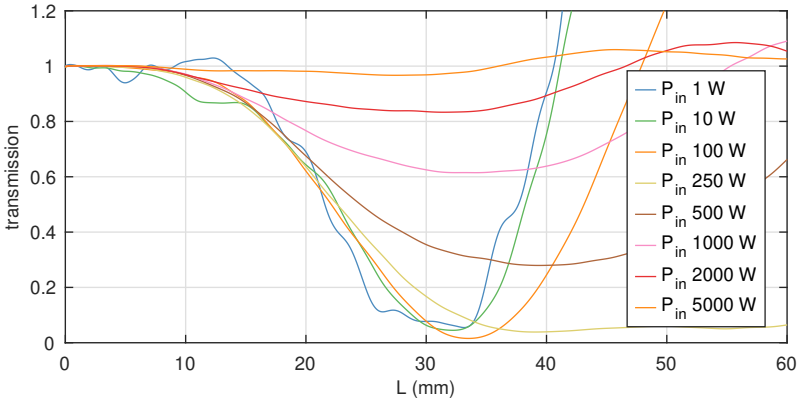

Figure 5.11: Transmission coefficient of a helical gyro-TWT operated as saturable absorber along the helical interaction region for different input signals at 263 GHz.

Another important observation is that the attenuation of input signals with very low powers $P_{\mathrm{in}} < 10\,\mathrm{W}$ decreases and signals with a power below $0.25\,\mathrm{W}$ are almost not attenuated anymore. However, the performed system analysis of the complete passive mode-locked oscillator in chapter 6 shows that this is unproblematic for the stability of the oscillator.

To determine the frequency dependence of the absorption and saturation effects, the saturation curves for input signals at different frequencies are shown in Fig. 5.12. It can be seen that the transmission coefficient ($P_{\mathrm{out}}/P_{\mathrm{in}}$) has only a low frequency dependence around the designed center frequency (263 ± 5 GHz). For frequencies below 256 GHz, the attenuation of low powers decreases while the attenuation of high power signals increases. For higher frequencies, the attenuation of low powers keeps similar but for high powers, even a small amplification of the input signals occurs.

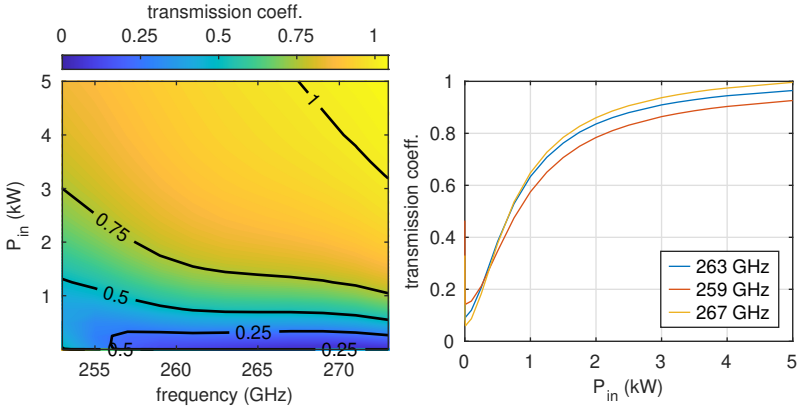

(a) (b)

Figure 5.12: Power and frequency dependence of the transmission coefficient for the helical gyro-TWT operated as saturable absorber.

5.2.2 Cyclotron Absorber

In a cyclotron absorber, the electromagnetic wave is absorbed from a rectilinear electron beam in a cylindrical interaction region (see chapter 3.2 for details). The dispersion of the electromagnetic wave in this cylindrical interaction region has a parabolic shape. To allow the propagation of ultra-short pulses and to allow the beam-wave interaction over a broad frequency band, the cut-off frequency of the interaction region must be far below the operation frequency. This strongly limits the maximal possible radius of the waveguide.

With a dispersion diagram, suitable parameter for the interaction region and the electron beam are found. In Fig. 5.13, the dispersion of n interaction region for a 263 GHz cyclotron absorber and the beam line of a well-suited rectilinear electron beam are shown. The radius of the waveguide is $0.36\,\mathrm{mm}$ and the kinetic energy of the electrons is $E_{\mathrm{kin}} = 40\,\mathrm{keV}$. The electron beam is guided from a magnetic field with $\mathfrak{B}_0 = 8.72\,\mathrm{T}$. As the electron beam is rectilinear, the pitch factor is $\alpha = 0$.

Power Capability

Similar to the helical gyro-TWT, the power capability of a cyclotron absorber is limited by the ohmic wall loading in the interaction region. In contrast to the eigenmode of a helically corrugated waveguide, the electromagnetic field at the waveguide wall is lower for the $\mathrm{TE}_{1,1}$ mode in a cylindrical waveguide. However, the waveguide radius is reduced compared to the helical waveguide which increases the ohmic wall loading.

For the cylindrical interaction region (made of copper), the ohmic loading for the superposition of a $1\,\mathrm{W}$ input signal and an output signal of similar power is $1.2\,\mathrm{W/cm^2}$. This value is more than twice the ohmic wall loading of the previous discussed helically corrugated waveguide. As a consequence of equation (5.1), this increased ohmic wall loading leads to reduced limits for the peak power or the pulse repetition frequency. If the limit of the peak power is set to $5\,\mathrm{kW}$ as for the helically corrugated waveguide, the allowed pulse repetition rate reduces to $250\,\mathrm{MHz}$.

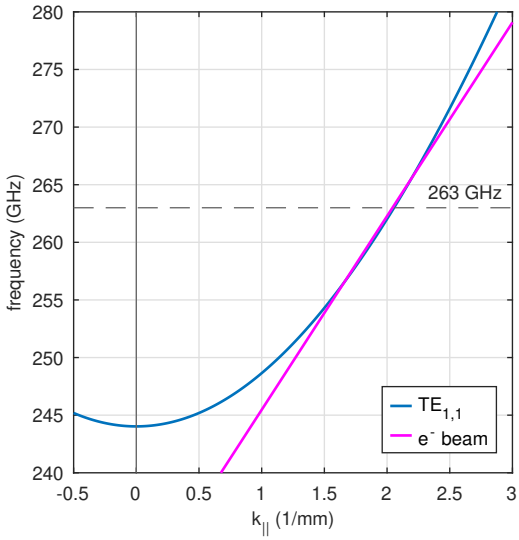

Figure 5.13: Dispersion curve and beam line for the interaction region of a 263 GHz cyclotron absorber.

Nonlinear Saturation

As shown in chapter 3.2, the nonlinear saturation effect is maximum for a certain length of the interaction region. This length can be determined by interaction simulations. The results of these simulations are shown in Fig. 5.14, where the transmission coefficients are plotted along the interaction region for CW input signals of different power.

For an operation with an upper limit of 5 kW for the input power, the optimum length is found to be 25 mm. At this length, a high-power signal of 5 kW is not attenuated while low power signals (< 10 W) are almost completely attenuated. It should be noted that the helical gyro-TWT absorber cannot attenuate low-power signals (< 1 W) while the cyclotron absorber attenuates these signals very efficiently.

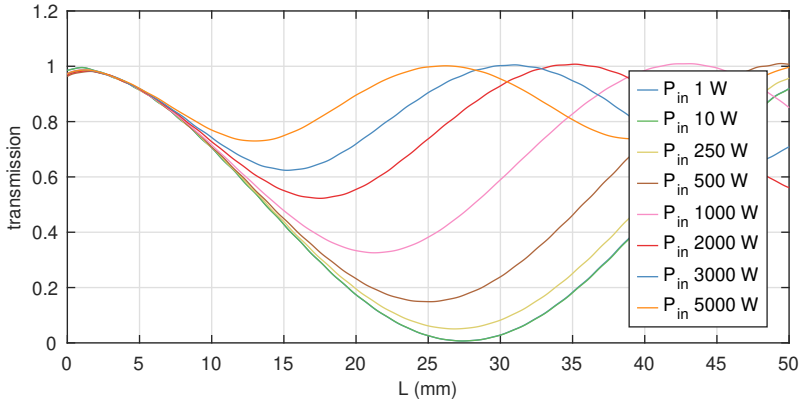

Figure 5.14: Transmission coefficient of a cyclotron absorber along the cylindrical interaction region for different input signals at 263 GHz.

For the shown simulation, an electron beam current of $I = 0.17\,\mathrm{A}$ is used. Similar to the helical gyro-TWT absorber, the optimum length of the absorber changes with the current. Only for specific currents, the points of maximal transmission of high-power signals and the point of maximum absorption for low-power signals coincide at the same length. As a consequence, the beam current can be only varied in a small range around the designed value if a good nonlinear saturation effect should be preserved.

To investigate the frequency dependence of the nonlinear absorption effect for the proposed cyclotron absorber ($R = 0.36\,\mathrm{mm}$ $L = 25\,\mathrm{mm}$, $E_{\mathrm{kin}} = 40\,\mathrm{keV}$, $\alpha = 0$ and $\mathfrak{B}_0 = 8.72\,\mathrm{T}$), interaction simulations are performed for input signals of different power and frequency. The results are shown in Fig. 5.15a. For a better comparability, in Fig. 5.15b the nonlinear transmission curves for 259 GHz, 263 GHz and 267 GHz are given. The results prove that the saturable absorption effect takes place over a broad frequency band. A comparison with the dispersion diagram in Fig. 5.13 shows an excellent agreement of the bandwidth observed by interaction simulations and the bandwidth expected from the dispersion diagram. In a band of 10 GHz around the center frequency of 263 GHz the transmission curve has only a negligible frequency dependency and the cyclotron absorber should be well suited for the shortening of ultra-short pulses.

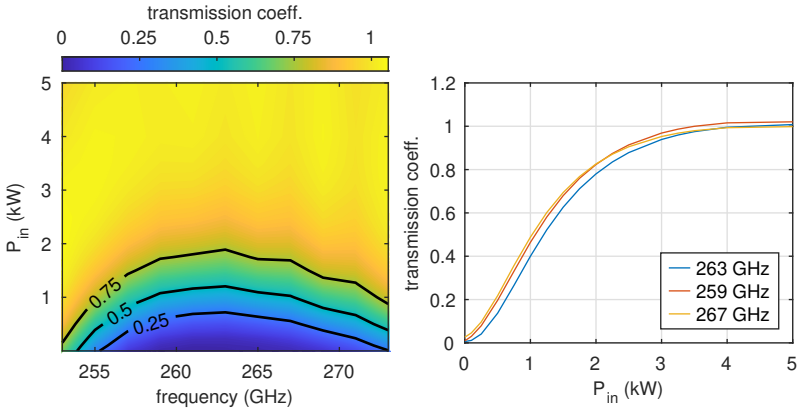

(a) (b)

Figure 5.15: Power and frequency dependence of the transmission coefficient for the cyclotron absorber.

A comparison with the helical gyro-TWT absorber shows a slightly better performance of the cyclotron absorber for lower frequencies while the helical gyro-TWT absorber performs better for higher frequencies. In both absorber devices, a good non-linear saturation of the absorption with the power is observed.

Interaction Region with Up-Taper

In devices with helically corrugated interaction region, the beam-wave interaction abruptly stops at the end of the interaction region where the helical waveguide turns into a circular one (by a tapering of the corrugation amplitude down to zero). In the circular interaction region of a cyclotron absorber, the electron-wave interaction takes place at the fundamental cyclotron harmonic with the $\mathrm{TE}_{1,1}$ mode. Consequently, an abrupt termination of the beam-wave interaction is difficult. However, an efficient cyclotron absorber is still possible. To demonstrate that, a more complete interaction region including an up-taper is designed as part of this work.

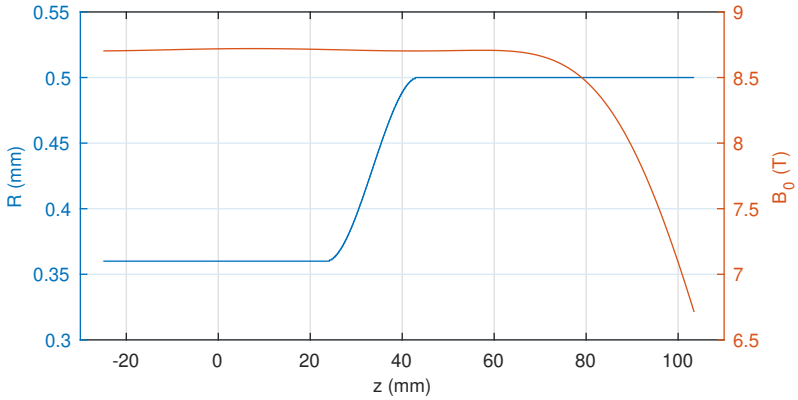

Figure 5.16: Geometry of the cylindrical interaction region and magnetic field strength at the z-axis for a realistic cyclotron absorber.

The best way to terminate the beam-wave interaction is an up-tapering of the waveguide radius. In Fig. 5.16, the interaction region including an up-taper is shown together with the magnetic field profile. The taper is designed in order to abruptly terminate the beam-wave interaction and to minimize the reflection at the same time. Mode conversion is not a problem for the shown up-taper because the maximum waveguide radius of $0.5\,\mathrm{mm}$ ensures that all higher-order modes are still below cut-off at the desired frequencies.

In Fig. 5.17, the nonlinear transmission curves for the ideal cylindrical and the realistic interaction region are compared. It can be seen that for both interaction regions similar transmission curves are observed. The interaction region with up-taper has a slightly higher absorption for low power signals and saturates slightly faster. A comparison of Fig. 5.17 and Fig. 5.15 reveals that the variations of the transmission curves caused by a change of the frequency exceed the variations caused by the new geometry. It can be concluded that the interaction region with up-taper still offers the required nonlinear absorption.

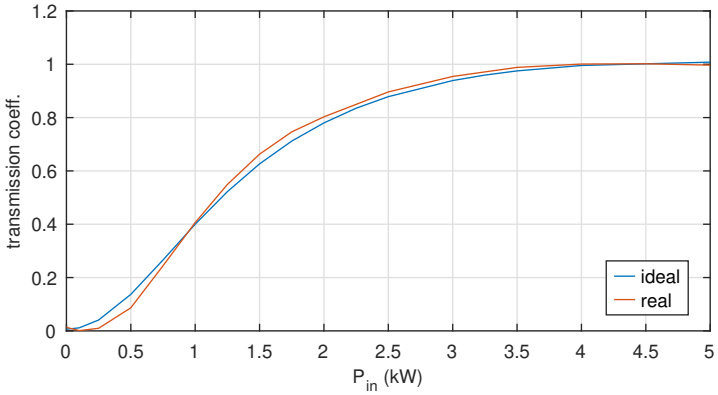

Figure 5.17: Comparison of the transmission curves of the ideal and realistic cyclotron absorber setups.

5.2.3 Ultra-Short Pulses in a Saturable Absorber

In the previous sections, CW input signals were used for an evaluation of the staturable absorbers. However, in a passive mode-locked oscillator the input signals are ultra-short pulses which are further shorten by the saturated absorption. For an evaluation of the behavior of ultra-short pulses in the designed absorber devices, simulations with input pulses of various pulse length and power are performed. Selected results are shown in the following.

Helical Gyro-TWT Absorber

It is expected that the shortening effect for a pulse is correlated with the peak power and length of the pulse. For a study of this correlation, the relative shortening that a pulse undergoes is simulated for input pulses with different pulse lengths and peak powers.

In Fig. 5.18, the results for the helical gyro-TWT absorber are plotted. As it is expected from the transmission curve Fig. 5.12b, the shortening effect is maximum for a power at which the change in the transmission curve is maximal (0.5-1 kW). For higher power, the absorber is operated closer to the saturation

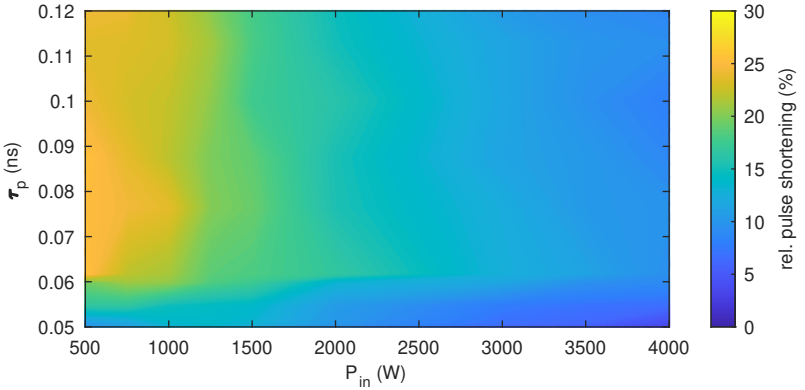

Figure 5.18: Relative shortening of the pulse length τ_p in a helical gyro-TWT absorber for input pulses of different power and pulse length.

limit and the shortening effect decreases. This appears because for a high-power pulse only small parts at the pulse slopes experience a high attenuation while the major part of the pulse is not attenuated.

From Fig. 5.18, it becomes clear that for pulse lengths above a specific limit the relative shortening is almost independent from the pulse length. However, if the pulse length becomes less than $0.06\,\mathrm{ns}$, the shortening effect drastically decreases. This is due to the limited bandwidth of the helical gyro-TWT absorber. If the bandwidth of a pulse exceeds the bandwidth of the absorber ($255\,\mathrm{GHz}$ - $275\,\mathrm{GHz}$, see Fig. 5.12), the absorption decreases and the pulse cannot be further shorten.

The relationship between the absorber bandwidth and the shortening of pulses is shown in Fig. 5.19. The pulse shapes and the corresponding frequency spectra for two pulses of different length, before and after the passage through the gyro-TWT absorber, are given.

In Fig. 5.19a and Fig. 5.19b, a pulse with a length of $0.075\,\mathrm{ns}$ is shown. From Fig. 5.18, a pulse shortening of $15\,\%$ is expected, which is actually observed. An inspection of the frequency spectrum shows that all frequency components are inside the absorber bandwidth and, consequently, all frequency components are attenuated in the absorber. This leads to an efficient shortening effect of

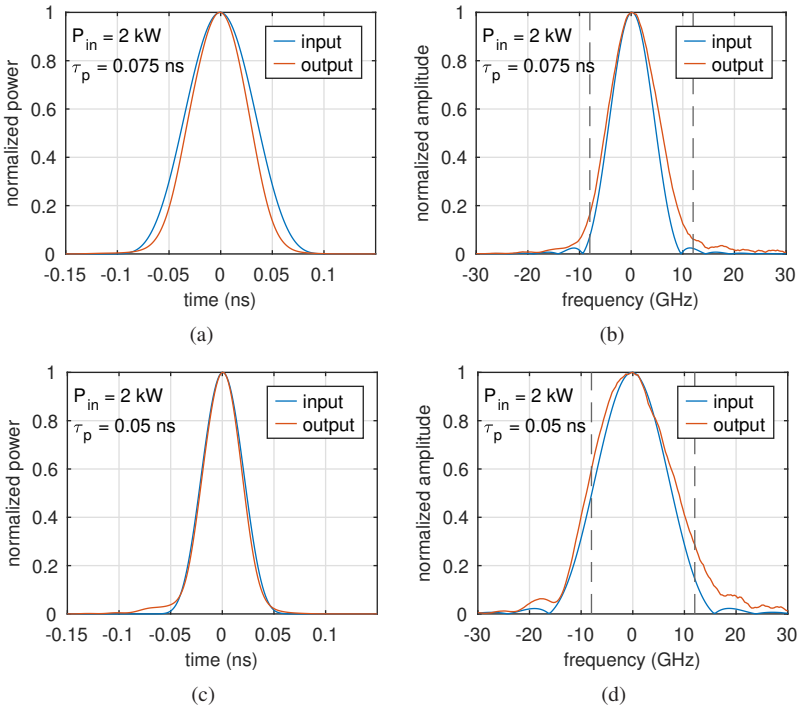

Figure 5.19: The shapes (a)+(c) and the spectra (b)+(d) of pulses before and after passing through the helical gyro-TWT absorber. The dashed lines represent the bandwidth of the absorber.

the pulse. A closer inspection of the frequency spectrum shows that the unsymmetrical bandwidth of the helical gyro-TWT absorber ($263 - 8\,\mathrm{GHz}$ to $263 + 12\,\mathrm{GHz}$) results in a slightly unsymmetrical frequency spectrum of the pulse after the passage through the absorber. This in turn results in a slightly unsymmetrical pulse shape.

In Fig. 5.19c and Fig. 5.19d, a shorter pulse with a length of $0.05\,\mathrm{ns}$ is shown. This pulse undergoes almost no shortening in the helical gyro-TWT absorber. The frequency spectrum of the pulse explains this. Significant parts of the frequency spectrum are outside the absorber bandwidth. The unsymmetrical absorption bandwidth in combination with the waveguide dispersion leads to

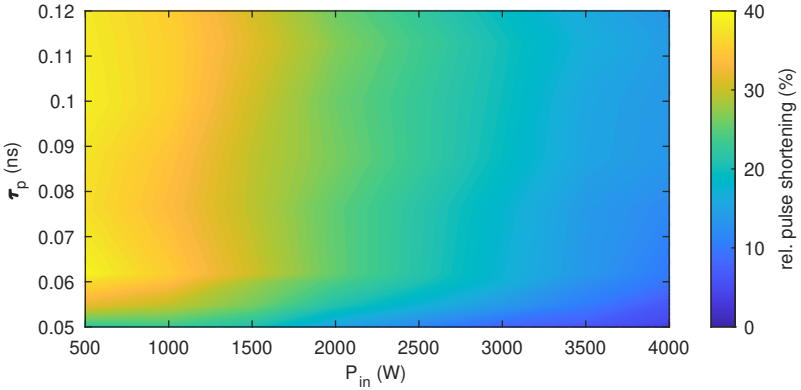

Figure 5.20: Relative shortening of the pulse length τ_p in a cyclotron absorber for input pulses of different power and pulse length.

a 'tail' at the end of the pulse. In a passive mode-locked oscillator, such a tail could lead to a splitting of the pulse into two pulses (see chapter 2.3.1) which could compromise the stability of the oscillator.

Cyclotron Absorber

In Fig. 5.20, the dependence of the pulse shortening on the pulse length and the pulse power is shown for the cyclotron absorber. The behavior is similar to the helical gyro-TWT absorber. The highest shortening can be observed at pulse powers where the derivative of the transmission coefficient is maximal (see Fig. 5.15b). For increasing powers, the relative pulse shortening decreases because the absorber is operated in saturation. If the pulse lengths falls below 0.06 ns, the shortening effect decreases abruptly. Above this limit, the relative pulse shortening does only slightly depend on the pulse length.

In comparison to the helical gyro-TWT absorber, the relative pulse shortening is noticeably higher for the cylcotron absorber while the pulse length limit has the same value of 0.06 ns. This is consistent with the similar bandwidth of the cyclotron absorber ($263-8$ GHz to $263+9$ GHz, see Fig. 5.15a) and the helical gyro-TWT absorber ($263-8$ GHz to $263+12$ GHz).

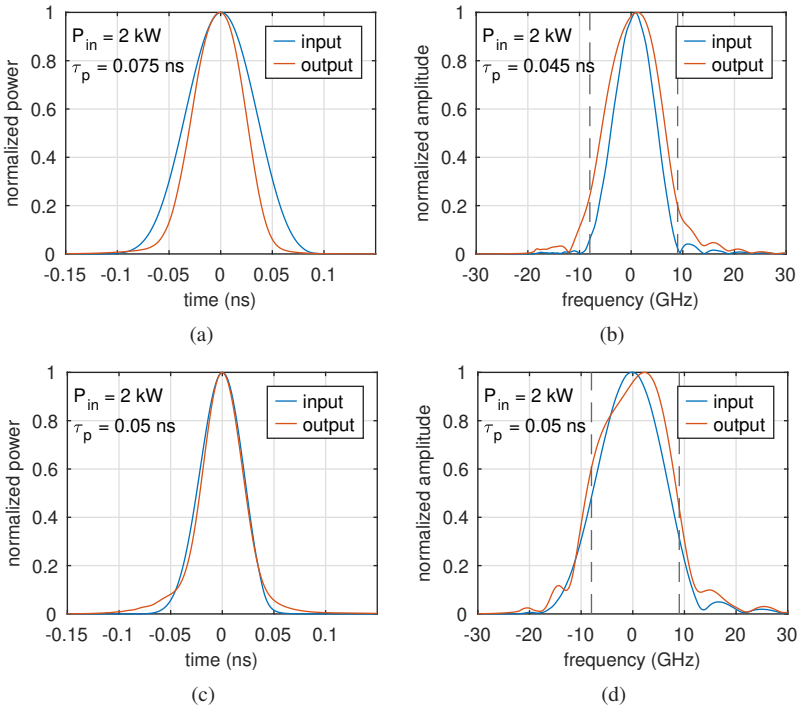

Figure 5.21: The shapes (a)+(c) and the spectra (b)+(d) of pulses before and after passing through the cyclotron absorber. The dashed lines represent the bandwidth of the absorber.

In Fig. 5.21, the pulse shape and the corresponding frequency spectra of two pulses, one above and one below the pulse length limit, are shown. As for the helical gyro-TWT absorber, a pulse undergoes a strong shortening in the absorber if the frequency spectrum does not exceed the bandwidth of the absorber (Fig. 5.21a and Fig. 5.21b). If significant parts of the spectrum are outside of the absorption bandwidth, the pulse cannot be shortened (Fig. 5.21c and Fig. 5.21d). Since the bandwidth of the cyclotron absorber is almost symmetrical around the center frequency of 263 GHz, the pulse spectrum and pulse shape remain more symmetrical after the passage through the absorber than for the helical gyro-TWT absorber.

Although the cyclotron absorber achieves a slightly stronger shortening effect than the helical gyro-TWT absorber, it can be concluded that both absorber concepts achieve a good shortening of pulses as long as the pulse length is above $0.06\,\mathrm{ns}$. The shortening is most effective for pulses with a peak power below $3.5\,\mathrm{kW}$. The general behavior of the absorbers can be summarized as follows: longer pulse and lower power $\rightarrow$ stronger shortening.

5.3 Effects of Manufacturing Tolerances

The influence of manufacturing tolerances on the beam-wave interaction is related to the operational frequency and, therefore, meeting these tolerances can be challenging at sub-THz frequencies. Especially for the complex geometry of a helically corrugated interaction region the production with high accuracy is challenging. The diameter of the interaction space is in the order of the free-space wavelength (for helical gyro-TWTs as well as for cyclotron absorbers) and the amplitude of the corrugations are one order smaller. The free-space wavelength at $263\,\mathrm{GHz}$ is $\approx 1.14\,\mathrm{mm}$ and consequently, for devices operating at this frequency the mean radius is $\approx 500\,\mu\mathrm{m}$ and the corrugation amplitude is $\approx 100\,\mu\mathrm{m}$. To find the margin for the required manufacturing tolerances, the dependence of the dispersion characteristics of the eigenwave on the geometry is studied.

Usually, the optimum beam-wave interaction occurs for a detuning of the cyclotron resonance frequency from the waveguides eigenwave of about $1\,\%$. Consequently, a deviation of the eigenwave dispersion exceeding $1\,\%$ could drastically decrease the beam-wave interaction.

For the tolerance study of a helically corrugated waveguide, the mean radius R, the corrugation amplitude $\tilde{r}$ and the axial corrugation period $\tilde{d}$ are individually changed and the corresponding dispersions are calculated. The calculations are performed with the method described in chapter 7.5, based on full-wave simulations.

In Fig. 5.22, the resulting dispersion curves are plotted for an assumed waveguide. It is found that R is most sensitive to deviations. A small variation of $\pm 5\,\mu\mathrm{m}$ leads already to deviations of the dispersion of $\pm 0.5\,\%$ (see Fig. 5.22a). The corrugation amplitude $\tilde{r}$ is also very sensitive to manufacturing tolerances.

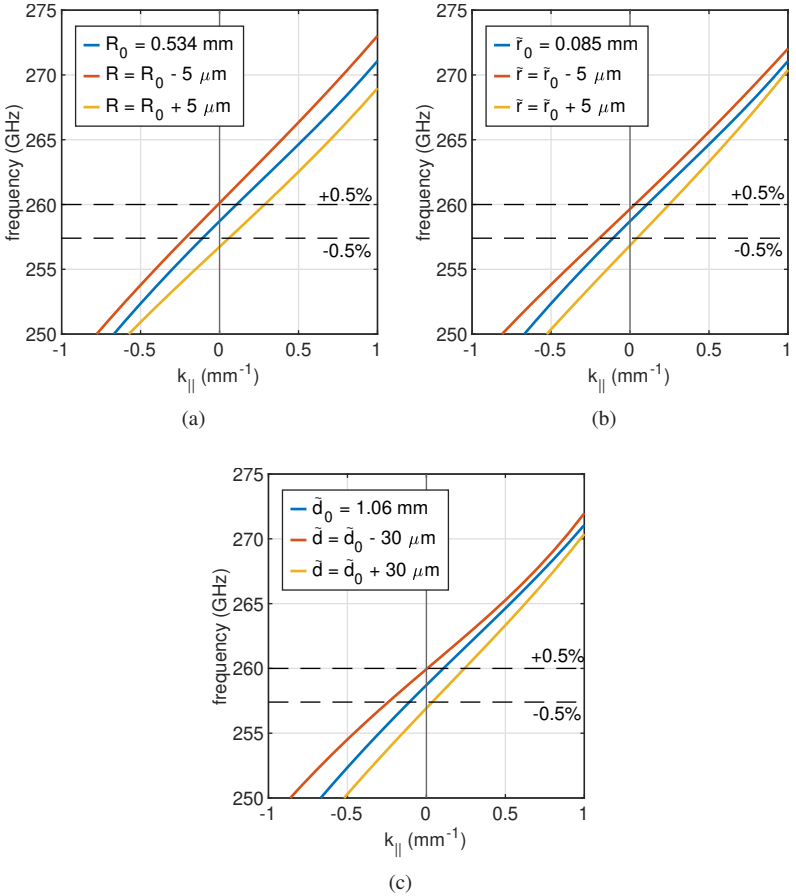

Figure 5.22: Simulated effects of geometrical variations on the dispersion of a helically corrugated waveguide with mean radius R, the corrugation's amplitude $\tilde{r}$ and the axial period $\tilde{d}$. (a) variation of the mean waveguide radius; (b) variation of the corrugation amplitude; (c) variation of the corrugation period.

To stay within the limits, the deviation must be less than ± 5 µm (see Fig. 5.22b). It is found that $\tilde{d}$ is the least critical parameter. A manufacturing tolerance of up to ± 30 µm is acceptable (see Fig. 5.22c).

The observed manufacturing tolerance limits are in good agreement with a similar study by Donaldson et al. for a 370 GHz helically corrugated waveguide [44]. In addition to the tolerance study, Donaldson et al. have proven the feasibility to manufacture the investigated helically corrugated waveguide for sub-THz frequencies [44].

With a similar study, limits for manufacturing tolerances for the cylindrical interaction region of a cyclotron absorber were found. With ± 5 µm, a similar limit for the waveguide radius R is observed.

It must be noticed that the performed tolerance study is of a very superficial nature. For example, it is not considered how deviations of the different parameters of a helically corrugated waveguide influence each other. Unsymmetrical deviations (e.g. elliptical deviations in cylindrical waveguides) are neglected. Nevertheless, it can be concluded from the analysis that an accuracy of at least ± 5 µm is required for the manufacturing process. However, modern CNC milling machines are able to work with this high precision [44].

6 System Design

In the previous chapter, alternative amplifier and absorber devices were designed and studied. Nevertheless, it is still an open question whether these devices can be successfully combined to a passive mode-locked oscillator and what performance can be expected from these oscillators. To answer this question, the passive mode-locked oscillator system is assembled from the previously developed devices and simulations of the coupled devices are carried out. For all simulation, the developed interaction simulation tool, presented in chapter 4, is used.

The designed helical gyro-TWT can be operated in two alternative operation regimes. Together with the two alternative absorber devices, in total four different passive mode-locked oscillators can be built up from the developed devices. Simulations for all possible combinations are performed and analyzed. The analysis will show that only the helical gyro-TWT operated in the slippage regime offers a reliable generation of ultra-short pulses and that the helical gyro-TWT absorber is preferable. For this passive mode-locked oscillator, a detailed study of the generated pulses, the spectra, the transient behavior, and the coherency is performed. At the end of the chapter, a novel method is proposed that will enable the operation of a sub-THz passive mode-locked oscillator in the hard excitation regime.

6.1 Simulation of a Passive Mode-Locked Oscillator

In chapter 2, the HME was introduced for a first investigation of the general properties of a passive mode-locked oscillator. The results were taken into account in the design of the amplifier and absorber devices. Consequently, the HME appears to be a good choice for the simulation of the final passive

mode-locked oscillator. However, an important assumption which is made in the HME is not fulfilled for a passive mode-locked oscillator based on electron tubes: In the HME it is assumed that a pulse experiences only a slight modification at every round trip. Only in this case, it is valid to average all effects over the full length of the device. Haus [62] gives a value of $< 20\,\%$ for this modification. While this assumption is typically fulfilled for lasers operated in the saturation region, it was shown in the previous chapter that a helical gyro-TWT has a higher gain and the assumption is not valid. As a result, the HME cannot be used for the simulation of a sub-THz passive mode-locked oscillator based on electron tubes.

As a solution, simulations based on the beam-wave interaction model developed in chapter 4 are used. In order to simulate a passive mode-locked oscillator with the developed program, the oscillator must be split into its single components, namely the amplifier, the absorber, the time delay, and the decoupling of the output signal. This is shown in Fig. 6.1.

As for the designed quasi-optical feedback system in chapter 8, the decoupling of a fraction K of the electromagnetic wave takes place after the absorber, before the pulse is fed back to the amplifier. The power decoupled from the feedback system calculates as:

$$P_{\mathrm{out}} = P_{\mathrm{out,abs}} \left(2K - K^2\right) \ , \tag{6.1}$$

where $P_{\mathrm{out,abs}}$ is the power of the signal after the transition though the saturable absorber.

All components can be individually simulated. To couple them in a feedback loop, the output signal of the amplifier simulation is used as an input for the simulations of the absorber. The simulated output of the absorber is used as an input for the simulation of a dispersion-free transmission line that represents the time delay. Finally, the output of the transmission line is fed back into the amplifier simulation. Although this procedure leads to the fact that the individual simulations are delayed to each other by one time step, this does not influence the final result due to the small time step used for the simulations ($\Delta t < 0.1\,\mathrm{ps}$).

The splitting of the passive mode-locked oscillator into individual simulations requires a serial computation of the sub-simulations. However, the approach

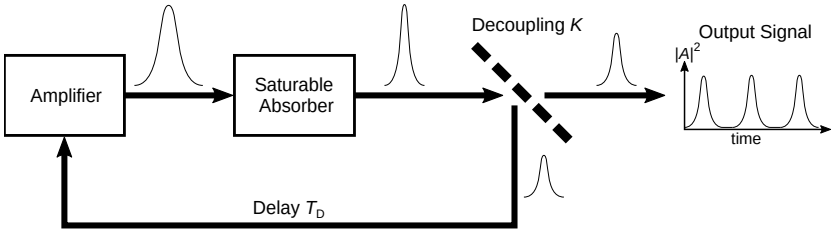

Figure 6.1: Schematic representation of a passive mode-locked oscillator used to subdivide the simulation of the entire passive mode-locked oscillator into several simulations of its components.

can be extended to enable a parallel computation of the sub-simulations. For this, the delay between the sub-simulations is increased to two time steps ($2\,\Delta t$). With this approach, the simulation of a following component can use the results from the upstream component at the previous time step and, therefore, has not to wait for the solution of the actual time step. Because of the small time step, the additional delay has still no measurable effect on the simulation result, but reduces the total simulation time by almost a factor of 3.

6.2 Different Passive Mode-Locked Oscillators

To find the most promising passive mode-locked oscillator, simulations of all four oscillators are performed. For the simulations in this section, the passive mode-locked oscillators are operated in the hard excitation regime. To realize this regime, the oscillator must initially run in a zero-drive stable state. For that, first the absorber and subsequently the amplifier is switched on. This results in an output signal that is stable below 1 W.

From the zero-drive operation, the pulsed operation regime is excited by the injection of a powerful signal into the oscillator. Although this start-up scenario seams to be unrealistic because of a lack of available high-power sources for the generation of the excitation signal, it has advantages for the following investigations: The results are reproducible and the start-up process is very fast, which reduces the required computational effort. In section 6.4, more realistic start-up scenarios of the passive mode-locked oscillator are discussed.

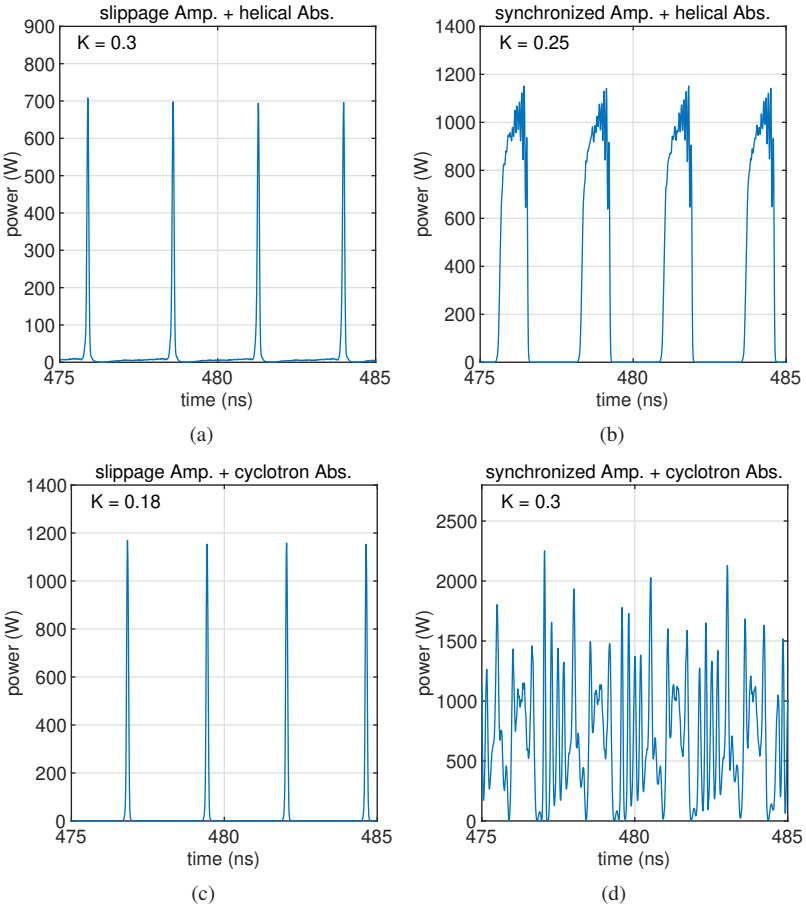

Figure 6.2: Output signals of the four different passive mode-locked oscillators operated in the hard excitation regime after a sufficiently long start-up time.

In Fig. 6.2, the generated output signals of the four different passive mode-locked oscillators after a sufficiently long start-up time are shown. In all cases, the delay time is set to 2 ns and the optimal decoupling factor K is chosen, which was found by a parameter sweep.

It can be seen that only the oscillators using the helical gyro-TWT in the slippage operation regime are able to generate the expected train of ultra-short pulses (Fig. 6.2a+c). In contrast, both oscillators with the helical gyro-TWT in the synchronized operation regime generate significantly longer pulses or an uncontrollable chaotic signal (Fig. 6.2b+d).

The reason for the longer pulses generated by the helical gyro-TWT operated in the synchronized regime in combination with the helical gyro-TWT absorber can be found in chapter 5.1.6 and chapter 5.2.3. For the amplification of high-power ultra-short pulses ($P = 1\,\mathrm{kW}$, $\tau_\mathrm{p} = 0.1\,\mathrm{ns}$) a broadening of $18\,\%$ was observed (see Fig. 5.9a) while the relative shortening of such a pulse in the helical gyro-TWT absorber was observed to be $15\,\%$ (see Fig. 5.18). Consequently, a broadening of the pulses arises and this oscillator cannot be operated in the passive mode-locked regime.

An obvious solution would be the usage of the cyclotron absorber in combination with the synchronized helical gyro-TWT. The cyclotron absorber has a stronger shortening effect ($\approx 25\,\%$, see Fig. 5.20) and should be therefore well suited for the realization of passive mode-locking in combination with the synchronized helical gyro-TWT. However, as shown in Fig. 6.2d, this is not the case. Although, the generated signal is somehow pulsed and periodic, it is not stable and varies slowly over longer time scales ($\approx 100\,\mathrm{ns}$). The spectrum of the generated signals reveals that the signal consist of frequency components in the range of $270\,\mathrm{GHz}$ to $285\,\mathrm{GHz}$, which is significantly above the designated center frequency of $263\,\mathrm{GHz}$.

The reason for that can be found in the bandwidth of the cyclotron absorber (see Fig. 5.15). Above $270\,\mathrm{GHz}$, the absorption effect drastically decreases. On the other hand, the synchronized helical gyro-TWT still has a significant gain at these frequencies. Therefore, the system corresponds to an amplifier with delayed feedback at these frequencies. As shown in [145], this leads to the generation of a chaotic signal. From this example, an important design criteria for a passive mode-locked oscillator can be derived: The bandwidth of the saturable absorber must exceed the bandwidth of the amplifier.

Because the helical gyro-TWT operated in the slippage regime has a reduced bandwidth that is completely covered from the cyclotron absorber, a feedback loop of the slippage helical gyro-TWT and the cyclotron absorber promises a stable passive mode-locked oscillator. As it can be seen in Fig. 6.2c, this is truly the case. However, a stable operation is only possible for relatively low values of the decoupling factor K which results in a very high-power signal oscillating in the feedback loop. This is necessary because the strong non-linearity of the cyclotron absorber for signals of lower power results in a strong shortening of these pulses. As a consequence, the pulses would fall below the minimum pulse length that is supported by the amplifier and, therefore, would not experience the necessary amplification.

The combination of the operation with pulses of highest power and the low-power capabilities of the cyclotron absorber (see chapter 5.2.2) reduces the maximal Pulse Repetition Frequency (PRF) to 250 MHz for this passive mode-locked oscillator. However, for the shown example with a delay time of 2 ns, the resulting PRF of 400 MHz already significantly exceeds this limit. While in the hard excitation regime, with a single pulse oscillating in the feedback system, the PRF can be controlled by the delay time, the PRF in the soft excitation regime is always significantly higher and cannot be controlled (see section 6.4). Consequently, the passive mode-locked oscillator consisting of the slippage helical gyro-TWT and the cyclotron absorber is not recommended and in the following a detailed analysis it is discarded.

It remains the oscillator that consists of the slippage helical gyro-TWT and the helical gyro-TWT absorber. As shown in Fig. 6.2a, this oscillator can be successfully operated in the passive mode-locking regime. Because of the lower non-linearity of the helical gyro-TWT absorber, the passive mode-locking regime can be realized at lower powers of the oscillating signals. As a result, a maximal PRF of 1200 MHz is possible which is sufficient even for an operation in the soft excitation regime (see section 6.4).

In [59], it is noted that for the broad spectra of ultra-short pulses, a helical gyro-TWT absorber could lead to undesirable amplification of frequency components far away from the maximum of the spectrum. However, this statement was given for a passive mode-locked oscillator in the Ka-band. The sub-THz helical gyro-TWT absorber designed in this work has a very broad absorption bandwidth that significantly exceeds the expected spectra. In addition, the bandwidth of the absorber is further increased by the combination with the

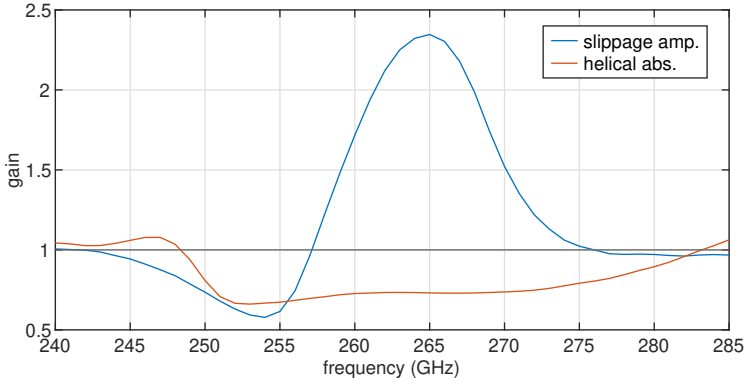

Figure 6.3: The gain for high power signals in the helical gyro-TWT operated in the slippage regime and the helical gyro-TWT absorber.

helical gyro-TWT operated in the slippage regime. This is shown in Fig. 6.3, where the gain for high power signals in the amplifier and the absorber are plotted. For frequencies below $257\,\mathrm{GHz}$, also the helical gyro-TWT operated in the slippage regime absorbs energy from the RF signal. Taking this into account, the designed passive mode-locked oscillator based on the slippage helical gyro-TWT and the helical gyro-TWT absorber has a wide region of $40\,\mathrm{GHz}$ for a stable operation without the risk of undesirable amplification.

In conclusion, a feedback loop of a slippage helical gyro-TWT and a helical gyro-TWT absorber is the most promising candidate for a realization of a $263\,\mathrm{GHz}$ passive mode-locked oscillator. This finding differs from existing considerations of passive mode-locking at lower microwave frequencies where a cyclotron absorber is preferable and is therefore an important result of this work.

6.3 Generated Output Signal

The properties of the passive mode-locked oscillator that consists of the helical gyro-TWT operated in the slippage regime and the helical gyro-TWT absorber

is investigated in more detail. First, the transient behavior of the generated signal is investigated, then the characteristics of a single pulse are examined and, finally, an analysis of the generated spectrum is performed.

6.3.1 Pulse Power and Length

For the selected passive mode-locked oscillator, the power and length of the generated pulses mainly depend on the decoupling factor K and the beam current I_{amp} of the amplifier.

Decoupling Factor

Simulations have shown that the oscillator is very sensitive to the decoupling factor K and that the regime of passive mode-locking is only possible for a very narrow range around the ideal decoupling factor. This can be seen in table 6.1, where the peak power and the length of the generated pulses are given for different values of K. A stable operation in the regime of passive mode-locking is only possible for K values in the range of 0.299 to 0.304.

For K values smaller than 0.299, no shortening of the pulses arises and the pulse length significantly increases. The reason is the increased power level of the pulses that oscillate in the feedback loop. This results in a decreasing nonlinear shortening effect in the saturable absorber. A further decrease of the decoupling factor leads to the generation of a quasi CW signal with chaotically distributed high-power peaks on top of it.

On the other hand, if the decoupling factor exceeds a specific limit ($K = 0.304$), the power decoupled from the feedback loop exceeds the power gained in the amplifier. The pulses degenerate, and the oscillator does not generate an output signal.

Table 6.1: Dependence of the output power and pulse length on the decoupling factor for the passive mode-locked oscillator with slippage helical gyro-TWT amplifier and helical gyro-TWT absorber.

K	P_{out} (W)	τ_{p} (ns)
0.298	880	0.17
0.300	750	0.072
0.302	710	0.072
0.304	620	0.070
0.306	< 1	–

Amplifier Current

In chapter 5.1, the helical gyro-TWT in the slippage regime was designed for a default current of 0.2 A. However, it can be also operated with higher currents which is of particularly interest if the output power of the oscillator should be increased.

The maximum energy that can be extracted from the feedback loop is limited by the gain of the amplifier. Consequently, an increased amplifier beam current and the correspondingly increased gain allows higher decoupling factors and therefore higher output powers. This relationship can be seen in table 6.2.

Besides the increased output power, an increased amplifier current leads to an increased pulse length. The reason is the increasing of the pulse-broadening effect with the gain (for amplifiers that are operated in saturation).

In addition, the maximum PRF is given in table 6.2. The maximum PRF is defined by the limited power capability of the helically corrugated interaction region and is calculated with (5.1). Because the power level of the pulses that oscillate in the feedback loop is similar for all beam currents (the narrow region of optimal pulse shortening in the saturable absorber requires this), the reduction of the PRF limit is caused by the increased pulse length. Nevertheless, the allowed PRF is above the maximal PRF that could be reached from this passive mode-locked oscillator (see section 6.4.3) for all shown currents.

Table 6.2: Dependence of the output power and pulse length on the beam current of the amplifier for the passive mode-locked oscillator with slippage helical gyro-TWT amplifier and helical gyro-TWT absorber.

I_{amp} (A)	P_{out} (W)	τ_{p} (ns)	max f_{r} (GHz)	optimal K
0.2	750	0.075	1.8	0.30
0.25	1100	0.090	1.3	0.44
0.3	1400	0.110	1.1	0.55

6.3.2 Pulse Shape

In a mode-locked laser, the temporal shape of the output pulse is mainly determined by the dispersion of the system. A small dispersion leads to sech^2 pulses, a moderate dispersion to Gaussian pulses, and for a large dispersion the result is somehow unpredictable [146]. While the pulse shapes of passive mode-locked lasers are known, the temporal shape of the generated pulses in passive mode-locked oscillators at microwave frequencies is not addressed in the existing literature.

In order to analyze the shape of the generated pulses, fits of expected pulse shapes, namely Gaussian and sech^2 pulses, to the simulated pulses are performed. In Fig. 6.4, the results of the fits are shown. It can be seen that both pulse shapes fit the generated pulse similarly well which results in almost equal root-mean-square errors (RMSEs) for both fits of 0.016 and 0.017, respectively. Interpreting these results from the laser physics point of view, the designed sub-THz passive mode-locked oscillator has a low to medium dispersion, which is actually the case because of the used helically corrugated interaction regions.

For a validation of the correlation of the pulse shape and the dispersion of the system, in appendix A.4 the generated pulse shape of the passive mode-locked oscillator consisting of the slippage helical gyro-TWT and the cyclotron absorber is shown. Although this oscillator is inappropriate for realization, the analysis helps to understand the basic principle of passive mode-locking at sub-THz frequencies. Because of the higher dispersion of the cyclotron absorber

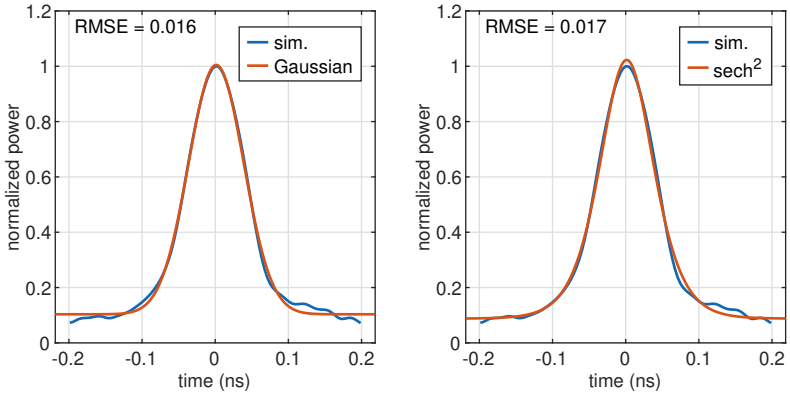

(a) (b)

Figure 6.4: Simulated pulse shape for the passive mode-locked oscillator with slippage helical gyro-TWT amplifier and helical gyro-TWT absorber together with a fitted Gaussian (a) and sech^2 (b) pulse.

compared to the helical gyro-TWT absorber, the pulse shape is expected to be almost Gaussian. As shown in Fig. A.8, this is actually observed which confirms the parallels to laser physics.

6.3.3 Spectrum

Of particular interest for a possible application in spectroscopy is the spectrum generated from the passive mode-locked oscillator. From the simulated time-domain results, the spectrum can be calculated by a Fourier transformation. The resulting spectrum of the passive mode-locked oscillator with slippage helical gyro-TWT amplifier and helical gyro-TWT absorber for an amplifier beam current of $0.2\,\mathrm{A}$ and a decoupling factor of 0.3 is shown in Fig. 6.5.

The spectral centroid [147] of the shown spectrum is $262.92\,\mathrm{GHz}$ and, therefore, in an excellent agreement with the designed value of $263\,\mathrm{GHz}$.

As discussed in chapter 1.3, the distance between the discrete frequency lines corresponds to the PRF. The generated pulse train has a PRF of

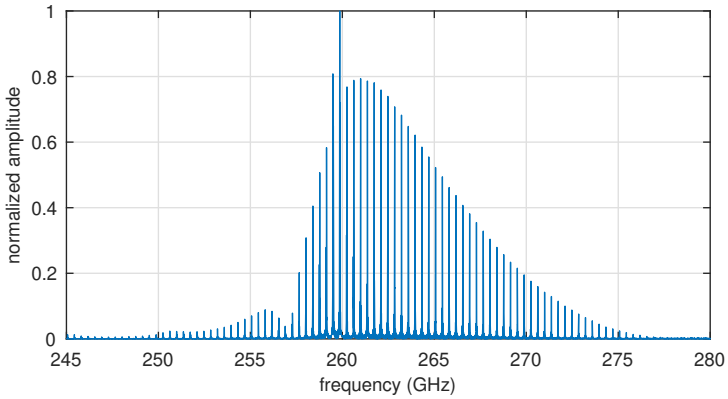

Figure 6.5: Generated spectrum of the passive mode-locked oscillator with slippage helical gyro-TWT amplifier and helical gyro-TWT absorber.

370.4 ± 0.5 MHz and the distance between the spectral lines is 371 ± 1 MHz. Both values are in a good agreement. For further discussion of the PRF see section 6.4.

A remarkable point is the peak in the spectrum at 260 GHz. The reason for it can be found by an analysis of the low power CW background signal that is generated between the high-power pulses. In Fig. 6.6, the spectrum of this background signal is shown and it clearly corresponds to the peak in Fig. 6.5. The CW background is generated at 260 GHz and has a power of less than 10 W. A comparison with Fig. 5.2 shows that the background signal is an emission of the gyrating electron beam at $k_{\parallel} = 0\,\mathrm{mm}^{-1}$.

A comparison of the spectrum with the bandwidth of the amplifier (see Fig. 6.3) for high-power pulses shows that the spectrum is clearly limited by the amplifier. Below 257 GHz and above 275 GHz, the gain of the helical gyro-TWT operated in the slippage regime vanishes and consequently a minimum in the spectrum is observed.

While the width of the spectrum is a result of the bandwidth and the distance of the spectral lines corresponds to the PRF, the envelope of the spectrum should correspond to the spectrum of a single pulse. The previous investigation has shown that the pulses have almost a Gaussian pulse shape which should

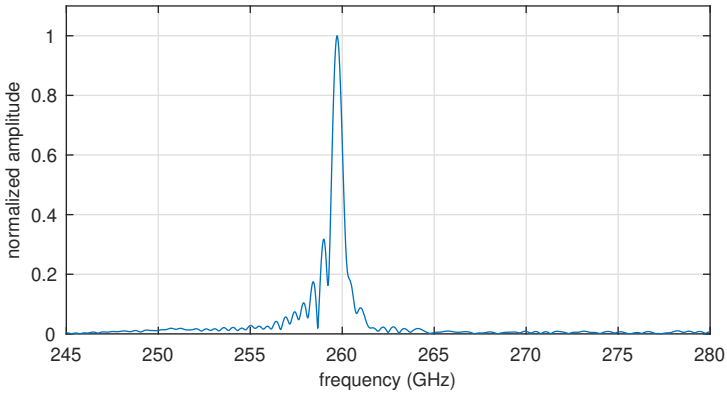

Figure 6.6: Spectrum of the CW background signal that is generated between the high power pulses of the passive mode-locked oscillator with slippage helical gyro-TWT amplifier and helical gyro-TWT absorber.

result in a Gaussian shaped spectrum. However, the observed envelope of the spectrum significantly differs from a Gaussian normal distribution. A closer study of this effect shows that the reason for the unexpected envelope of the spectrum is the chirp of the generated pulses. This is illustrated in Fig. 6.7, where the amplitude and the phase of a single simulated pulse and its spectrum are given. As expected, the spectrum of the pulse corresponds exactly to the envelope of the total signal and the chirp of the pulse is the reason for the unsymmetrical spectrum which differs significantly from the spectrum of an unchirped Gaussian pulse.

Because the observed phase distribution of the pulse (Fig. 6.7a) is not expected, a comparison with analytically created chirped Gaussian pulses is performed. The result that matches best has a trapezoidal distribution of the instant frequency. As shown in Fig. 6.7c and Fig. 6.7d, this trapezoidal chirp results in a similar phase distribution and spectrum.

In passive mode-locked lasers, a chirp of the generated pulses is typically caused by the dispersion characteristics of the system. However, the observed trapezoidal chirp cannot be explained by the dispersion of the system. This can be seen in Fig. 6.8, where the group velocity in the helically corrugated

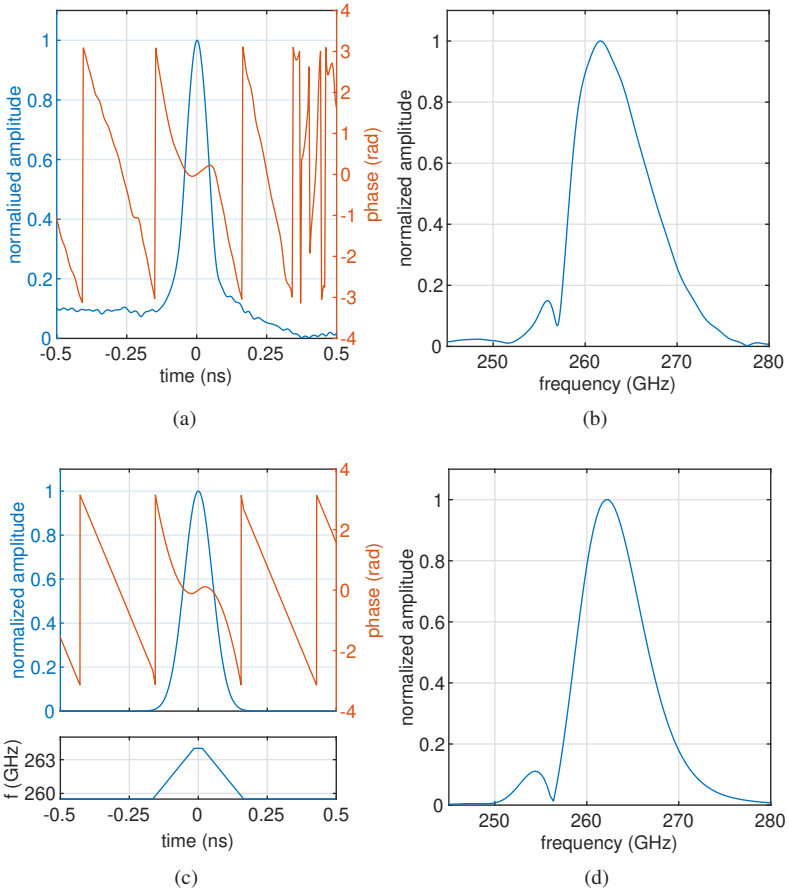

Figure 6.7: (a)+(b) Amplitude and phase distribution and the corresponding spectrum of a single pulse of the passive mode-locked oscillator with slippage helical gyro-TWT amplifier and helical gyro-TWT absorber. (c)+(d) The best matching analytically created chirped Gaussian pulse and its spectrum. The shown phase is relative to a harmonic 263 GHz signal.

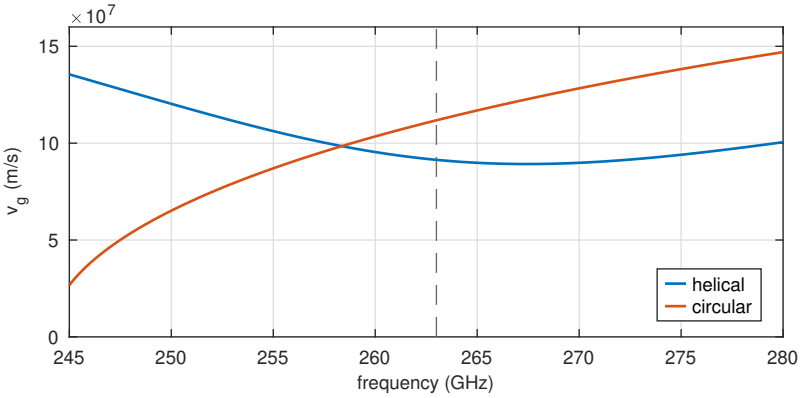

Figure 6.8: Frequency dependence of the group velocity in the cylindrical and helical interaction regions of the both absorber devices.

interaction region is plotted over the frequency (blue line). While lower frequency components have slightly higher group velocities, it is almost constant around 263 GHz and for higher frequencies. Consequently, the initial up-chirp is in a good agreement with the dispersion. Also the constant frequency at the center of the pulse, following the up-chirp, is expected because of the almost constant group velocity for frequencies in the range of 263 GHz to 270 GHz.

However, the down-chirp at the falling edge of the pulse cannot be explained by the dispersion. For an explanation of this effect, the influences of the beam-wave interaction in the amplifier and absorber devices must be investigated. For this, an ultra-short high-power pulse is fed into the oscillator, once with activated amplifier but deactivated absorber and once with activated absorber and deactivated amplifier. This allows the effect of the beam-wave interaction to be studied separately for both components, without neglecting the dispersion of the entire system. The results of these simulations are shown in Fig. 6.9.

For an activated absorber and an deactivated amplifier (Fig. 6.9a), the resulting phase distribution, and consequently the chirp, are as expected from the dispersion. An up-chirp of the rising edge and an almost constant frequency until the power of the pulse decreases to the noise level.

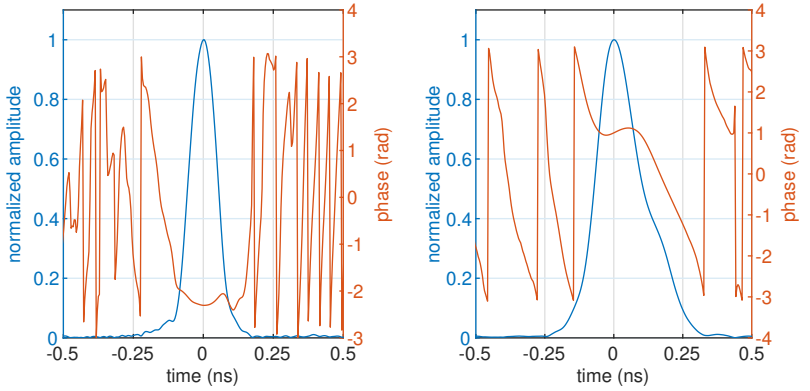

Figure 6.9: Amplitude and phase of a pulse after a passage through the feedback loop: (a) with deactivated amplifier and activated absorber; (b) with activated amplifier and deactivated absorber. The shown phase is relative to a harmonic 263 GHz signal.

The reason that the beam-wave interaction in the helical gyro-TWT absorber has no effect on the chirp is the synchronized electron beam. The propagation velocities of the beam and the wave are matched and, therefore, every fraction of the pulse interacts with a constant fraction of the electron beam which allows a broadband beam-wave interaction without favoring certain frequencies.

In contrast to the absorber, the amplifier is operated in the slippage regime where the wave propagates faster than the electron beam. In Fig. 6.9b, the resulting phase and amplitude distribution after one round tip of the pulse in the feedback loop with deactivated absorber is shown. Now, the same phase distribution as for the fully activated oscillator can be observed. This proves that the interaction of the RF field with the electron beam in the slippage regime causes the observed chirp.

In the slippage operation regime, the rising edge of the pulse interacts with 'fresh' electrons that have the full kinetic energy and the beam can efficiently amplify the RF field at all frequencies of the designed bandwidth. However, the falling edge of the pulse interacts with a spent fraction of the electron beam which has already transferred a part of its kinetic energy to the front part of the

pulse. As a result, the cyclotron frequency of the electrons is decreased and higher frequency components in the RF field cannot be amplified anymore. This leads to the preferred amplification of lower frequency components and, therefore, to the observed down-chirp at the falling edge of the pulse.

If the observed trapezoidal chirp is unfavorable for a future application of the passive mode-locked oscillator, it can be easily changed by adding a dispersive component to the feedback system.

6.4 Transient Behavior of the Oscillator

In the preceding discussion, the signal generated by the passive mode-locked oscillator was studied after it reached a quasi steady state. However, of particular interest are the transient behavior of the oscillator during the start-up phase as well as the long-term stability.

6.4.1 Start-up in the Hard Excitation Region

As in the previous sections, the special case of a start-up in the hard excitation is investigated first. In the hard excitation region, the passive mode-locked operation regime is excited from an initial zero-drive stable operation by the injection of a high-power RF pulse into the feedback loop.

In Fig. 6.10, such a start-up in the hard excitation is shown. Each point in the plot corresponds to a high-power pulse in the output signal. For the excitation, a Gaussian pulse with a center frequency of 263 GHz, a power of 100 W and a length of 0.25 ns is used. During the first 50 ns, the pulse is strongly amplified and at the same time strongly shortened at each turn in the feedback loop. After the pulse length reached 0.1 ns, the shortening is slowed down. At the pulse length of 0.1 ns, the pulse power has also reached its maximum and during the following further shortening process, the pulse power again decreases slightly. A quasi steady state is reached after 300 ns.

An excitation signal with a center frequency of 263 GHz is used in the shown simulations. However, an excitation signal with an arbitrary frequency in the

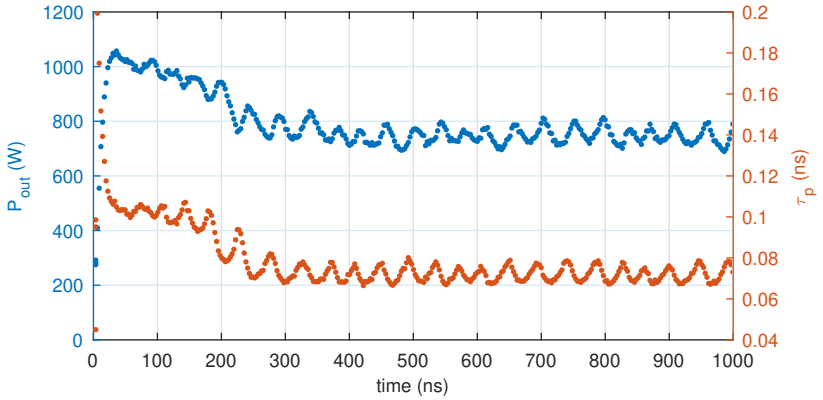

Figure 6.10: Transient behavior of the passive mode-locked oscillator with slippage helical gyro-TWT amplifier and helical gyro-TWT absorber in the hard excitation operation.

bandwidth of the amplifier is suitable. After a sufficiently long start-up time, the passive mode-locked oscillator always stabilizes at the same spectrum.

It must be noted that even after reaching a stable operation point, the power as well as the length of the pulses show a low-frequency harmonic oscillation. The period of this oscillation is $50\,\mathrm{ns}$ ($\equiv$ $20\,\mathrm{MHz}$) and the amplitudes for the oscillations of the pulse power and pulse length are $40\,\mathrm{W}$ and $0.005\,\mathrm{ns}$, respectively. These fluctuations correspond to a relative variation of $\pm 5\,\%$ and $\pm 6\,\%$.

Of particular interest is the offset between the oscillations of the power and the pulse length of $\approx 13\,\mathrm{ns}$. This corresponds to a phase offset of $\frac{\pi}{2}$ between the pulse length and the pulse power. Consequently, the derivative of the pulse length $\frac{\partial \tau_\mathrm{p}}{\partial t}$ depends on the power.

This observation is consistent with the properties of the amplifier and absorber devices. Depending on the power of the pulse, the non-linearity of the attenuation in the absorber varies. High-power pulses experience a stronger shortening than pulses of lower power. At the same time, the amplifier is operated close to its maximum bandwidth which results in a dependence of the gain on the pulse length. For a pulse length below $0.0725\,\mathrm{ns}$, the power decreases, for

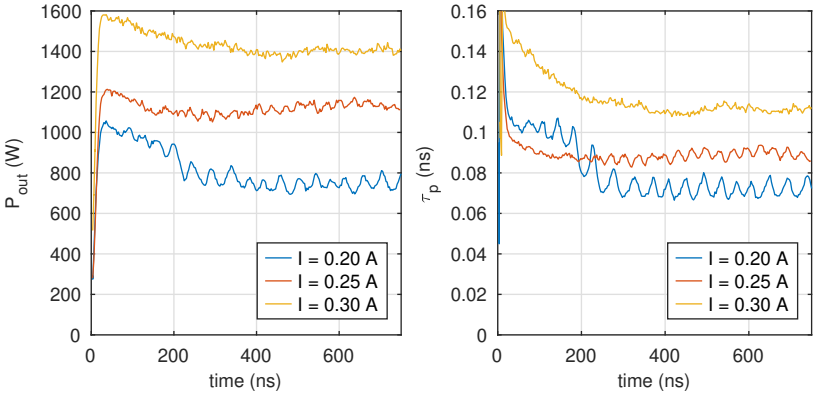

(a) (b)

Figure 6.11: Transient behavior of the output power and the pulse length of the passive mode-locked oscillator in the hard excitation regime for different amplifier beam currents.

pulse lengths above, it increases. This is in a good agreement with the results of chapter 5.1.6 where a decreasing gain for pulse lengths below $0.075\,\mathrm{ns}$ is observed for the helical gyro-TWT in the slippage regime.

Consequently, the oscillations can be avoided if the amplifier is operated far away from its maximal bandwidth. This is proven in Fig. 6.11 where the output power and the pulse length is plotted for different amplifier beam currents. As mentioned above, a higher beam current in the amplifier increases the output power, but also the pulse length. Since the spectra of longer pulses have a smaller bandwidth, the amplification becomes independent of the pulse length and the oscillations disappear.

6.4.2 Start-up in the Soft Excitation Region

In the soft excitation, the oscillator is started from noise and the regime of passive mode-locking is reached without the requirement of a powerful external excitation signal. Therefore, this scenario is of particular interest for first experiments.

To reach the passive mode-locking regime in the soft excitation, an initial noise level of significant power is required. To create this high-power RF noise without an external source, a simple trick is used: First the amplifier device is activated while the saturable absorber remains deactivated. The feedback system ensures that the unavoidable noise generated by the amplifier is amplified until the required power level is reached. In the simulations this happens usually after 10-50 ns, depending on the delay time in the feedback loop. Once the necessary power level is reached, the absorber is activated.

The transient behavior of a typical start-up in the soft excitation regime is shown in Fig. 6.12. Every point in the plot represents a pulse in the output signal.

A chaotic distribution of peaks can be observed in the initial high-power noise ($t < 50$ ns). After the activation of the absorber, first pulses are created (50 ns $< t < 400$ ns). These pulses still have different power levels and pulse lengths. In the following, the usual sharpening process occurs and the power as well as the pulse length converge to a stable equilibrium of pulse power and length (400 ns $< t < 1300$ ns). The resulting power and pulse length are the same as in the case of the start-up in the hard excitation regime.

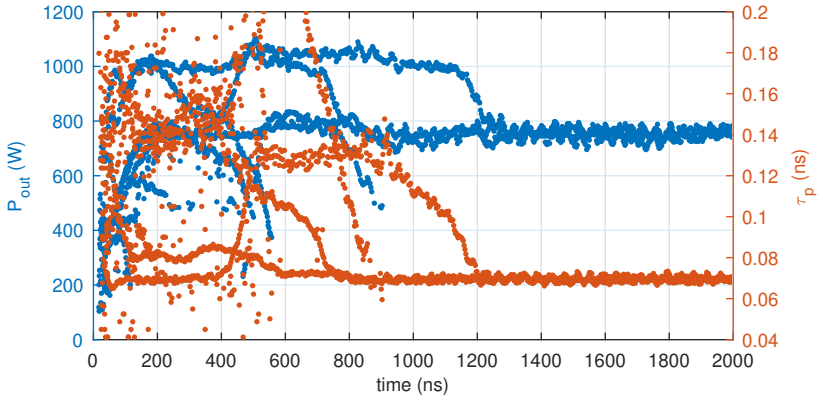

Figure 6.12: Transient behavior of the passive mode-locked oscillator with slippage helical gyro-TWT amplifier and helical gyro-TWT absorber in the soft excitation operation.

6.4.3 Achievable Repetition Rate

While the power and the pulse length of the generated signals are independent from the excitation regime, the PRF differs for the cases of hard and soft excitation. The reason is that only a single pulse oscillates in the feedback loop if the passive mode-locking regime is excited in the hard excitation by an initial powerful external signal. In contrast, several pulses are oscillating in the feedback system for a soft excitation and, therefore, the PRF is higher compared to the hard excitation case.

For an operation in the hard excitation regime, the PRF is mainly determined by the delay time in the feedback system. The PRF is inverse proportional to the total time that a pulse requires to propagate through the complete feedback system. This time is a sum of the delay time T_{D} introduced by the feedback system and the times T_{amp} and T_{abs} that the pulse requires to propagate through the amplifier and absorber devices, respectively. This is illustrated in Fig. 6.13, where the PRFs for several passive mode-locked oscillators with different delay time are plotted. A fit with the expected dependence on the delay time

$$f_{\mathrm{r}} \propto \frac{1}{T_{\mathrm{amp}} + T_{\mathrm{abs}} + T_{\mathrm{D}}} \tag{6.2}$$

shows an excellent agreement between simulations and theory.

The maximal PRF for the passive mode-locked oscillator with a single pulse oscillating in the system is reached for a vanishing delay time. For the shown passive mode-locked oscillator this would be $\approx 1.4\,\mathrm{GHz}$.

In the soft excitation regime with several pulses oscillating in the system, the maximal PRF is determined by the length of the oscillating pulses. For the expected pulse length of $0.075\,\mathrm{ns}$, this would be approximately $6.5\,\mathrm{GHz}$. However, the simulations of the soft excitation regime have shown a maximal PRF of only $1.11\,\mathrm{GHz}$.

The reason for the PRF limitation can be found in Fig. 6.14. Sections of the generated signal of the passive mode-locked oscillator with a delay time of $2\,\mathrm{ns}$ are shown in logarithmic scaling for the cases of hard and soft excitation. In the hard excitation case (Fig. 6.14a), a strong suppression of the CW background

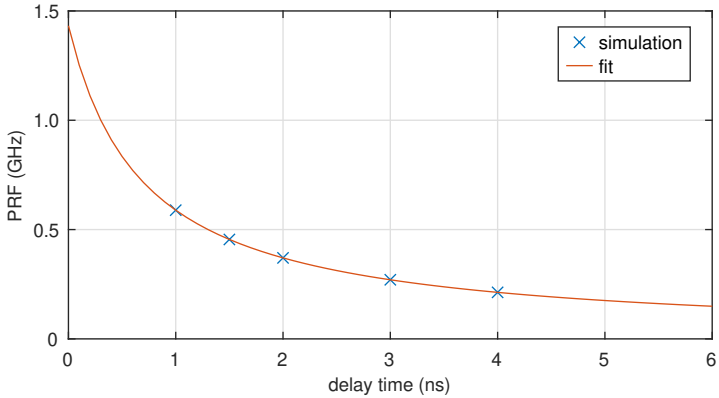

Figure 6.13: PRF of the passive mode-locked oscillator with slippage helical gyro-TWT amplifier and helical gyro-TWT absorber in the hard excitation operation for different delay times.

signal directly after the generated pulses is noticeable. The reason for this dip is the special characteristic of the amplifier.

As discussed in chapter 2.3.1, the helical gyro-TWT operated in the slippage regime corresponds to a slow device which cannot recover its initial properties on the timescale of an ultra-short pulse. This is a result of the different propagation velocities of the electron beam and the electromagnetic wave. In the previous discussion, this was identified as a reason for the observed chirps in the generated pulses. However, the different propagation velocities have a second important effect: the amplifier has a short dead time after the amplification of a pulse. During this dead time, an amplification of signals is not possible. This causes the drop of the CW background signal.

A comparison of the dead time of the amplifier with the distance between the pulses generated in the soft excitation operation regime (Fig. 6.14b) shows that both are in a great agreement. To clarify this, the hard and soft excitation cases are plotted together in Fig. 6.14c. It can be concluded that the maximum PRF for a passive mode-locked oscillator using the helical gyro-TWT operated in the slippage regime is limited to 1.12 GHz because of the dead time of the amplifier.

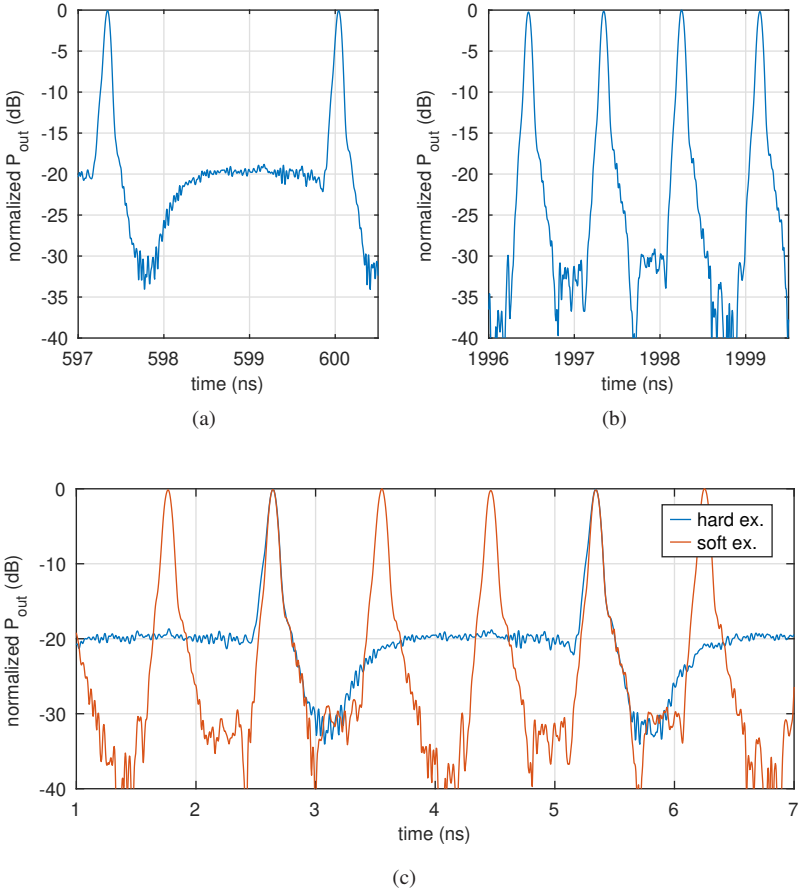

Figure 6.14: Normalized output signals in logarithmic scaling of the passive mode-locked oscillator with slippage helical gyro-TWT amplifier and helical gyro-TWT absorber operated (a) in the hard and (b) soft excitation regimes; (c) superposition of the soft and hard excitation regimes.

In [57], a similar value of 1 GHz for the PRF was observed by simulations of a Ka-band passive mode-locked oscillator operated in the soft excitation regime. However, no reason for this observed PRF is provided in the publication and the author is not aware of any publication that discusses the issue of the PRF limitation in passive mode-locked oscillators with electron tubes that have characteristics of slow devices.

As a result of the upper PRF limit of 1.12 GHz and the maximal tolerable PRFs for different amplifier beam currents (see table 6.2), a maximal allowed amplifier beam current with respect to the power capabilities of the devices can be estimated. For the investigated passive mode-locked oscillator with the slippage helical gyro-TWT and the helical gyro-TWT absorber an operation with amplifier beam currents of up to 0.3 A is possible in all operation regimes

6.4.4 Achievable Coherence

For future pulsed spectroscopy applications, pulses with a high temporal coherence are required. Therefore, the coherence of the generated pulses in the soft and the hard excitation cases are investigated in this section.

The spectra of the generated signals give a first evidence of the coherence. For a periodic signal with constant periodicity and constant shaped pulses, the spacing of the spectral lines corresponds to the periodicity of the signal and the envelope matches the spectrum of a single pulse.

This has proven to be true for the spectrum and the PRF generated by the passive mode-locked oscillator operated in the hard excitation regime (see the previous sections). However, for an operation in the soft excitation regime the spectrum differs from the expectations. This can be seen in Fig. 6.15, where the spectra for an operation in the hard and the soft excitation regimes are shown. For a better comparability of the soft and hard excitation cases, a very short delay time of 0.5 ns is used for the hard excitation case which results in a PRF of 0.9 GHz. Therefore, it is of the same order as the PRF of the soft excitation case (1.11 GHz).

A comparison of the spectra shows that the envelope of both spectra is similar. However, the spectrum for the operation in the soft excitation regime (Fig. 6.15b) appears to be a superposition of the spectra of two signals with

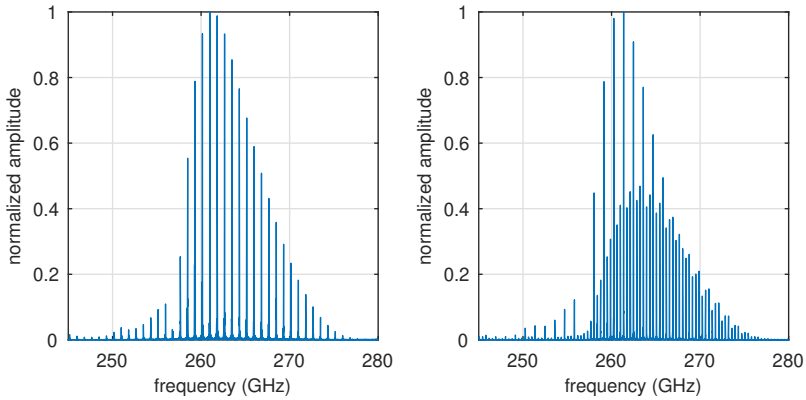

Figure 6.15: Spectra of an operation in the (a) hard and the (b) soft excitation regimes.

different periodicities. One of the signals seams to have a periodicity of $1.11\,\mathrm{GHz}$, the other one of $0.37\,\mathrm{GHz}$. The $1.11\,\mathrm{GHz}$ are clearly correlated to the observed PRF. However, a second periodicity seams to arise in the signal with a frequency of $0.37\,\mathrm{GHz}$. It should be noted, that $0.37\,\mathrm{GHz}$ is exactly $\frac{1}{3} \cdot 1.11\,\mathrm{GHz}$.

To clarify this phenomenon and for a further investigation of the coherence, a cross-correlation function can be used. In [67], a continuous cross-correlation function was used for the evaluation of the pulse reproducibility of a Ka-band passive mode-locked oscillator. However, such a continuous cross-correlation function is not optimal for the investigation of a pulsed signal because it results in a pulsed correlation coefficient that complicates the interpretation. Therefore, the usage of a discrete cross-correlation function is proposed in this work.

In the following, the discrete cross-correlation function

$$\overline{C}_{m,n}^{\mathrm{corr}} = \frac{\int_{T_m-\tau_\mathrm{p}}^{T_m+\tau_\mathrm{p}} \overline{A}(t)\overline{A}^*(t-(T_m-T_n))\,\mathrm{d}t}{\sqrt{\int_{T_m-\tau_\mathrm{p}}^{T_m+\tau_\mathrm{p}} \left|\overline{A}(t)\right|^2 \mathrm{d}t \;\cdot\; \int_{T_n-\tau_\mathrm{p}}^{T_n+\tau_\mathrm{p}} \left|\overline{A}(t)\right|^2 \mathrm{d}t}} \tag{6.3}$$

is used. It describes the cross-correlation of two pulses m and n with a pulse length of τ_p, located at T_m and T_n.

In general, $\overline{C}^{\mathrm{orr}}_{m,n}$ is a complex number. Its amplitude corresponds to the correlation of the shapes of the pulses m and n, while the phase of $\overline{C}^{\mathrm{orr}}_{m,n}$ corresponds to a phase offset between the two pulses. For an evaluation of the coherence, the cross-correlation function $\overline{C}^{\mathrm{orr}}_{m,n}$ between an arbitrary reference pulse m and all other pulses n is evaluated.

In Fig. 6.16, the resulting correlation coefficients for an operation in the hard excitation regime is shown. After the oscillator has reached a quasi steady state, the amplitude of the cross-correlation coefficient remains above 0.97 which proves a high reproducibility of the generated pulses. The remaining slight variation is a result of the previously observed variation of the pulses power.

In addition to the amplitude, the change of the phase offset from pulse to pulse

$$\Delta\overline{C}^{\mathrm{orr}}_{m,n} = \arg\left(\overline{C}^{\mathrm{orr}}_{m,n-1}\right) - \arg\left(\overline{C}^{\mathrm{orr}}_{m,n}\right) \tag{6.4}$$

is plotted in Fig. 6.16. It can be seen that $\Delta\overline{C}^{\mathrm{orr}}_{m,n}$ is almost constant in the region of a quasi steady state operation. This implies that the phase of the pulses changes by a constant value from pulse to pulse. The generated signal is therefore equivalent to a single pulse that is repeated continuously at a constant frequency and that has its phase shifted by a constant value with each repetition.

In Fig. 6.17, the same quantities are shown for the case of an operation in the soft excitation regime. After the oscillator has reached a quasi steady state ($t > 1300\,\mathrm{ns}$), the amplitude of the cross-correlation coefficient indicates again a very good reproducibility of the generated pulses. However, it can be seen that the final output signal is created by three different pulses that have been formed during the start-up process. This origin of the total output signal from three different pulses is also reflected in the pulse to pulse change of the phase offset $\Delta\overline{C}^{\mathrm{orr}}_{m,n}$.

The formation of the three discrete lines in $\Delta\overline{C}^{\mathrm{orr}}_{m,n}$ implies that the output signal consists of three pulses with similar pulse shapes and phase distributions but with a different phase offset. The reason for this can be found in the start-up scenario. In the soft excitation, the passive mode-locking regime is created

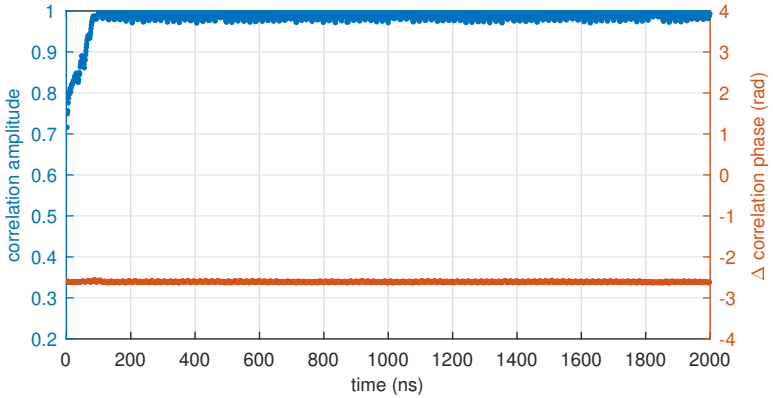

Figure 6.16: Amplitude of the cross-correlation coefficient $\overline{C}^{\mathrm{orr}}_{m,n}$ and the pulse to pulse change of the phase offset for an operation in the hard excitation regime.

from noise and, therefore, the initial phases of all signals that contribute to the steady state solution are arbitrary and not correlated with each other.

In the existing literature about the coherence of the signals generated from passive mode-locked oscillators at microwave frequencies, the investigation of phase offsets was neglected until now. Although in [54], [59], [67] the coherence of the generated pulses was already investigated by a continuous version of the cross-correlation function (6.3), all considerations were limited to the amplitude of the cross-correlation coefficient while its phase was neglected. As a consequence, the present work concludes with a different result than previous investigations: While the shape of the generated pulses from passive mode-locked oscillators are independent from the excitation regime, the phase is sensitive to the excitation regime. Only in the hard excitation regime the maximal coherency and reproducibility can be reached. In the soft excitation regime, an arbitrary phase offset between the pulses occurs. This offset is unpredictable and will change for every start-up of the oscillator because the pulses are created from noise. In the shown case with a relatively short delay time in the feedback system of 2 ns, only three different phase offsets are observed. Nevertheless, the number of contributing pulses and consequently phase offsets will increase for longer delay times.

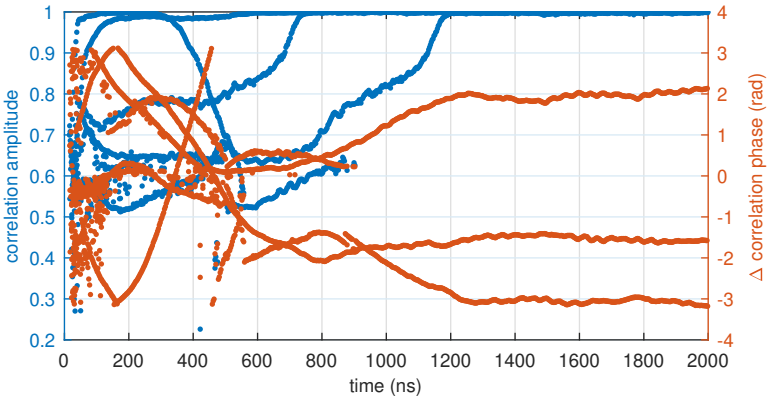

Figure 6.17: Amplitude of the cross-correlation coefficient $\overline{C}_{m,n}^{\mathrm{corr}}$ and the pulse to pulse change of the phase offset for an operation in the soft excitation regime.

6.5 Realistic Start-Up Scenarios

The previous investigations have shown that an operation in the hard excitation regime has advantages such as a controllable PRF and a high coherency of the generated pulses. In addition, the hard excitation regime would allow novel operation modes as the operation with well defined pulse sequences. For this, the passive mode-locking regime could be excited by a special pulse sequences instead of a single pulse. However, a very powerful external signal would be required for a hard excitation of the passive mode-locking.

For the presented passive mode-locked oscillator consisting of the slippage helical gyro-TWT and the helical gyro-TWT absorber, this excitation signal must have a power of at least 100 W. The only source that could provide such a powerful signal at 263 GHz in the medium run is an electron tube. That is an issue because the requirement of a third electron tube (including superconducting magnet, power supply, ...) would significantly increase the costs and the complexity of the passive mode-locked oscillator.

In this work, an innovative solution for an operation in the hard excitation regime is proposed which does not require a third high-power electron tube: the helical gyro-TWT could be replaced by a so-called high-gain helical gyro-

TWT. With this special kind of helical gyro-TWT an excitation power of $100 - 250\,\mathrm{mW}$ would be sufficient.

6.5.1 High-Gain Helical Gyro-TWT

A scheme of a high-gain helical gyro-TWT is shown in Fig. 6.18. The main difference to a classical helical gyro-TWT is the interaction region that is divided into two helically corrugated sections which are separated by a sub-cutoff waveguide section. In the high-gain helical gyro-TWT, the idea of gyrotron-type klystrons is utilized. While the helically corrugated sections are relatively short, the high gain is provided by the long sub-cutoff waveguide section that corresponds to a drift section. This idea for the realization of a high-gain helical gyro-TWT was first proposed in [148] and a first prototype for radar applications in the W-band was presented in [43].

Through an input coupler a low-power RF input signal is coupled into the first helically corrugated waveguide section. In this first section, the wave interacts with the electron beam which results in an energy modulation of the electron beam. Because the power of the input signal is very low and the helically corrugated waveguide section is short, only a minor amplification occurs and the RF can be absorbed by a short section of dielectric material with high losses immersed at the down-stream end of the section [148].

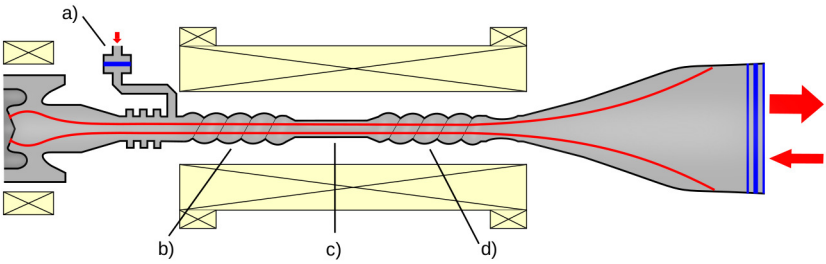

Figure 6.18: Scheme of a high-gain helical gyro-TWT with: (a) low-power input-port (b) pre-buncher section; (c) sub-cutoff drift region; (d) high-power interaction region.

In the long drift section, an effective phase bunching of the electron beam occurs. To prevent parasitic beam-wave interactions in the drift section, it is realized as a sub-cutoff waveguide.

In the second helically corrugated waveguide section, the bunched electron beam resonantly interacts with the eigenmode of the waveguide and transmits its energy to the wave. A high-power output signal is created that leaves the tube in the usual way (see chapter 3.1).

Originally, this type of helical gyro-TWT was designed because it offers the possibility of significantly increased gains (because of the long drift section) while it reduces the occurrence of parasitic oscillations at the same time. However, in this work an additional feature, which was never mentioned in the literature before, is used: A high-gain helical gyro-TWT can be fed with low-power signals through the low-power input-port or, it can be fed with high-power input signals through the output window, similar to a usual helical gyro-TWT in the single window operation (see chapter 3.1.8).

If the parameters of the second helical interaction section are matched with the previously designed helical interaction region, the high-gain helical gyro-TWT can replace the previously investigated helical gyro-TWT without the requirement of any other changes on the passive mode-locked oscillator. However, the high-gain helical gyro-TWT allows the excitation of the passive mode-locking regime by a low-power excitation signal.

To prove the suitability of the proposed high-gain helical gyro-TWT for a passive mode-locked oscillator and to show its advantages for the excitation of the passive mode-locking, in the following several simulations are performed. For the simulations, a high-gain helical gyro-TWT with two identical helical waveguide sections ($R = 0.528\,\mathrm{mm}$, $\tilde{r} = 0.08\,\mathrm{mm}$, $\tilde{d} = 1.11\,\mathrm{mm}$ and $L = 24\tilde{d}$) and a sub-cutoff drift region with a length of $66.6\,\mathrm{mm}$ is used.

The high-gain helical gyro-TWT is operated with the same electron beam as the previous helical gyro-TWT: an electron beam in the slippage regime. The usage of an electron beam in the slippage regime is novel for high-gain helical gyro-TWTs. Usually, high-gain helical gyro-TWTs are operated with an electron beam in the synchronized regime. To the knowledge of the author, it is the first time that the operation of a high-gain helical gyro-TWT with a slippage regime electron beam is shown. To increase the low-signal gain, the operation point with a $0.3\,\mathrm{A}$ amplifier electron beam is used in the following.

It must be mentioned that the used parameters (of the geometry as well as the electron beam) are probably not the optimal parameters for a high-gain helical gyro-TWT. Nevertheless, they are suitable for preliminary proof-of-concept simulations and the high-gain helical gyro-TWT reaches a gain of ≈ 35 dB for input signals with a power of 50 mW to 500 mW at 263 GHz.

6.5.2 Hard Excitation with a High-Gain Helical Gyro-TWT

To prove the suitability of the high-gain helical gyro-TWT, a hard excitation start-up of the passive mode-locked oscillator consisting of the slippage high-gain helical gyro-TWT and the helical gyro-TWT absorber is simulated. For a reduction of the required simulation time, a short delay time of 1.0 ns is used. The amplifier is operated with a beam current of 0.3 A. A 250 mW $\sin^2$ pulse with a pulse length of 0.5 ns and a center frequency of 263 GHz is used for the excitation of the passive mode-locking regime. The resulting output signal is shown in Fig. 6.19.

As in the case of the ordinary helical gyro-TWT with a beam current of 0.3 A, a decoupling factor of 0.55 is found to be ideal. It can be seen that after a short start-up phase the output power stabilizes around 1400 W which is similar to the generated output power of the oscillator with the usual helical gyro-TWT. Also the obtained pulse length of ≈ 0.12 ns is similar. However, the observed fluctuations of the output power are higher and of an almost chaotic distribution while previously a periodic oscillation of the output power was observed (see section 6.4). The reason is a parasitic self-modulation of the electron beam in the first helical waveguide section of the high-gain helical gyro-TWT. While such parasitic self-modulations are uncritical for the usual helical gyro-TWT with a short interaction region, the effect is significantly amplified in the long drift section of the helical gyro-TWT.

For a reduction of the parasitic self-modulation of the electron beam, the first helical waveguide section or the drift section could be shortened. On the other hand, this would reduce the gain of the amplifier. However, probably a carefully optimized high-gain helical gyro-TWT could reduce the parasitic self-modulation without a significant reduction of the gain. The design of such an optimized high-gain helical gyro-TWT could be a task for a following-up work.

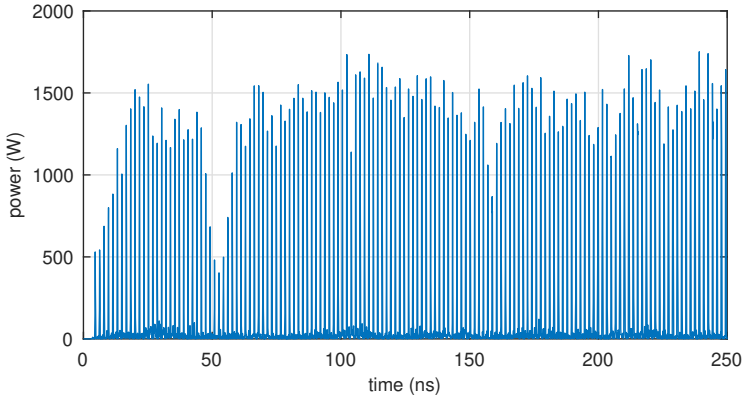

Figure 6.19: Output signal of the passive mode-locked oscillator consisting of the slippage high-gain helical gyro-TWT and the helical gyro-TWT absorber. The passive mode-locking regime is excited by an initial 250 mW pulse.

It can be concluded that the proposed usage of a high-gain helical gyro-TWT as amplifier for a passive mode-locked oscillator at sub-THz frequencies enables the operation in the hard excitation regime. This allows the creation of pulses with high coherency. Furthermore, it is a first step towards the development of new operation modes, such as the generation of well-defined pulse sequences. Such an operation could be especially of interest for novel pulsed DNP-NMR methods where well-defined pulse sequences are required [7], [149].

6.6 Conclusion

In this chapter, four different feedback loops consisting of different amplifier and absorber devices were investigated for their suitability to create a passive mode-locked oscillator at sub-THz frequencies. It was shown that a helical gyro-TWT operated in the slippage regime and a helical gyro-TWT absorber coupled in a feedback loop can be successfully operated in the passive mode-locking regime and this combination was found to be the most promising candidate for a realization.

An important finding is the requirement that the bandwidth of the absorber must exceed the bandwidth of the amplifier to avoid parasitic oscillations. Consequently, typical helical gyro-TWTs operated in the synchronized regime are inappropriate for a passive mode-locked oscillator because of their very high bandwidth and, in addition, because of the strong broadening of ultra-short pulses in these amplifiers. However, it was shown that a helical gyro-TWT operated in the slippage regime is well suited because of its efficient amplification of ultra-short pulses and the low broadening of these pulses. This finding is in good agreement with the observations made for passive mode-locking of electron tubes in the Ka-band [67].

In contrast to passive mode-locking of electron tubes in the Ka-band [59], it was shown that at sub-THz frequencies a helical gyro-TWT absorber is preferable to a cyclotron absorber because of its higher bandwidth, lower dispersion and the higher power capabilities.

A detailed study of the designed passive mode-locked oscillator was performed, and important findings were obtained. For the first time, it was shown that an excitation of the passive mode-locking in the soft excitation regime will lead to arbitrary phase offsets in the generated pulses. To maintain the phase coherency, the passive mode-locked oscillator should be operated in the hard excitation regime.

Because of a lack of the required high-power sub-THz sources ($> 100\,\mathrm{W}$) an operation in the hard excitation was unrealistic up-to now. For the first time, a solution for the operation in the hard excitation regime was proposed and verified by simulations: The usage of a high-gain helical gyro-TWT will enable the hard excitation of passive mode-locking with input signals of only several hundred milliwatt.

The proposed hard excitation operation will further enable the development of new operation modes, such as an operation with specific pulse sequences. Such an operation could be especially of interest for novel pulsed DNP-NMR methods where well-defined pulse sequences are required [7], [149].

7 Simulation Model for Passive Components

An important part of the passive mode-locked oscillator is a suitable feedback system that couples the amplifier and the saturable absorber. To enable the transmission of high-power signals with low losses, an appropriate technology for the feedback system are oversized quasi-optical components (see chapter 5). For the simulation of these components, specialized simulation tools are required that are presented in this chapter.

The feedback system is a passive structure (electric conductors in the absence of free charges) and its simulation can be well separated from the simulation of the electron tubes. For the simulation of the oversized structures in the feedback system, a simulation tool, named KarLESSS, has been developed which is based on a previously developed in-house electric field integral equation (EFIE) solver [150], [151]. With KarLESSS, the scattered electromagnetic fields of arbitrary perfect electric conductors (PECs) in free space can be calculated.

The chosen simulation model is based on a numerical solution of the EFIE and has a wide area of application. It allows an accurate simulation of structures from sizes in the sub-wavelength range up to highly oversized structures with dimensions of several hundreds of wavelengths. This wide range of applications is enabled by advanced approximation and numerical methods.

For the original EFIE solver, the method of moments (MOM) with higher order basis functions is used in combination with the adaptive cross approximation (ACA) for a compression of the resulting large system of linear equations. As part of this work, advanced compression techniques, namely the adaptive cross approximation with additional singular value decomposition (ACA-SVD) and the sparsified adaptive cross approximation (SACA) algorithms [152], [153] are implemented. To the knowledge of the author, it is the first time that the ACA-SVD and the SACA algorithms are combined with higher order basis functions and a higher order curved mesh.

Furthermore, a novel preconditioner is developed that significantly accelerates the iterative solution of the large systems of linear equations. In addition, the possibility to simulate ohmic losses for good electric conductors within the KarLESSS framework is implemented as part of this work.

In the following, a brief derivation of the EFIE and an overview of the numerical methods used for the solution of the EFIE are given. Subsequently, the novel preconditioner is presented in more detail. At the end of the chapter, a method for the calculation of the dispersion of helically corrugated waveguides using the EFIE is presented.

In the chapter 5, the developed tool KarLESSS is used for the design of the first feedback system for a sub-THz passive mode-locked oscillator.

7.1 Surface Integral Equations

For the simulation of passive components, a scattering problem must be solved. Such a scattering problem for quasi-optical components in free-space is efficiently described by EFIE. In the following, the EFIE for PECs is derived.

All expressions in this chapter are considered for a time-harmonic electric field at a single frequency ω with the corresponding harmonic current density:

$$\mathfrak{E}(\boldsymbol{r},t) = \mathrm{Re}\left\{\bar{\boldsymbol{E}}(\boldsymbol{r})\mathrm{e}^{\,j\omega t}\right\} \tag{7.1}$$

$$\mathfrak{J}(\boldsymbol{r},t) = \mathrm{Re}\left\{\bar{\boldsymbol{J}}(\boldsymbol{r})\mathrm{e}^{\,j\omega t}\right\}\ . \tag{7.2}$$

This allows a suppression of the time-dependence $\mathrm{e}^{\,j\omega t}$ in the following.

Scattering problems can be seen as radiation problems, where the currents are generated by the known incident field $\bar{\boldsymbol{E}}^i$. The currents then radiate the scattered field $\bar{\boldsymbol{E}}^s$.

For a known current density $\bar{\boldsymbol{J}}$, the solution of the radiation problem is simple: an integration over $\bar{\boldsymbol{J}}$ gives the radiated electric field [154]

$$\bar{\boldsymbol{E}}^r(\boldsymbol{r}) = -j\omega\mu \iiint_V \bar{\mathrm{G}}(\boldsymbol{r},\boldsymbol{r}')\left[\bar{\boldsymbol{J}}(\boldsymbol{r}') + \frac{1}{k^2}\nabla'\nabla'\cdot\bar{\boldsymbol{J}}(\boldsymbol{r}')\right]\mathrm{d}\boldsymbol{r}'\ , \tag{7.3}$$

where $\overline{\mathrm{G}}(\boldsymbol{r}, \boldsymbol{r}')$ is the free space Green's function [154]

$$\overline{\mathrm{G}}(\boldsymbol{r}, \boldsymbol{r}') = \frac{\mathrm{e}^{-jk|\boldsymbol{r}-\boldsymbol{r}'|}}{4\pi|\boldsymbol{r}-\boldsymbol{r}'|} \,. \tag{7.4}$$

Here, k is the free space wave number

$$k = \omega\sqrt{\epsilon\mu} = \frac{2\pi}{\lambda} \,, \tag{7.5}$$

and λ denotes the wavelength.

However, in contrast to a radiation problem the current density is unknown in a scattering problem. Therefore, (7.3) has to be solved for an unknown current density $\overline{\boldsymbol{J}}(r)$, induced by the known incident field $\overline{\boldsymbol{E}}^i(r)$. Afterwards, the radiated electric field $\overline{\boldsymbol{E}}^r(r)$ can be calculated by an integration over the induced currents using (7.3) and the scattered field $\overline{\boldsymbol{E}}^s$ is given as

$$\overline{\boldsymbol{E}}^s(\boldsymbol{r}) = \overline{\boldsymbol{E}}^i(\boldsymbol{r}) + \overline{\boldsymbol{E}}^r(\boldsymbol{r}) \,. \tag{7.6}$$

If PECs are assumed exclusively, the induced currents circulate on a surface instead of a volume and (7.3) reduces to:

$$\overline{\boldsymbol{E}}^r(\boldsymbol{r}) = -j\omega\mu \iint\limits_S \overline{\mathrm{G}}(\boldsymbol{r}, \boldsymbol{r}') \left[\overline{\boldsymbol{J}}(\boldsymbol{r}') + \frac{1}{k^2}\nabla'\nabla' \cdot \overline{\boldsymbol{J}}(\boldsymbol{r}')\right] \mathrm{d}\boldsymbol{r}' \tag{7.7}$$

Equation (7.7) can be solved by utilizing the boundary condition for the tangential electric field on a PEC:

$$\hat{\boldsymbol{n}}(\boldsymbol{r}) \times \overline{\boldsymbol{E}}^s(\boldsymbol{r}) = -\hat{\boldsymbol{n}}(\boldsymbol{r}) \times \overline{\boldsymbol{E}}^i(\boldsymbol{r}) \,. \tag{7.8}$$

Here, $\hat{\boldsymbol{n}}$ is the normal of the PEC surface. Applying (7.7) to (7.8) leads to the so called electric field integral equation (EFIE) [154]:

$$-\frac{j}{\omega\mu}\hat{\boldsymbol{n}}(\boldsymbol{r}) \times \overline{\boldsymbol{E}}^i(\boldsymbol{r}) = \hat{\boldsymbol{n}}(\boldsymbol{r}) \times \iint\limits_S \overline{\mathrm{G}}(\boldsymbol{r}, \boldsymbol{r}') \left[\overline{\boldsymbol{J}}(\boldsymbol{r}') + \frac{1}{k^2}\nabla'\nabla' \cdot \overline{\boldsymbol{J}}(\boldsymbol{r}')\right] \mathrm{d}\boldsymbol{r}' \tag{7.9}$$

Once solved for the current density $\overline{\boldsymbol{J}}(\boldsymbol{r})$, the scattered field at every point in space can be obtained by applying (7.6).

7.2 Numerical Solution

The most common numerical method for the solution of the EFIE is the MOM [155]. In the MOM, the current density is expanded into a sum of N weighted basis functions $\mathbf{f}$:

$$\bar{\boldsymbol{J}}(\boldsymbol{r}) = \sum_{n=1}^{N} \bar{a}_n \mathbf{f}(\boldsymbol{r}) \ . \tag{7.10}$$

Applying the expansion to (7.9), a residuum

$$R_{\mathrm{res}} = \|\mathcal{K}(\bar{\boldsymbol{J}}) - \sum_{n=1}^{N} \bar{a}_n \mathcal{K}(\mathbf{f})\| \tag{7.11}$$

can be defined, where $\mathcal{K}$ represents an arbitrary linear operator, which in this case is the linear operator corresponding to the EFIE. By the method of Galerkin [156], (7.11) is transformed into a system of linear equations that can be solved afterwards for the unknowns $\bar{a}_n$:

$$\bar{\boldsymbol{V}} = \bar{\boldsymbol{a}}\underline{\boldsymbol{M}} \tag{7.12}$$

with

$$\left(\bar{\boldsymbol{V}}\right)_m = \left\langle \mathbf{f}_m, \bar{\boldsymbol{E}}^i \right\rangle \ , \tag{7.13}$$

$$\left(\underline{\boldsymbol{M}}\right)_{m,n} = \langle \mathbf{f}_m, \mathcal{K}(\mathbf{f}_n) \rangle \ . \tag{7.14}$$

Here $\langle \cdot, \cdot \rangle$ donates the inner product. In the following, the matrix $\underline{\boldsymbol{M}}$ is referenced to as system matrix and the vector $\bar{\boldsymbol{V}}$ as the input vector.

In KarLESSS, two sets of basis functions are implemented: the Rao-Wilton-Glisson basis functions (RWG) [157] and a particular set of higher-order basis functions (HOBF) [158].

For a 3D problem, it is useful to approximate a surface by a series of triangles. Accordingly, both sets of basis functions are defined for triangular patches. While the RWG are basis functions of zeroth order, defined for planar triangles, the HOBF are of first order and support curved triangles. For surfaces with non-constant, slowly changing normal vectors, this approach results in a better approximation of the original surface than with flat triangles of similar size.

The complete formulas for the calculation of the system matrix and input vector elements for the RWG as well as the HOBF can be found in [150].

7.2.1 Adaptive Cross Approximation

The non-local kernel of the EFIE, namely the Green's function, causes a dense system matrix. Consequently, the calculation and storage requirements are of order $O(N^2)$, where N denotes the number of unknowns. Even if the system of linear equations is solved by an iterative solver, it would be impossible to solve the EFIE for highly oversized scatterers. Additionally, the computation costs for every matrix-vector product, required for the iterative solution of the system of linear equations, are of $O(N^2)$ complexity as well.

To overcome this problem, the ACA algorithm [159] is used to reduce the calculation time and storage overheads in the MOM. With the ACA algorithm, the system matrix can be compressed in a purely algebraic manner. The premise of the ACA algorithm is that interactions of well-separated parts of the geometry result in rank-deficient system matrices. Therefore, the dense system matrix $\underline{M}$ consists of many numerically rank deficient sub-matrices $\underline{M}^{m\times n}$.

The ACA uses this property to compresses the sub-matrices efficiently by a rank-revealing lower-upper (LU) decomposition. Every $\underline{M}^{m\times n}$ is approximated by a compressed sub-matrix $\underline{\tilde{M}}^{m\times n}$ which can be written as an outer product of two matrices

$$\underline{M}^{m\times n} \approx \underline{\tilde{M}}^{m\times n} = \underline{U}^{m\times r}\,\underline{V}^{r\times n} \,, \tag{7.15}$$

where r is the rank of the approximated matrix $\underline{\tilde{M}}$. If r satisfies the condition

$$r < \frac{m\cdot n}{m+n} \,, \tag{7.16}$$

the approximated matrix $\underline{\tilde{M}}$ requires a lower amount of memory and can be calculated faster than the exact matrix $\underline{M}$.

An advantage of the ACA algorithm is its iterative calculation of $\underline{\tilde{M}}$ (details can be found in [159]). Because of this iterative calculation, the compressed matrix can be calculated with only a partial knowledge of the original matrix

which reduces the calculation time in the same order as the required amount of memory.

7.2.2 Sparsified Adaptive Cross Approximation

The complexity of the ACA is in the order of $O(N^{3/2}\log(N))$ which is not as good as other approximation methods, e.g. the multilevel fast multipole method (MLFMM) [160]. Moreover, for electrical large problems with a size of more then 50 wavelength, the scaling of the ACA algorithm can even decline [153]. To overcome this undesirable behavior, several optimizations have been developed in the last years [153], [161].

In the frame of this work, the SACA [153] is implemented that can successfully reduce the complexity, even for highly oversized problems. Because a basic understanding of the SACA is required for the new developed preconditioner, a short overview over the SACA is given in the following.

The SACA introduces a further compression of the ACA impedance matrices $\underline{\tilde{M}}_{m,n}$ which describe the interaction between two domains D_m and D_n. In a first step, the basis functions of the domains D_m and D_n are sampled, and a new system matrix for these samples $\underline{\tilde{M}}_{s_m,s_n}$ is calculated.

In a second step, the domains D_m and D_n are subdivided into smaller subdomains $d_{m,k}$ and $d_{n,l}$. In the developed implementation, an octree is used to create the domains and subdomains.

Next, a system matrix $\underline{\tilde{M}}_{s_m,d_{n,l}}$ for the interaction of the samples in D_m and every individual subdomain $d_{n,l}$ of D_n is calculated. For the calculation of $\underline{\tilde{M}}_{s_m,d_{n,l}}$, the ACA-SVD [162] is used instead of the ordinary ACA algorithm.

In the ACA-SVD, the matrices $\underline{U}$ and $\underline{V}^{\mathrm{T}}$ of the usual ACA (see (7.15)) are recompressed by a singular value decomposition (SVD). This is possible, since $\underline{U}$ and $\underline{V}^{\mathrm{T}}$ are not orthogonal to each other. To further compress $\underline{U}$ and $\underline{V}^{\mathrm{T}}$, first a QR decomposition of both matrices is computed:

$$\underline{U} = \underline{Q}_{\mathrm{U}}\underline{R}_{\mathrm{U}} \,, \tag{7.17}$$

$$\underline{V}^{\mathrm{T}} = \underline{R}_{\mathrm{V}}^{\mathrm{T}}\underline{Q}_{\mathrm{V}}^{\mathrm{T}} \,. \tag{7.18}$$

The outer product of the two upper triangular matrices $\underline{R}_{\mathrm{U}}$ and $\underline{R}_{\mathrm{V}}^{\mathrm{T}}$ is then decomposed using a threshold SVD:

$$\underline{R}_{\mathrm{U}}\underline{R}_{\mathrm{V}}^{\mathrm{T}} = \hat{\underline{U}}\hat{\underline{\Sigma}}\hat{\underline{V}}^{\mathrm{T}} \ . \tag{7.19}$$

In the threshold SVD, all singular values below a threshold are removed from $\hat{\underline{\Sigma}}$ and $\tilde{\underline{M}}_{s_m,d_{n,l}}$ is given by

$$\tilde{\underline{M}}_{s_m,d_{n,l}} = \underline{U}\underline{V}^{\mathrm{T}} = \underline{Q}_{\mathrm{U}}\hat{\underline{U}}\hat{\underline{\Sigma}}\left(\underline{Q}_{\mathrm{V}}\hat{\underline{V}}\right)^{\mathrm{T}} = \underline{U}_{s_m,d_{n,l}}\hat{\underline{\Sigma}}_{s_m,d_{n,l}}\underline{V}_{s_m,d_{n,l}}^{\mathrm{T}} \ . \tag{7.20}$$

In a similar manner, the interaction $\tilde{\underline{M}}_{d_{m,k},s_n}$ of the samples in D_n and all subdomains of D_m are calculated.

From the matrices $\tilde{\underline{M}}_{s_m,d_{n,l}}$ and $\tilde{\underline{M}}_{d_{m,k},s_n}$, the interaction of the subdomains $d_{m,k}$ and $d_{n,l}$ can be reconstructed:

$$\begin{aligned}
\tilde{\underline{M}}_{d_{m,k},d_{n,l}} &= \tilde{\underline{M}}_{s_m,d_{n,l}}\tilde{\underline{M}}^{-1}_{s_m,s_n}\tilde{\underline{M}}_{d_{m,k},s_n} \\
&= \underline{U}_{s_m,d_{n,l}}\left(\hat{\underline{\Sigma}}_{s_m,d_{n,l}}\underline{V}^{\mathrm{T}}_{s_m,d_{n,l}}\tilde{\underline{M}}^{-1}_{s_m,s_n}\underline{U}_{d_{m,k},s_n}\hat{\underline{\Sigma}}_{d_{m,k},s_n}\right)\underline{V}^{\mathrm{T}}_{d_{m,k},s_n} \\
&= \underline{U}_{s_m,d_{n,l}}\underline{K}_{d_{n,l},d_{m,k}}\underline{V}^{\mathrm{T}}_{d_{m,k},s_n} \ .
\end{aligned} \tag{7.21}$$

Here, the dimension of the inner matrix $\underline{K}_{d_{n,l},d_{m,k}}$ corresponds to the ranks of $\tilde{\underline{M}}_{s_m,d_{n,l}}$ and $\tilde{\underline{M}}_{d_{m,k},s_n}$, which are usually small.

In a last step, the impedance matrices for all the subdomains can be combined into one sparse sequence approximation

$$\tilde{\underline{M}}_{m,n} = \underline{U}^s_{m,n}\underline{K}_{m,n}\left(\underline{V}^s_{m,n}\right)^{\mathrm{T}} \ , \tag{7.22}$$

where $\underline{U}^s_{m,n}$ and $\underline{V}^s_{m,n}$ are block-diagonal matrices and $\underline{K}_{m,n}$ is a dense matrix. To further reduce the memory requirements, an additional ACA-SVD compression of $\underline{K}_{m,n}$ can be performed.

In the original publication [153], the SACA is used together with the RWG basis functions. In the new developed implementation, the SACA is combined with HOBF and a higher order curved mesh. To the knowledge of the author, it is the first time that the ACA-SVD and SACA algorithms are combined with higher order basis functions and a higher order curved mesh.

7.3 New Zero-Cost Preconditioner

After the calculation of the compressed system matrix via the ACA, ACA-SVD or SACA algorithms, the system of linear equations (7.12) must be solved. Since the number of equations rapidly increases for large geometries ($O(n^2)$), it is not suitable to solve it with a Gaussian elimination or an other direct method. Therefore, an iterative solution method, namely the generalized minimal residual method (GMRES), is used.

7.3.1 GMRES with Preconditioner

The GMRES is a Krylov subspace method and was original proposed by Yousef Saad and Martin H. Schultz in 1986 [163]. In the GMRES, the solution is approximated by forming a vector with minimal residual in a Krylov subspace, which is found by an Arnoldi process [164].

For the iterative solution of the system of linear equations resulting from the discretization of the EFIE, it is a well-known problem that the convergence property of Krylov subspace methods gets worse as the problem size increases. The condition number of the system matrix increases and, hence, the number of required iterations needed to solve the matrix equation increases [165].

A preconditioner can be used to reduce the condition number of the system matrix and, therefore, to reduce the number of iterations required for a solution of the system of linear equations. In a so-called right preconditioned system, the following modified system of linear equations is solved:

$$\underline{M}\underline{P}^{-1}\left(\underline{P}\bar{\boldsymbol{a}}\right) = \bar{V} \,. \tag{7.23}$$

Several different candidates for suitable preconditioner matrices $\underline{P}$ for the EFIE were investigated in the past such as LU decomposition-based preconditioner [166] or analytical preconditioner [167].

In [168], an alternative preconditioning approach is presented: It is proposed to including a second, inner iterative solver to the GMRES that is executed during every iteration step of the outer solver. The underlying idea is that the

matrix $\underline{M}\underline{P}^{-1}$ in (7.23) does not need to be formed explicitly. Instead, only the equation

$$\underline{P}\bar{\boldsymbol{y}} = \bar{\boldsymbol{b}} \tag{7.24}$$

for an arbitrary vector $\bar{\boldsymbol{b}}$, can be solved whenever such an operation is required during the iterative solution of (7.23) by the GMRES.

For the solution of the inner system of linear equations (7.24), again the GMRES can be used (or every other iterative solver). The extension of the ordinary GMRES to an inner-outer solver is often called flexible generalized minimal residual method (FGMRES). The FGMRES algorithm with two nested GMRES solvers is well suited for the solution of large, preconditioned systems of linear equations.

7.3.2 FGMRES with Zero-Cost Preconditioner

The approach of nested iterative solvers is applied to the EFIE for example in [169]. They used the fast multipole method (FMM) to approximate the EFIE and decided to nest a second FMM approximation with low accuracy as preconditioner in an inner-outer FGMRES solver. In other words, a low accuracy approximation of the system matrix is used as preconditioner. Depending on the problem and the number of unknowns, an acceleration of the calculations by a factor of $2-3$ was observed in [169].

In [170], this idea is transferred to the MLFMM. They observed a speed-up of a factor of 2 compared to the nested FMM by the usage of a low accuracy MLFMM for the inner solver. This corresponds to an acceleration of the calculations by the factor 4-5 compared to a solver without preconditioner.

The idea of using a coarse approximation of the system matrix as a preconditioner is transferred to the ACA algorithm in [171]. It was shown that this approach is more advantageous for the ACA than for the previous investigated FMM based methods. In the cases of an inner FMM [169] as well as an inner MLFMM [170], an additional low accuracy approximation of the system matrix must be calculated which requires additional calculation time and memory. This is not the case for an inner ACA solver. A low accuracy approximation ACA solver can be implemented without the need to calculate an additional system matrix and therefore without any additional memory requirements or

additional calculation-steps. Therefore, this preconditioner is referenced as a 'zero-cost preconditioner' in the following.

In the ACA based algorithms, the system matrix is approximated by many low-rank submatrices. As lower the rank of the submatrices, as coarser the approximation of the original system matrix. Consequently, if a low accuracy approximation of the system matrix should be used as preconditioner, the rank of the ACA submatrices must be further decreased. Fortunately, this is simple.

Assumed, a submatrix is compressed by the ACA according to (7.15)

$$\underline{M}^{m\times n} \approx \underline{\tilde{M}}^{m\times n} = \underline{U}^{m\times r}\underline{V}^{r\times n} \ , \tag{7.25}$$

then the rank of the matrix $\underline{\tilde{M}}$ is determined by the dimension r of the matrices $\underline{U}$ and $\underline{V}$. To further decrease the rank, it is sufficient to remove a corresponding number of rows/columns from the matrices $\underline{U}$ and $\underline{V}$. This results in a significant speed up of the solution process since the cost of a matrix-vector product decreases with the rank of the submatrices. It should be noted that no additional memory is required because the lower rank system matrix is a subset of the original system matrix.

In this work, the zero-cost preconditioner is extended for the advanced ACA-SVD and SACA methods. The basic idea remains the same. For the ACA-SVD, the approach of removing rows/columns from the matrices $\underline{U}$ and $\underline{V}$ can be kept, if the matrices $\hat{\underline{\Sigma}}$ and $\hat{\underline{V}}^{\mathrm{T}}$ in (7.20) are multiplied first to derive a new $\underline{V}'$. This allows to reduce the rank of the system matrix by removing rows/columns from the matrices $\underline{U}$ and $\underline{V}'$.

For the SACA, the approach has to be changed: The compressed system matrix in the SACA is a product of 5 matrices:

$$\underline{\tilde{M}}^{m\times n} = \underline{U}_S^{m\times r}\underline{U}_T^{r\times k}\underline{\Sigma}_T^{k\times k}\left(\underline{V}_T^{r\times k}\right)^{\mathrm{T}}\left(\underline{V}_S^{n\times r}\right)^{\mathrm{T}} \ . \tag{7.26}$$

The diagonal matrix $\underline{\Sigma}_T$ with the singular values of the SVD can be included into $\underline{V}_T$ to derive a new $\underline{V}'_T$. Now, the rank r of the system matrix can be reduced $r \rightarrow r'$ by removing rows/columns from the matrices $\underline{U}_S$, $\underline{U}_T$, $\underline{V}'_T$ and $\underline{V}_S$.

In the following it is shown that the new zero-cost preconditioner for the ACA-SVD and SACA methods has a great performance and can clearly out-perform the original zero-cost preconditioner presented in [171].

7.3.3 Performance of the Zero-Cost Preconditioner

The advantages of the new zero-cost preconditioner are proven by numerical experiments with two different simulation setups, one of medium-size with 250 000 unknowns and one of large-size with 1 500 000 unknowns (see Fig. 7.1). The numerical experiments are carried out for problems of different size, since the condition number of the system matrix increases with the problem size and as a result, the convergence behavior of the solving algorithms becomes worse. However, a good preconditioner should compensate this effect.

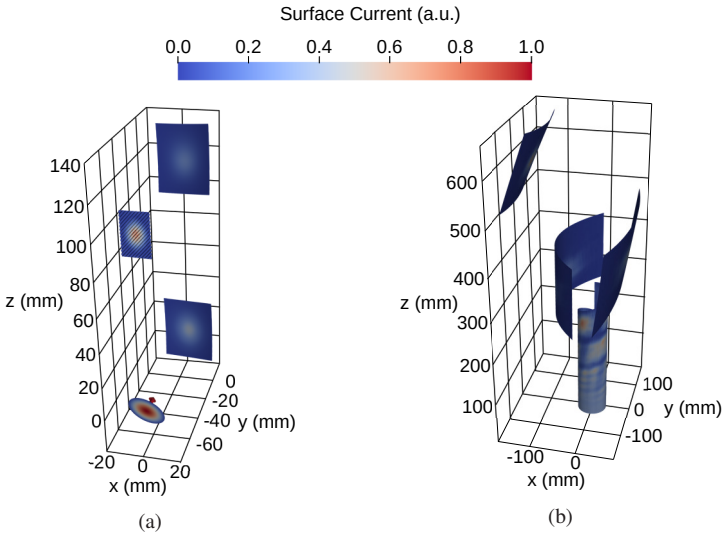

Figure 7.1: Test cases used for the evaluation of the zero-cost preconditioner. (a) Mirror system consisting of two parabolic and one sinusoidal graded mirror, designed for an incident Gaussian beam at 263 GHz; (b) Quasi-optical system of a 2 MW gyrotron [172], operated at 170 GHz, consisting of a waveguide antenna with a helical cut and three parabolic mirrors.

As medium size simulation case, a mirror system consisting of two parabolic and one sinusoidal graded mirror, designed for an incident Gaussian beam at 263 GHz (see Fig. 7.1a), is used. For the large-size problem, the quasi-optical system of a 2 MW gyrotron [172], operated with a $\mathrm{TE}_{34,19}$ cavity mode at 170 GHz, is used. The quasi-optical system consists of a waveguide antenna with a helical cut (the launcher) and three parabolic mirrors (see Fig. 7.1b).

Simulations are performed for both setups, all three ACA algorithms (ACA, ACA-SVD and SACA), with and once without preconditioner, respectively. In all cases, bi-cubic curved surfaces and first order basis functions are used. For the preconditioner, the rank for the submatrices is restricted to $r' = 3$ and the inner GMRES is terminated after 8 iterations. The simulations are performed on a dual-socked server with AMD EPYC 7452 Processors and 1 TB of available RAM.

Medium-Size Test-Case

In table 7.1, the results for the simulated mirror system (medium-size problem) are given. As expected, the memory required to store the compressed system matrix decreases from ACA over ACA-SVD to the SACA.

The time required to calculate the compressed impedance matrices $\underline{\tilde{M}}$ is similar for the ACA and ACA-SVD algorithm. This is not surprising because both algorithms are almost identical, the only difference is an additional SVD compression in the ACA-SVD. Since this compression is not computationally intensive, the required calculation times hardly differ. The SACA algorithm is slightly faster, since a lower number of interaction terms must be evaluated. The reason is the introduced sampling of the domains.

For all three ACA algorithms, the preconditioned solver for the system of linear equations clearly outperforms the ordinary GMRES without preconditioner. A significant speed-up by a factor of 3 is observed. While the number of iterations required to solve the system of linear equations is similar for all ACA algorithms, the required time decreases, from the ACA over ACA-SVD to the SACA. This is due to the fact that matrix-vector multiplications for large dense matrices are data-movement bandwidth bounded processes [173]. If less data has to be transferred from the RAM to the processors, the multiplication can be performed faster.

Table 7.1: Required time to solve a medium-size system of linear equations with 250 000 unknowns for the different ACA algorithms with (FGMRES) and without (GMRES) zero-cost preconditioner. The number of required iterations is given in brackets. For the FGMRES, only the number of outer iterations is given. In addition, the time and memory required to calculate and store the compressed impedance matrices is given.

	ACA	SVD-ACA	SACA
Memory	18.0 GB	12.0 GB	11.5 GB
$\underline{\tilde{M}}$-calc.	3:40 min	3:41 min	3:15 min
GMRES	33:38 min (1198)	31:31 min (1211)	30:12 min (1210)
FGMRES	11:09 min (199)	10:33 min (199)	9:05 min (202)

Large-Size Test-Case

The results for the quasi-optical system (large-size problem) are given in table 7.2. Compared to the previous medium-size case, the memory saving is more significant for the ACA-SVD and the SACA. This is an expected behavior. A known problem of the classical ACA is the decreased performance for highly oversized problems. The degrees of freedom grow for increasing problem sizes and this leads to inferior compression rates [153], [159]. This explains how the additional SVD compression can almost halve the memory required for the large-size case, while only small savings were possible for the medium-size case.

There are no surprises regarding the computing time needed to construct the system matrix. The behavior is similar to the previous example. However, there are significant differences in the performance when solving the linear systems of equations. First of all, it is noticeable that the GMRES solver requires more time for the ordinary ACA algorithm than for the ACA-SVD and SACA. This is again due to the larger system matrix which slows down the calculation of a single iteration. It must be noted that the FGMRES for the ordinary ACA takes three times longer than for the other two ACA algorithms.

In order to understand this, it is helpful to reconsider how the zero-cost preconditioner works. In the preconditioning step, the same physical problem as in the overall solver is solved. The difference is that the problem is strongly simplified

Table 7.2: Required time to solve a large-size system of linear equations with 1 500 000 unknowns for the different ACA algorithms with (FGMRES) and without (GMRES) zero-cost preconditioner. The number of required iterations is given in brackets. For the FGMRES, only the number of outer iterations is given. In addition, the time and memory required to calculate and store the compressed impedance matrices is given.

	ACA	SVD-ACA	SACA
Memory	403 GB	210 GB	109 GB
$\underline{\tilde{M}}$-calc.	2:19 h	2:20 h	2:08 h
GMRES	4:09 h (860)	3:18 h (843)	3:26 h (936)
FGMRES	2:49 h (334)	0:48 h (93)	0:45 h (103)

in order to solve it with less computing effort. This approach accelerates the solution process if the computing effort required to solve the reduced problem is significantly decreased and, at the same time, the information encoded in the reduced problem remains high.

This is fulfilled for the compressed impedance matrices created by the ACA algorithm. In the ACA algorithm, the low-rank approximation of the full matrix is constructed in an iterative matter: In every iteration, the remaining strongest interacting parts of the full matrix are extracted and the rank of the compressed matrix is increased by one. Usually, the gain on information in ever iteration decreases with increasing rank. Exactly this fact is exploited by the preconditioner.

For a highly approximated system matrix with very low rank, the saving of computing time needed to solve the resulting system of equations is much higher than the loss of information. However, as the size of the simulated problem increases, this advantage decreases, because the compression loses efficiency. Thus, a matrix of very low-rank does not contain enough information to describe the original physical problem sufficiently well and the preconditioner loses efficiency.

This problem is solved by the ACA-SVD. The SVD compression has the property of sorting the columns and rows of the compressed matrix according to their information content. As a result, a matrix with a very low rank

contains disproportionately much information. The result of this can be seen in table 7.2, the extended zero-cost preconditioner achieves a speed-up of the factor 4.5 compared to the case without preconditioner.

Comparison with Other Preconditioners

A comparison with other preconditioner algorithms is difficult. For a reliable comparison, the following conditions must be met: (1) an implementation in the same framework of all preconditioners under investigation is necessary; (2) all simulations must be performed on the same hardware; (3) all simulations must be performed with the same simulation cases. If one of these conditions is not met, unpredictable effects may occur. Nevertheless, a qualitative comparison to other preconditioners is given in the following.

First, a comparison of the developed ACA preconditioner with the originally proposed ACA preconditioner [171] is performed. For the developed implementation a speed-up of 1.6 compared to the case without preconditioner is observed for a simulation with $1\,500\,000$ unknowns. This is in a good agreement with the speed-up given in [171], where a speed-up of 1.5 for a comparable simulation setup is observed. For the medium-size problem of $250\,000$ unknowns, a speed-up of 2.8 is observed in this work while in [171] a speed-up of 2.2 for a simulation case with $110\,000$ unknowns is observed. The results are in a good agreement. The overall tendency of a decreasing efficiency for an increasing number of unknowns is clearly observed in both implementations.

As shown, the performance of the ACA preconditioner can be significantly improved if it is transferred to the ACA-SVD and SACA algorithms. For a classification of the results, a comparison is made with other preconditioner algorithms. A good candidate for a comparison is the preconditioner presented in [169]. It also uses a FGMRES solver with an inner GMRES and a low accuracy approximation FMM as preconditioner. For a simulation case with more than $1\,000\,000$ unknowns, the FMM based preconditioner achieves an acceleration of ≈ 2.

A second candidate for a comparison is the preconditioner presented in [170]. It is again based on an inner-outer FGMRES solver, but in combination with the

MLFMM. For a similar simulation setup with more than $1\,000\,000$ unknowns, the MLFMM based preconditioner in [170] achieves an acceleration of ≈ 4.

For the SACA zero-cost preconditioner, also a speed-up of ≈ 4 is observed for a comparable simulation case. Therefore, it can be concluded that the new zero-cost preconditioner for advanced ACA algorithms has a similar or even better performance as comparable preconditioners. However, a great advantage of the zero-cost preconditioner compared to other preconditioners is its simplicity. The implementation of the preconditioner should be possible in every implementation of the ACA algorithm or its derivatives. Furthermore, its zero-cost nature is a unique advantage compared to other preconditioner techniques. Based on the results an additional SVD compression of the ACA sub-matrices can be highly recommended. The additional compression has almost no computational overhead, reduces significantly the required memory and improves the efficiency of the zero-cost preconditioner.

7.4 Implementation and Verification

The presented methods for solving the EFIE are implemented in the program KarLESSS, which is written in an object-oriented manner in the programming language C++. For algebraic operations the library Armadillo [174] is used.

An advantage of the ACA based algorithms is the easy implementation for parallel computing. The developed implementation supports parallelized calculations on multiple cores of shared memory systems as well as on several devices in distributed memory systems. For a further speed-up, the post-processing calculations can be accelerated via a GPU. The parallelization is implemented via OpenMP [175] on shared memory systems and MPI [176] on distributed memory systems. The GPU routines are implemented in the CUDA language [177].

In addition, an interface for further post-processing and evaluation operations in MATLAB, with a large selection of helpful scripts, is provided. The implementation provides a high flexibility and the possibility for further developments and optimizations.

In Fig. 7.2, a flowchart for a simulation with KarLESSS is given. A simulation can be divided into the four major steps: mesh generation, calculation of the

surface currents by solving of the EFIE, calculation of the physical fields in a post-processing step and evaluation of the simulation results.

In the first step, the geometry for the object under investigation is defined and a triangular mesh representing the geometry is generated. In KarLESSS, an own mesh generator is available. In addition, an interface for external mesh generators (e.g. NETGEN [178]) is provided.

A special feature of KarLESSS is the support of curved surfaces of arbitrary order. The internal mesh generator (SurfaceCreator) is especially useful for the generation of meshes for surfaces which are provided as analytical functions or as point clouds (point clouds are often the result of synthesis processes). The SurfaceCreator generates curved meshes of second order with C^1 continuity over the complete surface (if the surface itself is of C^1 continuity). This is a very special feature, since state-of-the-art high order mesh generators ensure C^1 continuity only inside a mesh element while C^0 continuity between the elements is provided.

In the second step, the system matrix for the previously generated meshes is calculated. The system matrix can be calculated via several different ACA algorithms (ACA, ACA-SVD, SACA) and for basis functions of different orders. The matrix calculation is very computational intensive and therefore, implemented in a parallized form and highly optimized. The computationally most intensive step is the evaluation of the Green's function in the EFIE. To speed-up this calculation intensive step, a special implementation using the AVX2 Single Instruction-Multiple-Data (SIMD) instructions [179] for the exponential function is developed.

In the third step, the system of linear equations is solved. Three different solving algorithms are implemented in KarLESSS. For small problems up to several thousands of unknowns, the system of linear equations can be solved by a direct solver based on the Gaussian elimination. For larger problems (up to several millions of unknowns), two iterative solvers are available, the GMRES and the FGMRES. Because neither additional processor capacity nor additional memory is required for the previously presented 'zero-cost preconditioner', the FGMRES solver with zero-cost preconditioner should be always preferred to the ordinary GMRES solver.

The surface currents on the investigated geometry are the solution of the EFIE. From the surface currents, all physical values of interest can be calculated. In

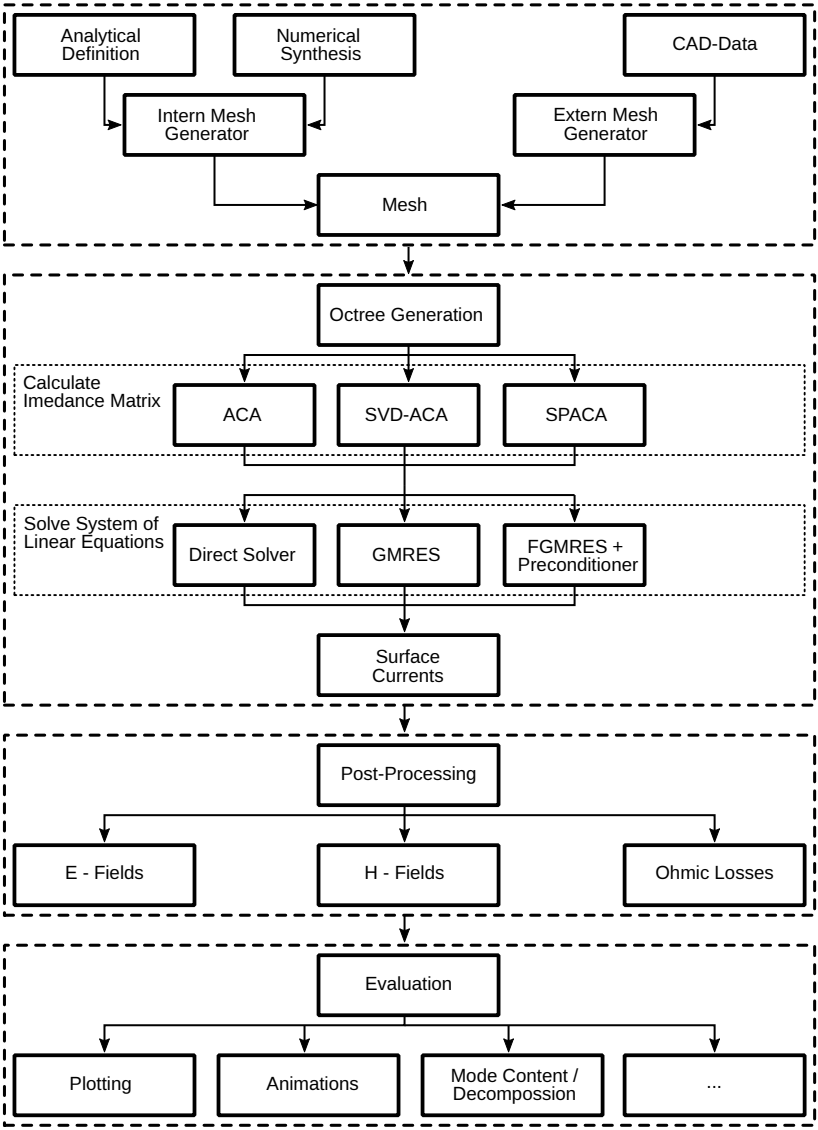

Figure 7.2: Flowchart of the simulation process with the KarLESSS framework.

the post processing step, the electromagnetic fields are calculated with equation (7.3). Since (7.3) can be solved independently for every point of interest, the post-processing step is a perfect candidate for an acceleration via GPUs, which are optimized for the parallel execution of many independent calculations.

An important step in the development of simulation programs is the verification of the developed methods and implementations. In appendix A.3, the electric fields as well as the ohmic losses simulated with KarLESSS are verified by a comparison with measurements.

7.5 Dispersion of Helically Corrugated Waveguides

As presented in chapter 3.1.1, the dispersion of a helically corrugated waveguide can be described analytically with the method of perturbation and coupled modes. For example a threefold, right-handed, helical corrugation couples the right-handed $\mathrm{TE}_{2,1}$ mode with the left-handed $\mathrm{TE}_{-1,1}$ mode. However, this method provides reasonable accuracy only if the corrugation depth is small compared to the operating wavelength. For cases that do not fulfill this restrictions or for the calculation of the dispersions of higher order modes, alternative methods based on finite-element eigenmode solvers can be used (see [180] and [181]).

In [182], the author proposed that the dispersion of a helically corrugated waveguide can be also efficiently calculated with EFIE based simulation tools such as KarLESSS. The possibility, provided by KarLESSS, to model the geometry of the waveguide with high order, curved, triangular patches, allows a particularly accurate modeling of helically corrugated waveguides without the requirement of extremely fine meshes. In addition, the benefit of methods based on the MOM and the EFIE compared to finite-element methods is that they are devoid of numerical dispersion and dissipation effects.

To calculate the dispersion of a waveguide structure (in general, an arbitrary, straight waveguide can be investigated) with KarLESSS, simulations of the waveguide under investigation are performed at different frequencies and the radial electric field distribution along a line parallel to the z axis is taken. With a spatial Fourier transformation of the field distribution, the axial wavenumber

$k_\parallel$ is determined. A similar approach is used in [180], however, in combination with a finite-element solver instead of a EFIE solver.

The accuracy of the simulated $k_\parallel$ values is mainly influenced by the length of the simulated waveguide section. A convergence study and comparisons with finite-element eigenmode solvers have shown that a length of $\approx 100\,\tilde{d}$ is sufficient for helically corrugated waveguides at sub-THz frequencies.

On a modern workstation, the simulation of a single frequency point can be performed in less than 1 minute with the tool KarLESSS. Depending on the desired resolution, 20-50 frequency points are typically sufficient.

As an example, the dispersion relation for a threefold helically corrugated waveguide with $R = 0.534\,\text{mm}$, $\tilde{r} = 0.085\,\text{mm}$ and $\tilde{d} = 1.6\,\text{mm}$, designed for a 263 GHz helical gyro-TWT, is shown in Fig. 7.3. The blue points correspond to the dispersion simulated with KarLESSS. For a comparison, the dispersion calculated with a 2D finite-element eigenmode solver [181] is shown in purple. Both results are in a good agreement.

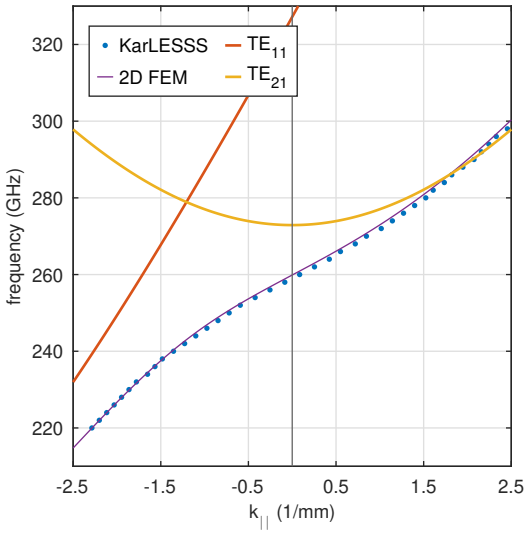

Figure 7.3: Dispersion of a threefold helically corrugated waveguide ($R = 0.534\,\text{mm}$, $\tilde{r} = 0.085\,\text{mm}$ and $\tilde{d} = 1.6\,\text{mm}$), calculated with KarLESSS (blue) and a 2D finite-element eigenmode solver [181] (purple).

8 Design of the Feedback System

The amplifier and absorber devices are realized in two separate electron tubes and, therefore, a feedback system is required to couple them in a feedback loop. The feedback system has to fulfill several requirements: it must provide a high bandwidth, low losses and must be suitable for high-power signals. Because the previous investigation in chapter 6 has shown that a very specific decoupling factor is required to enable the passive mode-locking regime, a variable decoupling coefficient is essential. Low back-reflections are also required ($S_{11} < -30\,\mathrm{dB}$) to prevent the transition from the mode-locked regime to the generation of chaotic signals.

Due to a lack of available feedback systems, two novel concepts are developed for the realization of feedback systems for a 263 GHz passive mode-locked oscillator as part of this work (see [183] and [184]).

The initially proposed feedback system, published in [183], is based on a quasi-optical transmission via a mirror system. While the overall performance of this mirror based feedback system is sufficient, it has a few disadvantages. The positioning of the mirrors is quite complicated and the performance is sensitive to misalignment. All mirrors are located very close together and to increase the total length of the feedback system, additional mirrors must be added to the system which further increases the complexity of the system. Furthermore, the dispersion of the mirrors with sinusoidal grading, that are used as polarization spitters, limits the bandwidth to $\approx 10\,\mathrm{GHz}$.

Therefore, an improved feedback system was designed where all components are oriented orthogonal to each other (published in [184]). This allows a realization of the feedback system with corrugated waveguides instead of a mirror system in free space. A further advantage is the higher bandwidth of 20 GHz. In addition, the waveguide-based system can be easily extended to allow the operation of the coupled devices in alternative regimes of operation (published in [185]). For example it will be possible to operate the two

coupled gyro-devices as a two stage amplifier instead of a passive mode-locked oscillator.

In the first part of this chapter, the requirements that the feedback system has to fulfill are discussed and the favorable feedback system based on overmoded waveguides is presented. In the second part, a further advantage of the developed feedback system is presented: a simple extension allows new regimes of operation for coupled gyro-devices beyond the passive mode-locking.

8.1 Requirements

The feedback system has to fulfill several requirements to guarantee an optimal performance of the passive mode-locked oscillator. As the output signal consists of ultra-short pulses (≈ 0.1 ns) of high power (up to 5 kW) at a center frequency of 263 GHz, the feedback system must provide a high bandwidth, a low dispersion and low ohmic losses. Especially the low dispersion and the high bandwidth are important requirements, as shown by the investigations in chapter 2 and chapter 6. Low ohmic losses prevent a reduction of the generated power (see chapter 2.2.6) and ensure a low thermal loading of the components. Based on the estimation of the maximal power capabilities of the designed helical gyro-TWTs in chapter 5.1.2, a maximal CW power of 300 W is expected. However, all components should resist a 1 kW CW signal to be safe.

To provide as much flexibility as possible for future experiments, a variable decoupling coefficient is a prerequisite and an additional tunable delay time would be favorable. Low back-reflections from the feedback system into the amplifier (<-30 dB) are essential to prevent the transition from the mode-locked regime to the generation of chaotic signals [145].

In addition to the previously defined requirements (high bandwidth, low ohmic losses, low back-reflections, variable decoupling, and tunable delay time) another requirement is essential for a stable operation of the passive mode-locked microwave oscillator: the decoupling of the output signal should take place only at the signal path from the absorber to the amplifier. This is important because a decoupling of a fraction of signal before the saturable absorber would decrease the saturation effect and therefore increase the total losses in the system. For a realization of this requirement, a separation of the signal paths

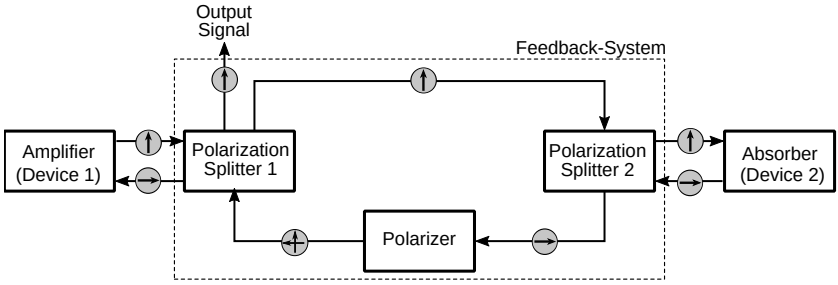

Figure 8.1: Schematic of a feedback system to couple two helical gyro-TWTs with a single input-output window. The encircled arrows symbolize the polarization of the wave oscillating in the feedback system.

'amplifier-to-absorber' and 'absorber-to-amplifier' is required. For this purpose, the polarization characteristic of a helical gyro-TWT in single-window operation can be utilized. As shown in chapter 3.1.8, the output wave is cross-polarized to the input wave and therefore, a polarization splitter can be used to separate the input and output signals. For the actual decoupling of a fraction of the signal oscillating in the feedback loop the polarization splitter is used in combination with a tunable polarizer in one of the signal trails. This is shown in Fig. 8.1.

In the following, the previously introduced Jones calculus (see chapter 3.4.1) is extensively used to describe the functionality of the feedback system. For the symbolization of the polarization states from the propagating $\mathrm{HE}_{1,1}$ modes respectively the Gaussian beams, the following symbols are used for linearly polarized modes:

$$\ominus = \begin{pmatrix} 1 \\ 0 \end{pmatrix}, \tag{8.1}$$

$$\oplus = \begin{pmatrix} 0 \\ 1 \end{pmatrix}. \tag{8.2}$$

Right- and left-handed, elliptically polarized modes are given by:

$$\circledcirc = \begin{pmatrix} -j\cos(\Theta) \\ \sin(\Theta) \end{pmatrix}, \tag{8.3}$$

$$\circledcirc = \begin{pmatrix} j\sin(\Theta) \\ \cos(\Theta) \end{pmatrix}. \tag{8.4}$$

For $\Theta = 45°$, a right- respectively left-handed, circular polarization is given.

With the Jones calculus also a very general description of the feedback system can be given. For this, every element in Fig. 8.1 is replaced by its corresponding Jones matrix. Starting from the output of the amplifier $e_{\mathrm{out}}^{\mathrm{dev1}}$, the output signal of the passive mode-locked pulsed oscillator is given by

$$e_{\mathrm{out}}(e_{\mathrm{out}}^{\mathrm{dev1}}) = S_{\mathrm{T}}^{1}\, P_{\Theta}\, S_{\mathrm{R}}^{2}\, D^{2}\, S_{\mathrm{T}}^{2}\, S_{\mathrm{T}}^{1}\, e_{\mathrm{out}}^{\mathrm{dev1}} \tag{8.5}$$

and the back-coupled signal reads as

$$e_{\mathrm{in}}^{\mathrm{dev1}}(e_{\mathrm{out}}^{\mathrm{dev1}}) = S_{\mathrm{R}}^{1}\, P_{\Theta}\, S_{\mathrm{R}}^{2}\, D^{2}\, S_{\mathrm{T}}^{2}\, S_{\mathrm{T}}^{1}\, e_{\mathrm{out}}^{\mathrm{dev1}}. \tag{8.6}$$

Since the two equations above differ only in whether the signal is transmitted or reflected at the polarization splitter 1, the polarizer determines the fraction $K_{\Theta}^{\mathrm{out}}$ of the power which is decoupled from the oscillator. The following relation holds:

$$K_{\Theta}^{\mathrm{out}}(e_{\mathrm{out}}^{\mathrm{dev2}}) = \| S_{\mathrm{T}}^{1}\, P_{\Theta}\, S_{\mathrm{R}}^{2}\, e_{\mathrm{out}}^{\mathrm{dev2}} \|^{2}. \tag{8.7}$$

8.2 Feedback System via Overmoded Waveguides

In the following, a waveguide based feedback system is presented (first published in [184]) that fulfills all previously discussed requirements. All components in the feedback system are oriented orthogonal to each other which allows a simplified alignment and handling. In addition, the orthogonality allows a tunable delay time which is difficult in alternative, mirror-based feedback systems, e.g. [183]. A schematic of the designed feedback system is shown in Fig. 8.2.

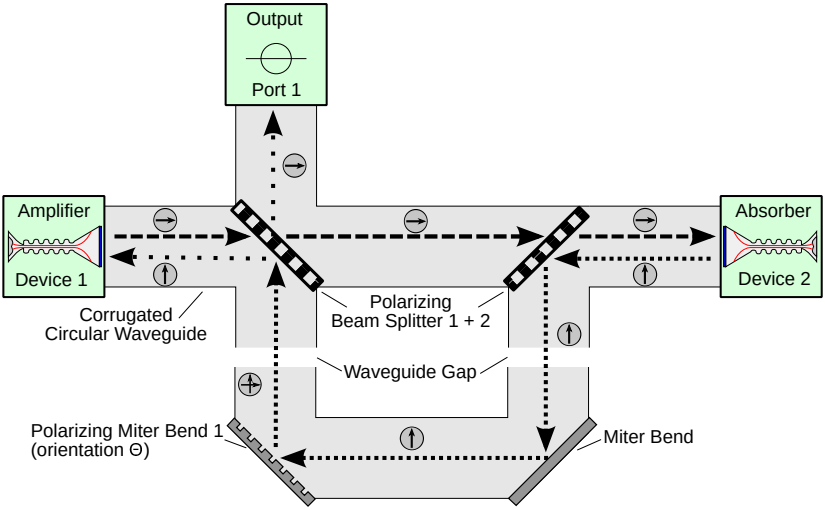

Figure 8.2: Amplifier and absorber devices working with single input-output window coupled by corrugated, overmoded waveguides. The encircled arrows symbolize the polarization of the $\mathrm{HE}_{1,1}$ mode.

A key feature of the developed feedback system is its realization within a waveguide transmission line. The output signals of the electron tubes are directly fed into the overmoded, corrugated, cylindrical waveguides. In the waveguides, the wave propagates as a linearly polarized $\mathrm{HE}_{1,1}$ mode. The output polarization of the amplifier is chosen such that it is transmitted by both polarizing beam splitters, while the cross-polarized output from the absorber is reflected. As polarizing beam splitters, wire-grid splitters (see chapter 3.4.2) are used.

To decouple a fraction of the signal oscillating in the feedback loop, one of the polarizing beam splitters is used in combination with a tunable polarizing miter bend. In a polarizing miter-bend, the flat mirror of a ordinary miter bend is replaced with a polarizing phase grid (see chapter 3.4.3). In the developed design, a reflective phase grid with rectilinear grating is used. The polarizer creates an elliptically polarized $\mathrm{HE}_{1,1}$ mode from the incident linearly polarized one. The elliptically polarized $\mathrm{HE}_{1,1}$ mode can be seen as a superposition of two cross-polarized, linearly polarized modes with a phase shift. Conse-

quently, the polarizing beam splitter separates the linearly polarized modes and a fraction of the signal, depending on the polarization, can be decoupled from the feedback loop.

Starting from the output of the amplifier, the Jones calculus for the output signal of the passive mode-locked oscillator is given by

$$e_{\mathrm{out}}(e_{\mathrm{out}}^{\mathrm{dev1}}) = S_{\mathrm{T}}^{1}\, P_{\Theta}^{1}\, P_{0^\circ}^{2}\, S_{\mathrm{R}}^{2}\, D^{2}\, S_{\mathrm{T}}^{2}\, S_{\mathrm{T}}^{1}\, e_{\mathrm{out}}^{\mathrm{dev1}} \tag{8.8}$$

and the back-coupled signal reads as

$$e_{\mathrm{in}}^{\mathrm{dev1}}(e_{\mathrm{out}}^{\mathrm{dev1}}) = S_{\mathrm{R}}^{1}\, P_{\Theta}^{1}\, P_{0^\circ}^{2}\, S_{\mathrm{R}}^{2}\, D^{2}\, S_{\mathrm{T}}^{2}\, S_{\mathrm{T}}^{1}\, e_{\mathrm{out}}^{\mathrm{dev1}}\ . \tag{8.9}$$

As it can be seen from (8.8), the fraction of power that is decoupled from the feedback loop depends on the orientation Θ of the polarizing phase grid. By an adjustment of Θ, the power decoupling can be precisely adjusted which is a basic requirement for the feedback system.

8.2.1 Waveguide

For the transmission line, an overmoded, circular waveguide with a rectangular corrugation is used (Fig. 8.3). For the expected signal with a center frequency around 263 GHz and a maximum CW power of 1 kW, a waveguide with a diameter of 22 mm and a rectangular corrugation with $\lambda/4 = 0.285$ mm corrugation depth, 0.38 mm corrugation period and 0.15 mm tooth width is sufficient. Such a waveguide allows a low-loss transmission of the expected broadband, high-power signal. A similar waveguide, made of copper, is used in [186] as a transmission line in a DNP-NMR experiment to guide the microwave radiation from a gyrotron to the spectrometer. They measured an upper limit for the attenuation of -24 dB/m.

As shown in chapter 6, the pulse repetition frequency for a passive mode-locked oscillator operated in the hard excitation regime it determined by the delay time. Consequently, a tunable delay time would be a preferable feature for a passive mode-locked microwave oscillator. Since the delay time is determined by the time a signal requires for a single pass through the complete feedback loop, a tunable delay time can be realized over a variable length of the transmission

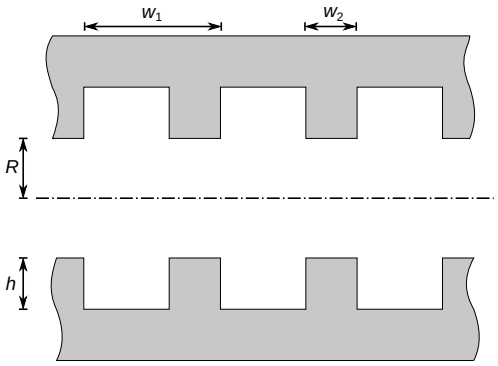

Figure 8.3: Schemata of a corrugated, cylindrical waveguide, with radius R, corrugation depth h, corrugation period w_1 and corrugation width w_2.

line. As the group velocity of a $\mathrm{HE}_{1,1}$ mode in an oversized waveguide is approximately the speed of light, an increase of the delay time of 1 ns corresponds to an increase of the signal path of 30 cm. Due to the known fact that the $\mathrm{HE}_{1,1}$ mode can be transmitted very effectively over small gaps in overmoded waveguides, the simplest approach is to cut the waveguides to create a gap between them. The transmission parameter of a $\mathrm{HE}_{1,1}$ mode over a gap can be approximated with the following equation [187]:

$$S_{21} \approx -1.7 \left(\frac{L\lambda}{2R^2} \right)^{\frac{3}{2}} \ \mathrm{dB} \, . \tag{8.10}$$

Here, L is the length of the gap, λ the wavelength of the wave and R the waveguide radius.

Since the amplifier and absorber devices are large and complex structures (the electron tube + cooling system + superconducting magnet + voltage supply), they cannot be moved in a simple way. Therefore, the only possible position for a tunable waveguide gap is in the signal path 'absorber-to-amplifier', between the miter bends and the polarisation splitters (see Fig. 8.2). The gap can be varied by moving the two miter bends.

Eq. (8.10) is plotted for a frequency of 263 GHz and varying lengths of the gap in Fig. 8.4. It can be clearly seen that for an increase of the delay time by

1 ns (two gaps of 15 cm), the attenuation would be unacceptable high. Only a small tunable delay of up to 0.25 ns is realizable with this concept. If a higher tunability is required, a more complex solution would be necessary.

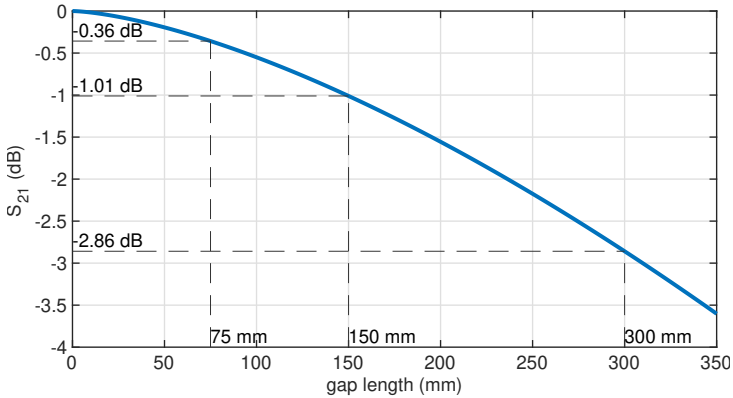

Figure 8.4: Transmission of a $HE_{1,1}$ mode at 263 GHz over a gap in a corrugated waveguide with diameter 22 mm (based on [184]).

8.2.2 Broadband Polarization Splitter

For the separation of two linearly, cross-polarized $HE_{1,1}$ modes, several approaches are possible (see chapter 3.4.2). While in the mirror based feedback-system [182] the signal paths are separated by sinusoidal grated mirrors, the favorable technology for a waveguide based feedback system is a wire-grid splitter. The main advantage of the wire-grid splitter compared to the sinusoidal mirrors is that it can be directly used in a 4-port configuration as required in the proposed design (see Fig. 8.5). In contrast to wire-grid splitters in optical applications, an all-metal design can be used at sub-THz frequencies.

For the optimization of the polarization splitter, 3D full-wave simulations of the complete polarization spitter, including the corrugated waveguides, are performed with KarLESSS. As the waveguide diameter is given (22 mm) the remaining parameters for the optimization are the radius d_r and the spacing d of the wires. The main focus in the optimization procedure is paid to a high transmission because the high-power output signal of the amplifier has

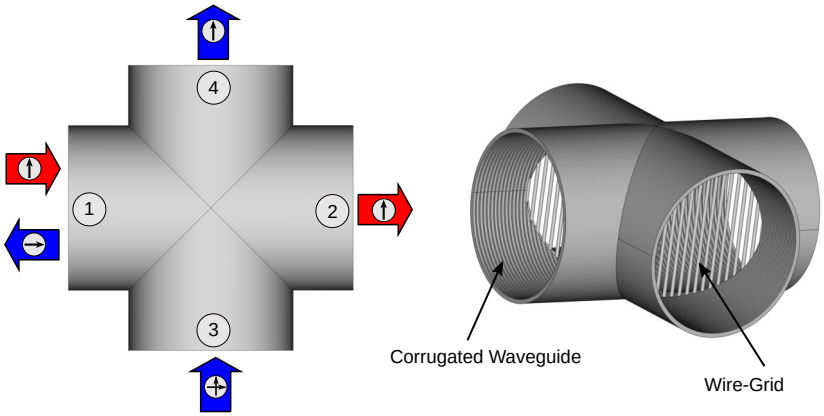

Figure 8.5: Wire-grid polarizing beam splitter in a 4-port configuration. In red the signal path 'amplifier-to-absorber'; in blue the signal path 'absorber-to-amplifier' (adapted from [184]).

to be transmitted through two splitters before it is injected into the saturable absorber. An optimal signal separation is less important in this setup. Only at the signal path 'absorber-to-amplifer', a good signal separation is important to prevent a parasitic feedback. However, since two polarization splitters are on the 'parasitic' signal path, even a low signal separation of for example $-15\,\mathrm{dB}$ would result in a total suppression of $-30\,\mathrm{dB}$.

The transmission increases with a decreasing diameter of the wires. As the wire diameter is mainly limited by the thermal loading caused by ohmic losses, it is set to a value of $0.1\,\mathrm{mm}$ which should be safe for the maximum estimated signal power of $1\,\mathrm{kW}$.

In Fig. 8.6, the S-parameters for an input signal at port 1 (port-numbering as in Fig. 8.5) are plotted for different wire distances. As expected, the transmission increases with an increasing distance between the wires. This applies until d exceeds a certain limit and the grid becomes a diffraction grid. Based on the shown parameter sweep over the wire spacing and an additional sweep over the frequency ($263 \pm 5\,\mathrm{GHz}$) a wire distance of $d = 0.15\,\mathrm{mm}$ is chosen as optimal.

The optimized polarization splitter achieves a high transmission of $-0.04\,\mathrm{dB}$ in the transmission path and of $-0.08\,\mathrm{dB}$ in the reflection path. The back

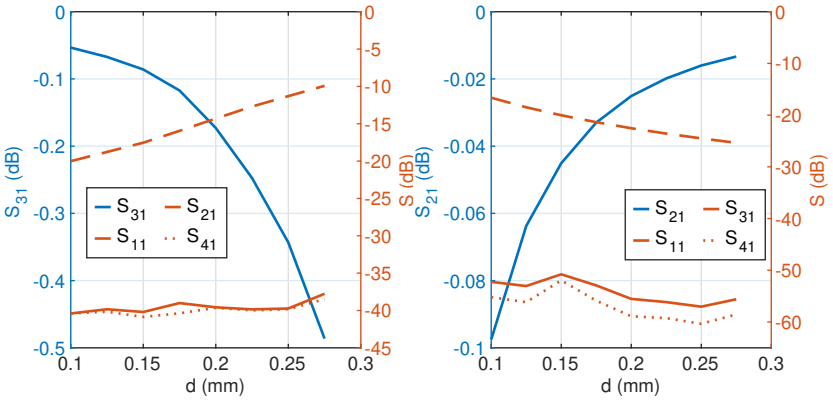

Figure 8.6: Simulated S-parameter for a wire-grid polarization splitter in a corrugated waveguide with diameter of 22 mm for different wire distances d and a wire diameter of 0.1 mm. (a) for the reflection path; (b) for the transmission path.

reflections are below −30 dB. The parasitic power leak to the other ports is below −20 dB in the transmission path and below −17 dB in the reflection path which is sufficient for our propose.

To avoid breakdowns, the maximal field strength occurring at the polarization splitter is controlled in a final step. In Fig. 8.7, the simulated electric fields for the reflection and transmission paths are shown. It is clear that in the reflection path the field strength is increased due to the interference of the incident and reflected beams. The simulation gives a maximum value of 0.225 kV/m for a 1 W input signal which corresponds to 10.1 kV/m at an input power of 2 kW. This electric field strength is uncritical.

For miter bends it is well known that the lowest ohmic losses occur for an incident H-plane polarized wave [188]. Since the wire grid polarization splitter in the reflection path behaves similar to a miter bend, the ohmic losses can be reduced by a clever choice of the polarization: The wire grid polarization splitters are chosen such that an E-plane polarized wave is transmitted and a H-plane polarized wave is reflected. This choice not only reduces the ohmic losses at the polarization spitters but also at the miter bend and the polarizing

miter bend. The calculated ohmic losses for an incident H-plane polarized wave at the polarization splitter is −30 dB.

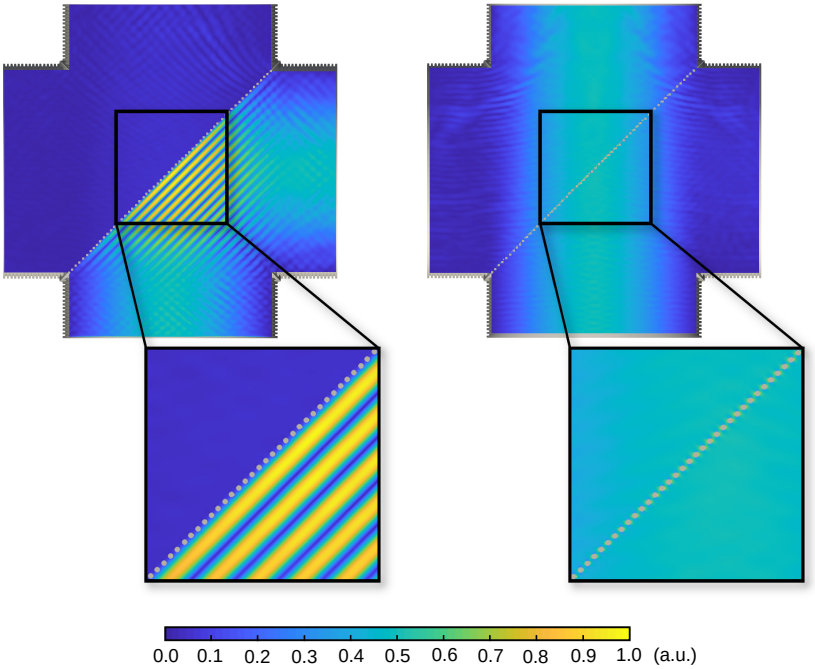

Figure 8.7: Electric field in the designed wire-grid polarizing beam splitter for a 263 GHz input signal: transmission path (left); reflection path (right). Simulations performed with KarLESSS.

8.2.3 Broadband Polarizer

To decouple a fraction of the signal oscillating in the feedback loop, the polarization splitter is used in combination with a tunable polarizer in the signal trail 'abosorber-to-amplifier'. The polarizer creates an elliptically polarized $HE_{1,1}$ mode from the incident linearly polarized one. Since the elliptically polarized $HE_{1,1}$ mode is equivalent to a superposition of two linearly, cross-polarized modes with an additional phase shift, the previously described polarization

splitter separates these linearly polarized modes and a fraction of the beam is decoupled from the feedback loop while the remaining fraction is fed back into the amplifier.

The polarizer is realized as a polarizing miter-bend. In a polarizing miter bend, the flat mirror of an ordinary miter bend is replaced with a polarizing phase grid. In the developed design, a reflective phase grid with rectilinear grating is used (see chapter 3.4.3). The grating can be characterized by the width w_2, height h and period w_1 of the grid (Fig. 3.18).

A requested property of the feedback system is a tunable decoupling of the output signal. Consequently, a tunable polarizer is required. In the proposed polarizing miter bend the generated polarization can be adapted if a rotatable grid is installed. By a variation of the angle Φ between the phase grid and the polarization plane of the incident wave, the fraction of power in the cross-polarized linear components can be controlled. In the used coordinate system, an angle of $\Phi = 90°$ does not change the polarization of an incident wave with $P_x = 1$ and $P_y = 0$ or $P_x = 0$ and $P_y = 1$. Although the preliminary investigations of passive mode-locked oscillators based on the HME (see chapter 2) and a comparison with mode-locked lasers suggest that only a small fraction of the oscillating signal can be decoupled at every round-trip, a tunable decoupling factor from at least 0-0.6 is demanded. This is motivated by the possibility to reach high gains in helical gyro-TWTs which could probably allow a higher decoupling than in lasers.

To minimize effects of the polarizer on the ultra-short pulses, a bandwidth of at least 10 GHz is demanded. As the optimal parameters for a reflective phase grid with high bandwidth are not available from analytical formulas, the numerical optimization routine described in chapter 3.4.3 is used to find a grid with a suitable broadband behavior. As result of the optimization process, the following parameters for a broadband reflective phase grid are obtained: $w_1 = 0.5\,\text{mm}$, $w_2 = 0.2\,\text{mm}$ and $h = 0.28\,\text{mm}$.

To verify the developed design, 3D full-wave simulations of the final polarizing miter bend are performed with KarLESSS. In Fig. 8.8, selected examples of these simulations are shown. The fraction of power $P_{\text{x,y}}$ in the x- and y-polarized $\text{HE}_{1,1}$ modes for various orientations Φ of the tunable polarizing miter bend is shown in Fig. 8.8a. The designed polarizing miter bend provides a high flexibility to tune the power decoupling in a wide range from 0 up to

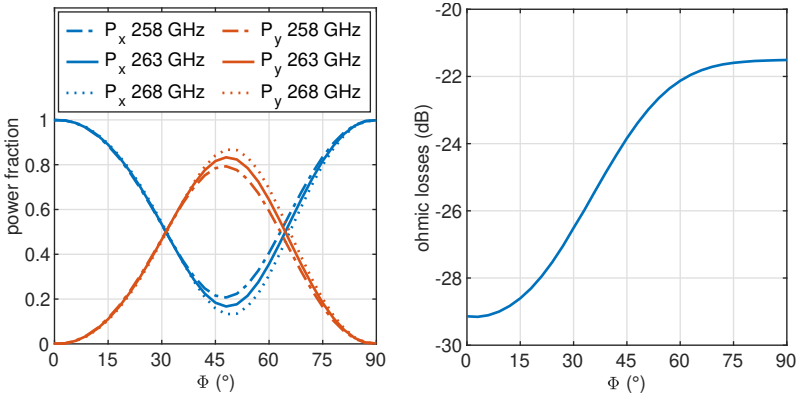

Figure 8.8: Full-wave simulation results of the optimized polarizing miter bend for different orientations Φ of the reflective phase grid. (a) power in x- and y-polarized fractions (P_x and P_y); (b) ohmic losses.

0.7. The previous interaction simulations in chapter 6 have shown that for the designed helical gyro-TWT amplifier and absorber a power decoupling factor in the range of 0.26 to 0.64 is sufficient.

In Fig. 8.8a, the results for three frequencies are shown: 258 GHz, 263 GHz and 268 GHz. It can be seen that the polarizer has a good broadband behavior. In particular for angles smaller than 40°, the frequency dependence is low. For higher angles, the frequency dependence slightly increases. This is an expected behavior. For $\Phi = 0°$, the incident wave is reflected at the 'top' of the reflective grid. Consequently, the reflective grid just acts as an ordinary flat mirror and no dispersive effects occur. For an increasing Φ, an increasing fraction of the power is reflected on the 'bottom' of the reflective grid and as a consequence a phase difference $\Delta\phi$ between the components reflected at the top and the bottom of the grid are introduced (that is the basic principal of the polarizer). Since the introduced phase difference $\Delta\phi$ depends on the wavelength, it is strongly dispersive. As a result, the strongest dispersive effects occur for angles Φ where the fraction of 'top-reflected' and 'bottem-reflected' field is approximately equal.

It should be noted that the maximum/minimum of the curves in Fig. 8.8a are not exactly at $\Phi = 45°$. The reason for this is that instead of an incident plane wave and an ideal polarizer of infinite size, a $HE_{1,1}$ mode in a miter bend is investigated. Therefore, low field components deviating from the axis of polarization exist which causes the observed shift (even a frequency dependent shift) in Φ.

The calculated ohmic losses on the polarizer are shown in Fig. 8.8b. As expected, they depend on the orientation Φ of the polarizer. A comparison with measurements of ohmic losses at polarizers in [188] shows a good agreement of the observed Φ dependency. For the important orientations ($\Phi \in [0°, 40°]$), the ohmic losses are in an acceptable range, below -25 dB. The calculated

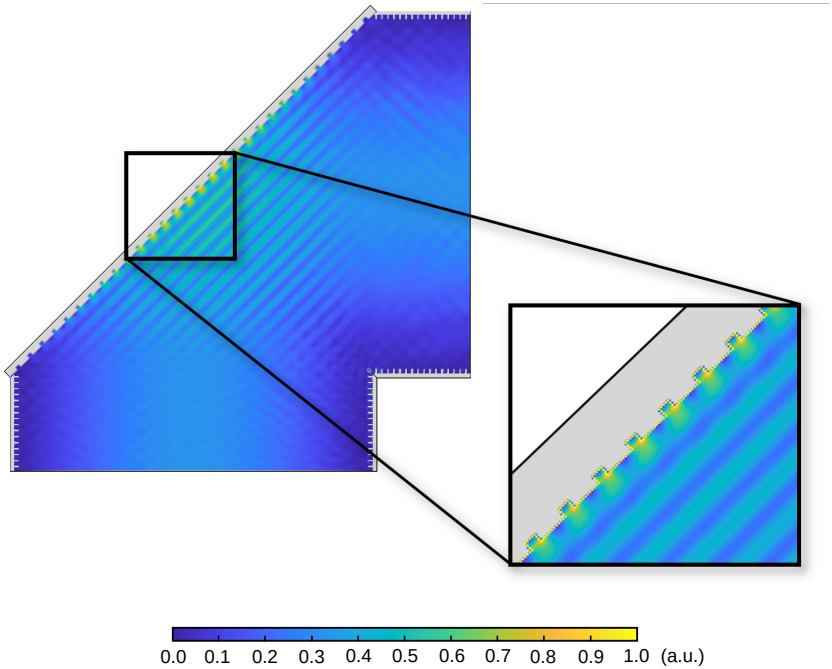

Figure 8.9: Electric field in the designed polarizing miter bend for a 263 GHz input signal. Simulation performed with KarLESSS.

back-reflections are consistently low ($\approx -40\,\mathrm{dB}$) for a wide frequency band of $20\,\mathrm{GHz}$ around the center frequency of $263\,\mathrm{GHz}$.

To avoid breakdowns, the maximal field strength occurring at the polarizer is controlled in a final step of the design process. In Fig. 8.9, the simulated electric field for $\Phi = 30^\circ$ ($P_x = P_y = 0.5$) is shown. The simulation gives a maximum value of $2\,\mathrm{kV/m}$ for a $1\,\mathrm{W}$ input signal which corresponds to $90\,\mathrm{kV/m}$ at a power of $2\,\mathrm{kW}$.

8.2.4 Performance of the Complete Feedback System

In order to obtain information about the mode content, the complete system must be simulated. Therefore, a complete feedback system is assembled by the previously presented components. To reduce the computational effort of this challenging simulation, the simulated feedback system is reduced to a minimum-size version where the straight waveguide sections are as short as possible. However, even the minimum-size version results in a simulation with $2 \cdot 10^6$ unknowns. On a dual-socked server with AMD EPYC 7452 Processors such a simulation with KarlESSS required $5\,\mathrm{h}$. A $\mathrm{HE}_{1,1}$ mode content of $98.5\,\%$ is obtained for the signal path 'amplifier-to-absorber' and of about $96\,\%$ for signal path 'absorber-to-amplifier' (for the signal at the amplifier port as well as at the output port).

To verify the simulated values of the $\mathrm{HE}_{1,1}$ mode content, the approximation formula (8.10) can be used [187]. Although the equation describes a gap in a waveguide, it can be also used to calculate the power lost in the $\mathrm{HE}_{1,1}$ mode caused by mode coupling to other modes and refraction in the miter bends. This is possible because the mode losses in a miter bend can be described by an equivalent gap with the length of $2R$ in the waveguide [189]. Since there are two waveguide gaps in the signal path 'amplifier-to-absorber', and four miter bends in the signal path 'absorber-to-amplifier', the expected mode contents based on (8.10) are $97.4\,\%$ respectively $95.0\,\%$. These values are in a good agreement with the simulated values.

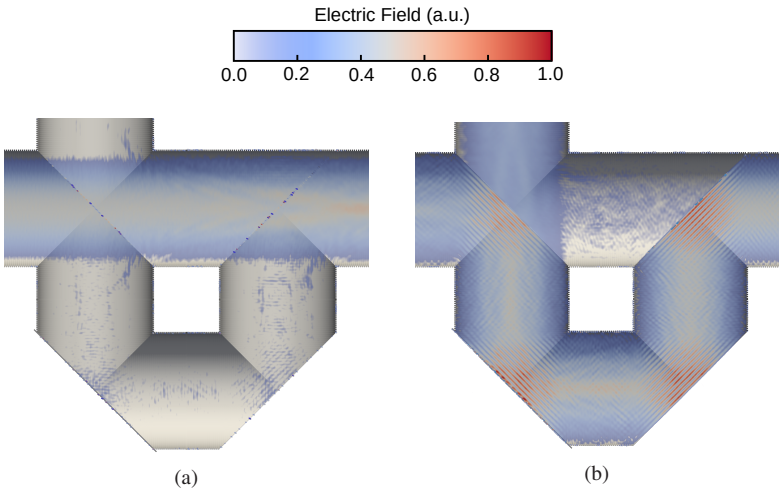

Figure 8.10: Full-wave simulations of a complete, minimum-size feedback system for a 263 GHz input signal. (a) Signal path 'amplifier-to-absorber'; (b) signal path 'absorber-to-amplifier'.

8.3 Additional Operation Modes

During the studies of the previously designed passive mode-locked oscillator, the author recognized that a simple extension to the developed, waveguide based feedback system would provide a range of new operating scenarios for the two coupled electron tubes. Therefore, in [185], an extension of the previously designed feedback system was proposed. This extension allows the input of an external signal into the feedback system.

First of all, this allows the operation of the passive mode locked oscillator in the hard excitation regime. In the hard excitation regime, the passive mode locked oscillator is started by an external signal rather than from noise. As shown in the chapter 6, the hard excitation guaranties the highest coherence of the generated pulses. However, the interaction simulations have shown that a very high excitation power is required that is not available up to now. An alternative method for the hard excitation was therefore presented in chapter 6.5 that uses an high-gain helical gyro-TWT. Nevertheless, the possibility to inject

external signals into a passive mode-locked oscillator, provided by the extended feedback system, will be briefly discussed in the following.

In addition to the operation as passive mode-locked oscillator, the extended feedback system will allow completely new scenarios for coupled gyro-devices. First of all, the coupled electron tubes could be operation as a two-stage amplifier. Here, two different configurations are possible: On the one hand, the original functionality of the components can be retained, the amplifier is operated as amplifier and the saturable absorber as saturable absorber. In this case, a low power input signal is first amplified while the absorber can be used either as a pulse compressor or to reduce low power noise. On the other hand, the helical gyro-TWT absorber can be operated as an amplifier. This allows a two-stage high-power amplifier, similar to the systems in [148]. However, the system presented in this work has a significant advantage: While in [148] the input signal is fed into the first amplifier stage by an state-of-the-art input coupler (see schemata of a helical gyro-TWT in Fig. 3.1), in the proposed system the input signal is inject via an overmoded waveguide which could reduce losses.

Furthermore, the system can be operated as a high-power sub-THz CW oscillator. For this, at least one of the electron tubes must be operated as BWO. In order to achieve higher frequency stability, the extended feedback system provides the possibility of injecting a locking signal for a phase locking of the oscillator.

In Fig. 8.11, the extended feedback system is shown. Two extensions to the original feedback system (see Fig. 8.2), are made: (1) The waveguide T-junction at the second polarizing beam splitter is replaced by a crossover, similar to the existing one at the first polarizing beam splitter. This adds an additional waveguide port which can be used either as an input or an additional output port, depending on the operation regime. (2) The ordinary miter bend is replaced by a polarizing miter bend, identical in construction to the existing polarizing miter bend. These two extensions enable a variety of new operating regimes for the system of two coupled gyro-devices. In the following they are discussed in detail.

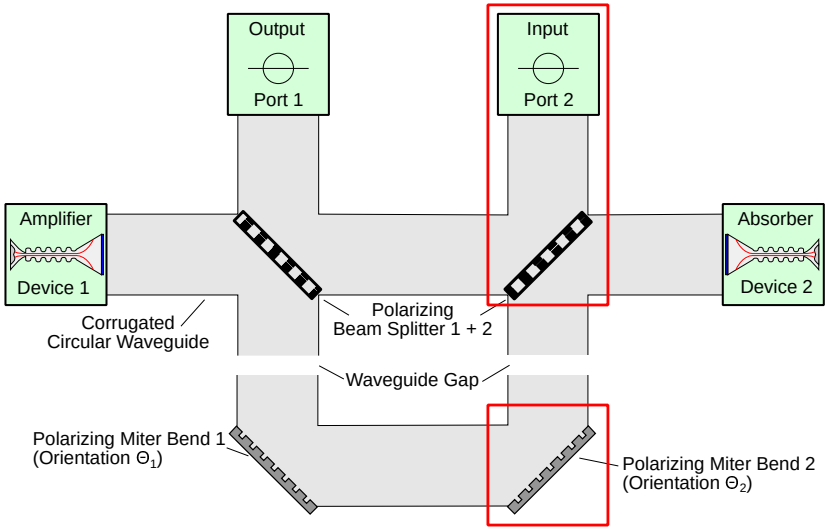

Figure 8.11: An extended version of the feedback system proposed in chapter 8.2 with an additional input/output port and a second polarizing miter bend (highlighted in red).

8.3.1 Operation in the Hard Excitation Region

As discussed previously, the passive mode-locked oscillator can be operated in both soft and hard excitation. For the operation in hard excitation, at the start-up of the oscillator, an initial pulse has to be injected into the oscillator. In the extended feedback system, this can be done through the new waveguide port 2. This is shown in Fig. 8.12. The initial pulse must be horizontally polarized (e_x) so that it is transmitted by the polarization splitter 2. The polarizing miter bend 2 is adjusted at $\Theta_2 = 0°$ so that the incident wave does not change its polarization at the polarizing miter bend 2 and therefore, it behaves as a usual miter bend.

However, it is not possible to feed the complete power of an excitation signal into the oscillator. While in the soft excitation regime the polarizing miter bend 1 only determines the fraction K_Θ^out of the oscillating signal which is decoupled from the oscillator, in the hard excitation it also determines the

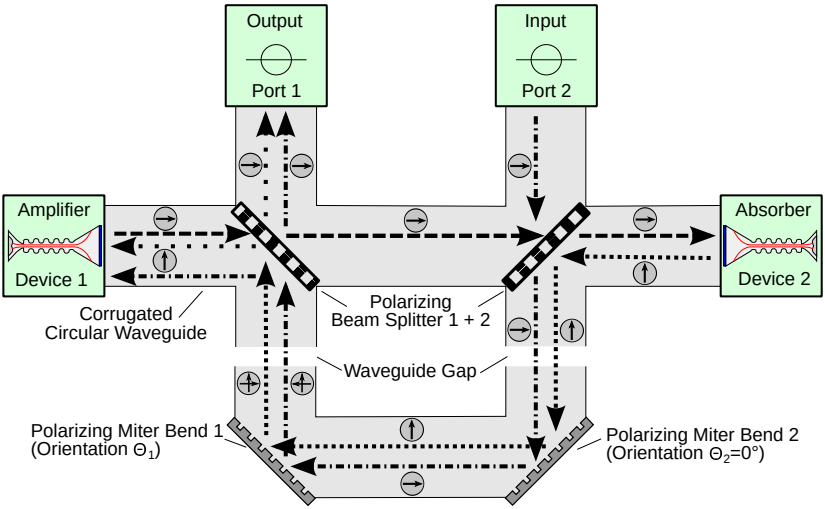

Figure 8.12: Amplifier and saturable absorber coupled as passive mode-locked oscillator. The extended design allows the input of a start-up signal to operate the passive mode locked oscillator in the hard excitation regime. Based on [185].

fraction K_{Θ}^{in} of the excitation signal that could be coupled into the oscillator. Utilizing the Jones calculus, expressions for K_{Θ}^{in} and $K_{\Theta}^{\mathrm{out}}$ can be given:

$$K_{\Theta}^{\mathrm{in}}(e_{\mathrm{in}}^{\mathrm{p2}}) = \| S_{\mathrm{R}}^{1}\, P_{\Theta}^{1}\, P_{0^\circ}^{2}\, S_{\mathrm{T}}^{2}\, e_{\mathrm{in}}^{\mathrm{p2}} \|^2 \,, \tag{8.11}$$

$$K_{\Theta}^{\mathrm{out}} = 1 - K_{\Theta}^{\mathrm{in}} \,. \tag{8.12}$$

It would be conceivable to choose Θ_1 such that for the start-up phase of the oscillator no output signal is decoupled of the feedback loop. This would allow to feed the complete excitation signal into the amplifier. Nevertheless, only sub-THz sources with very low power are available and the excitation of passive mode-locking by an external signal seams to be unrealistic. A more realistic method for the hard excitation was therefore presented in chapter 6.5 that uses a high-gain helical gyro-TWT. However, future research could maybe identify scenarios where the injection of an external signal into a passive mode-locked oscillator could be of interest.

8.3.2 New Type of Two-Stage Amplifier

In addition to the original purpose as a passive mode-locked oscillator, the operation as a two-stage amplifier is enabled by the possibility to feed an external signal into the extended feedback system. A schemata of the two-stage amplifier operation is shown in Fig. 8.13.

Two possible configurations exist for the two-stage amplifier. First, the original purpose of the electron tubes can be retained. In a two-stage amplifier consisting of an amplifier and a saturable absorber, the absorber reduces low power noise and works as a pulse compressor. In an alternative configuration, the absorber could be operated as an amplifier instead of an absorber. If the absorber is realized as a helical gyro-TWT this is particularly simple since a helical gyro-TWT absorber is just a detuned amplifier [55]. In the case of a cyclotron absorber this depends on the used electron gun. If a CUSP-gun is used, the cyclotron absorber could be also operated as a conventional gyro-TWT with a gyrating, halo electron beam. In this way, a two-stage, high-power amplifier, similar to the system presented in [148] could be realized.

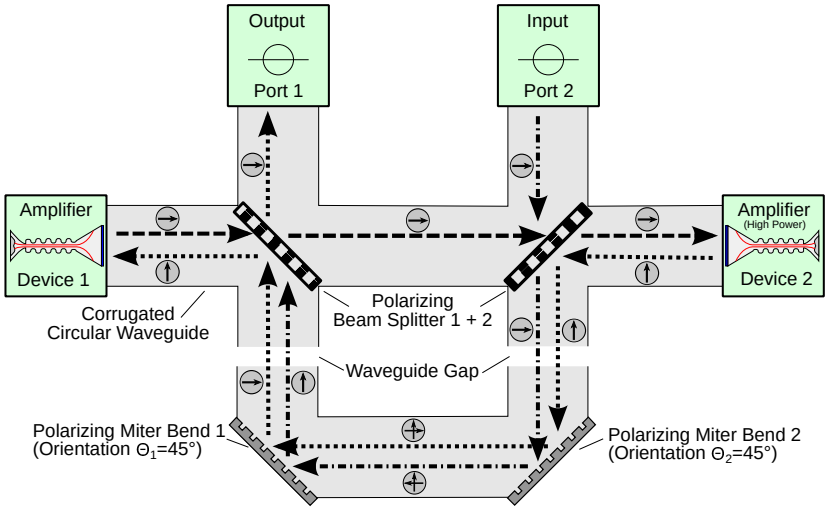

Figure 8.13: Two coupled gyro-devices with single input-output window, operated as a two-stage amplifier system to achieve a higher gain and output power. Based on [185].

A considerable advantage of the proposed two-stage amplifier system compared to the system in [148] is the inject of the input signal via an overmoded waveguide. The manufacturing of a classical input coupler (e.g. [190]) with typical dimensions below the vacuum wavelength of the signal, can be a challenging problem for sub-THz frequencies. This is eliminated by the input through overmoded waveguides. A further problem of conventional input couplers are the high losses. Typical input couplers offer only a transmission in the order of -1 dB [190]. Furthermore, a second broadband vacuum window is necessary for classical input couplers which leads to additional losses (transmission on the order of -0.5 dB [191]). Feeding via overmoded waveguides has the potential of achieving lower losses. Existing high-power gyrotron amplifiers for sub-THz frequencies are mostly limited by the available power of the input signal (e.g. [192]). Therefore, a reduction of the input losses could directly lead to a higher output power.

For the operation as an amplifier system, the additional polarizing miter bend (see Fig. 8.11) becomes necessary. The low power input signal is injected through the new waveguide port 2, similar as for the passive mode-locked oscillator in the hard excitation. The Jones calculus for the input path is:

$$e_{\mathrm{in}}^{\mathrm{dev1}}(e_{\mathrm{in}}^{\mathrm{p2}}) = S_{\mathrm{R}}^{1}\, P_{45^\circ}^{1}\, P_{45^\circ}^{2}\, S_{\mathrm{T}}^{2}\, e_{\mathrm{in}}^{\mathrm{p2}} \,. \tag{8.13}$$

The input signal $e_{\mathrm{in}}^{\mathrm{p2}}$ must be horizontally polarized so that the wave is transmitted by the polarizing beam splitter 2. The two polarizing miter bends must be oriented in such a way that the polarization of an incident linearly polarized wave is rotated by 90° after the transmission through both polarizing miter bends. Then the wave is reflected at the polarizing beam splitter 1 and a horizontally polarized input signal is completely fed into the amplifier (device 1 in Fig. 8.13). The output of device 1 is transmitted through both polarization splitters in the usual way and is fed into device 2.

For device 2, there are two possible operation modes: It can still be operated as a saturable absorber or, it can be operated as a second amplifier. Regardless of the operation regime, its output signal is first reflected by the polarizing beam splitter 2 and subsequently its polarization is rotated by 90° by the two polarizing miter bends. Thus, the signal is now transmitted by the polarization splitter 1. The Jones calculus for the complete signal path is:

$$e_{\mathrm{out}}^{\mathrm{p1}}(e_{\mathrm{in}}^{\mathrm{p2}}) = S_{\mathrm{T}}^{1}\, P_{45^\circ}^{1}\, P_{45^\circ}^{2}\, S_{\mathrm{R}}^{2}\, D^{2}\, S_{\mathrm{T}}^{2}\, S_{\mathrm{T}}^{1}\, D^{1}\, e_{\mathrm{in}}^{\mathrm{dev1}}(e_{\mathrm{in}}^{\mathrm{p2}}) \,. \tag{8.14}$$

8.3.3 Operation as a CW Source

In state-of-the-art DNP-NMR experiments, gyrotrons are used as high power CW sources [3], [37]. Gyrotrons are oscillators and provide a high-power CW signal without the requirement of an external source. It would be advantageous if the passive mode-locked oscillator could be operated in an alternative regime where it serves as a frequency tunable CW source for CW DNP-NMR applications. For this purpose, the fact that a helical gyro-TWT can be operated as an electronically tunable gyro-BWO [41], [193] is used. Due to the helical symmetry of the waveguide and the used large-orbit electron beam, the excitation of a wave with a negative group velocity (with respect to the motion of the electron beam) is possible.

For the gyro-BWO configuration, a helical gyro-TWT is operated with a static magnetic field of the inverse direction compared to the amplifier/absorber configuration [193]. By an adjustment of the magnetic field magnitude, the oscillation frequency can be varied smoothly. A broad frequency tuning band, on the order of the bandwidth of the amplifier operation [194], will be possible for a helical gyro-BWO. Because of this high frequency tunability, a CW source based on a helical gyro-BWO could be advantageous for DNP-NMR experiments compared to a gyrotron with a tunable frequency of only several hundred MHz [39].

As shown in chapter 5, the helical gyro-TWTs of a passive mode-locked oscillator have usually a shorter interaction space than ordinary helical gyro-TWTs for radar applications. This favors the additional operation of the devices as a BWO [193].

In Fig. 8.14, the configuration for BWO operation of device 1 is shown. In this case device 2 remains switched off. Special attention should be paid to the fact that the input and output ports of the feedback system have been swapped, compared to the amplifier and passive mode-locked oscillator configurations. This results from the fact that in the BWO operation the generated output mode of a helical gyro-TWT is cross polarized to the usual output mode in the amplifier/absorber operation. The corresponding Jones calculus for a BWO operation of device 1 is:

$$e_{\mathrm{out}}^{\mathrm{p2}}(e_{\mathrm{out}}^{\mathrm{dev1}}) = S_{\mathrm{T}}^{2}\, P_{45^\circ}^{2}\, P_{45^\circ}^{1}\, S_{\mathrm{R}}^{1}\, e_{\mathrm{out}}^{\mathrm{dev1}} \,. \tag{8.15}$$

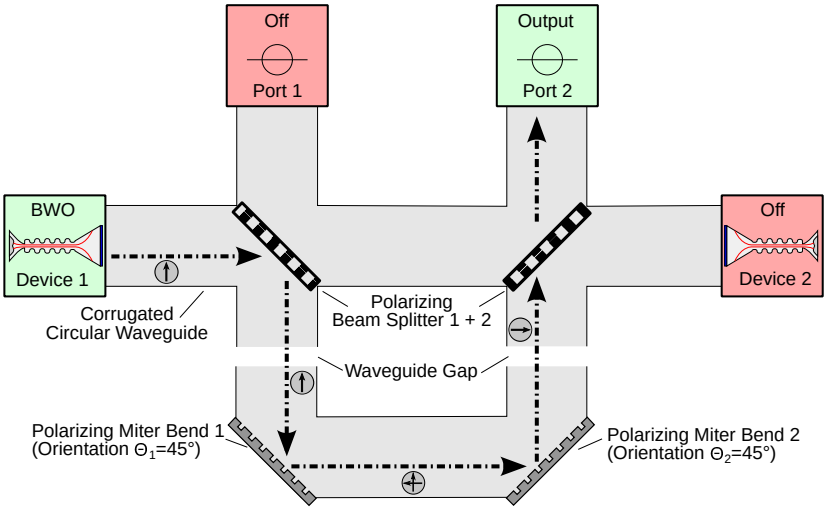

Figure 8.14: Device 1 is operated as a free running BWO. In a similar manner, device 2 can be operated as a BWO. Based on [185].

In the configuration shown in Fig. 8.14, device 1 is operated as gyro-BWO. However, it is also possible to operate device 2 as a BWO. In this case device 1 remains switched off. Since device 2 is designed in such a way that input and output signals are cross-polarized to the input/output signals of device 1, the generated RF power is first transmitted by the two polarization splitters and coupled into device 1. The polarization of the wave is rotated by $90°$ by device 1 and the wave leaves the system via port 2 as shown in Fig. 8.14. The Jones calculus for the operation of device 2 as a BWO is given by:

$$e_{\mathrm{out}}^{\mathrm{p2}}(e_{\mathrm{out}}^{\mathrm{dev2}}) = S_{\mathrm{T}}^{2}\, P_{45^\circ}^{2}\, P_{45^\circ}^{1}\, S_{\mathrm{R}}^{1}\, D^{1}\, S_{\mathrm{T}}^{1}\, S_{\mathrm{T}}^{2}\, e_{\mathrm{out}}^{\mathrm{dev2}}. \tag{8.16}$$

Aside from the operation as a simple BWO, the proposed system offers the possibility to feed in a locking signal. This makes it possible to operate a phase-locked oscillator instead of a free-running oscillator [195]–[197]. Due to the high frequency stability requirements of many spectroscopy applications, this could be an important feature. In Fig. 8.15, it is shown how a locking signal is fed into the BWOs. Regardless of which device (device 1 or 2) is used as

a BWO, the input of a locking system is possible with the proposed feedback system.

The interested reader will have noticed that in Fig. 8.15 both devices are active and operated as BWOs. This is a special case: both components are operated as BWOs at the same time. Due to a lack of powerful RF sources in the sub-THz range, the generation of a locking signal could be challenging. Therefore, it is proposed to operate device 2 as a BWO-based amplifier [198], to pre-amplify the locking signal so that device 1 can be operated as an injection-locked BWO. It must be underlined that it is not possible to use device 2 as a normal amplifier operating with a forward traveling mode, because of the inverted requirements for the polarization of the input/locking signal in the BWO operation of device 1. The Jones calculus for the complete signal path from the input of the locking signal until the output is given by:

$$e_{\mathrm{in}}^{\mathrm{dev2}}(e_{\mathrm{in}}^{\mathrm{p1}}) = S_{\mathrm{R}}^{2}\, P_{45^\circ}^{2}\, P_{45^\circ}^{1}\, S_{\mathrm{T}}^{1}\, e_{\mathrm{in}}^{\mathrm{p1}}\,, \tag{8.17}$$

$$e_{\mathrm{in}}^{\mathrm{dev1}}(e_{\mathrm{in}}^{\mathrm{p1}}) = S_{\mathrm{T}}^{1}\, S_{\mathrm{T}}^{2}\, D^{2}\, e_{\mathrm{in}}^{\mathrm{dev2}}(e_{\mathrm{in}}^{\mathrm{p1}})\,, \tag{8.18}$$

$$e_{\mathrm{out}}^{\mathrm{p2}}(e_{\mathrm{in}}^{\mathrm{p1}}) = S_{\mathrm{T}}^{2}\, P_{45^\circ}^{2}\, P_{45^\circ}^{1}\, S_{\mathrm{R}}^{1}\, D^{1}\, e_{\mathrm{in}}^{\mathrm{dev1}}(e_{\mathrm{in}}^{\mathrm{p1}})\,. \tag{8.19}$$

Last but not least, it should be mentioned that an operation of both devices as BWOs without an external locking signal could also be of interest (see for example [199]). In such a configuration, the output of device 2 is always fed completely into device 1, while an arbitrary fraction of the output from device 1 can be coupled back into device 2. This fraction can be easily controlled via the adjustable polarizing miter bend 2 (P_{Θ}^{2}). Such a system of coupled, carefully adjusted oscillators could probably offer higher frequency stability compared to a free running BWO without the requirement of an external locking signal.

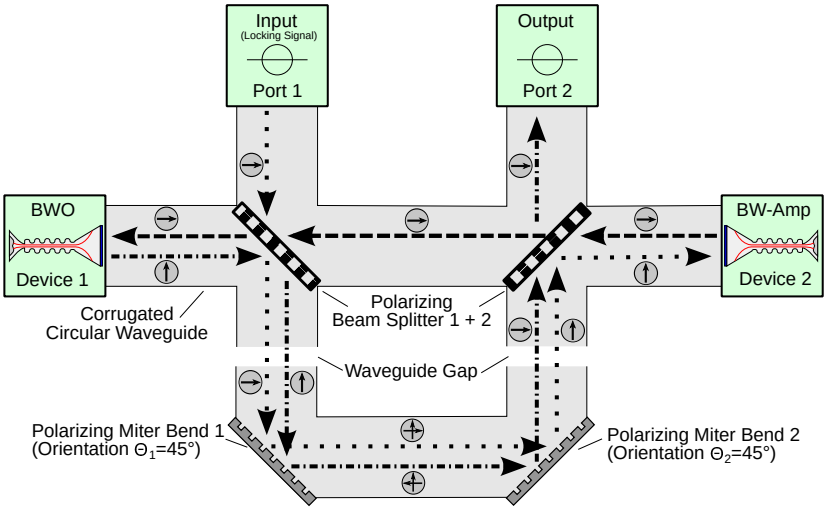

Figure 8.15: Device 1 is operated as a locked BWO while device 2 is operated as a backward-wave amplifier to pre-amplify the locking signal. Based on [185].

8.4 Conclusion

It can be concluded that the developed feedback system fulfills all the requirements to realize a passive mode-locked oscillator at 263 GHz. The presented concept is simple to implement and flexible. In addition, it offers a wide range of additional operation regimes for two coupled gyro-devices, far beyond the operation of a passive mode-locked oscillator. These new possibilities could make such a system of coupled gyro-devices a very interesting, new high-power RF source for spectroscopy applications.

Whether it is possible to realize all previously described operation regimes with identical gyro-devices is still an open question. For the realization of the additional operation regimes it would be advantageous if the absorber is realized as a helical gyro-TWT. The cylindrical interaction space of a cyclotron absorber would offer only very rudimentary possibilities of an additional operation as amplifier or BWO while the helical interaction space of a helical gyro-TWT is better suited for additional operation regimes.

In any case, the desired additional modes of operation should be considered during the design phase of the tubes. Then it is quite likely that a tube design can be found that supports the operation of the coupled devices in multiple operation regimes.

9 Conclusion and Outlook

In this work, a novel source of coherent ultra-short high-power pulses is investigated for the first time at sub-THz frequencies. The proposed source will enable new pulsed spectroscopy methods such as pulsed DNP-NMR for which powerful sub-THz pulses with highest coherency are required.

The developed pulsed source is based on the principle of passive mode-locking of two electron tubes [4]. As part of this work, an extended passive mode-locked oscillator is proposed that allows an operation in the hard excitation for the first time. As shown in this work, the operation in the hard excitation regime is of particular importance to reach the highest coherency of the generated pulses. In addition, the extended passive mode-locked oscillator will enable the generation of specific pulse sequences in addition to the generation of pulses with constant repetition frequency. This could be of particular interest for novel pulsed DNP-NMR methods where well-defined pulse sequences are required [7], [149].

Further benefits for future spectroscopy applications are provided by a novel feedback system [184]. The developed feedback system enables alternative operation regimes for the two coupled helical gyro-TWTs of the passive mode-locked oscillator. Besides the original purpose, the developed feedback system allows the realization of a two-stage amplifier and the possibility of operating the devices as frequency tunable, phase-locked BWOs. These new possibilities could make such a system of coupled helical gyro-TWTs a very promising new high-power RF source for spectroscopy applications.

The investigated frequency of 263 GHz, an established figure for CW DNP-NMR applications, will allow an easy integration of the new source into existing setups to enable novel spectroscopy experiments [1]–[3].

For a general investigation of the passive mode-locking mechanism and a derivation of the basic parameters for a passive mode-locked oscillator at sub-THz frequencies, the Haus Master Equation (HME) was used which is a well

known method from laser physics. The studies based on the HME have shown that the high gains of typical electron tube amplifiers, such as used in radar applications, are obstructive for passive mode-locked oscillators. Therefore, an atypically short helically corrugated interaction region was designed and two different operation points were identified. While one of the operation points, the so called synchronized operation regime, is a typical operation point for helical gyro-TWTs in radar applications, the second operation point, the so called slippage operation regime, is optimal for the amplification of sub-ns pulses.

Prior to this work, all investigations of passive mode-locking in electron tubes were limited to frequencies up to the Ka-band. At these frequencies, the slippage operation regime was already identified as a preferable operation point [67] for a passive mode-locked oscillator based on a helical gyro-TWT as an amplifier device. The simulations performed as part of this work have shown that this also applies to the sub-THz frequency range. To facilitate a later verification of these theoretical results by experiments, the interaction region as well as the two operation points were chosen such that both operation regimes can be realized by the same helical gyro-TWT.

As saturable absorber, two options were designed: (1) a so called cyclotron absorber with circular interaction region and rectilinear electron beam; (2) a helical gyro-TWT which is operated in the so called Kompfner dip regime. Observations of Ginzburg et al. [59] have suggested possible instabilities when using the latter. However, the performed simulations have shown that at sub-THz frequencies the helical gyro-TWT absorber can be successfully used and therefore is a preferred choice because of the reduced requirements for the magnetic field and due to the versatile possibilities that two coupled helical gyro-TWTs offer in combination with the proposed feedback system.

In a systematic study, it was shown that a feedback loop of the designed helical gyro-TWT operated in the slippage regime and the helical gyro-TWT absorber is a good candidate for the realization of passive mode-locking at 263 GHz. While previously performed studies of passive mode-locking at microwave frequencies are on a very fundamental level, in this work also limiting factors such as the power capability of the interaction region, were taken into account.

The performance and properties of the designed passive mode-locked oscillator were systematically investigated and important findings were obtained. The

generation of coherent pulses at 263 GHz with a power up to 1.4 kW, pulse lengths below 0.075 ns and pulse repetition frequencies up to 1.1 GHz could be possible with the proposed passive mode-locked oscillator.

For the first time, it was shown that an excitation of the passive mode-locking in the soft excitation regime will lead to arbitrary phase offsets in the generated pulses. Therefore, the passive mode-locked oscillator should be operated in the hard excitation regime to maintain the phase coherency.

However, an operation in the hard excitation was unrealistic up-to now due to a lack of the high-power sub-THz sources required for the generation of the excitation signal (> 100 W). In this work, for the first time a solution for the operation in the hard excitation regime was proposed and verified by simulations: The usage of a high-gain helical gyro-TWT will enable the hard excitation of passive mode-locking with signals of only several hundred milliwatt.

The proposed hard excitation operation will further enable the development of new operation modes, such as an operation with specific pulse sequences. Such an operation could be especially of interest for novel pulsed DNP-NMR methods where well-defined pulse sequences are required, e.g. [7], [149].

For the design and detailed analysis of the passive mode-locked oscillator, a large number of electron-wave interaction simulations were performed, which were made possible by a newly developed time-domain simulation program. The model used is based on a fixed transversal field approach combined with a 3D particle beam, and supports the simulation of the electron-wave interaction in helically corrugated interaction regions and in cylindrical interaction regions with a slowly varying radius.

In the literature, only one other time-domain simulation model for helical gyro-TWTs is published by Ginzburg [68]. The main difference between the models concerns the different derivation of the high-frequency electric current density. In this work, the electron beam is modeled as a beam of macro-particles with equations of motion solved by a 3D particle pusher, and the electric current density is derived in a PIC-like manner from the particles. In Ginzburg's model, the electric current density is derived from a differential equation for the electrons' slowly varying transverse momentum which is an averaged value over one or several cyclotron periods. Consequently, only effects with time scales significantly above the cyclotron period can be investigated with this

approach. In contrast, the cyclotron period is sampled by roughly 100 time-steps in the chosen PIC approach. This allows the investigation of very fast effects such as high-frequency fluctuation of the acceleration voltage due to high-frequency noise of the power supply. In addition, relativistic effects are neglected in the derivation of the slowly varying transverse momentum equation, whereas they are included in the 3D PIC model.

Further advantages of the 3D PIC approach include the more natural handling of spreads in the beam parameter and the investigation of additional beam parameters which is not at all possible with the slowly varying momentum method. For instance, the effect of an off-axis beam guiding center and a non-symmetric guiding magnetic field can be studied. Also the inclusion of additional physical effects such as space-charge is not possible in the model of slow transversal momentum.

An advantage of the PIC method regarding the simulation speed is that the equations of motion can be easily implemented in a parallel algorithm. This was used to develop a highly parallelized implementation of the particle pusher which supports the acceleration by GPUs. For a verification of the developed simulation program, simulations of the first sub-THz helical gyro-TWT, developed by He et al., were performed and compared with the experimental results published in [42].

A basic requirement for the proposed approach of passive mode-locking is a suitable system to couple the two helical gyro-TWTs in a feedback loop. The feedback system developed as part of this work is the first of its kind especially for a 263 GHz passive mode-locked oscillator and in general the first feedback system for passive mode-locking at microwave frequencies that can be realized in a closed waveguide environment.

The feedback system is an important step towards the realization of the passive mode-locked oscillator and was developed under the aspects of simplicity and robustness combined with excellent performance. Furthermore, it was shown that the feedback system can be easily extended to allow the operation of the coupled helical gyro-TWTs not only as a passive mode-locked oscillator but also in alternative operation regimes, such as a two stage amplifier or as coupled BWOs. This innovative approach of a multi-purpose source with several alternative operation regimes makes the proposed sub-THz source significantly more attractive for future applications. If the multi-purpose source is operated

as a passive mode-locked oscillator, trains of high-power ultra-short coherent pulses are generated. A CW signals is generated if it is operated in a BWO configuration and if it is operated as a two-stage amplifier, the amplification of arbitrary signals is possible.

A key prerequisite for the design of the feedback system and the determination of its properties was the development of the appropriate simulation methods. The chosen simulation model is based on a numerical solution of the EFIE and has a wide area of application. With the developed simulation program, the scattered electromagnetic fields of arbitrary PECs in free space can be calculated. It allows an accurate simulation of structures from sizes in the sub-wavelength range up to highly oversized structures with dimensions of several hundreds of wavelengths. To enable this wide range of applications, several optimized approximation techniques are used: higher-order basis functions are used for the representation of the surface currents; the surface is approximated with a higher-order curved mesh and the impedance matrix is approximated with the ACA, ACA-SVD and SACA algorithms respectively. To the knowledge of the author, it is the first time that the ACA-SVD and SACA algorithms are combined with higher-order basis functions and a higher order curved mesh.

In addition, a new preconditioner for the iterative solution of the resulting system of linear equations was developed, which can be seen as an advancement and transfer of the ACA preconditioner presented in [171] to the ACA-SVD and SACA. It was shown that the basic ACA preconditioner [171] can be significantly improved if the low-rank approximations are built from a SVD. The additional compression has almost no computational overhead, significantly reduces the required memory and improves the efficiency. A particularly unique feature is the zero-cost nature of the preconditioner. For a setup of the preconditioner, no additional computing time or memory is required. With numerical experiments it was shown that the developed zero-cost preconditioner for advanced ACA algorithms has a similar or even better performance than state-of-the-art preconditioners. A great advantage of the developed algorithm compared to other preconditioners is its simplicity. The implementation of the preconditioner should be possible with most of the ACA algorithms or its derivatives.

This work is the initial step towards the realization of a first passive mode-locked oscillator at sub-THz frequencies. Additional studies of the effects

as they occur in a real-world setup will need to be performed to further this goal. In particular, the following points should be validated in the future with theoretical and experimental studies:

- **Non-perfect feedback system**
  A coupling of the electron tubes with a real feedback system will always lead to a non-perfect isolation of the signal paths 'amplifier-to-absorber' and 'absorber-to-amplifier'. For example, the isolation between the signal paths is ≈ -40 dB for the designed feedback system. The influences of this parasitic crosstalk on a passive mode-locked oscillator is completely unknown up to now. Based on the Jones calculus, as introduced in this work to describe the performance of a feedback system, it should be possible to extend the electron-wave interaction simulations with a realistic crosstalk between the signal paths. In addition to the crosstalk, back reflections of the microwave window and influences of non-perfect polarizers should be included in the simulation model and studied in detail.

- **Manufacturing tolerances of the helically corrugated interaction region**
  While first limits for the manufacturing tolerances of the helically corrugated interaction region were derived based on the dispersion relation and a comparison with typical spreads in the electron beam, a detailed study of such tolerances should be performed based on interaction simulations. In particular, periodic manufacturing defects could lead to unwanted mode coupling and parasitic oscillations. Furthermore, the search of efficient manufacturing methods for the helically corrugated interaction regions is still ongoing. While the University of Strathclyde has shown first prototypes of sub-THz interaction regions [44], they where never tested in hot experiments.

- **Realistic electron distributions in the electron beam**
  In this work, ideal electron beams were studied exclusively. A non-ideal electron beam will mainly reduce the efficiency and the bandwidth of the designed helical gyro-TWTs. Especially the reduced bandwidth could become problematic for a passive mode-locked oscillator and could result in the generation of longer pulses. However, for a detailed study of the effects of non-ideal electron beams, first a design of the electron gun

must be developed. Simulations of such a gun will allow an estimation of realistic kinetic energy and velocity distributions in the electron beam.

This work prepared the way for the realization of the first high-power 263 GHz passive mode-locked oscillator. The new developed simulation tools in combination with existing simulation capabilities cover the complete design process of a sub-THz passive mode-locked oscillator. This includes the previously mentioned topics of further research. If the passive mode-locked oscillator will be realized in the frame of the proposed multi-purpose source, this has the potential to revolutionize future sub-THz spectroscopy methods.

A Appendix

A.1 Split-Step Fourier Method

A common method to solve the HME is the split-step Fourier method (SSFM) [200], [201]. In the SSFM, the operator O representing the differential equation under investigation, is split into a linear operator $\mathcal{K}$ and a non-linear operator $\mathcal{N}$:

$$\frac{\partial \overline{A}}{\partial T} = O\overline{A} = (\mathcal{K} + \mathcal{N})\,\overline{A}\ . \tag{A.1}$$

It is assumed that the linear and non-linear parts can be applied separately and therefore, can be solved in two separate steps. If a small time interval $[T_0, T_0 + \Delta T]$ is considered and the influence of the non-linear operator $\mathcal{N}$ is negligible in a first step, then (A.1) reduces to

$$\frac{\partial \overline{A}}{\partial T} = \mathcal{K}\overline{A}\ . \tag{A.2}$$

The solution to this differential equation can be found in the frequency space:

$$\frac{\partial \tilde{\overline{A}}}{\partial T} = \mathcal{F}\left(\mathcal{K}\overline{A}\right)\ . \tag{A.3}$$

For this ordinary differential equation (ODE), an analytical solution is given by

$$\overline{A} = \mathrm{e}^{j\Delta T\mathcal{K}} \tag{A.4}$$

In a similar manner, the non-linear part of the original partial differential equation is reduced to an ODE:

$$\frac{\mathrm{d}\overline{A}}{\mathrm{d}T} = \mathcal{N}\overline{A}\ . \tag{A.5}$$

While the linear part could be solved analytically in the frequency domain, it is difficult to find analytical solutions for a non-linear operator. A common approach is to use a numerical solution method for the non-linear ODE. In the implementation of the SSFM used in this work, the non-linear parts are solved numerically in the time domain with a Runge-Kutta method (RK).

If the HME is solved with the SSFM, the numerical stability can be improved by an asymmetric splitting as presented in [202]. In the asymmetric splitting procedure, first the linear effects are calculated analytically for a half time step. Then the non-linear effects are applied and solved with a RK solver, followed by the second, linear half step.

A great advantage of the SSFM is its simplicity. In a mathematical environment such as MATLAB, the algorithm can be implemented in a few lines.

A.2 Verification of Electron-Wave Interaction Simulations

An important step in the development of simulation programs is the verification of the developed models and implementations. In this section, the previously presented model and its implementation is evaluated by comparisons with experimental data.

For a validation of the electron-wave interaction in a cylindrical interaction region, the electron-wave interaction model is compared with measurements of the SP-ITER Gyrotron [140]. The SP-ITER Gyrotron is developed, produced and tested at the IHM and therefore sufficient setup data and experimental results are available. Because of the similar interaction space, a successful verification based on the SP-ITER Gyrotron can be directly transferred to a cyclotron absorber. Furthermore, the SP-ITER Gyrotron operates in the sub-THz region at 170 GHz and therefore in a similar frequency range as the devices under investigation in this work.

Since no experimental results for helical gyro-TWTs are available at the IHM, for a verification of the electron-wave interaction in helically corrugated interaction regions, a comparisons with published experimental results of the first W-Band helical gyro-TWT [42] are performed.

A.2.1 Short-Pulse ITER Gyrotron

For the plasma heating and current drive in future fusion plants, high-power microwave sources are required. The SP-ITER Gyrotron is a prototype of such a high-power microwave source for the high-power electron cyclotron resonance heating (ECRH) heating system of the ITER fusion plant [203]. It operates at a frequency of $170\,\mathrm{GHz}$ and is designed to deliver an output power of $1\,\mathrm{MW}$. While the final ITER gyrotron will deliver the power in CW, the prototype SP-ITER Gyrotron is designed for short pulses up to several milliseconds. The SP-ITER Gyrotron is developed, built and tested at the IHM [140].

For a validation of the derived electron-wave interaction model and the developed implementation, the switch-on process at several operation points is simulated and compared with measurement results as well as with simulations performed with Euridice [121]. In the following, the results for a specific operation point are presented in detail.

A suitable operation point for a validation with sufficient experimental data available is the so-called low-voltage operation point with an electron beam at a guiding center radius of $9.55\,\mathrm{mm}$, a magnetic field strength of $6.9\,\mathrm{T}$ at the cavity and a magnetic field angle at the electron emitter of $-2°$. During the start-up of a gyrotron, the acceleration voltage U_{acc} in the electron gun is ramped up. In Fig. A.1, the evolution of the beam parameters during the acceleration voltage ramp-up are shown. The shown beam parameters are simulated with the trajectory solver Ariadne [81].

In the experiment, the voltage ramp-up is applied over a time of several milliseconds. For the interaction simulations, this period is shortened by several magnitudes to $1500\,\mathrm{ns}$. This is necessary to reduce the required simulation time. A real time simulation would require a computational time in the order of one year while the shortened voltage ramp-up can be simulated in a few hours. The simulations are performed for the cavity region including the down- and up-taper sections. A realistic magnetic field profile and ohmic losses are taken into account in all simulations.

In Fig. A.2, the output power in the different modes at the end of the up-taper is shown. The cavity is designed for an operation with the $\mathrm{TE}_{32,9}$ mode. During the ramp up, the cavity mode is excited by the electron beam and the output

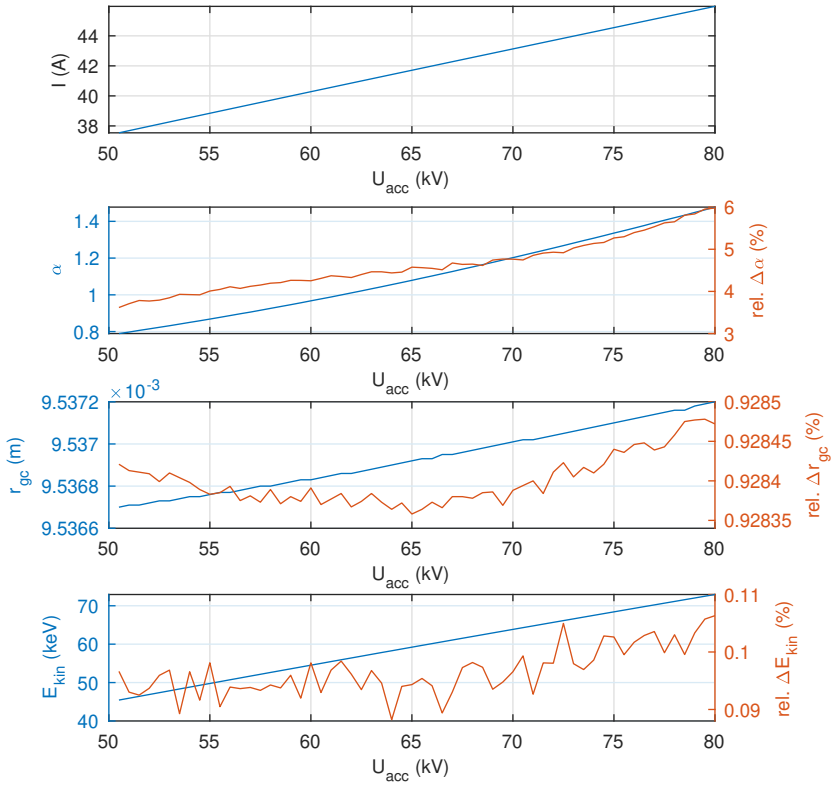

Figure A.1: Start-up electron beam parameters for the low voltage operation point with guiding center radius of 9.55 mm, magnetic field of 6.9 T and a magnetic-field angle at the electron emitter of $-2°$. The beam parameters are simulated with the Ariadne simulation tool.

power increases with an increasing transversal energy of the electrons. At a certain limit, the main mode is lost and the power drops. While the experiments are stopped at this point, the simulations are continued and a parasitic mode is excited after the loss of the main mode.

As it can be seen from Fig. A.2, a good agreement between the simulated and measured output power is observed. It must be emphasized that the obtained results are even more consistent with the measured values than the simulation

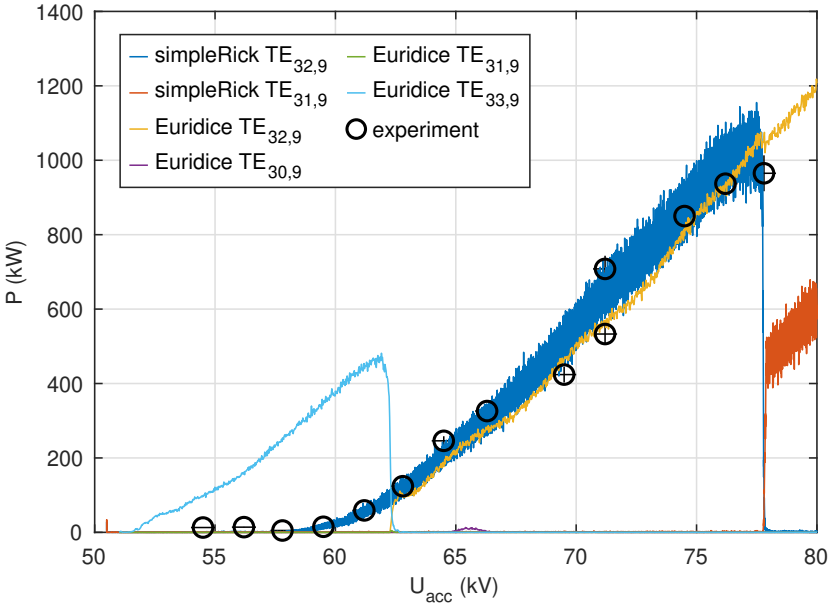

Figure A.2: Output power of the SP-ITER Gyrotron over the electron acceleration voltage for the low voltage operation point with guiding center radius of 9.55 mm and a magnetic-field angle at the electron gun's emitter of $-2°$. Thick lines are results of the developed interaction code (simpleRick), thin lines are results of the simulation tool Euridice and dots are measurement results. Only modes with non-zero power are shown.

results of the established tool Euridice. The position of the mode loss is correctly simulated as well as the expected output power. Furthermore, the excitation of the main mode ($TE_{32,9}$) corresponds very well to the experiment, whereas in Euridice the parasitic mode $TE_{33,9}$ is excited initially, which is not observed in the experiment.

The frequency of the generated RF signal is shown in Fig. A.3. In a first simulation run using the designed contour of the cavity, a significant shift in the frequency is observed (blue line in Fig. A.3). Therefore, an offset of $+16\,\mu m$ is added to the contour of the cavity. As a result, the frequency is shifted towards the measured data and the simulation results are in excellent agreement with the measured data. Since the manufacturing tolerances for this prototype cavity are $\pm 20\,\mu m$, the introduced offset is reasonable. The overall evolution

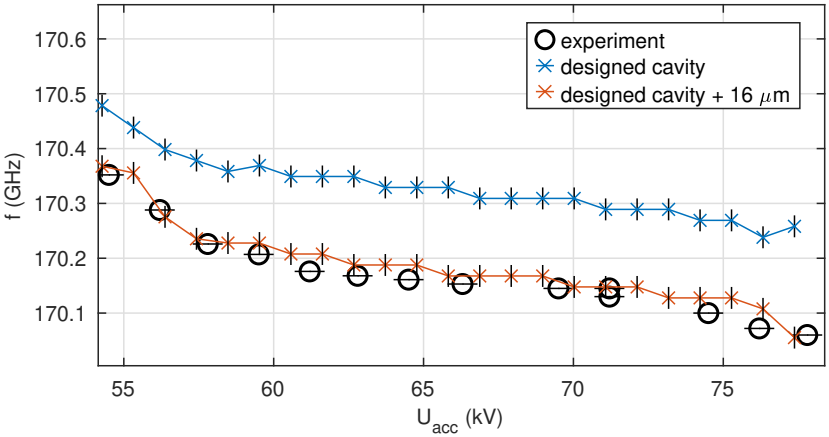

Figure A.3: Frequency of the generated RF signal of the SP-ITER Gyrotron over the electron acceleration voltage for the low voltage operation point with guiding center radius of 9.55 mm and a magnetic-field angle at the electron gun's emitter of $-2°$. In black the measured frequency, in blue the simulated frequency for the designed cavity and in red the simulated frequency for a cavity with a radius increased by 16 μm.

of the frequency over the acceleration voltage is in a good agreement between simulation and measurement. The simulated frequencies are determined by a Fourier transformation of the time dependent, slowly changing amplitude. The uncertainties at the simulated frequencies are caused by the limited time span of the Fourier transform (50 ns for every shown frequency point).

It can be concluded that the performed simulations of the SP-ITER Gyrotron cavity are in agreement with the experimental results and prove the correctness of the developed implementation. It should be highlighted that the derived model with a 3D PIC electron beam and a full source term, without any form of averaging, seams to model the electron-wave interaction in a gyrotron better than the established models. The new model is able to simulate the correct switch-on behavior without the excitation of parasitic modes which is in an excellent agreement with the experiments.

A.2.2 W-Band Helical Gyro-TWT

Since no helical gyro-TWT was available for experiments during this thesis, for a verification of the electron wave interaction in a helically corrugated waveguide, comparisons with published experimental results are performed. In the past, most helical gyro-TWTs have been realized in the X, Ku and Ka bands for radar applications. So far, only two different groups have published experimental results of helical gyro-TWTs operating in the low sub-THz region (W-band). In 2017, the group of He et al. at the University of Strathclyde (Glasgow, UK) has demonstrated the first W-band helical gyro-TWT [42] and in 2020, the group of Samsonov et al. at the IAP-RAS (Nizhny Novgorod, Russia) has demonstrated a W-band, high-gain helical gyro-TWT consisting of two helically corrugated waveguide sections [43]. Because the high-gain helical gyro-TWT with its two-section interaction region is significantly more complex than a usual helical gyro-TWT, the W-band helical gyro-TWT presented by He et al. in [42] is used in the following for the validation of the developed simulation program.

The interaction region of the helical gyro-TWT consist of a helically corrugated waveguide with a mean radius of $R = 1.45\,\mathrm{mm}$, a corrugation amplitude of $\tilde{r} = 0.23\,\mathrm{mm}$, a corrugation period of $\tilde{d} = 3.20\,\mathrm{mm}$ and a length of $L = 40\,\tilde{d}$ [1].

The guiding magnetic field is given with $\mathfrak{B}_0 \approx 1.82\,\mathrm{T}$. Since no profile of the magnetic field is provided in the publication, a constant profile is assumed for the simulations.

The electron beam has a kinetic energy of $E_{\mathrm{kin}} = 55\,\mathrm{keV}$ and a pitch factor of $\alpha \approx 1$. In [42], the spread for the pitch factor is given with $10\,\%$. The definition of spreads used in the publication is different from the definition used in this thesis[2] (see (3.25)). The $10\,\%$ refers to the FWHM relative to the mean of the distribution while in (3.25) the spread of a value is defined as the standard deviation relative to the mean value of the distribution. Consequently, the spread of the pitch factor is $\delta\alpha = 4.2\,\%$. The width of the electron beam is given with $0.1\,\mathrm{mm}$. This corresponds to a guiding center radius of $r_{\mathrm{g}} = 0.05\,\mathrm{mm}$.

[1] The length of the interaction region is not explicitly given in the publication, but a request to the research group of He et al. revealed a length of $L = 40\,\tilde{d}$.

[2] A request for clarification to the research group of He et al. revealed the exact definition of spreads.

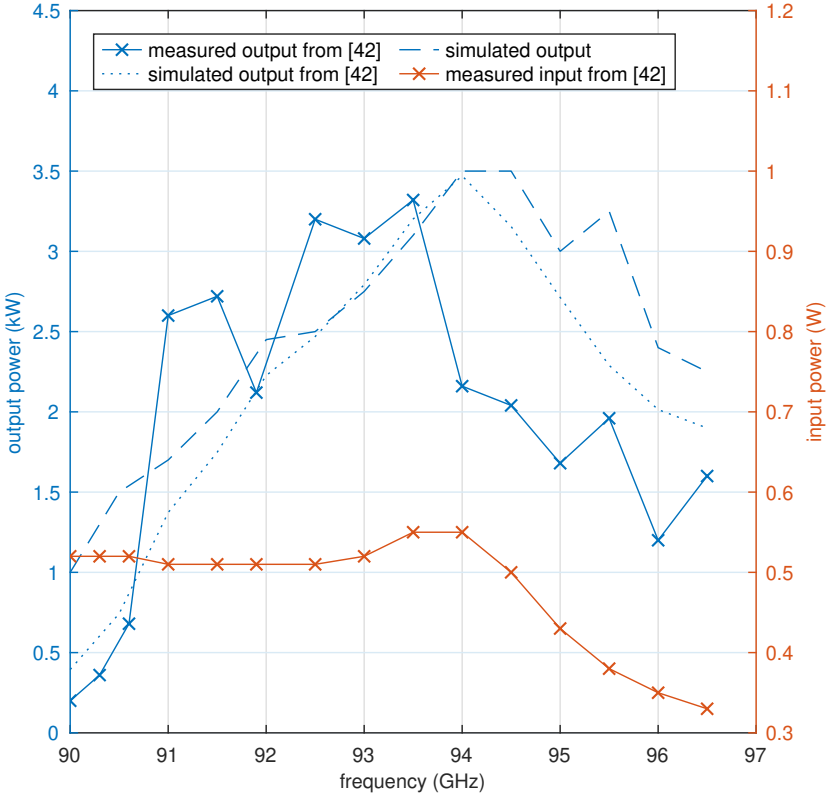

Figure A.4: Simulated and measured output power of the W-band helical gyro-TWT at different frequencies. The measured values are taken from [42]. For a comparison, also simulated data from [42] are shown.

For the performed simulations a time discretization step of $\Delta t = 0.1$ ps, a space discretization step of $\Delta z = 15$ µm and a particle macro factor of 10^4 are used. This results in two systems of 10000 linear equations for the amplitudes and 1 million equations of motion for the particles which have to be solved at every time step. On a workstation with an AMD Ryzen 5900x CPU and a Nvidia GTX 1070 Ti GPU the simulation of 1 ns requires approximately 1:30 minutes.

In Fig. A.4, the measured and simulated output powers for different frequencies of the input signal are shown. The measurement results are taken from [42]. For a better evaluation of the performed simulations, simulation results from the original publication are shown additionally. The simulations in [42] are performed with the 3D PIC program Magic [117]. From Fig. A.4 it can be seen that both simulations are in agreement. The total power level as well as the frequency dependency are similar for both simulation models. Only a slightly higher output power in the edge regions of the investigated frequency band is observed.

In [42], the guiding magnetic field $\mathfrak{B}_0$ is given with approximately $1.82\,\mathrm{T}$. For the performed simulations, a slightly higher value of $1.827\,\mathrm{T}$ is used. Since the magnetic field profile is unknown, a constant field is assumed. It must be mentioned that the simulated output power is strongly dependent on the magnetic field. A variation of $\pm 0.002\,\mathrm{T}$ results in a variation of the peak output power of $\pm 1\,\mathrm{kW}$. However, the observed frequency dependence is hardly dependent on the magnetic field. This is in great agreement with the expectations.

In comparison with the measurements, both simulations show a good agreement of the maximal output power but a shift of the frequency dependence of $1\,\mathrm{GHz}$ towards higher frequencies. A possible reason could be manufacturing tolerances of the helical interaction region. A slightly increased waveguide radius R of $+25\,\mu\mathrm{m}$ would result in the observed frequency shift. However, the original publication does not discuss the frequency shift and, therefore, the reason cannot be determined with certainty.

In Fig. A.5, the spectrum of the simulated output signals for input signals of $90\,\mathrm{GHz}$, $93\,\mathrm{GHz}$ and $96\,\mathrm{GHz}$ is shown. For all three input frequencies, a clear peak at the corresponding frequency can be observed in the spectrum. This proves that the amplifier is operated in a zero-drive stable amplification regime and no parasitic oscillations occur. The noise background in the spectra indicates a maximal bandwidth of 90 to $100\,\mathrm{GHz}$ of the helical gyro-TWT operated with the previously given parameters.

Finally, it can be concluded that the developed simulation model as well as the developed implementation have shown an accurate prediction of the output power of a sub-THz helical gyro-TWT. Thus, it can be assumed that the sim-

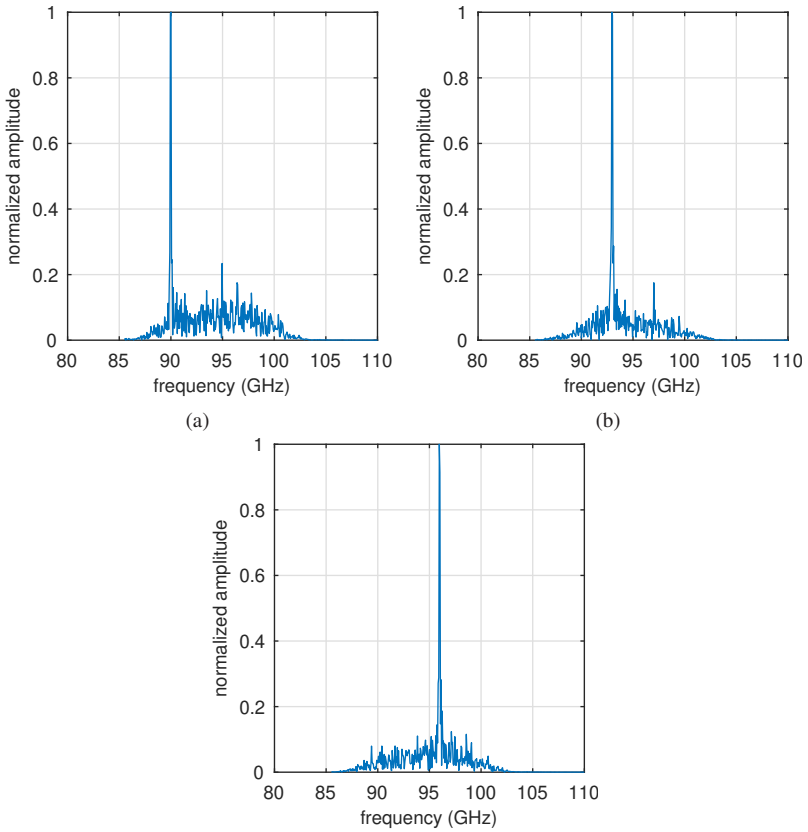

Figure A.5: Spectrum of simulated output signals of the W-band helical gyro-TWT in [42] for input signals of 90 GHz, 93 GHz and 96 GHz.

ulations in the following chapters of helical gyro-TWTs operated at 263 GHz also provide reliable predictions for the real tubes.

A.3 Verification of EFIE Solver

For the verification of the developed EFIE solver KarLESSS, the simulated field distributions and the simulated ohmic losses are compared with measurements.

A.3.1 Verification of Simulated Field Distribution

For a verification of the simulated field distributions, the well proven quasi-optical system of the 1 MW gyrotron developed for the Wendelstein 7-X stellarator (W7-X) [204] is simulated and compared with measurements. The W7-X 1 MW gyrotron is designed to deliver a CW microwave radiation of 1 MW at a frequency of 140 GHz and is successfully used at the W7-X stellarator since several years [205].

The quasi-optical system of the W7-X 1 MW gyrotron is chosen as verification case, because it fulfills the following requirements: (1) the quasi-optical system has a size in the order of $100\,\lambda$ and fits therefore perfectly into the scope of KarLESSS and the expected dimensions of a quasi-optical feedback system for a passive mode-locked sub-THz oscillator; (2) the required geometry files are available at the IHM-KIT; (3) it was possible to perform high-precision cold measurements [206].

The quasi-optical system consists of a waveguide antenna with helical cut (the so-called launcher) and three parabolic mirrors. The quasi-optical system is designed to transform a $\mathrm{TE}_{28,8}$ circular waveguide mode at a frequency of 140 GHz into a Gaussian beam. This Gaussian beam exits the gyrotron horizontally through a disc window, usually made of chemical vapor deposition diamond (CVD).

For a verification, the electric field distribution in the plane of the disc window is simulated and compared with measurements. In Fig. A.6, the simulated field and phase distributions are shown on the left and the measured distributions [206], shown on the right. A qualitative comparison of the simulated and measured distributions shows a good agreement. The shape and phase of the main lobe has a high agreement between measurement and simulation. Also, the side lobes are in agreement. In both, simulation and measurement,

diffraction effects caused by the helical cut of the launcher are visible at the side lobe on the left of the main lobe.

For a more objective comparison of the simulated electric fields $\mathfrak{E}_{\mathrm{sim}}$ and the measured fields $\mathfrak{E}_{\mathrm{meas}}$, a correlation coefficient C^{corr} can be determined by:

$$C^{\mathrm{corr}} = \frac{\left| \int \mathfrak{E}_{\mathrm{meas}} \mathfrak{E}^{\dagger}_{\mathrm{sim}} \, \mathrm{d}A \right|^2}{\left| \int \mathfrak{E}_{\mathrm{meas}} \mathfrak{E}^{\dagger}_{\mathrm{meas}} \, \mathrm{d}A \right| \cdot \left| \int \mathfrak{E}_{\mathrm{sim}} \mathfrak{E}^{\dagger}_{\mathrm{sim}} \, \mathrm{d}A \right|} \,. \tag{A.6}$$

The correlation coefficient C^{corr} considers amplitude and phase of the field and is sometimes also referred as vector correlation coefficient. Note, that in the literature regarding quasi-optical mode converters for gyrotrons often a so-called scalar correlation coefficient is used. The scalar correlation coefficient neglects the phase information and is therefore always higher than the vector correlation coefficient.

In table A.1, several correlation coefficients for the data in Fig. A.6 are calculated. First, it is noticeable that the correlation coefficient $C^{\mathrm{corr}}_{\mathrm{full}}$ for the data as shown in Fig. A.6 is only $92.4\,\%$. This is mainly caused by the high background noise level of the measured data. On the basis of Fig. A.6b, it can be estimated that the background noise level is about $-25\,\mathrm{dB}$. To verify this estimation, signals below $-30\,\mathrm{dB}$, $-25\,\mathrm{dB}$ and $-20\,\mathrm{dB}$ are filtered out and the correlation coefficients are recalculated.

From $C^{\mathrm{corr}}_{30\mathrm{dB}}$ and $C^{\mathrm{corr}}_{25\mathrm{dB}}$ it can be seen that the signals in the range of $-30\,\mathrm{dB}$ to $-25\,\mathrm{dB}$ strongly influence the correlation coefficient. If even higher signals are filtered out, the correlation coefficient decreases again since significant parts of the relevant signal are filtered out (compare $C^{\mathrm{corr}}_{25\mathrm{dB}}$ and $C^{\mathrm{corr}}_{20\mathrm{dB}}$). Therefore, a background noise level of $-25\,\mathrm{dB}$ can be assumed.

For high-power measurements at a gyrotron, only the field pattern in the area of the CVD diamond window is accessible. Therefore, the correlation coefficient of the field in the area of the window (radius $44\,\mathrm{mm}$) is additionally given in table A.1. Here, the correlation coefficient is as high as $97.0\,\%$.

To classify the results, the measurements should be briefly discussed. For measuring the quasi-optical mode generator, the high-order cavity mode ($\mathrm{TE}_{28,8}$ in this case) is required. In the gyrotron, it is generated in the cavity by a resonant

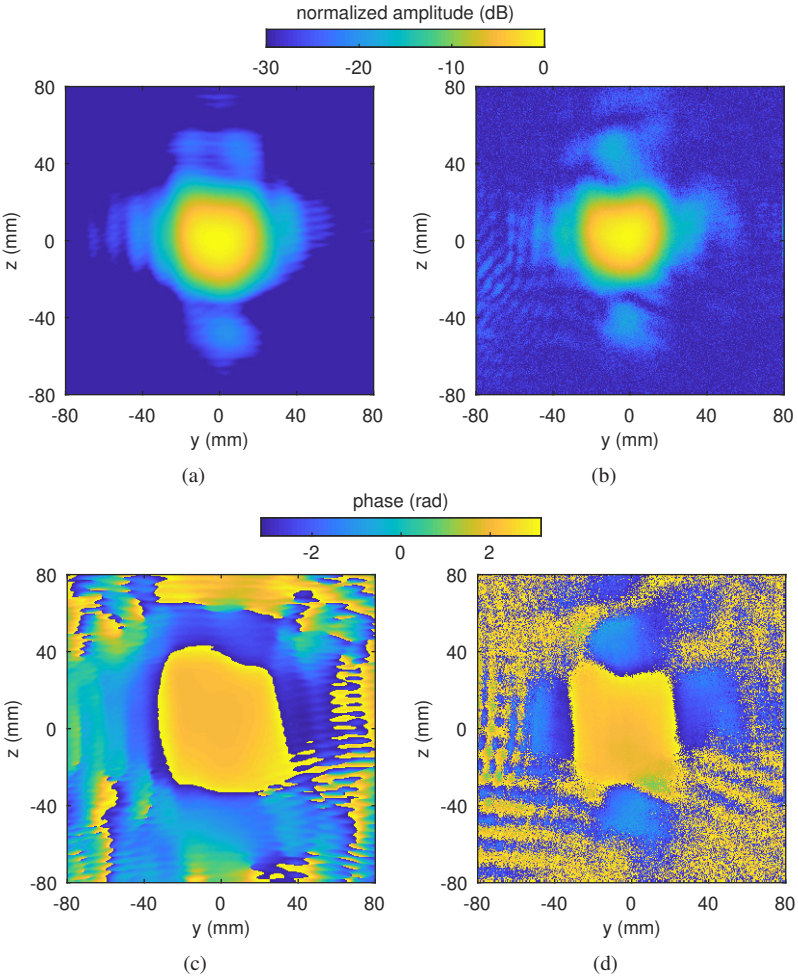

Figure A.6: Comparison of simulated (a+c) and measured (b+d) amplitude (a+b) and phase (c+d) distributions of the electric fields in the plane of the gyrotron's output window. A good agreement between simulation and measurement is observed. Measured data publicized in [206].

Table A.1: Vectorial correlation coefficients between the simulated and measured data (see Fig. A.6) of the W7-X gyrotron's quasi-optical system.

	Correlation coeff.	Description
$C^{\mathrm{corr}}_{\mathrm{full}}$	$92.4\,\%$	full data as shown in Fig. A.6
$C^{\mathrm{corr}}_{\mathrm{30dB}}$	$92.8\,\%$	filter values below -30 dB in the measurement
$C^{\mathrm{corr}}_{\mathrm{25dB}}$	$95.4\,\%$	filter values below -25 dB in the measurement
$C^{\mathrm{corr}}_{\mathrm{20dB}}$	$94.5\,\%$	filter values below -20 dB in the measurement
$C^{\mathrm{corr}}_{\mathrm{window}}$	$97.0\,\%$	area of the CDV diamond window ($r = 44$ mm)

interaction of the gyrating electron beam. However, the measurements are not performed in a gyrotron at high power. The $\mathrm{TE}_{28,8}$ mode is generated at very low power by means of a special mode generator [206]. In the mode generator, the required high-order cavity mode is excited by irradiating a low power microwave signal into a resonant cavity [207]. Thereby, the scalar purity of the generated $\mathrm{TE}_{28,8}$ mode is $\approx 95\,\%$ [206]. Since the exact composition of the generated mode is unknown, a perfect $\mathrm{TE}_{28,8}$ mode is used for the simulations. Consequently, a $100\,\%$ match between measurements and simulations is not expected.

It can be concluded that a good agreement between simulation and measurement is observed, particularly if the uncertainties of the generated $\mathrm{TE}_{28,8}$ mode are taken into account. If the background noise is filtered out, the correlation between simulation and measurement is higher than $95\,\%$. In the area of the gyrotron output window, the correlation approaches even $97\,\%$.

A.3.2 Verification of Simulated Ohmic-Loss

In [188], Wagner et al. measured the ohmic losses in miter bends of a high-power transmission line for future ECRH systems. For a verification of the ohmic losses calculated by KarLESSS, such a $90°$ miter bend is used as a test case.

The measurements in [188] are performed with high-power (375 kW) microwave radiation at 140 GHz from a gyrotron of the ASDEX Upgrade ECRH system [208]. Wagner et al. measured the ohmic losses in a 90° miter bend of a corrugated waveguide with an inner diameter of 87 mm for a $\mathrm{HE}_{1,1}$ mode at 140 GHz. The mirror of the miter bend is realized as a 5 mm thick stainless steel (VA 1.4311) plate with a diameter of 140 mm.

For a simple comparability of measurement and simulation, a normalization is introduced in [188]. The measured and simulated absorption coefficients ϖ are normalized to the absorption coefficient at perpendicular incidence $\Theta = 0°$, on a plane mirror:

$$\varpi_{\mathrm{norm}} = \frac{\varpi}{\varpi_{\perp}} , \tag{A.7}$$

$$\varpi_{\perp} = 4\frac{R_{\mathrm{surf}}}{Z_0} . \tag{A.8}$$

Here, R_{surf} is the surface resistance and Z_0 is the free space wave impedance. With this normalization, all material effects and also effects such as the surface roughness are removed.

In [188], measurements for different angles ϕ of the polarization plane of the incident, linear polarized $\mathrm{HE}_{1,1}$ mode relative to the miter bend's mirror are performed. Only for the angles $\phi = 0°$ and $\phi = 90°$ (E-plane and H-plane), analytical expressions for the expected losses are available [209]:

$$\begin{aligned} \varpi_{\phi=0°} &= \frac{\varpi_{\perp}}{\cos(\Theta)} , \\ \varpi_{\phi=90°} &= \varpi_{\perp}\cos(\Theta) , \end{aligned} \tag{A.9}$$

where Θ is the angle of the mirror, relative to the propagation direction of the incident wave. For a 90° miter bend, Θ is 45°.

In Fig. A.7, the measured absorptions from [188], the analytical vales for $\phi = 0°$ and $\phi = 90°$, and the absorptions simulated with KarLESSS are shown. All values are normalized according to (A.7).

A high agreement between the measured and the simulated data is observed. The simulated values also agree well with the theory for E-plane and H-plane incidence, respectively. From the theory, a normalized absorption of 1.414

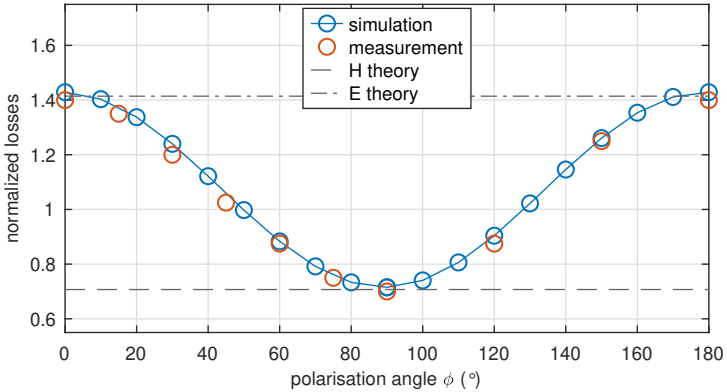

Figure A.7: Comparison of simulated and measured ohmic losses of a $HE_{1,1}$ mode on the plat mirror in a $45°$ miter bend. The ohmic losses are normalized to (A.8). Measured data is taken from [188].

and 0.707 for the E-plane and H-plane incidence are expected, respectively. The corresponding simulated normalized absorption coefficients are 1.429 and 0.715. Both values are only $1.1\,\%$ above the theoretical values.

In comparison with the measured absorption coefficients, the simulated values are again slightly higher, in average $\approx 3\,\%$. Unfortunately, no error limits are given for the measured values in [188]. Apart from the minor offset, the evolution of the absorption coefficients is in a good agreement between simulation and measurement.

It can be concluded that a good agreement between the simulations, the theory and the measurements is observed.

A.4 Passive Mode-locked Oscillator with Cyclotron Absorber

For a validation of the correlation of the pulse shape and the dispersion of the system, the generated pulse shape of the passive mode-locked oscillator consisting of the slippage helical gyro-TWT and the cyclotron absorber is ana-

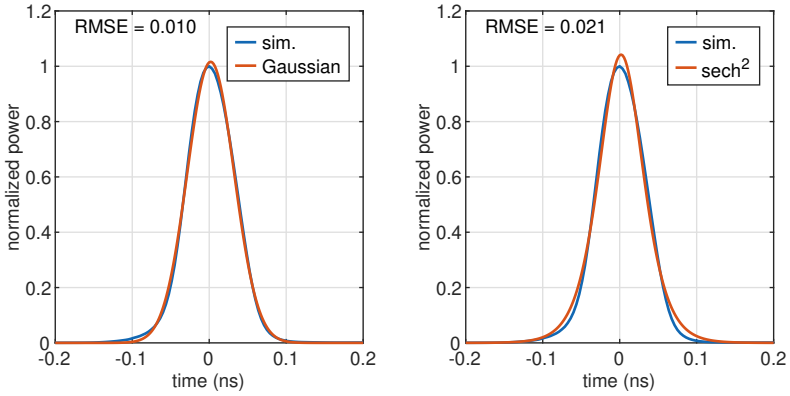

(a) (b)

Figure A.8: Simulated pulse shape for the passive mode-locked oscillator with slippage helical gyro-TWT amplifier and cyclotron absorber together with a fitted Gaussian (a) and sech^2 (b) pulse.

lyzed in addition to the mode-locked oscillator consisting of the slippage helical gyro-TWT and the helical gyro-TWT absorber (see chapter 6.3). Although this oscillator is inappropriate for realization, the analysis helps to understand the basic principle of passive mode-locking at sub-THz frequencies. Because of the higher dispersion of the cyclotron absorber compared to the helical gyro-TWT absorber, a Gaussian-like pulse shape is expected for this oscillator than for the one analyzed in chapter 6.3. As shown in Fig. A.8, this is actually observed which confirms the parallels to laser physics.

Bibliography

[1] A. Gaponov-Grekhov and V. Granatstein, *Applications of high-power microwaves*. Artech House Publishers, 1994, ISBN: 9780890066997.

[2] V. Denysenkov, M. J. Prandolini, M. Gafurov, D. Sezer, B. Endeward, and T. F. Prisner, "Liquid state DNP using a 260 GHz high power gyrotron", *Physical Chemistry Chemical Physics*, vol. 12, p. 5786, 2010. DOI: 10.1039/c003697h.

[3] R. G. Griffin, T. M. Swager, and R. J. Temkin, "High frequency dynamic nuclear polarization: New directions for the 21st century", *Journal of magnetic resonance*, vol. 306, pp. 128–133, 2019. DOI: 10.1016/j.jmr.2019.07.019.

[4] N. S. Ginzburg, G. G. Denisov, M. N. Vilkov, I. V. Zotova, and A. S. Sergeev, "Generation of a periodic sequence of powerful ultrashort pulses in a traveling wave tube with bleachable absorber in the feedback loop", *Technical Physics Letters*, vol. 41, no. 9, pp. 836–839, Sep. 2015. DOI: 10.1134/S1063785015090047.

[5] J. Herrmann and B. Wilhelmi, *Laser für ultrakurze Lichtimpulse: Grundlagen und Anwendungen*. Physik-Verlag, 1984, ISBN: 978311-2528891.

[6] T. Brabec and F. Krausz, "Intense few-cycle laser fields: Frontiers of nonlinear optics", *Reviews of Modern Physics*, vol. 72, pp. 545–591, 2000. DOI: 10.1103/revmodphys.72.545.

[7] T. V. Can, J. J. Walish, T. M. Swager, and R. G. Griffin, "Time domain DNP with the NOVEL sequence", *The Journal of Chemical Physics*, vol. 143, no. 5, p. 054 201, 2015. DOI: 10.1063/1.4927087.

[8] K. O. Tan, C. Yang, R. T. Weber, G. Mathies, and R. G. Griffin, "Time-optimized pulsed dynamic nuclear polarization", *Science Advances*, vol. 5, no. 1, eaav6909, 2019. DOI: 10.1126/sciadv.aav6909.

[9] G. Mathies, S. Jain, M. Reese, and R. G. Griffin, "Pulsed dynamic nuclear polarization with trityl radicals", *J. Phys. Chem. Lett.*, vol. 7, no. 1, pp. 111–116, Jan. 2016. DOI: 10.1021/acs.jpclett.5b02720.

[10] F. Arecchi and R. Bonifacio, "Theory of optical maser amplifiers", *IEEE Journal of Quantum Electronics*, vol. 1, no. 4, pp. 169–178, 1965. DOI: 10.1109/jqe.1965.1072212.

[11] A. W. Fliflet, M. E. Read, K. R. Chu, and R. Seeley, "A self-consistent field theory for gyrotron oscillators: Application to a low Q gyromonotron", *International Journal of Electronics Theoretical and Experimental*, vol. 53, pp. 505–521, 1982. DOI: 10.1080/00207218208901545.

[12] A. Marek, J. Jin, J. Jelonnek, M. Thumm, and A.-S. Muller, "Development of an advanced vector analysis code for simulation of electromagnetic fields in quasi-optical systems of high power gyrotrons", in *Eighteenth International Vacuum Electronics Conference (IVEC)*, 2017. DOI: 10.1109/ivec.2017.8289599.

[13] P. G. Kryukov, "Ultrashort-pulse lasers", *Quantum Electronics*, vol. 31, no. 2, pp. 95–119, Feb. 2001. DOI: 10.1070/qe2001v031n02abeh001906.

[14] Y. Han, Y. Guo, B. Gao, C. Ma, R. Zhang, and H. Zhang, "Generation, optimization, and application of ultrashort femtosecond pulse in mode-locked fiber lasers", *Progress in Quantum Electronics*, vol. 71, p. 100 264, 2020. DOI: 10.1016/j.pquantelec.2020.100264.

[15] F. J. McClung and R. W. Hellwarth, "Giant optical pulsations from ruby", *Journal of Applied Physics*, vol. 33, no. 3, pp. 828–829, 1962. DOI: 10.1063/1.1777174.

[16] B. Hitz, J. J. Ewing, and J. Hecht, *Introduction to Laser Technology, Hitz/Introduction to Laser Technology*. John Wiley & Sons, 2001, ISBN: 978-0470916209. DOI: 10.1002/0471723126.

[17] H. W. Mocker and R. J. Collins, "Mode competition and self-locking effects in a Q-switched ruby laser", *Applied Physics Letters*, vol. 7, no. 10, pp. 270–273, 1965. DOI: 10.1063/1.1754253.

[18] D. Bimberg, M. Grundmann, and N. N. Ledentsov, *Quantum dot heterostructures*. John Wiley & Sons, 1999, ISBN: 9780471973881.

[19] E. U. Rafailov, M. A. Cataluna, and E. A. Avrutin, *Ultrafast lasers based on quantum dot structures: Physics and devices*. John Wiley & Sons, 2011, ISBN: 9783527409280.

[20] R. Köhler, A. Tredicucci, F. Beltram, *et al.*, "Terahertz semiconductor-heterostructure laser", *Nature*, vol. 417, no. 6885, pp. 156–159, 2002. DOI: 10.1038/417156a.

[21] B. S. Williams, S. Kumar, Q. Hu, and J. L. Reno, "High-power terahertz quantum-cascade lasers", *Electronics Letters*, vol. 42, no. 2, pp. 89–91, 2006. DOI: 0.1049/el:20063921.

[22] B. S. Williams, "Terahertz quantum cascade lasers", in *Asia Optical Fiber Communication and Optoelectronic Exposition and Conference*, Optical Society of America, 2008, SuG3. DOI: 10.1364/AOE.2008.SuG3.

[23] K. Reimann, "Table-top sources of ultrashort THz pulses", *Reports on Progress in Physics*, vol. 70, no. 10, pp. 1597–1632, Sep. 2007. DOI: 10.1088/0034-4885/70/10/r02.

[24] G. Mourou, C. V. Stancampiano, and D. Blumenthal, "Picosecond microwave pulse generation", *Applied Physics Letters*, vol. 38, no. 6, pp. 470–472, 1981. DOI: 10.1063/1.92407.

[25] K. E. Niebuhr, "Generation of laser axial mode difference frequencies in a nonlinear dielectric", *Appl. Phys. Lett.*, vol. 2, no. 7, pp. 136–137, Apr. 1963. DOI: 10.1063/1.1753811.

[26] F. Zernike and P. R. Berman, "Generation of far infrared as a difference frequency", *Phys. Rev. Lett.*, vol. 15, pp. 999–1001, 26 Dec. 1965. DOI: 10.1103/PhysRevLett.15.999.

[27] D. J. Cook and R. M. Hochstrasser, "Intense terahertz pulses by four-wave rectification in air", *Opt. Lett.*, vol. 25, no. 16, pp. 1210–1212, Aug. 2000. DOI: 10.1364/OL.25.001210.

[28] G. G. Denisov, S. V. Kuzikov, and A. V. Savilov, "Q-switching in the electron backward-wave oscillator", *Physics of plasmas*, vol. 18, p. 103 102, 2011. DOI: 10.1063/1.3644472.

[29] A. Gaponov, M. Petelin, and V. Yulpatov, "The induced radiation of excited classical oscillators and its use in high-frequency electronics", *Radiophysics and Quantum Electronics*, vol. 10, no. 9-10, pp. 794–813, 1967. DOI: 10.1007/bf01031607.

[30] G. S. Nusinovich, M. K. Thumm, and M. I. Petelin, "The gyrotron at 50: Historical overview", *Journal of Infrared, Millimeter, and Terahertz Waves*, vol. 35, no. 4, pp. 325–381, 2014. DOI: 10.1007/s10762-014-0050-7.

[31] M. Thumm, "Recent advances in the worldwide fusion gyrotron development", *IEEE Transactions on Plasma Science*, vol. 42, no. 3, pp. 590–599, 2014. DOI: 10.1109/tps.2013.2284026.

[32] A. G. Litvak, G. G. Denisov, V. E. Myasnikov, E. M. Tai, E. A. Azizov, and V. I. Ilin, "Development in Russia of megawatt power gyrotrons for fusion", *Journal of Infrared, Millimeter, and Terahertz Waves*, vol. 32, no. 3, pp. 337–342, 2011. DOI: 10.1007/s10762-010-9743-8.

[33] K. Sakamoto, "Progress of high-power-gyrotron development for fusion research", *Fusion Science and Technology*, vol. 52, no. 2, pp. 145–153, 2007. DOI: 10.13182/FST07-A1493.

[34] J. Jelonnek, K. Avramidis, J. Franck, *et al.*, "KIT contribution to the gyrotron development for nuclear fusion experiments in europe", in *GeMiC 2014; German Microwave Conference*, 2014, pp. 1–4.

[35] N. Kumar, U. Singh, A. Bera, and A. Sinha, "A review on the sub-THz/THz gyrotrons", *Infrared Physics & Technology*, vol. 76, pp. 38–51, 2016. DOI: 10.1016/j.infrared.2016.01.015.

[36] T. Idehara, K. Kosuga, L. Agusu, *et al.*, "Gyrotron FU CW VII for 300 MHz and 600 MHz DNP-NMR spectroscopy", *Journal of Infrared, Millimeter, and Terahertz Waves*, vol. 31, no. 7, pp. 763–774, 2010. DOI: 10.1007/s10762-010-9637-9.

[37] M. Blank, P. Borchard, S. Cauffman, K. Felch, M. Rosay, and L. Tometich, "Development of high frequency CW gyrotrons for DNP / NMR application", in *Proc. of IVEC 2013 Intl. Vac. Electron. Conf.*, 2013.

[38] J. Hogge, F. Braunmueller, S. Alberti, *et al.*, "Detailed characterization of a frequency-tunable 260 GHz gyrotron oscillator planned for DNP/NMR spectroscopy", in *2013 38th International Conference on Infrared, Millimeter, and Terahertz Waves (IRMMW-THz)*, 2013, pp. 1–2. DOI: 10.1109/IRMMW-THz.2013.6665407.

[39] F. J. Scott, E. P. Saliba, B. J. Albert, *et al.*, "Frequency-agile gyrotron for electron decoupling and pulsed dynamic nuclear polarization", *Journal of Magnetic Resonance*, vol. 289, pp. 45–54, 2018. DOI: 10.1016/j.jmr.2018.02.010.

[40] G. G. Denisov, V. L. Bratman, A. D. R. Phelps, and S. V. Samsonov, "Gyro-TWT with a helical operating waveguide: New possibilities to enhance efficiency and frequency bandwidth", vol. 26, pp. 508–518, 1998. DOI: 10.1109/27.700785.

[41] W. He, C. R. Donaldson, L. Zhang, K. Ronald, P. McElhinney, and A. W. Cross, "High power wideband gyrotron backward wave oscillator operating towards the terahertz region", *Phys. Rev. Lett.*, vol. 110, p. 165 101, 16 Apr. 2013. DOI: 10.1103/PhysRevLett.110.165101.

[42] W. He, C. R. Donaldson, L. Zhang, K. Ronald, A. D. R. Phelps, and A. W. Cross, "Broadband amplification of low-terahertz signals using axis-encircling electrons in a helically corrugated interaction region", *Phys. Rev. Lett.*, vol. 119, p. 184 801, 18 Oct. 2017. DOI: 10.1103/PhysRevLett.119.184801.

[43] S. V. Samsonov, G. G. Denisov, I. G. Gachev, and A. A. Bogdashov, "CW operation of a W-band high-gain helical-waveguide gyrotron traveling-wave tube", *IEEE Electron Device Letters*, vol. 41, no. 5, pp. 773–776, 2020. DOI: 10.1109/LED.2020.2980572.

[44] C. R. Donaldson, L. Zhang, M. Beardsley, M. Harris, P. G. Huggard, and W. He, "CNC machined helically corrugated interaction region for a THz gyrotron traveling wave amplifier", *IEEE Transactions on Terahertz Science and Technology*, vol. 8, no. 1, pp. 85–89, 2018. DOI: 10.1109/tthz.2017.2778944.

[45] T. S. Taylor, *Introduction to Laser Science and Engineering*. CRC Press, 2020, ISBN: 9781138036390.

[46] J.-C. Diels and W. Rudolph, *Ultrashort laser pulse phenomena*. Elsevier, 2006, ISBN: 978-0122154935.

[47] E. Ippen, C. Shank, and A. Dienes, "Passive mode locking of the CW dye laser", *Applied Physics Letters*, vol. 21, no. 8, pp. 348–350, 1972. DOI: 10.1063/1.1654406.

[48] R. Ell, U. Morgner, F. X. Kärtner, *et al.*, "Generation of 5 fs pulses and octave-spanning spectra directly from a Ti:sapphire laser", *Optics Letters*, vol. 26, no. 6, pp. 373–375, Mar. 2001. DOI: 10.1364/OL.26.000373.

[49] J. H. Booske, R. J. Dobbs, C. D. Joye, *et al.*, "Vacuum electronic high power terahertz sources", *IEEE Transactions on Terahertz Science and Technology*, vol. 1, no. 1, pp. 54–75, 2011. DOI: 10.1109/TTHZ.2011.2151610.

[50] N. S. Ginzburg, G. G. Denisov, M. N. Vilkov, I. V. Zotova, and A. S. Sergeev, "Generation of gigantic ultra-short microwave pulses based on passive mode-locking effect in electron oscillators with saturable absorber in the feedback loop", *Physics of Plasmas*, vol. 23, no. 5, p. 050 702, 2016. DOI: 10.1063/1.4948553.

[51] R. Kompfner, "On the operation of the travelling wave tube at low level", *Journal of the British Institution of Radio Engineers*, vol. 10, pp. 283–289, 1950. DOI: 10.1049/jbire.1950.0028.

[52] N. S. Ginzburg, G. G. Denisov, M. N. Vilkov, *et al.*, "Generation of trains of ultrashort microwave pulses by two coupled helical gyro-TWTs operating in regimes of amplification and nonlinear absorption", *Physics of Plasmas*, vol. 24, no. 2, p. 023 103, 2017. DOI: 10.1063/1.4975084.

[53] N. S. Ginzburg, G. G. Denisov, M. N. Vilkov, *et al.*, "Passive mode-locking and generation of ultrashort pulses in electron oscillators with saturable absorber in the feedback loop", in *47th European Microwave Conference (EuMC)*, IEEE, 2017, pp. 684–686. DOI: 10.23919/eumc.2017.8230939.

[54] N. S. Ginzburg, E. B. Abubakirov, M. N. Vilkov, I. V. Zotova, and A. S. Sergeev, "Generation of a periodic sequence of high-power ultrashort pulses in a chain of coupled backward-wave and traveling-wave tubes operating in the regimes of amplification and nonlinear Kompfner suppression", *Technical Physics*, vol. 63, pp. 1205–1211, 2018. DOI: 10.1134/s1063784218080078.

[55] N. S. Ginzburg, G. G. Denisov, M. N. Vilkov, *et al.*, "Ultrawideband millimeter-wave oscillators based on two coupled gyro-TWTs with helical waveguide", *IEEE Transactions on Electron Devices*, vol. 65, pp. 2334–2339, 2018. DOI: 10.1109/ted.2018.2801021.

[56] N. S. Ginzburg, G. G. Denisov, M. N. Vilkov, *et al.*, "Development of ultrashort pulse generators based on helical gyro-TWT with saturable cyclotron resonance absorber in the feedback loop", in *International Vacuum Electronics Conference (IVEC)*, 2019. DOI: 10.1109/ivec.2019.8745048.

[57] N. S. Ginzburg, G. G. Denisov, M. N. Vilkov, A. S. Sergeev, S. V. Samsonov, and I. V. Zotova, "Generation of train of ultrashort Ka-band pulses by helical gyro-TWTs with nonlinear cyclotron resonance absorber in the feedback loop", in *43rd International Conference on Infrared, Millimeter, and Terahertz Waves (IRMMW-THz)*, 2018. DOI: 10.1109/irmmw-thz.2018.8509900.

[58] M. N. Vilkov, N. S. Ginzburg, I. V. Zotova, and A. S. Sergeev, "Generation of ultrashort microwave pulses in passive mode-locked electron oscillators with homogeneous and inhomogeneous line broadening", *EPJ Web of Conferences*, vol. 195, p. 01 020, 2018. DOI: 10.1051/epjconf/201819501020.

[59] N. S. Ginzburg, G. G. Denisov, M. N. Vilkov, *et al.*, "Nonlinear cyclotron resonance absorber for a microwave subnanosecond pulse generator powered by a helical-waveguide gyrotron traveling-wave tube", *Physical Review Applied*, vol. 13, 2020. DOI: 10.1103/physrevapplied.13.044033.

[60] J. L. Doane, "Design of circular corrugated waveguides to transmit millimeter waves at ITER", *Fusion Science and Technology*, vol. 53, no. 1, pp. 159–173, 2008. DOI: 10.13182/FST08-A1662.

[61] G. J. Linde, M. T. Ngo, B. G. Danly, W. J. Cheung, and V. Gregers-Hansen, "WARLOC: A high-power coherent 94 GHz radar", *IEEE Transactions on Aerospace and Electronic Systems*, vol. 44, no. 3, pp. 1102–1117, 2008. DOI: 10.1109/taes.2008.4655367.

[62] H. A. Haus, "Theory of mode locking with a fast saturable absorber", *Journal of Applied Physics*, vol. 46, no. 7, pp. 3049–3058, 1975. DOI: 10.1063/1.321997.

[63] H. Haus, "Theory of mode locking with a slow saturable absorber", *IEEE Journal of Quantum Electronics*, vol. 11, no. 9, pp. 736–746, 1975. DOI: 10.1109/JQE.1975.1068922.

[64] H. A. Haus, "Mode-locking of lasers", *IEEE Journal of Selected Topics in Quantum Electronics*, vol. 6, no. 6, pp. 1173–1185, 2000. DOI: 10.1109/2944.902165.

[65] E. P. Ippen, "Principles of passive mode locking", *Applied Physics B*, vol. 58, no. 3, pp. 159–170, 1994. DOI: 10.1007/BF01081309.

[66] O. E. Martinez, R. L. Fork, and J. P. Gordon, "Theory of passively mode-locked lasers for the case of a nonlinear complex-propagation coefficient", *Journal of the Optical Society of America B: Optical Physics*, vol. 2, no. 5, pp. 753–760, May 1985. DOI: 10.1364/JOSAB.2.000753.

[67] N. S. Ginzburg, E. R. Kocharovskaya, M. N. Vilkov, A. S. Sergeev, and S. E. Fil'chenkov, "Dissipative solitons in electron oscillators with a saturable absorber", *Physics of Plasmas*, vol. 25, no. 9, p. 093 111, 2018. DOI: 10.1063/1.5046651.

[68] N. S. Ginzburg, I. V. Zotova, A. S. Sergeev, *et al.*, "Mechanisms of amplification of ultrashort electromagnetic pulses in gyrotron traveling wave tube with helically corrugated waveguide", *Physics of Plasmas*, vol. 22, no. 11, p. 113 111, 2015. DOI: 10.1063/1.4935905.

[69] F. X. Kärtner, J. A. der Au, and U. Keller, "Mode-locking with slow and fast saturable absorbers-what's the difference?", *IEEE Journal of Selected Topics in Quantum Electronics*, vol. 4, no. 2, pp. 159–168, 1998. DOI: 10.1109/2944.686719.

[70] A. Gilmour, *Klystrons, traveling wave tubes, magnetrons, crossed-field amplifiers, and gyrotrons*. Artech House, 2011, ISBN: 978-1608071845.

[71] G. G. Denisov and M. G. Reznikov, "Corrugated cylindrical resonators for short-wavelength relativistic microwave oscillators", *Radiophysics and Quantum Electronics*, vol. 25, no. 5, pp. 407–413, 1982. DOI: 10.1007/BF01035315.

[72] B. Z. Katsenelenbaum, L. M. Del Rio, M. Pereyaslavets, M. Thumm, and M. S. Ayza, *Theory of nonuniform waveguides: The cross-section method*. Iet, 1998, ISBN: 978-0852969182.

[73] L. Zhang, W. He, K. Ronald, *et al.*, "Multi-mode coupling wave theory for helically corrugated waveguide", *IEEE Transactions on Microwave Theory and Techniques*, vol. 60, no. 1, pp. 1–7, 2012. DOI: 10.1109/TMTT.2011.2170848.

[74] S. J. Cooke and G. G. Denisov, "Linear theory of a wide-band gyro-TWT amplifier using spiral waveguide", *IEEE Transactions on Plasma Science*, vol. 26, no. 3, pp. 519–530, 1998. DOI: 10.1109/27.700786.

[75] B. G. Danly and R. J. Temkin, "Generalized nonlinear harmonic gyrotron theory", *The Physics of Fluids*, vol. 29, no. 2, pp. 561–567, 1986. DOI: 10.1063/1.865446.

[76] V. L. Bratman, Y. K. Kalynov, and V. N. Manuilov, "Large-orbit gyrotron operation in the terahertz frequency range", *Phys. Rev. Lett.*, vol. 102, p. 245 101, 24 Jun. 2009. DOI: 10.1103/PhysRevLett.102.245101.

[77] S. E. Tsimring, *Electron beams and microwave vacuum electronics*. John Wiley & Sons, 2006, vol. 191, ISBN: 978-0470048160.

[78] J. Trumpp, "Design and numerical optimization of a cusp gun for high-power-amplifiers in the sub-THz-range", 31.03.02; LK 01, M.S. thesis, Karlsruher Institut für Technologie (KIT), 2018.

[79] M. J. Rhee and W. W. Destler, "Relativistic electron dynamics in a cusped magnetic field", *The Physics of Fluids*, vol. 17, no. 8, pp. 1574–1581, 1974. DOI: 10.1063/1.1694936.

[80] W. W. Destler and M. J. Rhee, "Radial and axial compression of a hollow electron beam using an asymmetric magnetic cusp", *The Physics of Fluids*, vol. 20, no. 9, pp. 1582–1584, 1977. DOI: 10.1063/1.862029.

[81] J. G. Pagonakis and J. L. Vomvoridis, "The self-consistent 3d trajectory electrostatic code ariadne for gyrotron beam tunnel simulation", in *Infrared and Millimeter Waves, Conference Digest of the 2004 Joint 29th International Conference on 2004 and 12th International Conference on Terahertz Electronics, 2004.*, 2004, pp. 657–658. DOI: 10.1109/ICIMW.2004.1422262.

[82] S. Illy, J. Zhang, and J. Jelonnek, "Gyrotron electron gun and collector simulation with the ESRAY beam optics code", in *2015 IEEE International Vacuum Electronics Conference (IVEC)*, 2015, pp. 1–2. DOI: 10.1109/IVEC.2015.7223779.

[83] G. G. Denisov, A. A. Bogdashov, I. G. Gachev, S. V. Mishakin, and S. V. Samsonov, "New radiation input/output systems for millimeter-wave gyrotron traveling-wave tubes", *Radiophysics and Quantum Electronics*, vol. 58, no. 10, pp. 769–776, 2016. DOI: 10.1007/s11141-016-9649-y.

[84] M. Thumm and H. Kumri, "High-power TE11 and TM11 circular polarizers in oversized waveguide at 70 GHz", in *1987 Twelth International Conference on Infrared and Millimeter Waves*, 1987, pp. 336–337. DOI: 10.1109/IRMM.1987.9127056.

[85] P. I. Sandsmark, "Effect of ellipticity on dominant-mode axial ratio in nominally circular waveguides", *IRE Transactions on Microwave Theory and Techniques*, vol. 3, no. 5, pp. 15–20, 1955. DOI: 10.1109/TMTT.1955.1124971.

[86] J. L. Doane, "Polarization converters for circular waveguide modes", *International Journal of Electronics*, vol. 61, no. 6, pp. 1109–1133, 1986. DOI: 10.1080/00207218608920943.

[87] C. W. Robertson, A. R. Young, K. Ronald, A. W. Cross, and C. G. Whyte, "Circular polariser for use in a gyro-travelling wave amplifier", *IET Microwaves, Antennas Propagation*, vol. 7, no. 11, pp. 942–948, 2013. DOI: 10.1049/iet-map.2012.0415.

[88] S. V. Samsonov, A. A. Bogdashov, I. G. Gachev, G. G. Denisov, and S. V. Mishakin, "Proof-of-principle experiment on high-power gyrotron traveling-wave tube with a microwave system for driving and extracting power through one window", *IEEE Microwave and Wireless Components Letters*, vol. 26, no. 4, pp. 288–290, 2016. DOI: 10.1109/LMWC.2016.2537541.

[89] S. N. Vlasov, L. I. Zagriadskaia, and M. I. Petelin, "Transformation of a whispering gallery mode, propagating in a circular waveguide, into a beam of waves", *Radiotekhnika i Elektronika*, vol. 20, pp. 2026–2030, Oct. 1975.

[90] P. McElhinney, C. R. Donaldson, J. E. McKay, *et al.*, "An output coupler for a W-band high power wideband gyroamplifier", *IEEE Transactions on Electron Devices*, vol. 64, no. 4, pp. 1763–1766, 2017. DOI: 10.1109/TED.2017.2660304.

[91] L. Zhang, W. He, C. R. Donaldson, *et al.*, "Optimization and measurement of a smoothly profiled horn for a W-band gyro-TWA", *IEEE Transactions on Electron Devices*, vol. 64, no. 6, pp. 2665–2669, 2017. DOI: 10.1109/TED.2017.2687949.

[92] D. M. Pozar, *Microwave engineering*, 4. ed. Hoboken, NJ: Wiley, 2012, ISBN: 9780470631553. [Online]. Available: http://www.gbv.de/dms/ilmenau/toc/666138737.PDF.

[93] H.-U. Nickel, "Plane transverse waveguide windows: survey of formulas for reflection, transmission, and absorption", in *16th International Conference on Infrared and Millimeter Waves*, M. Q. Tran, Ed., International Society for Optics and Photonics, vol. 1576, SPIE, 1991, pp. 499–500. DOI: 10.1117/12.2297936.

[94] H.-U. Nickel, "Hochfrequenztechnische Aspekte zur Entwicklung rückwirkungsarmer Ausgangsfenster für Millimeterwellengyrotrons hoher Leistung", *EUR(Luxembourg)*, 1995. DOI: 10.5445/IR/46595.

[95] Y. Zhang, L. Zhang, W. He, *et al.*, "Design and measurement of a W-band Brewster window", *IEEE Microwave and Wireless Components Letters*, vol. 25, no. 12, pp. 826–828, 2015. DOI: 10.1109/LMWC.2015.2495110.

[96] C. R. Donaldson, W. He, L. Zhang, and A. W. Cross, "A W-band multi-layer microwave window for pulsed operation of gyro-devices", *IEEE Microwave and Wireless Components Letters*, vol. 23, no. 5, pp. 237–239, 2013. DOI: 10.1109/LMWC.2013.2251619.

[97] Y. Wang, G. Liu, W. Wang, C. Fang, Z. Wu, and Y. Luo, "Millimetre-wave design and verification of a meta-surface dielectric window made of polytetrafluoroethylene in Ka- and Q-band", *IET Microwaves, Antennas & Propagation*, vol. 14, no. 15, pp. 2007–2010, 2020. DOI: 10.1049/iet-map.2020.0385.

[98] J. E. Rowe, *Nonlinear electron-wave interaction phenomena*. Academic Press, 2013, ISBN: 978-1483211770.

[99] C. S. Kou, K. R. Chu, D. B. McDermott, and N. C. Luhmann, "Effective bandwidth and the Kompfner dip for cyclotron autoresonance maser amplifiers", *Phys. Rev. E*, vol. 51, pp. 642–648, 1 Jan. 1995. DOI: 10.1103/PhysRevE.51.642.

[100] M. V. Oleinik and D. I. Trubetskov, "A small signal theory of gyrodevices using the concept of space-charge waves", *IEEE Transactions on Plasma Science*, vol. 24, no. 3, pp. 707–717, 1996. DOI: 10.1109/27.533072.

[101] R. W. Gould, "A coupled mode description of the backward wave oscillator and the Kompfner dip condition", *IRE Transactions on Electron Devices*, vol. 2, no. 4, pp. 37–42, 1955. DOI: 10.1109/T-ED.1955.14089.

[102] J. L. Doane, "Grating polarizers in waveguide miter bends", *International Journal of Infrared and Millimeter Waves*, vol. 13, no. 11, pp. 1727–1743, Nov. 1992. DOI: 10.1007/BF01010741.

[103] R. C. Jones, "A new calculus for the treatment of optical systems", *Journal of the Optical Society of America*, vol. 32, no. 8, pp. 486–493, Aug. 1942. DOI: 10.1364/JOSA.32.000486.

[104] S. V. Samsonov, V. I. Belousov, A. A. Bogdashov, G. G. Denisov, S. V. Mishakin, and D. I. Sobolev, "Quasi-optical orthomode splitters for input-output of a powerful W-band gyro-TWT", *IEEE Transactions on Electron Devices*, vol. 65, no. 10, pp. 4600–4606, 2018. DOI: 10.1109/TED.2018.2866030.

[105] C. W. Berry and M. Jarrahi, "Broadband terahertz polarizing beam splitter on a polymer substrate", *Journal of Infrared, Millimeter, and Terahertz Waves*, vol. 33, no. 2, pp. 127–130, 2012. DOI: 10.1007/s10762-011-9858-6.

[106] E. Marx, T. A. Germer, T. V. Vorburger, and B. C. Park, "Angular distribution of light scattered from a sinusoidal grating", *Appl. Opt.*, vol. 39, no. 25, pp. 4473–4485, Sep. 2000. DOI: 10.1364/AO.39.004473.

[107] L. Botten, M. Cadilhac, G. Derrick, *et al.*, *Electromagnetic theory of gratings*. Springer Science & Business Media, 2013, vol. 22, ISBN: 978-3642815027. DOI: 10.1007/978-3-642-81500-3.

[108] C. A. Palmer and E. G. Loewen, *Diffraction grating handbook*. Thermo RGL New York, 2002, vol. 5, ISBN: 978-0824799236.

[109] H. Kogelnik, "Coupled wave theory for thick hologram gratings", *The Bell System Technical Journal*, vol. 48, no. 9, pp. 2909–2947, 1969. DOI: 10.1002/j.1538-7305.1969.tb01198.x.

[110] D. J. Cooke and L. Solymar, "Comparison of two-wave geometrical optics and N-wave theories for volume-phase holograms", *Journal of the Optical Society of America (1917-1983)*, vol. 70, p. 1631, Jan. 1980.

[111] C. A. Balanis, *Antenna theory analysis and design*. 2005, ISBN: 978-0471667827.

[112] T. Ii, S. Kubo, T. Shimozuma, *et al.*, "Design of polarizers for a megawatt long-pulse millimeter-wave transmission line on the large helical device", *Review of Scientific Instruments*, vol. 86, no. 2, p. 023 502, 2015. DOI: 10.1063/1.4907355.

[113] D. Haas, A. Marek, M. Thumm, J. Jelonnek, M. Jirousek, and M. Peichl, "Broadband polarizer miter bend for high-power radar applications", in *2020 German Microwave Conference (GeMiC)*, 2020, pp. 76–79. DOI: 10.5445/IR/1000119933.

[114] D. Haas, "Auslegung eines übermodigen Übertragungssystems fürein mmW-Hochleistungsradar hoher Bandbreite", German, M.S. thesis, Karlsruher Institut für Technologie (KIT), 2019.

[115] M. Jayawardene and J. Vardaxoglou, "3-d EM simulation of infinite periodic arrays and finite frequency selective horns", 2006.

[116] C. M. Studio, *CST studio suite 2019*, 2019.

[117] B. Goplen, L. Ludeking, D. Smith, and G. Warren, "User-configurable MAGIC for electromagnetic PIC calculations", *Computer Physics Communications*, vol. 87, no. 1, pp. 54–86, 1995, Particle Simulation Methods. DOI: 10.1016/0010-4655(95)00010-D.

[118] C.-D. Munz, M. Auweter-Kurtz, S. Fasoulas, *et al.*, "Coupled particle-in-cell and direct simulation monte carlo method for simulating reactive plasma flows", *Comptes Rendus Mécanique*, vol. 342, no. 10-11, pp. 662–670, 2014. DOI: 10.1016/j.crme.2014.07.005.

[119] S. Kern, "Numerische Simulation der Gyrotron-Wechselwirkung in koaxialen Resonatoren", Ph.D. dissertation, 1996. DOI: 10.5445/IR/55396.

[120] J. Jelonnek, *Untersuchung des Lastverhaltens von Gyrotrons*. VDI-Verlag, 2000, ISBN: 978-3183297214.

[121] Avramides, K. A., Pagonakis, I. Gr., Iatrou, C. T., and Vomvoridis, J. L., "Euridice: A code-package for gyrotron interaction simulations and cavity design", *EPJ Web of Conferences*, vol. 32, p. 04 016, 2012. DOI: 10.1051/epjconf/20123204016.

[122] S. Alberti, T. M. Tran, K. A. Avramides, F. Li, and J. Hogge, "Gyrotron parasitic-effects studies using the time-dependent self-consistent monomode code TWANG", in *2011 International Conference on Infrared, Millimeter, and Terahertz Waves*, 2011, pp. 1–2. DOI: 10.1109/irmmw-THz.2011.6105097.

[123] C. Y. Wang, "Cutoff frequencies of perturbed circular waveguides and polygonal waveguides", *Journal of Electromagnetic Waves and Applications*, vol. 16, no. 2, pp. 151–158, 2002. DOI: 10.1163/156939302X00813.

[124] A. Malygin, S. Illy, I. G. Pagonakis, *et al.*, "Analysis of mode competition in 10kW/28GHz gyrotron", in *2013 IEEE 14th International Vacuum Electronics Conference (IVEC)*, 2013, pp. 1–2. DOI: 10.1109/IVEC.2013.6571021.

[125] Q. Zhao, S. Yu, and T. Zhang, "Theoretical study of mode competition in terahertz gyrotron with second harmonic oscillation", *IEEE Transactions on Plasma Science*, vol. 43, no. 9, pp. 3155–3160, 2015. DOI: 10.1109/TPS.2015.2464491.

[126] C.-H. Du, P.-K. Liu, Q.-Z. Xue, and M.-H. Wang, "Effect of a backward wave on the stability of an ultrahigh gain gyrotron traveling-wave amplifier", *Physics of Plasmas*, vol. 15, no. 12, p. 123 107, 2008. DOI: 10.1063/1.3041161.

[127] F. Braunmueller, T. M. Tran, Q. Vuillemin, *et al.*, "TWANG-PIC, a novel gyro-averaged one-dimensional particle-in-cell code for interpretation of gyrotron experiments", *Physics of Plasmas*, vol. 22, no. 6, p. 063 115, 2015. DOI: 10.1063/1.4923299.

[128] M. Abramowitz, I. A. Stegun, and R. H. Romer, "Handbook of mathematical functions with formulas, graphs, and mathematical tables", *American Journal of Physics*, vol. 56, no. 10, pp. 958–958, 1988. DOI: 10.1119/1.15378.

[129] R. G. Kleva, T. M. Antonsen, and B. Levush, "The effect of the time-dependent self-consistent electrostatic field on gyrotron operation", *The Physics of Fluids*, vol. 31, no. 2, pp. 375–386, 1988. DOI: 10.1063/1.866871.

[130] J. Qiang and R. D. Ryne, "Parallel 3d poisson solver for a charged beam in a conducting pipe", *Computer Physics Communications*, vol. 138, no. 1, pp. 18–28, 2001. DOI: 10.1016/S0010-4655(01)00185-0.

[131] J. Crank and P. Nicolson, "A practical method for numerical evaluation of solutions of partial differential equations of the heat-conduction type", *Advances in Computational Mathematics*, vol. 6, no. 1, pp. 207–226, 1996. DOI: 10.1007/BF02127704.

[132] Intel Corporation, *Intel math kernel library developer reference*, 2016. [Online]. Available: https://www.intel.com/content/dam/develop/external/us/en/documents/onemkl-developerreference-c.pdf.

[133] C. S. Peskin, "The immersed boundary method", *Acta Numerica*, vol. 11, p. 479 517, 2002. DOI: 10.1017/S0962492902000077.

[134] J. M. Dawson, "Particle simulation of plasmas", *Reviews of Modern Physics*, vol. 55, pp. 403–447, 2 Apr. 1983. DOI: 10.1103/RevModPhys.55.403.

[135] C. Runge, "Ueber die numerische Aufloesung von Differentialgleichungen", *Mathematische Annalen*, vol. 46, no. 2, pp. 167–178, 1895.

[136] J. P. Boris, "Relativistic plasma simulation-optimization of a hybrid code", in *Proc. Fourth Conf. Num. Sim. Plasmas*, 1970, pp. 3–67.

[137] B. Ripperda, F. Bacchini, J. Teunissen, *et al.*, "A comprehensive comparison of relativistic particle integrators", *The Astrophysical Journal Supplement Series*, vol. 235, no. 1, p. 21, Mar. 2018. DOI: 10.3847/1538-4365/aab114.

[138] ISO, *ISO/slash IEC 14882:2017 Information technology — Programming languages — C++*, Fifth. pub-ISO, Dec. 2017, p. 1605. [Online]. Available: https://www.iso.org/standard/68564.html.

[139] R. Ierusalimschy, L. H. d. Figueiredo, and W. Celes, *Lua 5.1 Reference Manual*. Lua.Org, 2006, ISBN: 8590379833.

[140] I. G. Pagonakis, G. Gantenbein, J. Jelonnek, *et al.*, "Design of the EU-1MW gyrotron for ITER", in *2013 IEEE 14th International Vacuum Electronics Conference (IVEC)*, 2013, pp. 1–2. DOI: 10.1109/IVEC.2013.6571106.

[141] N. Mattor, T. J. Williams, and D. W. Hewett, "Algorithm for solving tridiagonal matrix problems in parallel", *Parallel Computing*, vol. 21, no. 11, pp. 1769–1782, 1995. DOI: 10.1016/0167-8191(95)00033-0.

[142] N. S. Ginzburg, G. G. Denisov, M. N. Vilkov, *et al.*, "PIC simulations of Ka-band ultra-short pulse oscillator with resonance cyclotron absorber in the feedback loop", *EPJ Web Conf.*, vol. 187, p. 01 021, 2018. DOI: 10.1051/epjconf/201818701021.

[143] M. S. Misko, "Multiphysik-Simulation von Wechselwirkungsräumen fürzukünftige Gyro-TWTs", German, 31.03.02; LK 01, Abschlussarbeit - Bachelor, Karlsruher Institut für Technologie (KIT), 2020.

[144] C. R. Donaldson, W. He, A. W. Cross, *et al.*, "A cusp electron gun for millimeter wave gyrodevices", *Applied Physics Letters*, vol. 96, no. 14, p. 141 501, 2010. DOI: 10.1063/1.3374888.

[145] N. S. Ginzburg, R. M. Rozental, A. S. Sergeev, I. V. Zotova, and V. P. Tarakanov, "Chaotic millimeter wave generation in a helical-waveguide gyro-TWT with delayed feedback", *Physics of Plasmas*, vol. 23, no. 10, p. 103 106, 2016. DOI: 10.1063/1.4964918.

[146] Y. Chen, F. X. Kärtner, U. Morgner, *et al.*, "Dispersion-managed mode locking", *J. Opt. Soc. Am. B*, vol. 16, no. 11, pp. 1999–2004, Nov. 1999. DOI: 10.1364/JOSAB.16.001999.

[147] G. Peeters, "A large set of audio features for sound description (similarity and classification) in the cuidado project", *CUIDADO Ist Project Report*, vol. 54, no. 0, pp. 1–25, 2004.

[148] S. V. Samsonov, A. A. Bogdashov, G. G. Denisov, I. G. Gachev, and S. V. Mishakin, "Cascade of two W-band helical-waveguide gyro-TWTs with high gain and output power: Concept and modeling", *IEEE Transactions on Electron Devices*, vol. 64, no. 3, pp. 1305–1309, 2017. DOI: 10.1109/TED.2016.2646065.

[149] A. Detken, E. H. Hardy, M. Ernst, and B. H. Meier, "Simple and efficient decoupling in magic-angle spinning solid-state NMR: The XiX scheme", *Chemical Physics Letters*, vol. 356, no. 3, pp. 298–304, 2002. DOI: 10.1016/S0009-2614(02)00335-4.

[150] A. Marek, "Development of a vector analysis code for the simulation of electromagnetic fields in the quasi-optical system of gyrotrons", M.S. thesis, Karlsruher Institut für Technologie (KIT), 2016.

[151] A. Marek, J. Jin, J. Jelonnek, and A.-S. Müller, *Development of a vector analysis code for the simulation of electromagnetic fields in the quasi-optical system of gyrotrons*, Paper presented at the Workshop on RF Heating Technology of Fusion Plasma (US-EU-JPN), Leinsweiler, September 21-23, 2016, 31.03.02; LK 01, 2016.

[152] M. Bebendorf and S. Kunis, "Recompression techniques for adaptive cross approximation", *The Journal of Integral Equations and Applications*, vol. 21, no. 3, pp. 331–357, 2009. DOI: 10.1216/JIE-2009-21-3-331.

[153] A. Heldring, J. M. Tamayo, C. Simon, E. Ubeda, and J. M. Rius, "Sparsified adaptive cross approximation algorithm for accelerated method of moments computations", *IEEE Transactions on Antennas and Propagation*, vol. 61, no. 1, pp. 240–246, 2013. DOI: 10.1109/TAP.2012.2215292.

[154] W. C. Gibson, "The method of moments in electromagnetics", 2007.

[155] R. F. Harrington, *Field Computation by Moment Methods*. Wiley-IEEE Press, 1993, ISBN: 0780310144.

[156] B. G. Galerkin, "Series solution of some problems of elastic equilibrium of rods and plates", *Vestnik inzhenerov i tekhnikov*, vol. 19, no. 7, pp. 897–908, 1915.

[157] S. Rao, D. Wilton, and A. Glisson, "Electromagnetic scattering by surfaces of arbitrary shape", *IEEE Transactions on Antennas and Propagation*, vol. 30, no. 3, pp. 409–418, 1982. DOI: 10.1109/TAP.1982.1142818.

[158] W. Cai, "High-order mixed current basis functions for electromagnetic scattering of curved surfaces", *Journal of Scientific Computing*, vol. 14, no. 1, pp. 73–105, 1999. DOI: 10.1023/A:1025624822162.

[159] K. Zhao, M. N. Vouvakis, and J. F. Lee, "The adaptive cross approximation algorithm for accelerated method of moments computations of EMC problems", *IEEE Transactions on Electromagnetic Compatibility*, vol. 47, no. 4, pp. 763–773, 2005. DOI: 10.1109/TEMC.2005.857898.

[160] C.-C. Lu and W. C. Chew, "A multilevel algorithm for solving a boundary integral equation of wave scattering", *Microw. Opt. Technol. Lett.*, vol. 7, no. 10, pp. 466–470, Jul. 1994. DOI: 10.1002/mop.4650071013.

[161] J. M. Tamayo, A. Heldring, and J. M. Rius, "Multilevel adaptive cross approximation (MLACA)", *IEEE Transactions on Antennas and Propagation*, vol. 59, no. 12, pp. 4600–4608, 2011. DOI: 10.1109/TAP.2011.2165476.

[162] J. M. Rius, J. Parron, A. Heldring, J. M. Tamayo, and E. Ubeda, "Fast iterative solution of integral equations with method of moments and matrix decomposition algorithm-singular value decomposition", *IEEE Transactions on Antennas and Propagation*, vol. 56, no. 8, pp. 2314–2324, 2008. DOI: 10.1109/TAP.2008.926762.

[163] Y. Saad and M. H. Schultz, "Gmres: A generalized minimal residual algorithm for solving nonsymmetric linear systems", *SIAM J. Sci. and Stat. Comput.*, vol. 7, no. 3, pp. 856–869, Jul. 1986. DOI: 10.1137/0907058.

[164] W. E. Arnoldi, "The principle of minimized iterations in the solution of the matrix eigenvalue problem", *Quarterly of Applied Mathematics*, vol. 9, no. 1, pp. 17–29, 1951. [Online]. Available: http://www.jstor.org/stable/43633863.

[165] G. C. Hsiao and R. E. Kleinman, "Mathematical foundations for error estimation in numerical solutions of integral equations in electromagnetics", *IEEE Transactions on Antennas and Propagation*, vol. 45, no. 3, pp. 316–328, 1997. DOI: 10.1109/8.558648.

[166] M. Bebendorf, "Hierarchical LU decomposition-based preconditioners for BEM", *Computing*, vol. 74, no. 3, pp. 225–247, 2005. DOI: 10.1007/s00607-004-0099-6.

[167] X. Antoine, A. Bendali, and M. Darbas, "Analytic preconditioners for the electric field integral equation", *Int. J. Numer. Meth. Engng.*, vol. 61, no. 8, pp. 1310–1331, Oct. 2004. DOI: 10.1002/nme.1106.

[168] Y. Saad, "A flexible inner-outer preconditioned GMRES algorithm", *SIAM J. Sci. Comput.*, vol. 14, no. 2, pp. 461–469, Mar. 1993. DOI: 10.1137/0914028.

[169] B. Carpentieri, I. S. Duff, L. Giraud, and G. Sylvand, "Combining fast multipole techniques and an approximate inverse preconditioner for large electromagnetism calculations", *SIAM Journal on Scientific Computing*, vol. 27, no. 3, pp. 774–792, 2005. DOI: 10.1137/040603917.

[170] T. Malas and L. Giirel, "The solution of large efie problems via preconditioned multilevel fast multipole algorithm", 2007. DOI: 10.1049/ic.2007.1165.

[171] A. Ida, T. Iwashita, T. Mifune, and Y. Takahashi, "Variable preconditioning of Krylov subspace methods for hierarchical matrices with adaptive cross approximation", *IEEE Transactions on Magnetics*, vol. 52, no. 3, pp. 1–4, 2016. DOI: 10.1109/TMAG.2015.2464104.

[172] T. Rzesnicki, B. Piosczyk, S. Kern, *et al.*, "2.2 MW record power of the 170 GHz european preprototype coaxial-cavity gyrotron for ITER", *IEEE Transactions on Plasma Science*, vol. 38, no. 6, pp. 1141–1149, 2010. DOI: 10.1109/TPS.2010.2040842.

[173] S. E. Kurt, V. Thumma, C. Hong, A. Sukumaran-Rajam, and P. Sadayappan, "Characterization of data movement requirements for sparse matrix computations on GPUs", in *2017 IEEE 24th International Conference on High Performance Computing (HiPC)*, 2017, pp. 283–293. DOI: 10.1109/HiPC.2017.00040.

[174] C. Sanderson and R. Curtin, "Armadillo: A template-based C++ library for linear algebra", *Journal of Open Source Software*, vol. 1, no. 2, p. 26, 2016. DOI: 10.21105/joss.00026.

[175] OpenMP Architecture Review Board, *OpenMP 5.0 reference guide*, May 2019. [Online]. Available: https://www.openmp.org/wp-content/uploads/OpenMPRef-5.0-0519-print.pdf.

[176] L. Clarke, I. Glendinning, and R. Hempel, "The MPI message passing interface standard", in *Programming environments for massively parallel distributed systems*, Springer, 1994, pp. 213–218. DOI: 10.1007/978-3-0348-8534-8_21.

[177] NVIDIA Corporation, *Cuda toolkit programming guide v11.0.0*, 2020. [Online]. Available: https://developer.nvidia.com/cuda-11.0-download-archive.

[178] J. Schöberl, "Netgen an advancing front 2d/3d-mesh generator based on abstract rules", *Computing and Visualization in Science*, vol. 1, no. 1, pp. 41–52, 1997. DOI: 10.1007/s007910050004.

[179] Intel Corporation, "Advanced vector extensions programming reference", *Intel Corporation*, 2011. [Online]. Available: https://software.intel.com/sites/default/files/m/0/5/7/7/f/19151-AVX_319433_005.pdf.

[180] G. Burt, S. V. Samsonov, K. Ronald, *et al.*, "Dispersion of helically corrugated waveguides: Analytical, numerical, and experimental study", *Phys. Rev. E*, vol. 70, p. 046 402, 4 Oct. 2004. DOI: 10.1103/PhysRevE.70.046402.

[181] S. V. Mishakin and S. V. Samsonov, "Analysis of dispersion and losses in helically corrugated metallic waveguides by 2-d vector finite-element method", *IEEE Transactions on Microwave Theory and Techniques*, vol. 59, no. 9, pp. 2189–2196, 2011. DOI: 10.1109/TMTT.2011.2160201.

[182] A. Marek, K. A. Avramidis, N. S. Ginzburg, *et al.*, "Benefits of advanced full-wave vector analysis codes for the design of high-power microwave tubes", in *2018 11th German Microwave Conference (GeMiC)*, 2018, pp. 279–282. DOI: 10.23919/GEMIC.2018.8335084.

[183] A. Marek, K. A. Avramidis, S. M. Copplestone, *et al.*, "Contributions to the joint DFG-RSF project - generation of ultra-short microwave pulses -", *EPJ Web Conf.*, vol. 187, p. 01 027, 2018. DOI: 10.1051/epjconf/201818701027.

[184] A. Marek, K. A. Avramidis, N. S. Ginzburg, *et al.*, "Simple feedback system for passive mode locked gyro-devices at 263 GHz", in *2020 German Microwave Conference (GeMiC)*, 2020, pp. 56–59. DOI: 10.5445/IR/1000119937.

[185] A. Marek, K. A. Avramidis, N. S. Ginzburg, *et al.*, "Extended feedback system for coupled sub-THz gyro-devices to provide new regimes of operation", *IEEE Transactions on Electron Devices*, pp. 1–7, 2020. DOI: 10.1109/TED.2020.3028531.

[186] P. P. Woskov, V. S. Bajaj, M. K. Hornstein, R. J. Temkin, and R. G. Griffin, "Corrugated waveguide and directional coupler for CW 250-GHz gyrotron DNP experiments", *IEEE Transactions on Microwave Theory and Techniques*, vol. 53, no. 6, pp. 1863–1869, 2005. DOI: 10.1109/TMTT.2005.848097.

[187] J. L. Doane and C. P. Moeller, "HE11 mitre bends and gaps in a circular corrugated waveguide", *International Journal of Electronics*, vol. 77, no. 4, pp. 489–509, 1994. DOI: 10.1080/00207219408926081.

[188] D. Wagner, F. Leuterer, W. Kasparek, J. Stober, and A. S. D. E. X. U. Team, "Minimization of the ohmic loss of grooved polarizer mirrors in high-power ECRH systems", *Journal of Infrared, Millimeter, and Terahertz Waves*, vol. 38, no. 2, pp. 191–205, 2017. DOI: 10.1007/s10762-016-0329-y.

[189] E. J. Kowalski, D. S. Tax, M. A. Shapiro, *et al.*, "Linearly polarized modes of a corrugated metallic waveguide", *IEEE Transactions on Microwave Theory and Techniques*, vol. 58, no. 11, pp. 2772–2780, 2010. DOI: 10.1109/TMTT.2010.2078972.

[190] L. Zhang, W. He, C. R. Donaldson, J. Garner, and A. W. Cross, "Measurement of an upgraded input coupling system for W-band gyro-TWA", in *2017 Eighteenth International Vacuum Electronics Conference (IVEC)*, 2017, pp. 1–3. DOI: 10.1109/IVEC.2017.8289708.

[191] L. Zhang, C. R. Donaldson, A. W. Cross, and W. He, "A pillbox window with impedance matching sections for a W-band gyro-TWA", *IEEE Electron Device Letters*, vol. 39, no. 7, pp. 1081–1084, 2018. DOI: 10.1109/LED.2018.2834859.

[192] E. A. Nanni, S. Jawla, S. M. Lewis, M. A. Shapiro, and R. J. Temkin, "Photonic-band-gap gyrotron amplifier with picosecond pulses", *Applied Physics Letters*, vol. 111, no. 23, p. 233 504, 2017. DOI: 10.1063/1.5006348.

[193] V. L. Bratman, G. G. Denisov, S. V. Samsonov, A. W. Cross, A. D. R. Phelps, and W. Xe, "High-efficiency wideband gyro-TWTs and gyro-BWOs with helically corrugated waveguides", *Radiophysics and Quantum Electronics*, vol. 50, no. 2, pp. 95–107, 2007. DOI: 10.1007/s11141-007-0009-9.

[194] S. V. Samsonov, G. G. Denisov, V. L. Bratman, *et al.*, "Frequency-tunable CW gyro-BWO with a helically rippled operating waveguide", *IEEE Transactions on Plasma Science*, vol. 32, no. 3, pp. 884–889, 2004. DOI: 10.1109/TPS.2004.828871.

[195] C. S. Kou, S. H. Chen, L. R. Barnett, H. Y. Chen, and K. R. Chu, "Experimental study of an injection-locked gyrotron backward-wave oscillator", *Phys. Rev. Lett.*, vol. 70, pp. 924–927, 7 Feb. 1993. DOI: 10.1103/PhysRevLett.70.924.

[196] A. A. Koronovsky, D. I. Trubetskov, and A. E. Khramov, "Influence of an external signal on self-oscillations in the distributed system helical electron beam-backward electromagnetic wave", *Radiophysics and Quantum Electronics*, vol. 45, no. 9, pp. 706–724, 2002. DOI: 10.1023/A:1021797418844.

[197] K. A. Sharypov, S. A. Shunailov, N. S. Ginzburg, *et al.*, "Development of the concept of high-power microwave oscillators with phase locking by an external signal", *Radiophysics and Quantum Electronics*, vol. 62, no. 7, pp. 447–454, 2019. DOI: 10.1007/s11141-020-09990-2.

[198] A. E. Khramov, "Signal amplification in a gyro-backward-wave tube", *Technical Physics Letters*, vol. 29, no. 6, pp. 467–470, 2003. DOI: 10.1134/1.1589560.

[199] M. V. Beloglazkina, A. A. Koronovskii, and A. E. Hramov, "Nonlinear nonstationary processes in a pair of coupled gyro-backward-wave oscillators", *Technical Physics*, vol. 54, no. 6, pp. 775–782, 2009. DOI: 10.1134/S1063784209060036.

[200] K. A. Bagrinovskii and S. K. Godunov, "Difference schemes for multidimensional problems", in *Doklady Akademii Nauk*, Russian Academy of Sciences, vol. 115, 1957, pp. 431–433.

[201] G. Strang, "On the construction and comparison of difference schemes", *SIAM Journal on Numerical Analysis*, vol. 5, no. 3, pp. 506–517, 1968. DOI: 10.1137/0705041.

[202] S. Wang, A. Docherty, B. S. Marks, and C. R. Menyuk, "Comparison of numerical methods for modeling laser mode locking with saturable gain", *Journal of the Optical Society of America B: Optical Physics*, vol. 30, no. 11, pp. 3064–3074, Nov. 2013. DOI: 10.1364/JOSAB.30.003064.

[203] M. Henderson, S. Alberti, P. Benin, *et al.*, "EU developments of the ITER ECRH system", *Fusion Engineering and Design*, vol. 82, no. 5, pp. 454–462, 2007, Proceedings of the 24th Symposium on Fusion Technology. DOI: 10.1016/j.fusengdes.2007.01.029.

[204] G. Dammertz, S. Alberti, D. Bariou, *et al.*, "140 GHz high-power gyrotron development for the stellarator W7-X", *Fusion Engineering and Design*, vol. 74, no. 1, pp. 217–221, 2005, Proceedings of the 23rd Symposium of Fusion Technology. DOI: 10.1016/j.fusengdes.2005.06.067.

[205] K. J. Brunner, H. Braune, V. Erckmann, *et al.*, *Continuous high power microwave heating at the W7-X stellarator*, 2017. DOI: 10.1051/epjconf/201714903011.

[206] T. Ruess, K. A. Avramidis, G. Gantenbein, *et al.*, "Automated generation of high-order modes for tests of quasi-optical systems of gyrotrons for W7-X stellarator", in *2019 12th German Microwave Conference (GeMiC)*, 2019, pp. 226–228. DOI: 10.23919/GEMIC.2019.8698142.

[207] M. Pereyaslavets, O. Braz, S. Kern, M. Losert, A. Mobius, and M. Thumm, "Improvements of mode converters for low-power excitation of gyrotron-type modes", *International Journal of Electronics*, vol. 82, no. 1, pp. 107–116, 1997. DOI: 10.1080/002072197136291.

[208] D. Wagner, J. Stober, F. Leuterer, *et al.*, "Status, operation, and extension of the ECRH system at ASDEX upgrade", *Journal of Infrared, Millimeter, and Terahertz Waves*, vol. 37, no. 1, pp. 45–54, 2016. DOI: 10.1007/s10762-015-0187-z.

[209] W. Kasparek, A. Fernandez, F. Hollmann, and R. Wacker, "Measurements of ohmic losses of metallic reflectors at 140 GHz using a 3-mirror resonator technique", *International Journal of Infrared and Millimeter Waves*, vol. 22, no. 11, pp. 1695–1707, 2001. DOI: 10.1023/A:1015064616703.

Acknowledgment

The presented work was performed during my time as research assistant at the Institute for Pulsed Power and Microwave Technology (IHM) at the Karlsruhe Institute of Technology (KIT). This work would not have been accomplished without the support that I received from many people.

First and foremost, I want to express my sincere and deepest thanks to Prof. Dr.-Ing. John Jelonnek for giving me the opportunity to participate in the very exciting research on gyrotron amplifiers and for his steady support at the Institute for Pulsed Power and Microwave Technology (IHM) at KIT. His continuous supportive and valuable feedback at every stage of my research work encouraged me to give my best. Apart from the technical knowledge, I learned many helpful skills from him.

Sincere thanks also to Prof. Dr.-Ing. Arne Jacobfor volunteering as co-Referee of this thesis and for his helpful feedback to my work.

I would like to express my deep gratitude to Prof. Dr. rer. nat. Dr. h.c. Manfred Thumm for the supportive and motivating involvement in my work. Through the course of this work, discussions with Prof. Thumm initiated many activities and helped me to keep up to date with the advancement in the field of vacuum electron devices.

A big thanks goes to Dr. Stefan Illy for his strong support during my doctoral research time. Without his support in both scientific and technical questions, this work would not have been possible.

Additionally, I would like to thank all the members of the IHM for their support, in particular Dr. Gerd Gantenbein, Dr. Jianbo Jin, Dr. Tomasz Rzesnicki, Dr. Sebastian Stanculovic, Dipl.-Ing Thorsten Kobarg and Dipl.-Ing Jörg Weggen. I am furthermore really grateful to Prof. Dr. Konstantinos Avramidis for his support. I would also like to thank secretariats of the institute, Mrs. Martina Huber and Mrs. Melanie Mai for supporting me in every possible way.

I kindly thank all my former and current Ph.D. colleagues at the IHM-KIT for providing me a homely environment and their continued help, particularly,

Benjamin Ell, Tobias Ruess, Julia Hofele, Laurent Krier, Lukas Feuerstein, Max Vöhringer, Dr.-Ing. Chuanren Wu, and Dr.-Ing. Sebastian Ruess.

I am thankful to Prof. Dr. Naum Samuilovich Ginzburg, Federal research center Institute of Applied Physics of the Russian Academy of Sciences, for showing kind interest in my work and our fruitful discussions.

Above all, a big thanks goes to my parents, Andrea and Matthias Marek, for their continuous support in all phases of my life. Many thanks also to my brother, Felix Marek, my girlfriend Arada Jaidee and my friend Daniel Săvoiu, for the great times and motivating support.

Karlsruhe, September 2022
Alexander Marek